A quantum approach to dynamical quarkonia suppression in high energy heavy ion collisions

Roland Katz

Thèse de Doctorat

Roland KATZ

Mémoire présenté en vue de l'obtention du

grade de Docteur de l'École des Mines de Nantes

sous le label de L'Université Nantes Angers Le Mans

École doctorale : 500 (3MPL)

Discipline : Constituants élémentaires et physique théorique
Spécialité : Physique des particules
Unité de recherche : SUBATECH UMR6457

Soutenue le 14 décembre 2015 à Nantes
Thèse N° : 2015EMNA0227

A quantum approach to dynamical quarkonia suppression in high energy heavy ion collisions

JURY

Rapporteurs :	**Wolfgang CASSING**, Professeur, Université de Giessen
	Frédéric FLEURET, Directeur de Recherche, École Polytechnique
Examinateurs :	**Joerg AICHELIN,** Professeur, Université de Nantes
	Hamza BERREHRAH, Docteur, Université de Goethe Francfort
	Stéphane PEIGNÉ, Chercheur, CNRS, Ecole des Mines de Nantes

ENCADREMENT

Directeur de Thèse :	**Pol-Bernard GOSSIAUX**, Professeur, HDR, Ecole des Mines de Nantes
Co-directeur de Thèse :	**Elena BRATKOVSKAYA**, Professeur, Université de Goethe Francfort

Abstract

The theory of quantum chromodynamics (QCD) predicts the existence of a new state of matter: the Quark-Gluon Plasma (QGP). The latter may have existed at the first moments of the Universe following the Big Bang and can be, in theory, reproduced under the extreme conditions of temperature and density reached in high energy heavy ion collisions (at the LHC for instance). One of the QGP observables is the suppression of the quarkonia (heavy quark/antiquark bound states), characterised by a smaller production of these states in heavy ion collisions in comparison to proton-proton collisions, in which no QGP production would be possible. This suppression has indeed been observed experimentally, but the puzzling evolution of its trend from RHIC to LHC energies requires a better theoretical understanding. The present thesis aims at studying the real-time dynamics of correlated heavy quark/antiquark pairs described as open quantum systems which permanently interact with a cooling QGP. More explicitly, the continuous interaction between the medium and the pair internal degrees of freedom is obtained through 1) a temperature dependent color screening (Debye like) due to color charges in their vicinity and 2) some fluctuation/dissipation mechanisms reflecting the continuous collisions. It leads to a dynamical and continuous picture of the dissociation, recombination and possible transitions to other bound states. This investigation is at the crossroads of different theoretical frameworks: semi-classic, quantum and quantum fields. The deduced predictions are compared to experimental data and to the results of other theoretical models.

Keywords : Quark-Gluon Plasma, quarkonia suppression, dynamical approach, open quantum system, Schrödinger-Langevin equation

Résumé

La chromodynamique quantique (QCD) prédit l'existence d'un nouvel état de la matière: le plasma de quarks et de gluons (PQG). Celui-ci aurait existé dans les premiers instants suivant le Big Bang et peut en principe être produit sous les conditions extrêmes de température et de densité atteintes lors de collisions d'ions lourds à haute énergie (au LHC par exemple). Un des marqueurs de sa présence est la suppression des quarkonia (états liés de quark/antiquark lourds), caractérisée par une production inférieure de ces états dans les collisions d'ions lourds relativement aux collisions proton-proton où le PQG ne pourrait être créé. Cette suppression a bien été observée expérimentalement, mais l'évolution de ses tendances aux énergies du RHIC et du LHC est un véritable défi qui requiert une meilleure compréhension théorique. La présente thèse a pour but d'étudier la dynamique en temps réel de paires corrélées de quark/antiquark lourds considérées comme des systèmes quantiques ouverts en interaction permanente avec un PQG en refroidissement. Explicitement, l'interaction continue entre le milieu et les degrés de liberté internes de la paire est obtenue par 1) un écrantage de couleur dit de Debye dû à la présence de charges de couleur dans leur voisinage et 2) des mécanismes de fluctuation/dissipation qui reflètent les collisions permanentes. Cela mène à une image dynamique et continue de la dissociation des quarkonia, de leur recombinaison et des transitions entre états liés. L'étude est transversale à différents cadres théoriques: semi-classique, quantique et quantique des champs. Les prédictions du modèle sont comparées aux résultats expérimentaux et aux résultats d'autres modèles théoriques.

Mots clés : Plasma de quarks et gluons, suppression des quarkonia, approche dynamique, système quantique ouvert, équation de Schrödinger-Langevin

Introduction

Has Schrödinger's Katz nine lives ? ...

According to the Big Bang theory, the elementary particles which compose our Universe have passed through a very hot ($\gtrsim 10^{12}$ K) and dense stage of Quark-Gluon Plasma (QGP), some $< 10^{-5}$ s after the Big Bang, before gathering into nucleons, atoms, molecules, living things, stars, galaxies, superclusters... It might be one of the key stages to understand how an initially homogeneous distribution of matter has become inhomogeneous, leading to the current structures of matter observed in space. The QGP consists in a dense and deconfined state of quarks and gluons (together called partons). The latter are the elementary components of the nuclear matter and are, in normal conditions, confined as composite systems (hadrons) such as protons and neutrons. Since the 80's, an intense experimental and theoretical investigation has been carried out to prove the existence of such a state of matter and to characterise its properties. A possible way to reproduce the extreme conditions required to obtain a QGP, is to collide ultra-relativistic heavy ions in gigantic colliders like the RHIC[1] or the LHC[2]. It possibly results in incredibly small ($\sim 10^{-14}$ m) and short-lived ($\sim 10^{-21}$ s) "drops" of QGP whose study is a great challenge. Indeed, one can only consider indirect observables resulting from their expansion and cooling, i.e. the final produced hadrons. One of the QGP observables is the so-called "quarkonia suppression". It corresponds to a smaller production of heavy quark/antiquark ($Q\bar{Q}$) bound states in heavy ion collisions in comparison to proton-proton collisions, in which no QGP production would be possible. This suppression has indeed been observed experimentally, but does not systematically correspond to the expected picture. Matsui and Satz [1] indeed predicted the different quarkonium states to behave like a thermometer for the initial maximal temperature of the produced QGP. However, the puzzling evolutions of the suppression trends at RHIC and LHC depict a more complex picture which requires a better theoretical understanding. In the present thesis, we propose a dynamical description of the quarkonia suppression leading to the picture of a continuous thermometer. Explicitly, the correlated $Q\bar{Q}$ pairs are described as open quantum systems in continuous interaction with the deconfined medium. To this end,

The first part (I) progressively introduces all the basic concepts of particle and ultra-relativistic heavy ion physics. We first focus on quarks, gluons and the properties of their strong interaction. We then discuss their confined states with a main emphasis on quarkonia physics. We explore the phase transition to deconfined states and discuss the phase diagram of partonic and hadronic

[1]Relativistic Heavy Ion Collider
[2]Large Hadron Collider

matter. We finally describe an ultra-relativistic heavy ion collision to introduce the physics of the QGP and review its possible observables.

☞ To motivate the present work, part II gives an experimental and theoretical overview of quarkonia suppression in high energy heavy ion collisions. To this end, the relevance of the quarkonia as probes of the QGP is first discussed. We then review the various phenomena likely to interfere with the quarkonia yield and the most common models. We discuss the puzzling evolutions of the experimental data with the collision energy and point out their irregular descriptions. Finally, as an answer to the model assumptions, we motivate our quantum dynamical approach.

☞ In part III, as a first application to quantum dynamical approaches, we study the dynamics of a correlated $Q\bar{Q}$ pair subject to color screening from color charges in its vicinity while neglecting the effect of direct collisions with the medium.

☞ To find how these direct collisions can be included, we present in part IV the basic concepts of open quantum systems and review the common approaches. Then, we briefly discuss the existing literature on quarkonia seen as dynamical systems and motivate our so-called Langevin-like approach.

☞ As a first attempt to implement this approach, we explore in part V a semi-classical framework based on classical Langevin evolution of Wigner distributions, initially proposed by Young and Shuryak [2]. Its limitations are discussed.

☞ The part VI is devoted to the properties and solutions of a Langevin-like extension of the fundamental Schrödinger equation, the so-called Schrödinger-Langevin (SL) equation, initially proposed by Kostin [3] to study the quantum Brownian motion in a thermal environment. We investigate the thermal relaxation given by the SL equation with different potentials and noises.

☞ In the last part (VII), we apply the SL equation to a correlated $Q\bar{Q}$ pair immersed in a QGP bath within a simple model. We then carry out the study within a more realistic collision framework extracted from the state-of-the-art EPOS event generator: finite volume, inhomogeneous temperature and quarkonia position-momentum distributions. The predictions are finally compared to experimental data (in some extent) and other models.

... No, only seven !

Contents

Acknowledgment

We are grateful for the support from TOGETHER project Région Pays de la Loire.

I first wish to express my gratitude to my thesis supervisor, Prof. Pol-Bernard Gossiaux, who was abundantly helpful and offered invaluable assistance, support and guidance. Gratitude are also due to my co-supervisor Prof. Elena Bratkovskaya and to the members of the thesis committee, Prof. Jean-Phillipe Lansberg and Prof. Stéphane Peigné. I also wish to thank Prof. Joerg Aichelin, Prof. Thierry Gousset and Dr. Hamza Berrehrah for endless discussions and support. Special thanks also to all my PhD fellows, Benjamin Guiot, Benjamin Sintes, Martin Rohrmoser, Charlotte Duchemin, Florian Gate, Lucia Gallego-Manzano, Javier Martin Blanco, Lucile Ronflette... for sharing good times, literature and passion. I would also like to convey thanks to the administrative staff of Subatech and Ecole des Mines de Nantes for their warm permanent assistance. Last but not least, I wish to express my love and gratitude to my beloved families, girlfriend and close friends; for their support, understanding and endless love through the duration of this thesis. A special thanks to my father, Luc Katz, for sharing passion in physics and astronomy since my childwood.

Part I

From the standard model to heavy ion collisions

I.1 Quarks, gluons and confined states

I.1.1 Particle physics

All the matter inside and around us from the tiniest grain of sand to the biggest star in space, is composed of a large amount of atoms. For around a century now, the atom (size $\sim 10^{-10}$ m) is known to be composed of electrons "orbiting" via the electromagnetic force around a nucleus of protons and neutrons (see figure I.1). In the 60s [4], it was discovered that proton and neutron ($\sim 10^{-15}$ m $= 1$ fm) were not elementary particles but composite systems made of three *quarks* interacting via the *strong interaction* (which also holds the protons and neutrons together).

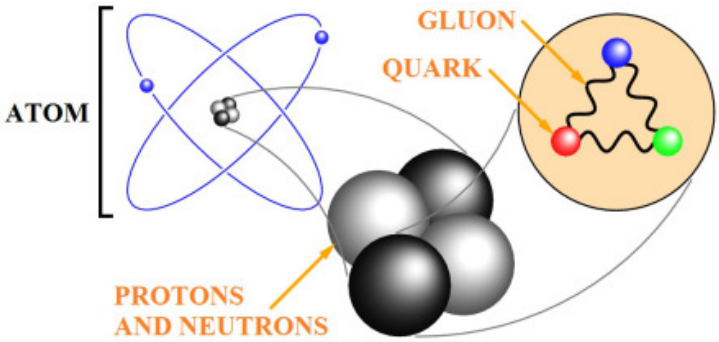

Figure I.1: From the atom to quarks and gluons.

As summed up in figure I.2, the electrons and the quarks are not the only elementary particles that build up our universe. From the joint effort of experiment and theory, was indeed discovered twelve elementary "matter" particles (fermions) and their associated anti-particles[3], the force carriers (gauge bosons) which mediate the fundamental interactions, and the Higgs boson which gives them masses. The photon - which composes the light for instance -, the Z and $W^{\pm}$ bosons - which are observed in the beta decay - and the eight *gluons* - which hold the quarks together - are respectively the force carriers of the electromagnetic, electroweak and strong interactions. There are six quarks in total (or six "flavours": $N_f = 6$) from the lightest "up" quark to the hundred thousand times heavier "top" quark. The quark family is distinguished from the leptonic family (which includes the electron) because the quarks carry a *color charge*, an intrinsic property at the root of the strong interaction. The color charge for the latter is the equivalent of the electric charge for Quantum Electrodynamics (QED) (electromagnetism) and allows the emission of the corresponding gauge bosons, called the gluons (the photon for QED). Unlike the photon which does not carry an electric charge, the gluons carry a color charge which allows them to interact among themselves.

All these particles have been directly or indirectly observed in particle accelerators and colliders, such as the gigantic LHC, where "natural" particles are accel-

[3] Anti-particles are thought to have the same masses than their associated particles but opposite charges.

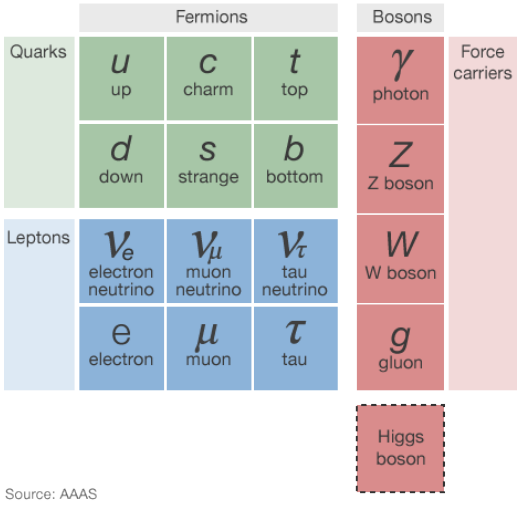

Figure I.2: The 12 matter particles (fermions), 12 force carriers (gauge bosons) and the Higgs boson.

erated near light-speed and collided to transform their energy into "new" particles following Einstein's famous relation "$E \leftrightarrow mc^2$" (mass-energy equivalence). The properties of these new particles, e.g. their energy, mass and spin, are studied by large detectors around the collision area(s) (such as ALICE at the LHC: see figure I.3).

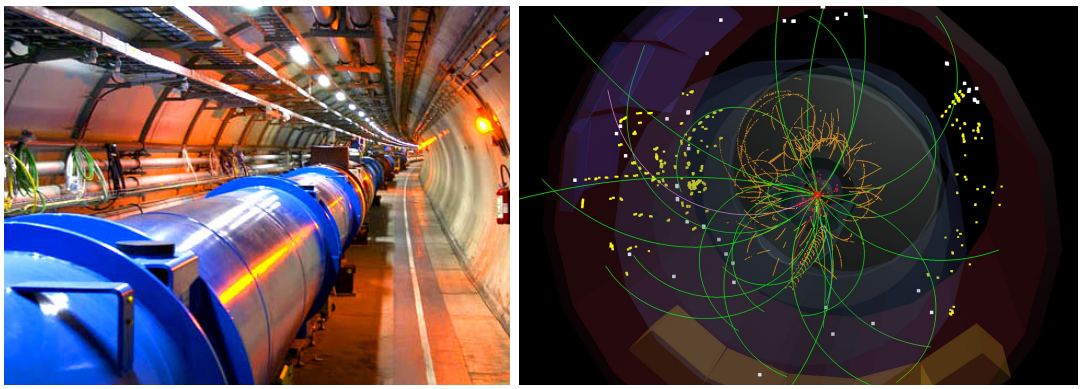

Figure I.3: *Left:* A small portion of the LHC circular pipe. *Right:* An LHC event in the ALICE detector. Each line corresponds to a "new" particle track in the detector.

On the theoretical side, the *Standard Model* of particle physics describes the particles properties, interactions and productions to a high precision. It has even predicted the existence of previously unobserved particles such as the quarks (discovered between 1968 and 1995), the gluons (1978), the W and Z bosons (1983), the tau neutrino (2000) and the Higgs Boson (2013). In a few words, the Standard Model is a relativistic quantum field theory [5] where the particles are described as dynamical fields that fill space-time. The field gauge symmetries[4] give rise to

[4]The physics which describes the field dynamics is invariant under some internal transformations called gauge symmetries.

the fundamental interactions. Their dynamics and interactions are described by the Lagrangian of the Standard Model (which has more than a hundred terms !). In practice, the Lagrangian can be used through the Feynman path integral formalism. Quantities like the S-matrix and the propagators are then developed in *perturbative* expansions in powers of the coupling constants[5], where each term can be schemed by a Feynman diagram. A term in power of n gives a Feynman diagram with n interactions ("vertices"). A process can then be seen as the sum of all possible Feynman diagrams (all the quantum mechanically possible and indistinguishable paths) as shown for instance in figure I.4.

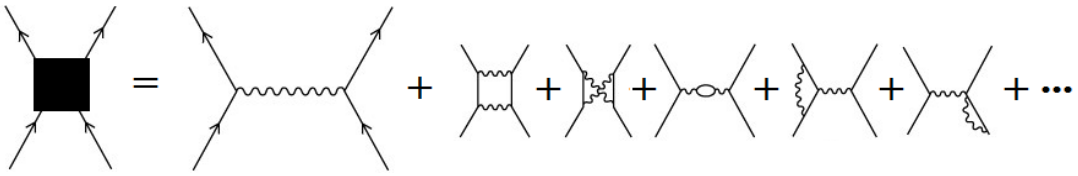

Figure I.4: In perturbative QCD, a $2 \to 2$ process can be seen as the sum of all possible Feynman diagrams.

The total amplitude[6] of the process is then given by the sum of each Feynman diagram amplitude. As the number of terms/diagrams is infinite, this sum is computable when the coupling constants are small compared to 1. Then, only the first orders of these expansions are necessary to obtain high precision predictions. Despite its successes, some important open questions remain, e.g. how to treat properly nonperturbative phenomena (i.e. when the coupling constant is larger than - or of the order of - 1) ? What are the dark matter and energy that appear in cosmological observations ? ...

I.1.2 Quantum Chromodynamics

As part of the Standard Model, *Quantum Chromodynamics* (QCD) [6] focuses on the dynamics of the color charged particles (the quarks and gluons, together called *partons*) and on their interactions through gluon exchange. Quark fields $\psi_{j=1,...N_f}^{i=1,...N_c}$, where j is the quark flavour, can have three possible colors ($N_c = 3$) commonly called red, blue and green. The Lagrangian of the free quark field,

$$\psi_j = \begin{pmatrix} \psi_j^1 \\ \psi_j^2 \\ \psi_j^3 \end{pmatrix}, \tag{I.1}$$

writes

$$\mathcal{L}_{\text{free}} = \overline{\psi}_j (i\gamma^\mu \partial_\mu - m_j)\psi_j. \tag{I.2}$$

[5] A coupling constant, which is directly related to the conserved particle charges, defines the strength of an interaction.

[6] The probability of a process is given by the squared modulus of its amplitude.

In QCD, the Lagrangian is invariant under the color gauge symmetry SU(3) transformation:

$$\psi_j(x) \longrightarrow \tilde{\psi}_j(x) = e^{-i\theta_a(x)T_a}\psi_j(x), \tag{I.3}$$

where the group generators $2\,T_{a=1,...8}$ are the Gell-Mann matrices and $\theta_{a=1,...8}$ real functions. To obtain this invariance, the usual derivative ∂_μ (μ and ν are Lorentz indices) is replaced by the covariant derivative

$$D_\mu = \partial_\mu - ig_s T_a G^a_\mu, \tag{I.4}$$

where $g_s = \sqrt{4\pi\alpha_s}$ is the gauge coupling parameter and $G^{a=1,...8}_\mu$ are the eight gauge fields which quanta are the gluons. The gauge invariance requirement therefore leads to the introduction of the quark interactions with the gluons. To obtain the QCD Lagrangian, one finally needs to add the gauge invariant Lagrangian for the gluonic fields,

$$\mathcal{L}_g = -\frac{1}{4}F^a_{\mu\nu}(x)F^{\mu\nu}_a(x), \tag{I.5}$$

where the gluonic field tensor F is

$$F^a_{\mu\nu} = \partial_\mu G^a_\nu - \partial_\nu G^a_\mu - g_s f_{abc} G^b_\mu G^c_\nu. \tag{I.6}$$

The first two terms of the gluonic field strength tensor give the gluon dynamics whereas the third term translates the gluon self-interactions. The latter originates from the non-abelian[7] nature of the SU(3) group, i.e. the constants f_{abc}, defined by

$$[T_a, T_b] = if_{abc}T_c, \tag{I.7}$$

are not all null. Finally, the QCD Lagrangian writes

$$\mathcal{L}_{\text{QCD}} = \sum_{j=1}^{N_f} \overline{\psi}_j(i\gamma^\mu D_\mu - m_j)\psi_j - \frac{1}{4}F^a_{\mu\nu}F^{\mu\nu}_a. \tag{I.8}$$

As a unique property in the standard model, the gluon self-interaction has important consequences on the strong interaction properties. Indeed, when two colored particles interact through a gluon exchange, the QCD predicts the possibility that the exchanged gluon splits into a loop of quarks or self-interacts at the next-to-leading order (NLO) of the perturbative expansion (see figure I.5). Qualitatively, whereas the former[8] is the source of screening effects between the two interacting partons, the gluon self-interaction is the source of dominant antiscreening effects. The screening (antiscreening) effects lead to a decrease (increase) of the interaction coupling with an increasing distance between the interacting particles. Therefore, unlike the electromagnetic interaction, the strong interaction coupling - and thus the value of the QCD renormalised coupling "constant" α_s - increases with the distance

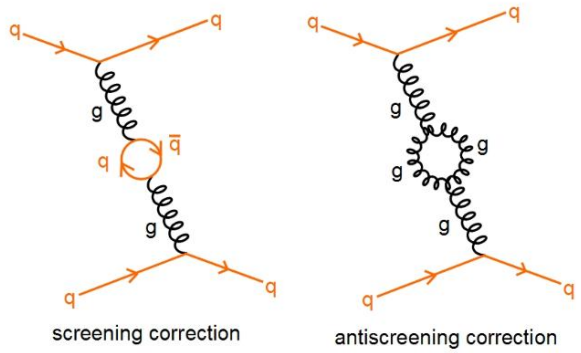

Figure I.5: Whereas the gluon splitting into a loop of quarks (left) leads to screening effects between the two initial partons, the gluon self-interaction (right) leads to antiscreening effects.

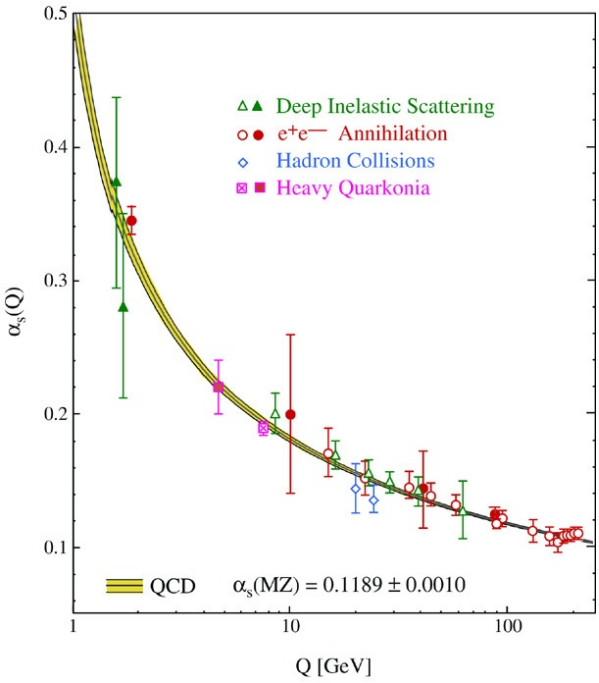

Figure I.6: The QCD coupling "constant" α_s function of the transfered energy Q between the two color charges [7].

or equivalently decreases with larger transfered energy (see I.6).

The typical energy scale $\Lambda_{\text{QCD}} \sim 200$ MeV separates the regime ($Q \gtrsim \Lambda_{\text{QCD}}$) where perturbative QCD can be applied ($\alpha_s \lesssim 1$) from the one ($Q \lesssim \Lambda_{\text{QCD}}$) where the strong interaction becomes highly nonlinear and non-perturbative methods are required ($\alpha_s \gtrsim 1$). This "running" of the coupling constant leads to noticeable features at the limits: the asymptotic freedom and the confinement. The so-called asymptotic freedom regime corresponds to the high energy scales $Q \gg \Lambda_{\text{QCD}}$ where

[7] A group is abelian if its generators commute.
[8] Which is similar to QED where the photon splits into a loop of charged particles

the interaction becomes relatively weaker. At the low energy scales $Q \lesssim \Lambda_{\mathrm{QCD}}$ (relatively large distances $\gtrsim 1$ fm), the confinement corresponds to the phenomenon which makes (a priori) impossible to observe an individual particle carrying a color charge. Indeed, in normal conditions, they are always observed to be confined into composite systems (see next section) such as to be in a color singlet (or "color neutral" or "white") global state. As a non-perturbative effect, the confinement is still poorly understood. The most famous model, the phenomelogical Lund string model [8], describes the confinement as a consequence of a gluonic string breaking into a quark/antiquark pair as the colored particles move away from each other. Indeed, as the interaction becomes stronger and stronger between the colored particles, the creation of a pair from the gluonic field becomes energetically favorable (it reduces the gluon field energy [9]) and leads to new independent composite systems (see figure I.7).

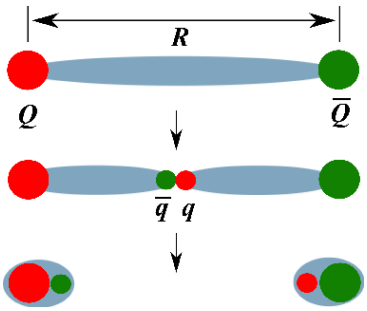

Figure I.7: As the quarks move away from each other, the gluonic field energy increases until it breaks into a quark/antiquark pair. It finally leads to two new independent composite systems. [10]

I.1.3 Hadrons and quark masses

Probed at intermediate momentum transfer, the proton (p) and neutron (n) can be understood as composed of three "valence" quarks (and some strings of gluons): two up and one down quarks (uud) for the proton, and one up and two down quarks (udd) for the neutron. When one probes them deeper, one also observes some individual gluons and "sea" quarks (mainly u, d and s quarks) originating from pair production and individual gluons. Of course, many other composite systems, called hadrons, can be formed with quarks. For now, only systems of quark/antiquark (called mesons), e.g. the pion π^+ ($u\bar{d}$), and of three quarks or antiquarks (called baryons), e.g. the charmed sigma Σ_c^0 (ddc), have been observed. Exception made of the proton and neutron, all hadrons are unstable under ordinary conditions and decay within short life times ($\lesssim 10^{-8}$ s). Moreover, each hadron can exist under different possible energy states (called resonances), with the excited states having extremely short life time ($\lesssim 10^{-24}$ s), e.g. the ground state $\Lambda^0(m = 1115\ \mathrm{MeV}/c^2)$ (uds) and its exited states $\Lambda^0(1405)$, $\Lambda^0(1520)$... where m is the resonance mass.

The mass of a hadron is usually quite different from the sum of its constituent free masses (e.g. $m_u + m_d + m_s = 102\ \mathrm{MeV}/c^2$ for the Λ^0) because most of its mass

originates from the large amount of energy involved in the QCD dynamics (mass-energy equivalence). Reciprocally, because the confinement prevents the unbinding of hadrons and makes impossible the isolation of a colored particle, the mass of the free quarks (as written in the renormalised QCD Lagrangian) cannot be measured directly. The free quark masses[9] are indirectly determined ([11] and ref. therein) from the combinations of experimental values (a set of hadron masses usually), a renormalisation[10] scheme and chosen scales, lattice QCD calculation and effective theories such as the Chiral Perturbation Theory (for light quarks) or Heavy Quark Effective Theories. The commonly chosen $\overline{\text{MS}}$ renormalisation scheme and scales leads to the masses given in Tab. I.1.

Light quark flavour	Up (u)	Down (d)	Strange (s)
Mass (MeV/c^2)	$2.3^{+0.7}_{-0.5}$	$4.8^{+0.5}_{-0.3}$	95 ± 5
Heavy quark flavour	**Charm (c)**	**Bottom (b)**	**Top (t)**
Mass (GeV/c^2)	1.275 ± 0.025	4.180 ± 0.030	160 ± 5

Table I.1: Quarks masses given by the common $\overline{\text{MS}}$ renormalisation scheme and scales ($\mu = 2$ GeV for light quarks and $\mu = m_{Q=c,b,t}$ for heavy quarks). We note that another calculation (the so-called 1S scheme) using B meson decay measurements leads to $m_b = 4.66 \pm 0.03$ GeV/c^2. [11]

I.1.4 Quarkonia

I.1.4.1 Characterisation and decay

— Charmonia —			
Quantum state	Name	Mass (MeV/c^2)	Interesting decays
1^3S_1	J/ψ or $\psi(1S)$	3097	leptonic (12.8 %)
1^3P_0	χ_{c0}	3415	$\gamma J/\psi$ (1.17 %)
1^3P_1	χ_{c1}	3511	$\gamma J/\psi$ (34.4 %)
1^3P_2	χ_{c2}	3556	$\gamma J/\psi$ (19.5 %)
2^3S_1	ψ' or $\psi(2S)$	3686	J/ψ anything (59.5 %)

Table I.2: Some interesting charmonium states and decays. [11]

[9] Also called "current" masses.

[10] In the perturbative regime, for the Feynman diagrams at the NLO (and higher orders), the integrals over the 4-momenta - of arbitrary energies as a quantum effect - of the loop constituents diverge at high energies. The renormalisation method proposes that the parameters, such as the particle masses or the coupling constants (see figure I.6 with $\mu = Q$), depend on the interaction scale μ at stake ("bare" parameters corresponds to free particles and "renormalised" parameters to interacting ones) such as to introduce counter-terms that cancel out the divergences.

In the present thesis, we will mainly focus on heavy quark/antiquark "$Q\bar{Q}$" mesons, called *quarkonia*, and more especially on the charm/anticharm "$c\bar{c}$" bound states, called *charmonia* (see table I.2 for some interesting states), and the bottom/antibottom "$b\bar{b}$" bound states, called *bottomonia* (see table I.3). From a Quantum Mechanics point of view, a quarkonium can be considered as a quantum oscillator. Its states are then denoted by $n^{2S+1}L_J$ where n is the main quantum number, S the intrinsic angular momentum, L the orbital angular momentum (its value 0 defined the "S" state, $1 \leftrightarrow$ "P", $2 \leftrightarrow$ "D"...) and J the total angular momentum (such that $|L - S| \leq J \leq L + S$)[11].

— Bottomonia —			
Quantum state	Name	Mass (MeV/c^2)	Interesting decays
1^3S_1	$\Upsilon(1S)$	9460	leptonic (7.5 %)
1^3P_0	χ_{b0}	9859	$\gamma\Upsilon(1S)$ (1.76 %)
1^3P_1	χ_{b1}	9893	$\gamma\Upsilon(1S)$ (33.9 %)
1^3P_2	χ_{b2}	9912	$\gamma\Upsilon(1S)$ (19.1 %)
2^3S_1	$\Upsilon(2S)$	10023	$\Upsilon(1S)$ pions (26.5 %)
3^3S_1	$\Upsilon(3S)$	10355	$\Upsilon(1S)$ pions (6.6 %) $\Upsilon(2S)$ anything (10.6 %)

Table I.3: Some interesting bottomonium states and decays. [11]

I.1.4.2 Quarkonia production

One of the basic ideas of QCD is the factorisation of short ("hard scale") and long ("soft scale") distance interactions. For quarkonia, this concept is realised both in the initial and final states of their production mechanism. The initial state factorisation separates the initial soft scale physics, which describes the parent (colliding) hadrons through their phenomenological *parton distribution functions* (PDFs)[12], and the hard scale physics, which describes the $Q\bar{Q}$ production from parton scatterings with the perturbative QCD. In high energy hadron-hadron collisions, the $Q\bar{Q}$ pairs are mainly produced in the interaction and/or fragmentation of energetic gluons emitted by the parent partons. The final state factorisation, in turn, assumes that the latter hard scale process is independent of the *hadronisation*[13] of the $Q\bar{Q}$ pair

[11] S, L and J are multiple of the quantum angular momentum action $\hbar$, the reduced Planck constant.

[12] This is essentially the probability density to find a parton at a scale Q^2 carrying a fraction x of the initial momentum of the parent/colliding hadron. A PDF can be decomposed into an unintegrated PDF, which is purely nonperturbative (at a soft scale Q_0^2), and its evolution towards the considered hard scale Q^2, given by an equation of evolution based on pQCD.

[13] The formation of a specific hadron out of the produced quarks and gluons.

into a specific bound state. The hadronisation is usually described by effective theories such as the Lund string model or a non-perturbative QCD approximation. For the quarkonia, the Non-Relativistic QCD framework[14] [12], based on an expansion over the small $Q\bar{Q}$ relative velocity (due to their heavy mass), is commonly used.

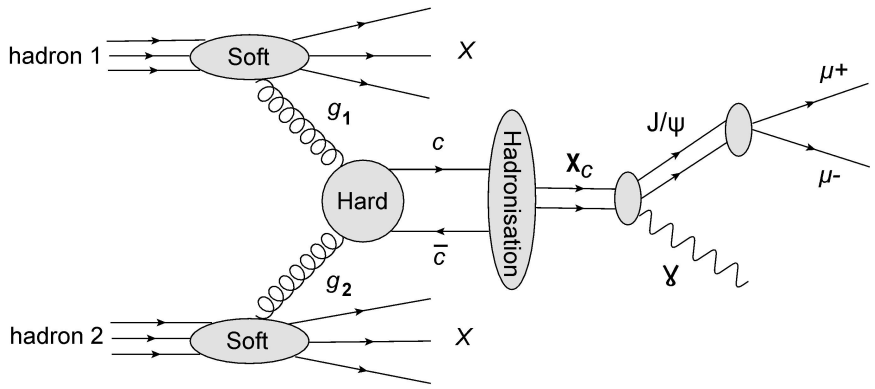

Figure I.8: The QCD mechanism leading to the inclusive indirect J/ψ production in a hadron-hadron collision going through the intermediate radiative decay of the χ_c state.

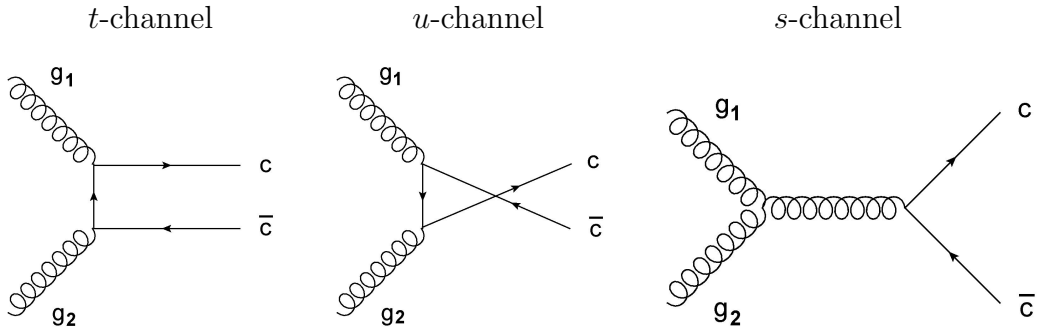

Figure I.9: The three Feynman diagrams (t, u and s channels) of $gg \to c\bar{c}$ at tree level (leading order of the perturbative expansion).

As an example of a global production scheme, the J/ψ indirect production from gluon fusion through χ_c radiative decay is shown in figure I.8. The hard process $gg \to c\bar{c}$ writes as a superposition of different perturbative QCD interactions schematised by Feynman diagrams. At the leading order of the perturbative expansion, there are three possible interactions: the so-called t, u and s channels shown in figure I.9. In this way, the $Q\bar{Q}$ pair is created either in a *color singlet state* from the t and u channels, which means $i = \bar{k}$, or in a *color octet state* ($i \neq \bar{k}$) from any channel, where i and k are the color indices of the quarks. Hadrons being usually color neutrals, only the color singlet state contribution was first thought to hadronise into a bound state (color singlet model [13, 14]), but the predictions underestimated the data [15]. The proposed solution for this discrepancy was to add the color octet

[14]It is an effective theory that disentangles physics at the scale of the heavy quark of mass m_Q, relevant to the production of a heavy quark pair, from physics at the scale given by the bound state's binding energy $m_Q v^2$, relevant to the formation of the quarkonium (where v is the relative quark-antiquark velocity).

model contribution [16, 17], by turning the color octet states into a color singlet by soft gluon exchanges with hadron remnants. The sum of the color singlet and color octet contributions is in good agreement with the data [15], but the color octet model introduces incalculable non-perturbative parameters, the color octet matrix elements describing the transitions, which are determined by a fit to the data. Furthermore, it does not give a good description of polarised charmonium production data [18]. To conclude, the models for quarkonia production in p-p collisions lead to rather good predictions of the p_T spectra, but important uncertainties remain on the actual mechanism (especially concerning the hadronisation). In section II.1, we will discuss the typical times related to this production mechanism.

There are two major experimentally distinguishable ways to produce inclusive[15] charmonia in high energy hadron collisions: *the non-prompt production* going indirectly through the decays of produced B-mesons and bottomonia, and *the prompt production* which goes either directly to the considered charmonia states - from a charm/anti-charm quark pair produced in a gluon-gluon fusion subprocess -, or indirectly through decays ("*feed-downs*") of more excited charmonia states. In figure I.10, the contributions of the different feed-downs to the J/ψ and $\Upsilon(1S)$ states are summed up.

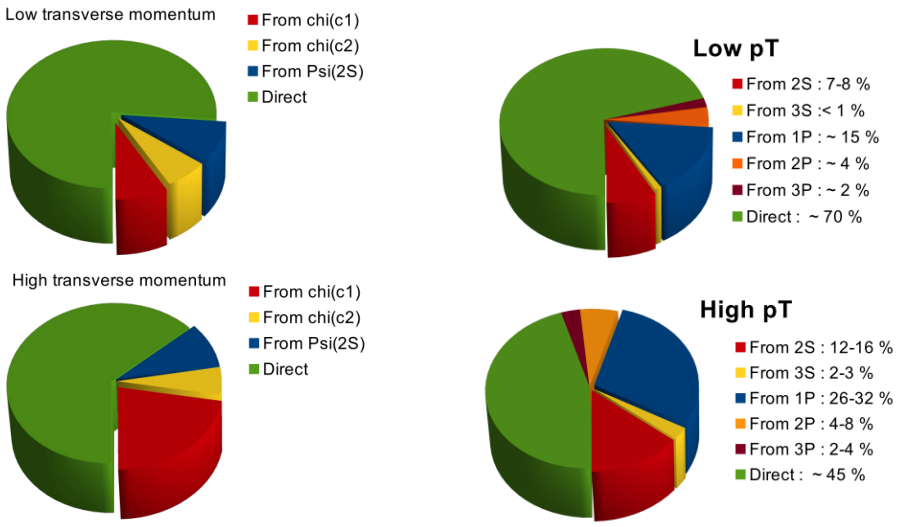

Figure I.10: Feed-downs from excited states: typical sources of prompt J/ψ (*left* panel) and $\Upsilon(1S)$ (*right* panel) at low (top figures) and high (bottom figures) p_T determined from experiments ([19] and references therein).

I.1.4.3 The relevance of quarkonia in proton-proton collisions

For a few decades by now, the quarkonia (and the J/ψ in particular) have been one of the most important sources of information about both perturbative and non-perturbative QCD, as well as relevant probes for the hadronic matter formed in

[15]The inclusive production means that the initial colliding hadrons may be destroyed during the scattering process and create a multitude of extra hadronic products that are not measured.

ultra-relativistic heavy ion collisions (see section II.1). They are especially relevant for the study of high energy collisions, or in other words in the low x regime[16], where only[17] the quarkonia can be used [20] to study the unintegrated PDFs and to distinguish among the equations of evolution (such as DGLAP[18][21], BFKL[19] [22]...) towards the hard scales.

The theoretical treatment of the quarkonia is indeed simplified by the large mass of their constituents ($m_c \sim 1.3$ GeV and $m_b \sim 4.2$ GeV) and their symmetry. First, quarkonia are simple symmetrical two body systems in comparison to the three body baryons or asymmetrical open mesons[20]. The theoretical determination of their binding potentials and states are then more attainable. Second, the large mass of their constituent quarks ($m_Q \gg \Lambda_{\mathrm{QCD}}$) might guarantee the factorisations of the different scales and the use of the Non-Relativistic QCD framework in their production mechanism.

I.2 A deconfined state of matter: the quark-gluon plasma

As explained in section I.1.2, in ordinary conditions the color charged particles (quarks and gluons) are confined "within hadrons". At extremely high temperatures and/or density, the theory of QCD however predicts [23, 24] the existence of a "deconfined" state of the nuclear matter, the Quark-Gluon Plasma[21] (QGP). The idea is that when the density of partons becomes really large, they have no distinguishable partners for a specific hadron: they become unbound. Moreover, as the coupling becomes relatively weak (asymptotic freedom regime) they can move "freely" inside the QGP area. Besides the interest of studying a new state of matter in itself, the QGP (and the phase transition to hadrons) may have played a crucial role at the first moments of the Universe (up to a fraction of second after the Big Bang) and may compose the core of dense neutron stars. The description of its properties and behaviour may thus improve our understanding of the Universe history, of the QCD dynamics in general and of strongly coupled many-body systems. Though (a priori) impossible to observe directly in Nature, small droplets of QGP can be, in theory, re-produced in heavy ion collisions at high energy colliders (e.g. the LHC).

[16] Small longitudinal momentum fraction carried by the initial-state partons, given by $x \equiv 2p_z/\sqrt{s}$ in the center-of-mass frame, where p_z is the longitudinal momentum of the considered parton and s is the initial hadron energy.

[17] Their large masses might ensure the factorisations of perturbative and non-perturbative mechanisms.

[18] Dokshitzer-Gribov-Lipatov-Altarelli-Parisi. Also called collinear factorisation.

[19] Balitskii-Fadin-Kuraev-Lipatov. Also called k_T factorisation.

[20] *Open mesons* are mesons with a quark and antiquark of a different flavour, e.g. the pion π^+ ($u\bar{d}$).

[21] Named by analogy with the electromagnetic plasma where the positive and negative electric charges are unbound from each other.

I.2.1 The QCD phase diagram from the lattice

The physical states of matter and the transitions between them, under the different conditions of temperature and density are usually summarised in graphical representation called phase diagrams. Part of the phase diagram of partonic matter can be theoretically determined from *lattice QCD* (lQCD) calculations.

As a discrete formulation of QCD, lQCD [25] is a powerful effective tool to investigate non-perturbative phenomena, among which QCD thermodynamics, hardly accessible to analytical theories. The lQCD is based on the formal analogy between Quantum Field Theory (path integrals in Euclidean space[22]) and Statistical Mechanics (partition functions). The QCD partition function [26],

$$Z(V,T,\mu_B) = \int \mathcal{D}A_\nu \, \mathcal{D}\bar{\psi} \, \mathcal{D}\psi \; e^{-S_E(V,T,\mu_B)}, \tag{I.9}$$

indeed writes as a Euclidean path integral over gauge A_ν, quark (ψ, $\bar{\psi}$) fields. The QCD thermodynamic variables are here the volume V, the temperature T and the baryon chemical potential μ_B (associated to the baryon number density[23]). The Euclidean action $S_E = S_G + S_F$ can be decomposed into a gluonic contribution,

$$S_G(V,T) = \int_0^{T^{-1}} dx_0 \int_V d^3x \, \frac{1}{2} \, \mathrm{Tr}(F_{\mu\nu}F_{\mu\nu}), \tag{I.10}$$

and a fermionic contribution S_F,

$$S_F(V,T,\mu_B) = \int_0^{T^{-1}} dx_0 \int_V d^3x \sum_{f=1}^{N_f} \bar{\psi}_f \left(\gamma^\mu[\partial_\mu - ig_s A_\mu] + m_f - \mu\gamma_0\right) \psi_f, \tag{I.11}$$

which couples the gauge and the fermion fields (N_f flavours). The system under consideration is then discretised and reduced to a 4D lattice ($V = (N_{\text{space}}a)^3$ and $T^{-1} = N_\tau a$), where the quark and gluon degrees of freedom are respectively on the lattice sites and the links connecting the sites. The number of these degrees of freedom is then finite and the path integral ultraviolet divergences are naturally regularised by the lattice spacing a. The path integrals are then computed over the most relevant system configurations and extrapolated to the continuum limit $a \to 0$ while keeping some observables constant (e.g. some hadron masses). Finally, the QCD equation of state can be obtained through the determination of thermodynamic observables from the partition function such as the energy density ϵ, the pressure p,

[22] Which includes the imaginary time τ dimension, stemming from the Wick rotation $\tau = it$, in order to obtain the formal connection between Quantum Mechanics and Statistical Mechanics.

[23] The baryon number B is a conserved quantity defined as the difference $1/3(n_q - n_{\bar{q}})$ between the number of quarks n_q and antiquarks $n_{\bar{q}}$. To the corresponding baryon density can then be associated a baryochemical potential μ_B which translates the change of free energy with respect to a change in baryon number composition. Finally, note that the more energetic the heavy ion collisions are, the smaller the stopping of the initial baryons gets, the smaller the baryon density/chemical potential is.

the free energy density f or the entropy density s:

$$p = -f = \frac{T}{V} \ln Z(V, T, \mu_B) \tag{I.12}$$
$$\frac{\epsilon - 3p}{T^4} = T\frac{d}{dT}\left(\frac{p}{T^4}\right)$$
$$\frac{s}{T^3} = \frac{\epsilon + p}{T^4}$$

Figure I.11 shows the energy density and pressure variations with the temperature obtained at zero baryon density (or chemical potential). As the energy density is

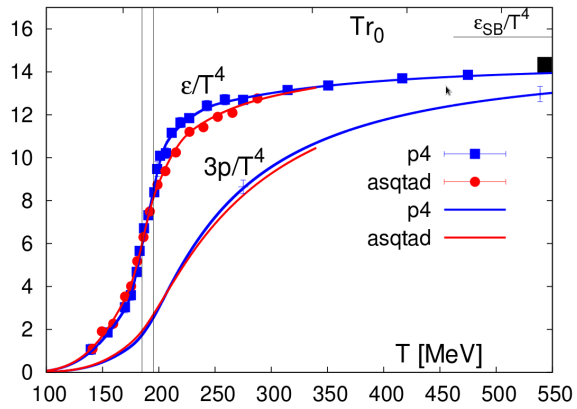

Figure I.11: Energy density and pressure calculated with the lQCD (3 light flavours, $\mu_B = 0$) with two different fermionic actions. The bars indicate the transition region $185 < T < 195$ MeV. [27]

directly related to the effective number of degrees of freedom d ($d \propto \epsilon/T^4$ [28]), the large variation around $T = 190$ MeV can be understood as a transition between a hadronic gas (small d) at lower temperatures to a deconfined partonic phase (very large d) at larger temperatures. At larger temperatures, the energy density increases slowly but does not reach the Stefan-Boltzmann limit value ϵ_{SB}, which corresponds to a perfect gas, indicating some remaining partonic interactions in the deconfined phase. This is a first indication that the deconfined medium found for temperatures $T \in [200, 500]$ MeV might be a strongly-coupled QGP (sQGP) *where some correlations could survive*. From the non-singular behaviour of the observables, one might conclude to a cross-over transition between the two phases, i.e. a fast but continuous transition where both hadron and parton degrees of freedom coexist.

At positive baryon density (i.e. when there are more quarks than antiquarks), one can gather the results from lQCD - where new methods are required with larger uncertainties as μ_B increases - and other models (MIT bag [29], NJL [30]...) to suggest a phase diagram for the partonic matter as shown in figure I.12. It shows a crossover in a region between $0 \leq \mu_B \leq \mu_B^{\mathrm{crit}}$, a critical point [31] at μ_B^{crit}, and beyond a first order transition [32]. During a first order transition (discontinuity in the first derivative of the free energy), the temperature of the system remains constant while the released energy is used to transform a phase into the other (mixed-phase

regime). Other parameters such as the susceptibilities and the quark condensate $\langle 0|\psi_f\bar{\psi}_f|0\rangle$ can be studied to describe the properties of the transitions such as the transition order (see figure 8 in [33] for instance) or the modifications of the light quark masses (restoration of the chiral symmetry in the deconfined phase). Last, note that though the equation of state is rather well understood from lQCD calculations, the latter leads to more fluctuating predictions concerning other important parameters and properties of the deconfined matter obtained in heavy ion collisions (such as the actual temperature, the viscosity, the transport coefficients...) to which heavy flavours could be relevant probes (see II.1).

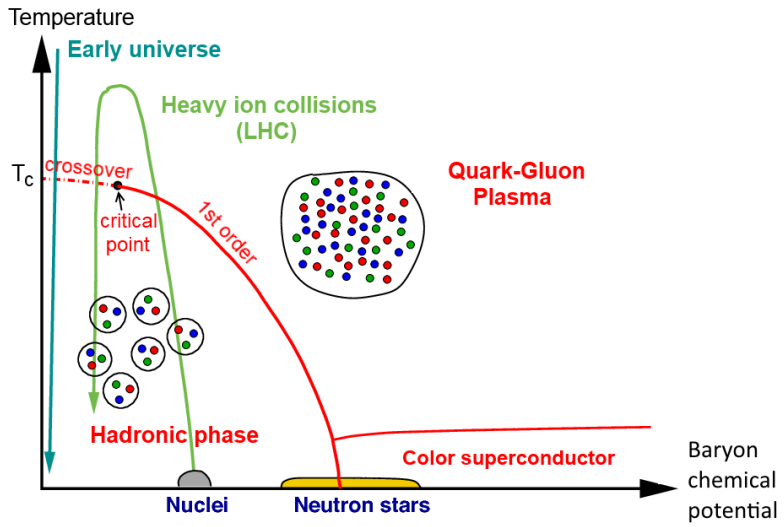

Figure I.12: A schematic phase diagram of QCD as a function of temperature and baryon chemical potential μ_B. The critical temperature (inflexion point) is evaluated to $T_c \simeq 170 \pm 25$ MeV ($\sim 10^{12}$ Kelvin !) at $\mu_B \simeq 0$ [34].

I.2.2 High energy heavy ion collisions.

For now, the unique way to reach such extremely high temperatures and/or densities is to collide heavy ions (U-U, Cu-Cu, In-In, Pb-Pb...) in high energy colliders such as the SPS[24], RHIC or the LHC. Indeed, their numerous nucleons and their high energy (ultra-relativistic velocity) ensure a high level of energetic particle production within a relatively small volume (called *fireball*), that may lead to a deconfined state if the conditions required by the phase diagram I.12 are reached.

As schemed in figure I.13, a heavy ion collision can be decomposed into few successive stages from the two initial ions to the many hadrons observed in the detectors. These stages corresponds to the Shuryak-Bjorken model where the QGP is assumed to be produced. The next three subsections (I.2.2.1, I.2.2.2 and I.2.2.3) describe this scenario.

[24]Super Proton Synchrotron

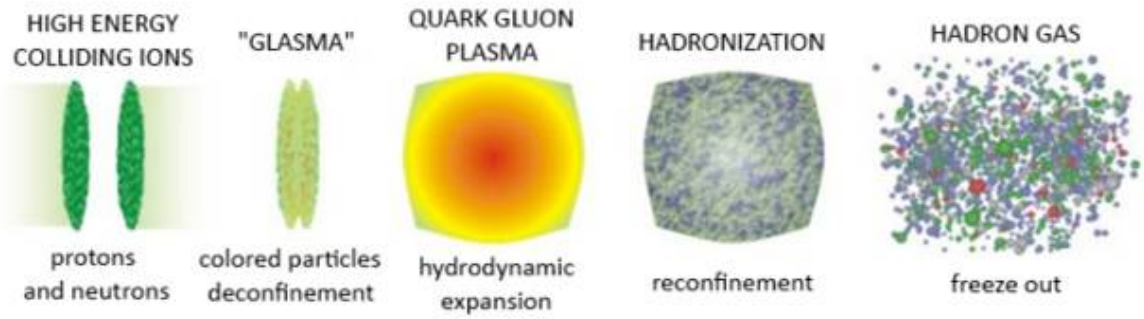

Figure I.13: Schematic representation of the successive stages of a high energy heavy ion collision from the initial ions to the many hadrons observed in the detectors.

I.2.2.1 The initial ions and the first fm/c following the impact

Due to their relativistic kinematics, the geometry of the initial ions is Lorentz contracted along the beam axis, making them look like two "pancakes" in the laboratory frame (instead of "spheres"). In parallel, all their internal timescales such as the gluon lifetimes or the interaction times are dilated. As the collision energy increases, gluons with smaller and smaller longitudinal momentum fraction x can interact to produce particles of matter. Then, the amount of visible gluons increases continuously with the collision energy and becomes much larger than the amounts of valence and sea quarks (the latter being smaller by one power of the coupling constant as they are produced by gluon splittings) [35]. The description of the initial parton compositions is usually realised through nuclear-PDFs (*nPDFs*) $f^A_{g,u,d...}$ such as EPS09, DSSZ... [36] They are not the simple sums of the nucleon PDFs $f^N_{g,u,d...}$: they take into account the modifications caused by the interactions between nucleons. In particular, these interactions can lead to a decrease (*shadowing*) or an increase (*anti-shadowing*) of the gluon density in the initial nuclei relatively to the one in nucleon collisions [37]. This modification is usually quantified through the nuclear modification ratio,

$$R^A_g(x,Q^2) = \frac{f^A_g(x,Q^2)}{A\, f^N_g(x,Q^2)}, \tag{I.13}$$

where A is the number of nucleons of the considered nucleus. For instance in figure I.14, one can see the evolution of the $R^A_g(x,Q^2)$ factor with the longitudinal momentum fraction x, at some fixed energy scales Q^2, obtained with the lead nucleus within the EKS98 nPDF model [38]. The shadowing effects are dominant at LHC energies ($R^A_g < 1$) whereas the anti-shadowing effects are predicted at SPS (lower) energies ($R^A_g > 1$). Note however that the anti-shadowing effect has never been observed at SPS.

Unfortunately, the very large gluon density at high energies leads to processes with multiple interactions inside the initial ions and shortly after the collision (as shown in figure I.15), which should be described by highly nonperturbative methods even if the couplings are weak [39]. In this regime, the nPDFs are no more relevant (needs for "multigluon" states) and alternative methods should be used. The Color

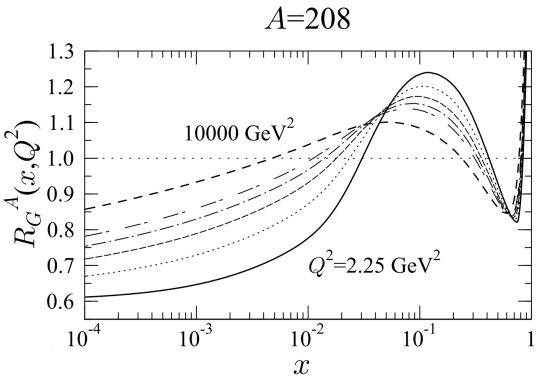

Figure I.14: Evolution of the ratio R_g^A as a function of longitudinal momentum fraction x for fixed energy scales Q^2 for a lead nucleus ($A = 208$). The energy scales are respectively $Q^2 = 2.25$ GeV^2 (solid lines), 5.39 GeV^2 (dotted), 14.7 GeV^2 (dashed), 39.9 GeV^2 (dotted-dashed), 108 GeV^2 (double-dashed) and 10000 GeV^2 (dashed). [38]

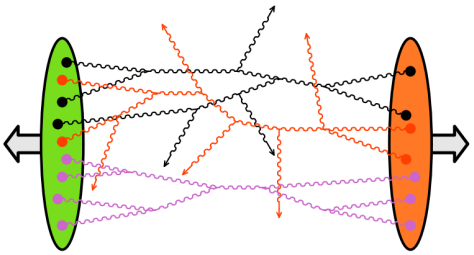

Figure I.15: The many gluon scatterings in the dense regime lead to an infinite number of Feynman diagrams at each order [39].

Glass Condensate (CGC) model proposes an effective description of the initial ions in a "saturated" regime. Indeed, the gluon density enhancement should saturate from a certain energy scale, thanks to non-linear gluon recombinations [40], and weak coupling methods could still be used. Shortly after the collision, the CGC model leads to the formation of a non-equilibrated medium (the "Glasma"). The Glasma is composed of the initial interacting partons and the newly produced particles (light and heavy quarks, direct photons...) originating mainly from gluon scatterings. In a very short time, the particle density and the system temperature increase dramatically. The system then locally equilibrates to form the QGP phase after a ~ 1 fm/c ($\sim 10^{-24}$ s) lifetime [41], but this equilibration is still poorly understood within the CGC model.

I.2.2.2 The Quark Gluon Plasma stage

If the conditions are reached, the Glasma leads to a deconfined phase of the partonic matter (the QGP) which should thermalise[25] locally at LHC energies. The

[25] A medium is thermalised when the spatial fluctuations of the temperature are small compared to its average value.

QGP fireball has an initial spatial size of $\sim 10-20$ fm and might survive $\approx 5-10$ fm/c . The QGP lifetime depends on the spatial expansion of its constituent. As the medium expands, its average temperature should decrease from a few T_c to T_c, around which the parton degrees of freedom are thought to coalesce into hadrons (see the freeze-out section below).

QGP properties are expected to depend on its temperature. Naïvely, at very high temperatures ($T \gg T_c$), the coupling becomes very weak $\alpha_s(T \gg \Lambda_{\mathrm{QCD}}) \ll 1$, and the QGP may behave like a gas of relatively weakly interacting partons. In this case, the QGP has a large viscosity[26], its evolution follows a viscous hydrodynamic expansion, and its parameters obey approximatively Stefan-Boltzmann equation of state: at $\mu_B = 0$ its pressure and density are proportional to T^4 and its entropy to T^3 [33]. For temperatures $T_c \lesssim T \lesssim 5T_c$ (the region of current interest), the theoretical expectations are more ambiguous. As shown in figure I.16, lQCD calculations predict a deconfined medium with a low viscosity quite far from pQCD results [42]. The parton degrees of freedom may therefore interact relatively strongly, leading to the so-called strongly interacting QGP (sQGP). The sQGP may behave like an almost perfect fluid with very low viscosity which can be described by a quasi ideal hydrodynamics.

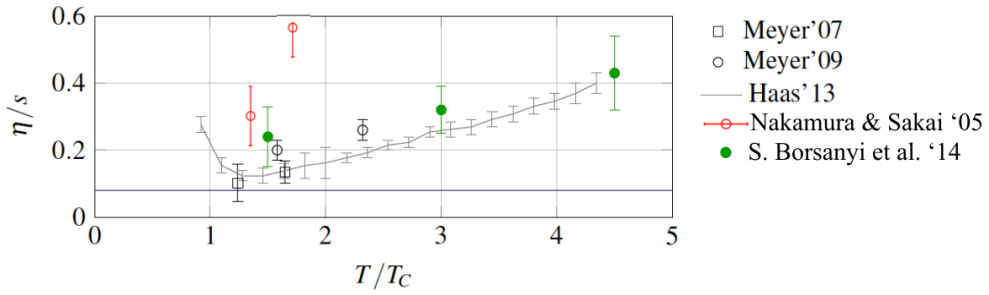

Figure I.16: A compilation of lQCD predictions for the shear viscosity to entropy density ratio as a function of temperature [43].

I.2.2.3 Hadronisation, physical and chemical freeze out

When the medium temperature decreases to the crossover region (figure I.12), the parton degrees of freedom progressively hadronise into hadrons. These hadrons may still interact inelastically with each other and with the nucleons that did not interact initially ("nuclear absorption"). The so-called *chemical freeze-out* occurs when the number and the nature of the hadrons gets fixed, i.e. when the hadronisation and the inelastic scatterings stop. The medium then forms an expanding hadron gas (with additional leptonic particles), which behaviour can be described by kinetic theory. The so-called *kinetic freeze-out* occurs when the particle kinematics

[26]The (shear) viscosity quantifies the transverse momentum diffusion and is inversely proportional to the fluid inter-particle cross section (or coupling). The larger the coupling, the smaller the mean free path, the smaller the transverse energy diffusion and the viscosity.

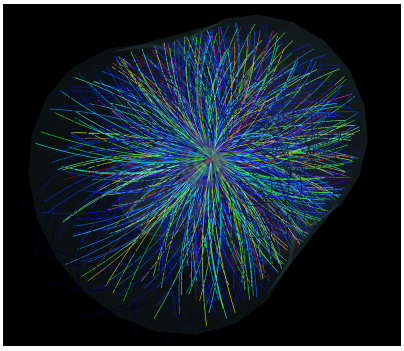

Figure I.17: Example of spatial expansion of the final particles produced in a high energy ion collision (from ALICE detector at the LHC).

get fixed, i.e. when the elastic collisions stop. Finally, the hadrons or their decay products and the other particles expand spatially toward the detectors where they can be characterised (see figure I.17 for instance).

I.2.3 Experimental observables, observations and analysis.

The experimental quest for the production of a QGP, for the proof of its existence and the characterisation of its properties has started in the 80s. Since then, several accelerators have focused on heavy ion collisions, progressively increasing their energy from few GeV at the Alternating Gradient Synchrotron (fixed target) to few thousands GeV at the LHC. A heavy ion collision is usually defined by:

- The nature of the chosen ions: Pb-Pb or S-U at SPS, Au-Au, Cu-Cu or U-U at RHIC and so far Pb-Pb at LHC for instance. It can mainly have an influence on the cold nuclear matter and initial state effects (see part II).

- Its energy through the *center-of-mass energy per nucleon pair* $\sqrt{s_{NN}}$. The center of mass referential is the laboratory referential in symmetric collisions. Alternatively, one can use the *beam energy per nucleon* AGeV.

- Its *centrality* through the impact parameters b or the number of participants $\langle N_{\text{part}} \rangle$. The latter is the number of nucleons participating in the collision (see figure I.18). It can be evaluated from the number of particles observed in the detectors (called *multiplicity*) while using a simple geometrical picture for the initial ions (e.g. the Glauber model [44]) [45]. The centrality can also be expressed in terms of a percentage through the cumulative distribution function, where 0% means that all the nucleons interact (*central collision*) and 100% means that no nucleon collides (ultra-*peripheral collision*).

As only an incredibly small ($\sim 10^{-14}$ m) and short-lived ($\sim 10^{-21}$ s) "bubble" of QGP may be produced in these collisions, its experimental study is a great challenge. In order to prove its existence and to describe its properties, one can only consider indirect observables, i.e. the final hadrons. An observable is relevant if one can distinguish the different medium effects (initial state, cold nuclear matter, hadronic

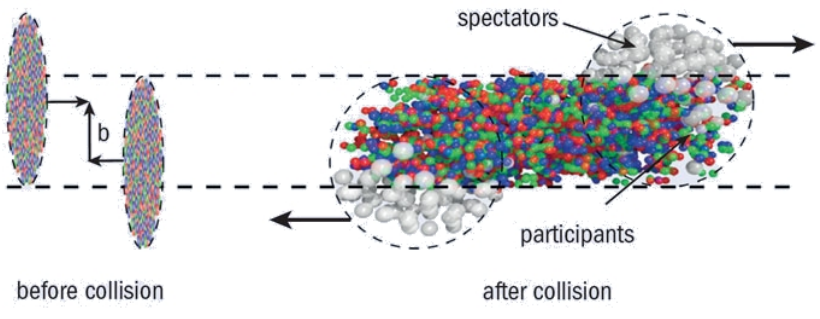

Figure I.18: Schematic view of a noncentral ($b \neq 0$ or $\langle N_{\rm part} \rangle < \langle N_{\rm part}^{\rm max} \rangle$) high energy heavy ion collision. Spectator nucleons (which do not collide - in grey) continue their trajectories along the beam axis whereas participant nucleons (in the region where the ions overlap) interact and produce many new particles (colored).

and/or partonic hot media, final state effects...). Quite generally, observables can be divided into two categories: the soft and hard probes.

The soft probes are particles produced all along the process (they form the bulk) and are used to describe the collective behaviours or thermodynamical properties. They correspond mainly to the light quarks and gluons which form the fireball. The related observables are for instance the corresponding low $p_{\rm T}$ hadrons which can be used to determine the flow [46, 47] and the critical temperature. But also the thermal photons[27] and dileptons [48, 49] which may be used to evaluate the average temperature of the medium. In parallel, strangeness enhancement [50, 51, 52] could be a sign of chiral symmetry restoration[28] (a possible consequence of QGP production).

Hard probes are produced from pQCD processes in the first moments of the collision (before the QGP phase) and can perform a "tomography" of the medium if they propagate through it. For instance, high $p_{\rm T}$ particles and open heavy meson spectra can be used to probe the achieved densities as well as to evaluate transport coefficients and test pQCD in a thermal medium. The quarkonia suppression could be used to evaluate the medium temperature and probe the color deconfinement (see part II). In parallel, as they do not interact strongly with the produced medium, weakly interacting bosons ($W^{\pm}$ and Z) and prompt photons[29] can help to constrain the nPDFs [53, 54] and test the Glauber model [55].

Although these observables have been intensively studied both experimentally and theoretically, it is not obvious to find an experimental signature of the QGP production consisting in a unique observable. Indeed, most of the experiments may pass through the crossover region (see figure I.12 for multiplicities at the chemical freeze-out), leading to no plateau or sharp behaviors of the thermodynamic variables.

[27] Photons are said to be "thermal" when they are produced by the thermalised medium.

[28] The chiral symmetry is the invariance of the QCD Lagrangian with respect to the quark spin orientation. It is spontaneously broken by the quark masses and is predicted to be restored at high temperatures.

[29] Prompt photons are produced during the hard initial collisions.

One should thus look for experimental results which cannot be explained by hadronic models only, or alternatively one can determine some medium properties which are consistent with the QGP formation (high energy density...). Though there is no absolute proof for now (no net transition observed), the comparisons between data and partonic and/or hadronic models tend to confirm the formation of a QGP from SPS/RHIC/LHC energies. The community is now investigating its properties.

I.2.3.1 Light hadron multiplicity and hydrodynamic flow

Individually, light hadrons (formed by the light quarks u, d, and s) cannot be used as probes of the QGP. Indeed, if the medium is deconfined, they cannot exist inside the QGP and will only form at the phase boundary (between the QGP and the vacuum) where the physics of hadronisation at the critical temperature is independent of the interior properties [33]. Collectively however, these light hadrons can bring insights into the produced medium through their integrated and azimuthal multiplicity.

Thanks to its "independence", hadronisation should always lead to a similar "thermal" distribution of the light hadron multiplicities (see figure I.19), which can be used in its turn to evaluate the critical temperature. Reciprocally, the presence of such a hadronisation temperature can be seen as an indirect proof that the medium was deconfined: if the hot medium was purely hadronic, the inelastic interactions would not stop at such a high temperature and would a priori lead to distributions corresponding to much lower temperatures.

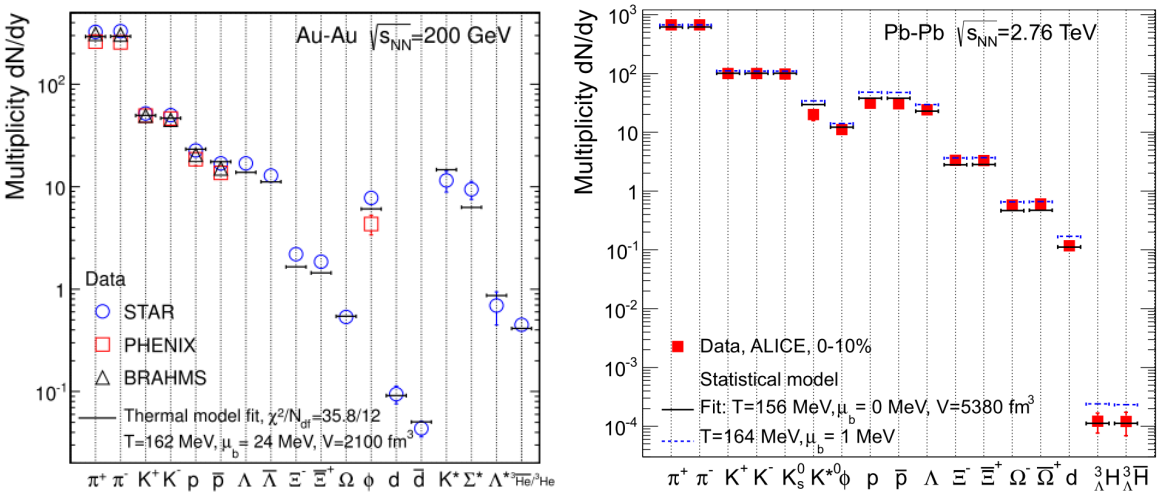

Figure I.19: Comparison of thermal model predictions with RHIC (left) and LHC (right) data. It is consistent with hadrons being produced at $T_c \approx 160$ MeV. [56, 57]

According to the hydrodynamic model, the collective expansion (or "flow") of the light hadrons can be correlated to the QGP initial energy density, centrality and

medium viscosity [58]. The flow can be studied through the multiplicity (N) distribution at the kinetic freeze-out over the azimuthal angle ϕ in the transverse plane (relatively to the beam axis) at different rapidity [30] windows. Some azimuthal flow parameters v_n can then be defined by a Fourier decomposition of the distribution,

$$\frac{dN}{d\phi} = \frac{N}{2\pi}(1 + 2v_1\cos(\phi - \psi_1) + 2v_2\cos(2(\phi - \psi_2)) + 2v_3\cos(3(\phi - \psi_3)) + ...)$$

The first term corresponds to an isotropic radial flow, v_1 to an anisotropic flow called directed flow[31], v_2 to an elliptic flow with an "elliptic-like" shape, v_3 to a triangular flow with a "triangular-like" shape [60]... In the case of a noncentral collision, the fireball should have an "almond" like shape in the transverse plane (see schematic situation in figure I.20). Then, if the medium quickly thermalises (at least partially), the radial pressure should vary with the direction and one should observe an anisotropic transverse flow which is mainly radial and elliptic (following the fireball shape).

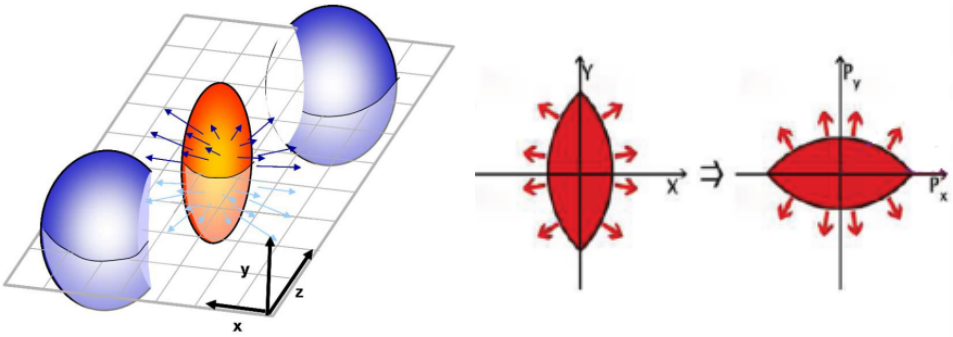

Figure I.20: A noncentral collision leads to a fireball with an almond like shape in the transverse planes (left). If the medium thermalises quickly, the pressure (and thus the particle momenta) will be larger along the minor axis x, resulting in a mainly elliptic anisotropic flow (right).

As shown in figure I.21, average (radial and) elliptic flows have indeed been observed in heavy ion collisions, confirming the existence of collective effects in the medium. The fits with hydrodynamic models (left panel) depict a medium which behaves like a perfect fluid with a very low viscosity (shear viscosity to entropy density ratio $\eta/s \sim 0.2$ at LHC energies) [59, 61]. The elliptic flow evolution with the collision energy (right) exhibits no transition, which can correspond to a continuous transition (crossover) between the confined and deconfined phases. These elements are consistent with the production of a sQGP as described in section I.2.2.2.

[30] The rapidity of a particle quantifies the boost along the beam axis required to go from the laboratory frame to the frame where the particle has only a transverse momentum. It is computed from the particle's energy and longitudinal momentum with $y = \frac{1}{2}\ln\frac{E+p_L}{E-p_L}$.

[31] A shift of the isotropic flow toward the direction of the azimuthal angle ψ_1 and of strength v_1

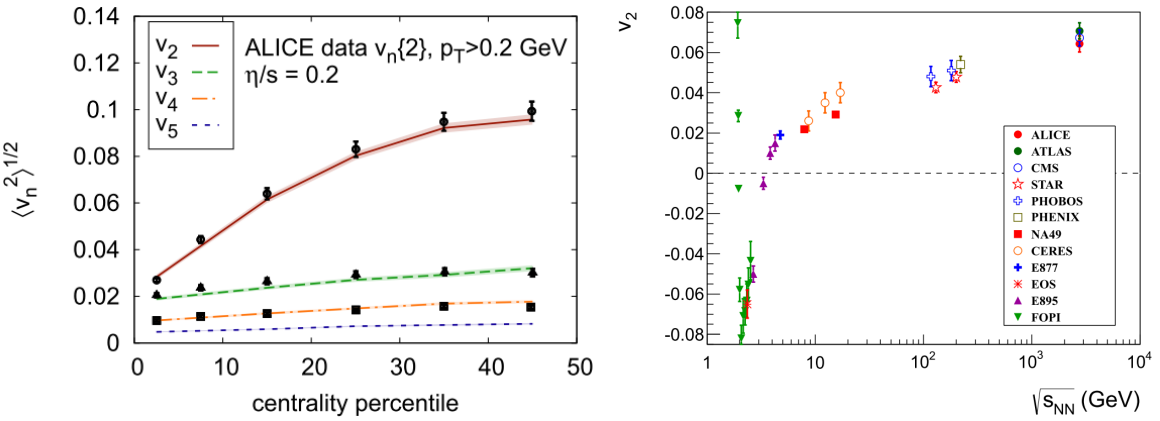

Figure I.21: *Left*: The centrality dependence of average v_n in $\sqrt{s_{NN}} = 2.76$ TeV Pb+Pb collisions measured by ALICE compared to viscous hydrodynamic model calculations [59]. *Right*: Average elliptic flow v_2 dependence on the collision energy $\sqrt{s_{NN}}$.

I.2.3.2 Light hadron suppression and jet quenching

The amounts of particles produced in heavy ion (AB or AA)[32] collisions are usually compared to the ones produced in proton-proton (pp) collisions. The latter can indeed be seen as a "reference" where no cold or hot medium effects can modify the particle production. More precisely, one commonly studies the *nuclear modification factor* $R_{\rm AA}$, i.e. the ratio of the cross section (or multiplicity N) in AA collisions to the one in pp scaled by the total number of binary nucleon-nucleon collisions $\langle N_{\rm coll}\rangle$ evaluated from the Glauber model [44] as a function of the centrality,

$$R_{\rm AA}(p_{\rm T},\eta) = \frac{dN^{\rm AA}/d^2p_{\rm T}d\eta}{\langle N_{\rm coll}\rangle\, dN^{\rm pp}/d^2p_{\rm T}d\eta}, \tag{I.14}$$

where the standard variables are the transverse momentum $p_{\rm T}$ and the (pseudo-) rapidity[33] η. If an AA collision is the simple superposition of nucleon-nucleon collisions then the ratio $R_{\rm AA}$ is equal to unity. On the contrary, if the particle production and/or kinetics is modified by the cold and hot medium effects and is not the simple superposition of nucleon-nucleon collisions, one obtains an $R_{\rm AA} \neq 1$. One usually speaks of a production *enhancement* if $R_{\rm AA} > 1$ and *suppression* if $R_{\rm AA} < 1$.

To investigate the cold and hot media it can thus be interesting to study how they change particle production and/or kinetics. For instance, one can focus on the dependence of the $R_{\rm AA}$ on the transverse momentum obtained for charged hadrons $h^{\pm}$ or for specific hadrons.

- One can first observe that for the low $p_{\rm T}$ hadrons ($1 < p_{\rm T} < 5$ GeV), the suppression increases (the $R_{\rm AA}$ decreases) with the collision energy and the

[32] Denoted AA (AB) if the ion A collides with a similar ion A (with a different type of ion B).

[33] The pseudorapidity is related to the angle θ of a particle relative to the beam axis and is defined by $\eta \equiv -\ln\left[\tan\left(\frac{\theta}{2}\right)\right] = \frac{1}{2}\ln\left(\frac{|\mathbf{p}|+p_z}{|\mathbf{p}|-p_z}\right)$. The pseudorapidity is used instead of the angle θ because its differences do not depend on the frame (Lorentz invariant).

centrality (see figures I.22 and I.23). The energy dependence is consistent with the evolution of the gluon shadowing as the collision energy increases (see figure I.14): a relative lower gluon density leads to smaller production cross sections. The centrality dependence is also expected from the increase of the hot medium density and size which might lead to a higher average number of scatterings and radiations per parton and to a larger pseudorapidity broadening (the measurement is here limited to $|\eta| < 1$). The complete characterisation of this suppression may thus be given by a complex mix of shadowing, medium density and size, parton scatterings and radiations, flow, hadronisation processes and final (in)elastic hadronic scatterings. Including more or less of these ingredients, hydrodynamic [62] and microscopic transport (Ultra relativistic Quantum Molecular Dynamics [63], Parton Hadron String Dynamics [64]...) models attempt to describe the fireball behaviour and lead to rather good experimental fits[34].

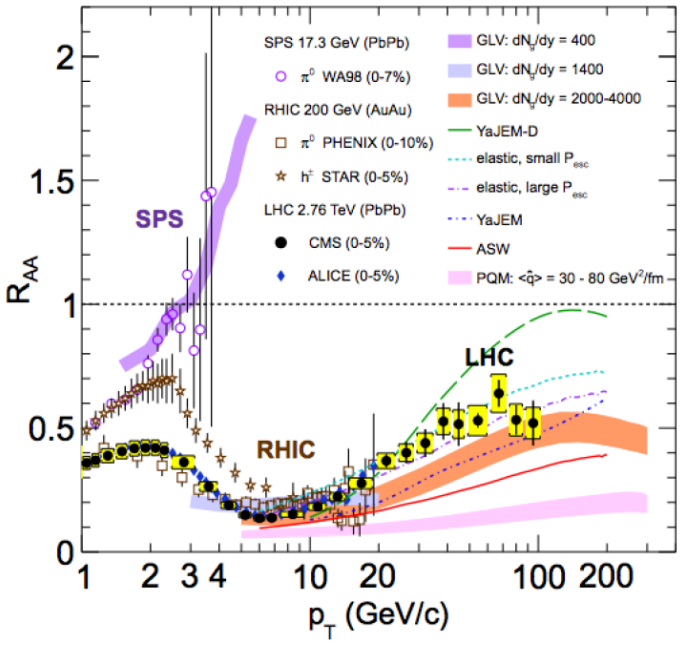

Figure I.22: *Left*: For most central collisions, nuclear modification factors R_{AA} of the pion π^0 and of the charged hadrons $h^{\pm}$ as a function of their transverse momentum at SPS ($\sqrt{s_{NN}} = 17.3GeV$), RHIC ($\sqrt{s_{NN}} = 200GeV$) and LHC ($\sqrt{s_{NN}} = 2.76TeV$) collision energies. [70]

- For central collisions at both RHIC and LHC (figure I.22), one can observe an important suppression of the hadrons for $5 < p_{\mathrm{T}} < 10$ GeV, followed by a linear rise of the R_{AA} for high p_{T} hadrons ($p_{\mathrm{T}} > 10$ GeV) which levels off from ~ 40 GeV at the LHC. The evolution of this suppression with the centrality (figures I.22 and I.23) first shows that the productions of a hot and cold medium, in most central and peripheral collisions respectively, result on very different

[34]The hot nuclear medium created in these collisions is such a dynamical and complex medium that its description requires the use of all-included simulation codes.

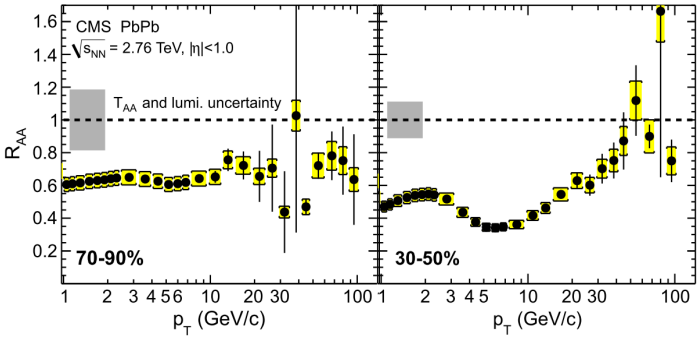

Figure I.23: At LHC energy, the nuclear modification factors R_{AA} of the charged hadrons $h^{\pm}$ as a function of their transverse momentum and for two different centrality ranges (left: most peripheral and center: peripheral). See figure I.22 for the central situation. [70]

suppressions for high p_{T} final hadrons. Furthermore, the independence of the high p_{T} suppression upon specific light hadrons (see figure I.24) suggests that the main energy loss mechanism (see below) acts at the partonic level [65]. Indeed, at the hadronic level the different hadrons would have different interaction cross sections with the medium and would therefore be affected differently. The high p_{T} suppression can therefore be seen as a signature of QGP production. A high energy parton should loose part of its kinetic energy through radiation and elastic collisions as it propagates in the hot medium. The radiative energy loss originates from medium stimulated gluon emissions ("Bremsstrahlung") and depends mainly on the parton momentum, its propagation length within the medium and a transport coefficient. It is predicted to dominate the collisional energy loss at high energies (see [66] and references therein). Common models of radiative energy loss, such as BDMPS[35] [67], lead to a weak dependence of the energy loss ΔE on the parton energy E. A decrease of the $\Delta E/E$ ratio (e.g. $\Delta E/E \propto \ln(E)/E$) as p_{T} increases, can qualitatively lead to the R_{AA} rise from $p_{\mathrm{T}} > 10$ GeV and flattening from $p_{\mathrm{T}} > 40$ GeV. The dependence of radiative energy loss on the propagation length might explain that the overall suppression at high p_{T} increases with the centrality, i.e. as the partonic medium size increases. Finally, it is interesting to emphasise that all this complex physics of energy loss interactions can be reduced to a single transport coefficient. The very high p_{T} suppression results in spectacular and relatively rare effects such as jet quenching and monojet. A jet is a set of energetic final hadrons situated in a narrow "cone" that come from the fragmentations of a very energetic parton. The latter is usually produced in a back-to-back hard process together with another equally energetic particle (parton, photon...) which can also result in a jet in the opposite direction ("dijet"). If one of these partons interacts with the hot medium (through energy losses), one observes the attenuation of the corresponding final jet ("jet quenching") or even its full suppression (leading to a "monojet" if the second parton interacts weakly) [68]. The photon-parton ("gamma jet") situation is especially interesting because the photon does not

[35] Baier-Dokshitzer-Mueller-Peigné-Schiff model for induced gluon radiation.

interact strongly with the hot medium and gives access to the initial parton energy. Gamma jet are then relevant experimental probes to energy loss and initial hot medium models [69].

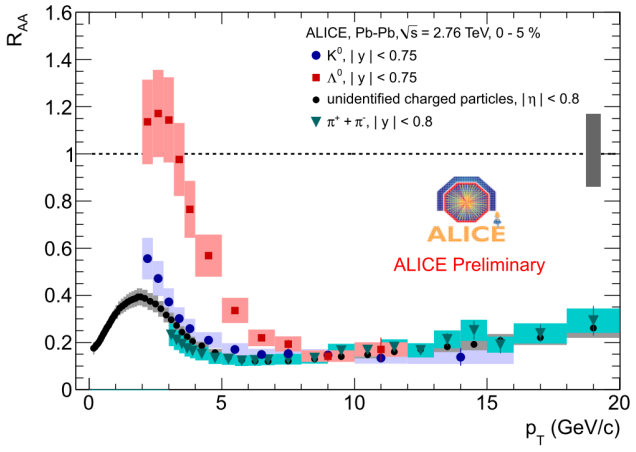

Figure I.24: At LHC energy and for most central collisions, the $R_{AA}(p_{\mathrm{T}})$ for different light hadrons. [65]

Main ideas and transition

To conclude, the experimental results and phenomenological models that we have presented so far seem[36] to confirm the production of a Quark-Gluon plasma in high energy heavy ion collisions. The QGP is now pictured as a strongly (or at least not very weakly) interacting, nearly perfect, quark-gluon fluid with a very low viscosity, interesting collective behavior and at least partial thermalisation. It is quite different from the initial expectations of a gas of very weakly interacting quarks and gluons at high temperature. Based on this conclusion, the production of a QGP in these collisions will be taken for granted in the next parts. We have seen that the light hadron multiplicity (chemical abundance) allows the measurement of the temperature at the boundary between the deconfined and confined phases and sketched that jet quenching is a convenient way to access density profiles along the path length. They are, however, not directly sensitive to the temperature. In the next part, we will discuss another observable, "the suppression of quarkonia", that might allow one to measure the temperature beyond the phase boundary, i.e. of the QGP itself.

[36] As no undeniable proof of net transition nor deconfinement has been observed for now, one should remain cautious before coming to a final conclusion.

Part II

Review on quarkonia suppression

We now focus on the suppression of the quarkonia, a possible observable of the quark-gluon plasma. The quarkonia are said to be suppressed when their amounts detected per binary nucleon-nucleon collisions in heavy ion collisions are smaller to the ones in proton-proton collisions. This is usually quantified by the nuclear modification factor R_{AA} defined in section I.2.3.2. In this part, after a discussion on the relevance of heavy flavours in heavy ion collisions (section II.1), we discuss the different possible phenomena which might play a role in quarkonia suppression according to the standard wisdom, and describe the different approaches developed with or without the presence of a QGP (section II.2). Then, we give an overview of the experimental data and their puzzling evolution with the collision energy and other kinematics (section II.3), and compare them to model predictions. Finally, we expose the resulting problematics and the motivations for the present work (section II.4).

II.1 The relevance of heavy flavours in heavy ion collisions

As introduced in the last part, quarkonia are an interesting probe to perform a "tomography" of the hot nuclear medium. The heavy quarks indeed enjoy many qualities [71].

1) The heavy quarks are produced at the very beginning of the collision in a rather well mastered amount from hard gluon fusion[37] and are mainly distributed within the core of the fireball. Indeed, thanks to their large mass, the typical time to produce a $Q\bar{Q}$ pair - the so-called "coherence" time - given by $\tau_c \sim \hbar/(2m_Q)$ in the $Q\bar{Q}$ frame ($\tau_c \sim 0.08$ fm/c for the charm and ~ 0.02 fm/c for the bottom quark) is much smaller than the QGP formation time ($\lesssim 1$ fm/c) and the medium life-time (~ 10 fm/c). Furthermore, their thermal production during the evolution should be negligible [72]. Spatially, according to calculations derived from the Glauber model [73, 74], their production density is favoured in the central part of the overlapping area. The typical times required for the $Q\bar{Q}$ pair to bound into quarkonium states, the so-called formation times in the vacuum, should be much larger than τ_c but are subject to debate [19]. They might correspond to the time interval required for the quarkonium wave functions to develop. In the $Q\bar{Q}$ frame, it might be related to the difference of mass between the 1S and 2S states for instance, i.e. $\tau_f \sim \hbar/(m_{2S} - m_{1S}) \sim 0.3 - 0.4$ fm/c, or to the QCD scale, i.e. $\tau_f \sim 1/\sqrt{2m_Q\Lambda_{\rm QCD}} \sim 0.1$ and 0.4 fm/c for bottomonia and charmonia respectively. For higher excited states, the formation times are correspondingly larger. Note that these estimations are assumed to be independent of the surrounding medium, which could seem curious if the states form inside a very dynamic and dense pre-equilibrium phase. It is therefore not obvious whether the states form before, during or at the end of the deconfined medium stage. Last, note that radiative decays of excited states (the feed-downs) occur far outside the medium, so that the feed-down calculations can be realised independently of the considered model and produced medium. The $Q\bar{Q}$ pairs or their bound states can thus propagate inside the high temperature nuclear media and probe its properties all along its evolution.

2) The influence of the heavy quarks on the hot medium is negligible, but not vice versa. Indeed, as they are produced in a quite small amount as compared to the light quarks, they might not influence the global dynamics of the QGP and might not modify its properties. Reciprocally, the observations of an elliptic flow for the open heavy flavours [75, 76], the quenching of open mesons with high transverse momentum [77] and the quarkonia suppression (see below), showed that the heavy flavours quite strongly couple with the medium [78] and thermalise at least partially with a probable delay due to their important inertia. For the single heavy quark and unlike the light quarks, the radiative energy losses could not explain alone this strong

[37] As discussed in section I.1.4.2, one should however keep in mind that there are still doubts about the actual production mechanism for the quarkonia and especially about their hadronisation. Then, it is not obvious to evaluate physical quantities such as the time required for a quarkonium state to be formed.

coupling at intermediate/high transverse momentum [79, 80, 81]. A non-negligible contribution of the collisional energy loss - from diffusion on light partons - was then reconsidered [82, 83, 84]. At low transverse momentum, radiative energy losses become negligible and the contribution of the collisional energy loss dominates [19]. For the quarkonia, as we will see in this part, the influence of the medium manifest itself in a different way.

3) The quarkonia are thought to deconfine at larger temperatures than the critical temperature T_c, leading to a possible evaluation of the medium temperature above T_c [1] (see section II.2.1.2). To this end, the bottomonia offer several advantages over the charmonia [19]. Firstly, in the $\mu^+\mu^-$ decay channel, the relative abundances of the $\Upsilon(1S)$, $\Upsilon(2S)$ and $\Upsilon(3S)$ states are $7:2:1$, respectively, while it is $50:1$ for the J/ψ and ψ' states. Bottomonia excited states are therefore more accessible to R_{AA} experimental measurement. Secondly, $\Upsilon(1S)$ is the most strongly bound state, allowing to probe a wider range of QGP temperature. Finally, the picture gets simplified thanks to their larger mass, the absence of non-prompt production channels, the small probability for uncorrelated $b\bar{b}$ pairs to recombine at the phase boundary[38] (see II.2.1.4), their small nuclear absorption, comover cross sections and expected shadowing (see II.2.1.1). However, the bottomonia initial production rate is around 200 times smaller than the one of the J/ψ, making their statistic only accessible from RHIC/LHC energies.

4) At the end of the evolution, heavy quarks hadronise to heavy mesons or baryons. These heavy hadrons have a large inertia and might therefore be not so sensitive to the elastic and inelastic collisions of the freeze-out stages. The heavy hadrons are thus only weakly affected by the final hadronic phase and the information about the heavy quark kinematics inside the QGP is not lost. The open heavy flavours go even further in this way: according to fragmentation models [85, 86] and unlike light quarks, their kinematics is very close to the one of the original heavy quarks.

II.2 Common approaches to quarkonia suppression

In this section, we will first briefly discuss the different possible phenomena which might play a role in the quarkonia suppression/enhancement in heavy ion collisions as compared to pp collisions. They include partonic and hadronic aspects from the initial to the final stage. Next, we will describe the different typical models, using more or less of these ingredients, developed to predict or postdict the experimental observations. A more extensive analysis of the theoretical approaches to quarkonia suppression can be found in the literature [19].

[38]The number of produced $b\bar{b}$ pairs is indeed much smaller than $c\bar{c}$, diminishing the probability for uncorrelated $b\bar{b}$ pairs to recombine at the hadronisation stage.

II.2.1 The different possible aspects of quarkonia suppression/enhancement in heavy ion collisions

II.2.1.1 Cold nuclear matter effects

These effects were initially studied to explain the observed quarkonia suppression and strangeness enhancement while assuming a pure hadronic phase (i.e. without QGP formation). However, they have been shown repeatedly to be insufficient to describe the data ([87] and references below). Nevertheless, even with the formation of a QGP they might still play an important role in the quarkonia suppression during the initial and final hadronic phases.

Shadowing

As the $Q\bar{Q}$ pairs mainly originate from gluon fusion, their production rate depends on the initial gluon density. As already discussed in section I.2.2.1, the physics of parton saturation at small x is described by the nPDFs or the CGC model. Within the former, the gluon density of colliding nuclei is modified by the interactions between nucleons, leading to a possible decrease (shadowing) or increase (anti-shadowing) of the initial heavy quark production depending on the collision energy (see figure I.14). The nPDFs have been mainly studied in p-A collision experiments and can be used for A-A collisions resorting to the factorisation theorem [19].

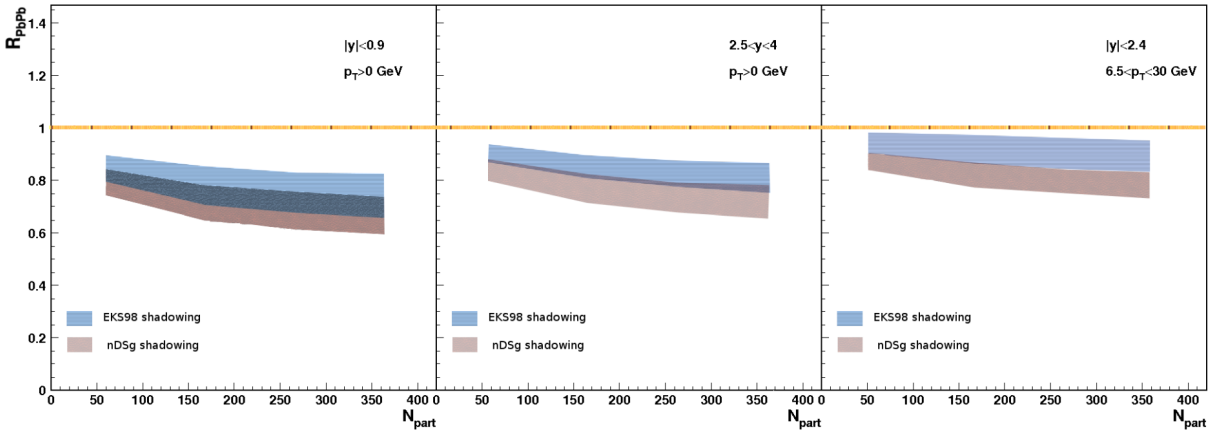

Figure II.1: Shadowing effect on J/ψ suppression obtained with EKS98 LO and nDSg LO nPDFs in PbPb collisions at $\sqrt{s_{NN}} = 2.76$ TeV [88, 89].

As illustrated in figure II.1, the quarkonia suppression obtained from the different shadowing models (nPDFs) have mainly in common:

- The suppression decreases with increasing transverse momentum p_T and becomes small at high p_T.
- The suppression decreases with increasing rapidity.

– The suppression is smaller with bottomonia.

– The shadowing can lead to a suppression of maximum $\sim 30\%$.

These effects can be understood from the expressions of the longitudinal momentum fractions of the fusing gluons as functions of these parameters (p_T, y, m_Φ) and from the general shadowing pattern in a single nucleus[39].

Cronin effect

During the first moments of the collision, the initial partons (among which the fusing gluons) may undergo multiple elastic scatterings on the colliding nuclei leading to a p_T broadening known as the Cronin effect. Indeed, at each elastic collision the partons acquire some transverse momentum - their initial momentum being almost only longitudinal - and lead to a broadening of the quarkonia p_T distributions in p-A and A-A collisions as compared to p-p collisions.

Parton energy losses

The propagation of the initial partons and newly produced color octet $Q\bar{Q}$ pairs inside the two colliding nuclei leads to collisional and coherent medium-induced radiative energy losses[40] and quarkonia suppression. The energy loss models are based on the ideas that 1) the heavy flavours are produced before any hot medium, 2) τ_f in any of the nucleus frames is much larger[41] than the nuclear size at LHC and 3) the $Q\bar{Q}$ pairs propagate with a high kinetic energy inside each of the colliding nuclei. Thanks to the model success in describing the quarkonia suppression in p-A collisions [90, 91], parton energy loss might be seen as the leading effect in these collisions (and the shadowing effect as a simple correction). However, it has failed to reproduce alone the observed suppression in A-A collisions, especially at RHIC and for the $\Upsilon(1S)$ state [92]. One can nevertheless note a quite remarkable description of the J/ψ suppression dependence on $N_{\rm part}$ in Pb-Pb collisions at LHC and that the predicted quarkonia suppressions are up to $\sim 20\%$ at RHIC (200 GeV) and to $\sim 40\%$ at LHC (2.76 TeV) and should therefore be taken into account in addition to the QGP effects (especially at forward rapidities).

Nuclear absorption

According to this model, the $Q\bar{Q}$ pair or its bound states can interact inelastically with the nuclei right after its formation and dissociate. This is the so-called nuclear absorption, which have presumably led to the "normal" suppression of the quarkonia observed at SPS (see section II.3.1). The nuclear absorption has been especially studied in p-A collisions in order to quantify its effects. Within the usual nuclear absorption framework, the quarkonia survival probability $S_{\rm abs}$ inside a nucleus is

[39] See figure I.14.

[40] See section I.2.3.2.

[41] In the nucleus frame, one needs to apply a Lorentz factor to the τ_f computed in the quarkonia rest frame.

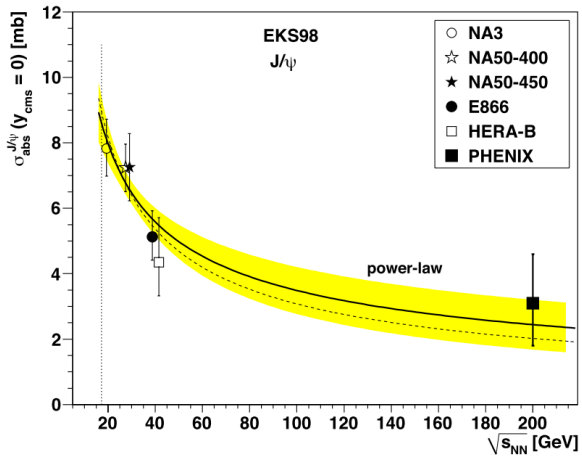

Figure II.2: The cross section $\sigma_{\rm abs}$ for the J/ψ shows a strong dependence on the collision energy. Here, its estimated values at SPS and RHIC are compared to the EKS98 and CTEQ6 nPDFs prediction at midrapidity [88, 93].

expressed as an exponential decay,

$$S_{\rm abs} = \exp(-\rho_A \sigma_{\rm abs} L) \tag{II.15}$$

where ρ_A is the nuclear density, L the mean propagation length and $\sigma_{\rm abs}$ an "effective break-up" cross section, which is the inelastic cross section of a quarkonium with a nucleon. The latter can be estimated from the analysis of p-A collisions and be extrapolated to A-A collisions thanks to the Glauber model. The cross section $\sigma_{\rm abs}$ was observed to decrease with the collision energy (see figure II.2) and its extrapolation to LHC energies leads to a negligibly small cross section.

Comovers

The Comovers model was introduced in the 90s to explain the "abnormal" suppression observed at SPS. It describes the quarkonium dissociation (or recombination) by inelastic interactions with the produced "comoving" hadrons $h_{\rm co}$ of the medium, leading to new open heavy mesons through the process $Q\bar{Q} + h_{\rm co} \rightarrow D/B + D/B + X$ or to quarkonia through $D/B + D/B \rightarrow Q\bar{Q} + X$. Similarly to nuclear absorption, a corresponding approximate survival probability $S_{\rm co}$ can be derived from the gain and loss differential equation in transport theory for the quarkonium state $\Phi = J/\psi, \psi', \Upsilon(1S)...$,

$$S_{\rm co} = \exp\left(-\sigma_{\rm co}\left(N_{\rm co} - \frac{N_Q N_{\bar{Q}}}{N_\Phi} \right) \ln\left[\frac{N_{\rm co}}{N_{\rm f}} \right] \right) \tag{II.16}$$

where N_Q (N_Φ) the density of the considered heavy quark (quarkonium state) and $\sigma_{\rm co}$ is the cross section of the quarkonium dissociation with the comoving medium of density $N_{\rm co}$. Thanks to the term $\ln[N_{\rm co}/N_{\rm f}]$, the interaction stops when the comoving medium density reaches its freeze-out value $N_{\rm f}$. As $N_{\rm co}$ is proportional to the

medium energy density, the quarkonia suppression is then continuously dependent on the medium energy density. Without assuming any QGP, the comovers model (including the shadowing) leads to a reasonable agreement (but limited) with the data at RHIC and LHC [94, 95]. With the presence of a QGP, the comover contributions could therefore occur during the mixed phase and the following hadronic stage. Note finally that, thanks to the large gluon density in the QGP and to the large cross section of quarkonium dissociation by gluons, an equivalent comoving process might also occur in the partonic deconfined medium [96]. The latter will be further discussed in section II.2.1.3.

II.2.1.2 Sequential suppression

In 1986, Matsui and Satz [1] were the first to predict that the quarkonia suppression could be a sign of QGP production. Their so-called sequential suppression model is based on the idea that quarkonium states could be melted by color screening effects. More explicitly, inside the QGP, the range of the strong interaction binding the $Q\bar{Q}$ pair tends to be reduced by the presence of color charges in its vicinity. The range of the screened force is usually described by the Debye screening radius - by analogy with the electromagnetic plasma - and is inversely proportional to the color charge density ε in the deconfined medium. Consequently, the higher the temperature of the QGP, the smaller the Debye screening radius. Within its dualistic description, the sequential suppression assumes that a quarkonium state is melted if its radius is larger than the Debye radius while nothing happens if not. To each state then corresponds a dissociation temperature T_d above which the state is completely melted, i.e. if $T_{\mathrm{QGP}} > T_d$. Indeed, the heavy quarks of the melted state are then assumed to move freely inside the QGP until the hadronisation, where it is most probable that they hadronise as open heavy mesons. Hence, if this scenario is correct, one should observe for the J/ψ a suppression by "steps" as the different higher excited states (and their feed-downs) melt with increasing medium density (see figure II.3). As the whole sequential suppression occurs in the very early QGP where the temperature is maximal, one can thus see the quarkonia suppression as an early QGP thermometer.

To "calibrate" the quarkonia thermometer, the different dissociation temperatures T_d need to be estimated. Unfortunately, this evaluation is far from being obvious: several approaches have been developed and have led to a wide range of results as shown in figure II.4. The most common approaches are the use of potential models [99, 100, 101] or the evaluation of correlators and spectral functions in finite temperature lQCD [102, 103]. Within the spectral function approach, the bound states manifest themselves as peaks which are characterised by their mass and spectral width (formation/destruction rate). One can then determine the dissociation temperature when the spectral peak disappears while increasing the temperature of the lattice (see figure II.5). Within the potential model framework[42], the potential possible shapes and temperature dependences are determined either from "old"

[42] See section III.1.1.

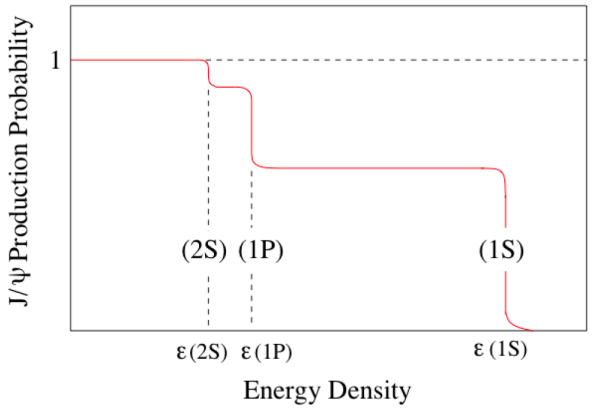

Figure II.3: Illustration of the J/ψ sequential suppression as a function of the QGP color charge density ε. $\varepsilon(\Phi)$ is the dissociation density of a state Φ. [97].

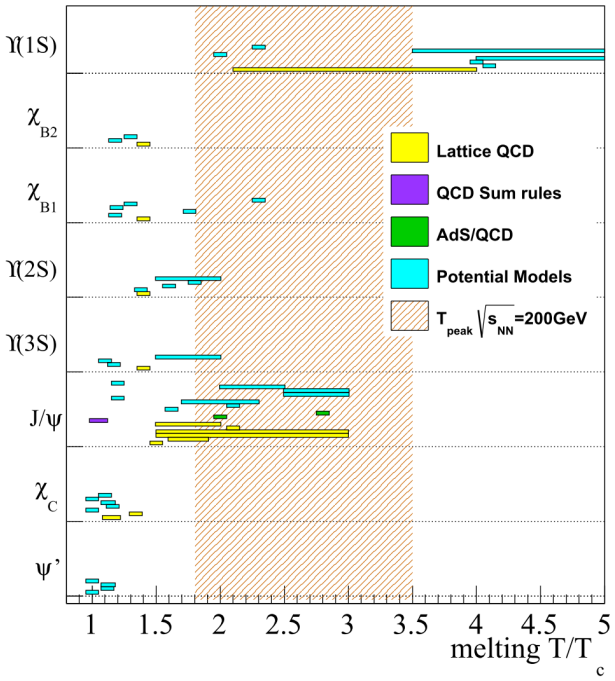

Figure II.4: Compilation of state dissociation temperatures T_d evaluated from different approaches and calculations: Lattice QCD, QCD sum rules, AdS/QCD , effective field theories and potential models. One should note that these evaluations are performed assuming different T_c values and that the horizontal bar corresponds to the temperature extension where the state undergoes a mass/size evolution until it completely melts at the right end of the bar (see [98] and references therein for more details).

effective models or more recent lQCD results. The energy and state spectra are first determined with the time independent Schrödinger equation. The dissociation temperature of a state Φ is then given by the cancellation of its dissociation energy,

$$E_{\rm diss}(T) = V_{Q\bar{Q}}(r \to \infty, T) - (E_\Phi - 2m_Q). \tag{II.17}$$

where r is the distance between the two heavy quarks. For instance, the dissociation

temperatures obtained with the $Q\bar{Q}$ internal energy (evaluated from a fit to lattice results [104]) are summed up in figure II.6.

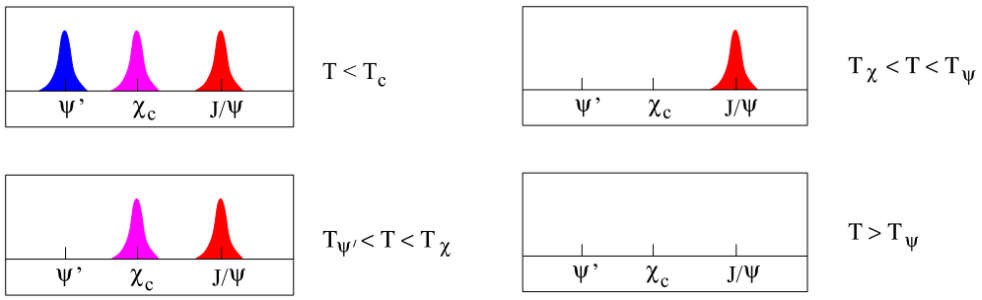

Figure II.5: The sequential suppression and the disappearance of the spectral components as the QGP temperature increases [105].

state	J/$\psi(1S)$	χ_c(1P)	$\psi'(2S)$	$\Upsilon(1S)$	$\chi_b(1P)$	$\Upsilon(2S)$	$\chi_b(2P)$	$\Upsilon(3S)$
T_d/T_c	2.10	1.16	1.12	> 4.0	1.76	1.60	1.19	1.17

Figure II.6: Reduced quarkonium dissociation temperatures as obtained with a potential model [97].

II.2.1.3 Elastic and inelastic collisions with hard probes: the cross sections approach

Another important contribution to the quarkonia suppression in the QGP could originate from inelastic collisions with the medium gluons and light quarks, which cross section calculations can be treated with pQCD [19]. In the QGP, for a tightly bound state (dissociation energy $E_{\rm diss} > T$ or very small size), the dominant inelastic process is the hard gluo-dissociation of the quarkonium Φ introduced by Bhanot and Peskin [106, 107, 108, 109], $g + \Phi \rightarrow Q + \bar{Q}$, so that a sufficiently energetic gluon can break the binding. The gluo-dissociation cross section calculation carried out within the dipole approximation and operator product expansion [106] yields

$$\sigma_{g-\Phi} \sim \frac{1}{m_Q^2} \frac{(k/E_B - 1)^{3/2}}{(k/E_B)^5}, \tag{II.18}$$

where k is the gluon momentum in the Φ rest frame and $E_B = 2m_Q - m_\Phi$ the binding energy. In a formulation where the color screening is taken into account, $\sigma_{g-\Phi}$ depends on a temperature dependent dissociation energy which can be evaluated from the screened potential models as in section II.2.1.2. The gluo-dissociation

is only expected to be efficient in a hot deconfined medium because the gluons coming from hadrons are too soft to allow this process [97] (see figure II.7). The J/ψ suppression obtained with the gluo-dissociation process is illustrated in figure II.8. For loosely bound states ($E_{\text{diss}} < T$, i.e. for excited and partially screened states), the phase space for gluo-dissociation rapidly shuts off, rendering the parton dissociation $p + \Phi \rightarrow Q + \bar{Q} + p$ (where $p = q, \bar{q}$ or g) the dominant process [110]. Of course, the reciprocal recombination process $p + Q + \bar{Q} \rightarrow \Phi + p$ is also possible. The knowledge of the inelastic cross sections leads to the evaluation of one of the key transport coefficients - the inelastic reaction rates for dissociation and formation - commonly used by transport models to continuously flip between quarkonia and "free" $Q + \bar{Q}$ (see section II.2.2.2).

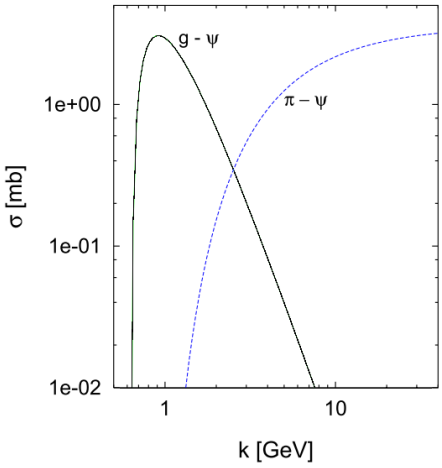

Figure II.7: Comparison between gluon and hadron cross-sections for J/ψ dissociation [106]. In a deconfined medium, the typical thermal gluon momentum of $\sim$ 1 GeV corresponds to a large dissociation cross-section. Whereas in a confined medium, hadron typical thermal momenta (up to 2 - 3 GeV) lead to vanishingly small cross-sections [97].

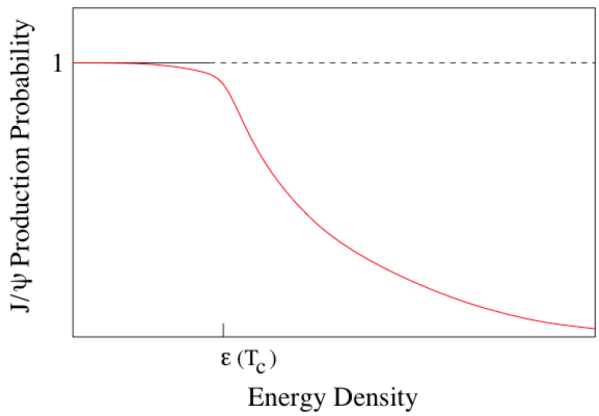

Figure II.8: Illustration of the J/ψ suppression obtained from gluo-dissociation as a function of the medium density [97].

The calculations of the quarkonia and heavy quarks elastic cross sections for the processes $\Phi/Q + p \rightarrow \Phi'/Q + p$ (where Φ' can be Φ or another state) have

also been carried out to study their diffusion in the medium [106, 109, 111]. They have received recently a renewed attention [109] with the perspective of explaining the "suppression of the suppression" observed at RHIC and LHC (see section II.3). From the elastic cross sections, one can evaluate the collisional energy loss and the diffusion coefficients used by kinetic equations (Fokker-Planck, Boltzmann...) for the evolution of the quarkonium center-of-mass motion [109, 112].

II.2.1.4 Recombinations

The recombination was first introduced to explain the observed "suppression of the suppression". It predicts an enhancement of the quarkonium production from a recombination of uncorrelated Q and $\bar{Q}$ at the phase boundary [113]. The idea of a recombination mechanism at the phase boundary is commonly used within the statistical hadronisation and transport approaches, and will be further discussed in section II.2.2.

II.2.2 The different models

II.2.2.1 Statistical hadronisation models

Driven by its successful description of light hadrons multiplicity (see figure I.19), the statistical hadronisation model has also been applied to the quarkonia yield. This model is based on the possible secondary production of quarkonia from recombinations of uncorrelated Q and $\bar{Q}$ at the phase boundary [113, 114, 115]. This secondary production might occur only if the number of uncorrelated heavy quarks N_Q in the medium is statistically non-negligible in comparison to the light quarks. N_Q is directly proportional to the number of heavy quark pairs produced from the primary production (from gluon fusions), and should therefore increase with the centrality. It also increases with the collision energy: one expects the production of a hundred $Q\bar{Q}$ pairs at LHC and around ten times less at RHIC [116, 117]. The recombination is expected to increase quadratically with N_Q, so that at high energy density (which increases with N_{part} and $\sqrt{s_{NN}}$) it becomes the dominant production mechanism (see figure II.9). Furthermore, it should be favoured at mid rapidity - the phase space region where the charm yield is the more important - and should be observed dominantly at small p_T because single heavy quarks are expected to thermalise at least partially with the medium [118]. Then, its contribution might be important at LHC, moderate at RHIC and negligible at SPS. Some hints that the recombination process would occur are the enhancement of the closed to open heavy hadrons ratio with the density energy or the observation of quarkonia elliptic flow (which should be negligible with only neutral primary quarkonia). Finally, note that it could be a deal breaker for the idea of a quarkonia thermometer.

Within the statistical hadronisation models, the initial $Q\bar{Q}$ pairs get first fully color screened in the deconfined QGP as the other partons. Then, assuming that

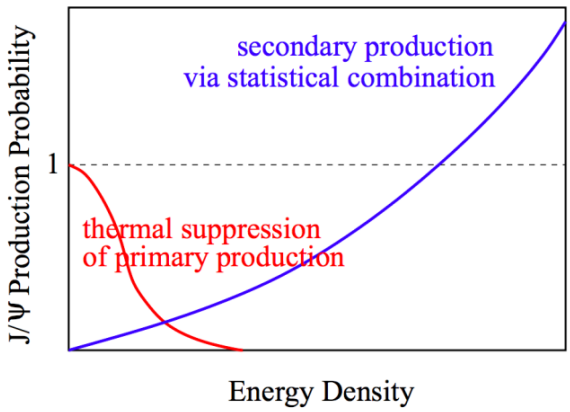

Figure II.9: Comparison between the expected R_{AA} from screening only and from statistical recombinations [119].

the QGP reaches a thermal and chemical equilibrium at hadronisation, the single heavy quarks hadronise with light or heavy quarks at the phase boundary to form open hadrons or quarkonia according to their statistical weights and masses. The statistical weight of the different states is given by the corresponding statistical distribution at the hadronisation temperature (which is already fitted to the light hadron multiplicities). The $\psi'/J/\psi$ ratio measurement should then be a crucial test for its predictions. The only uncertainties of the model are the initial $Q\bar{Q}$ pair yield, which is usually calculated using the nPDFs and the values of the baryon chemical potential, temperature and medium volume (the fireball decay is considered as a grand canonical ensemble).

II.2.2.2 Transport models

As already introduced in the introduction I.2.3.2, the transport models are the necessary almost "all-included" simulations which attempt to describe the dynamic behaviour of the fireball from the initial colliding hadrons to the final freeze-out [112, 63, 64]. They are usually based on more or less of the following ingredients [19]:

- Primordial productions of light and heavy quarks from pQCD and nPDFs (including the shadowing).
- The initial cold nuclear matter effects such as the nuclear absorption and the Cronin effect.
- The quarkonium formation times τ_f which affect quarkonium suppression at high p_T [120].
- An initial sequential-like suppression of the quarkonia in the early QGP: if $T(\tau_f) > T_d$ the state melts, otherwise forms.

– An isotropically expanding fireball model, with local temperatures, reproducing the measured hadron yields and phase space spectra, or alternatively an hydrodynamic description.

– For the quarkonia in the deconfined matter, a space-time evolution of the phase-space distributions f_Φ described by classical kinetic equations[43] such as the relativistic Boltzmann equation (or the rate equation),

$$p^\mu \partial_\mu f_\Phi(\vec{r},\vec{p},\tau) = -E_p \Gamma_\Phi(\vec{r},\vec{p},\tau) f_\Phi(\vec{r},\vec{p},\tau) + E_p \beta_\Phi(\vec{r},\vec{p},\tau), \qquad \text{(II.19)}$$

where $p_0 = E_p = (\vec{p}^2 + m_i^2)^{1/2}$, $\vec{r}$ is the spatial coordinate, τ the proper time, Γ_Φ the dissociation rate and β_Φ the formation rate which depends on the single heavy quark phase-space distributions. The quarkonia then propagate along straight lines until their possible dissociation into two single heavy quarks. The dissociation and formations rates are evaluated from the inelastic cross sections of the $\Phi + p \rightleftarrows Q + \bar{Q} + p$ processes (see II.2.1.3). The latter depend on the quarkonium dissociation energies which are determined from simple or color screened potentials (see III.1.1). The dissociation rate can also be evaluated from the finite widths of the states while using imaginary potentials from lQCD [121, 122, 123]. The single heavy quarks are evolved with an equivalent Boltzmann equation but with an additional diffusive term determined from the elastic cross sections of the process $Q+p \to Q+p$ (see II.2.1.3). In practice, one can also use the Fokker-Planck equation[44] (or relativistic Langevin simulations [112]) which drag and diffusive coefficients are derived from the elastic cross sections. The theoretical advantage of the Fokker-Planck equation over the Boltzmann equation - which assumes a diluted medium - is that it can be used without making any assumption on the medium density.

– A secondary quarkonia production from recombinations at the phase boundary.

– The final elastic and inelastic scattering from cross sections calculations.

– Quarkonia feed-downs from excited states and non-prompt productions.

The most widespread transport simulations treating of the quarkonia are the TAMU by Zhao et al. [124, 125] and THU by Liu et al. [126, 127] models, which differs mainly on their ratio of primary/secondary quarkonia productions and on details of the implementation (potential model...).

II.3 Experimental observations: from SPS to LHC

Since the 80s, the production of quarkonia in heavy ion collisions - and especially of the J/ψ - has been intensively investigated experimentally. The p-A collisions have allowed the study of the (anti-)shadowing effect and the propagation of heavy

[43] The kinetic equations describe the time evolution of a system consisting of a large number of particles.

[44] The Fokker-Planck equation is derived from an expansion of the Boltzmann equation within the Brownian approximation. See part IV for more details.

hadrons inside the cold nuclear matter. In AA collisions, the formation of a QGP was expected to be obtained from SPS energies and with larger and larger life-times and temperatures as the collision energy increases at RHIC and LHC. As many extensive reviews can be found in the literature [19, 109, 128], we will only focus on the main experimental data relevant to the present work.

II.3.1 SPS

The Super Proton Synchrotron (SPS) and its various experiments (NA38, NA50, NA51, NA60...) have explored different kinds of ions and energies: 158 AGeV ($\sqrt{s_{NN}} = 17.3$ GeV) in In-In and Pb-Pb collisions, 200 AGeV ($\sqrt{s_{NN}} = 19.4$ GeV) in S-U collisions and 400 AGeV in pA collisions (where A is either a Be, Al, Cu, Ag, W or Pb ion). To get rid of the systematic errors[45] and to give a reference measurement[46], the quarkonia cross sections are normalised by the medium-independent cross sections of the Drell-Yan (DY) process ($q + \bar{q} \rightarrow \gamma/Z \rightarrow \mu^+\mu^-$). The first indication of QGP production came from the observation of an abrupt "abnormal" suppression of the J/ψ from semi-peripheral Pb-Pb collisions (see figure II.10 - left and right panels).

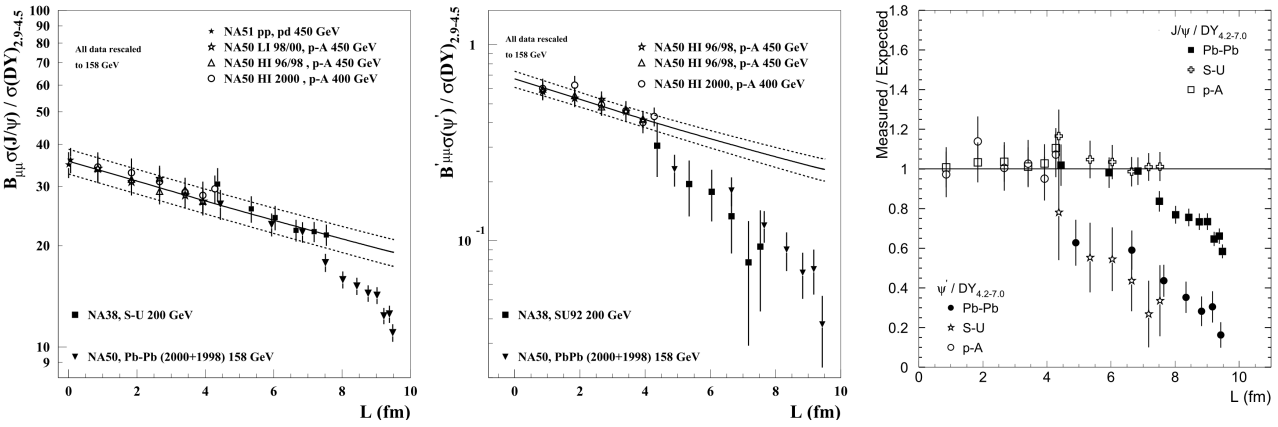

Figure II.10: The ratio cross sections J/ψ/DY (left panel) and ψ'/DY as a function of L (center panel). L is the penetration length inside the nuclear matter, determined from the Glauber model and the geometry of the collision. The same ratios divided by the expected values from cold nuclear matter effects deduced from p-A collisions (right panel).[129]

By abnormal suppression, one means that the suppression does not follow the expected linear behaviour of the cold nuclear matter suppression which corresponds to the solid lines. In the right panel (where the expected suppression from cold nuclear matter effects is subtracted), the flattish part of the Pb-Pb collision spectrum confirms that the abnormal suppression is not due to the mere transition from pA to AA collisions. This first indication with the J/ψ was soon followed by an even more revealing measurement: the ψ' abnormal suppression (see the central and

[45] The systematic errors are related to the detection efficiency, the beam intensity and luminosity... and are too important at SPS to obtain correct quarkonia cross sections.

[46] The reference measurement (which is not influenced by the medium effects) at RHIC and LHC is played by the quarkonia cross sections in pp collisions.

right panels). One can indeed observe that its abnormal suppression begins from a smaller penetration length and is higher by a factor ~ 2.5. Such behaviours might correspond to the sequential suppression by color screening predicted by Matsui and Satz [1] but .

II.3.2 RHIC

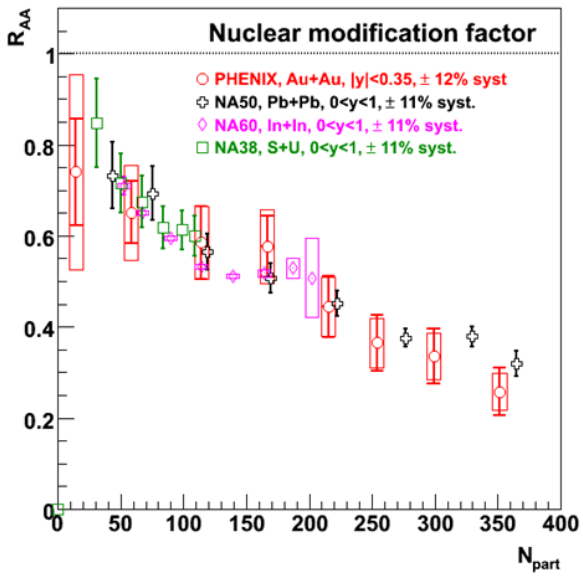

Figure II.11: Nuclear modification factor R_{AA} data for the J/ψ as a function of centrality. Comparison of the J/ψ suppression between SPS and RHIC energies at mid rapidity and low p_T [130, 131].

With a maximum collision energy ($\sqrt{s_{NN}} = 200$ GeV) more than ten times larger than at the SPS, the Relativistic Heavy Ion Collider (RHIC) and its PHENIX and STAR detectors are almost only dedicated to heavy ion collisions (p-p, d-Au, Cu-Cu, Au-Au, U-U and Cu-Au). At this energy, the theory predicts the production of a QGP with a maximum initial temperature well above the critical temperature T_c and a much larger production of $Q\bar{Q}$ pairs (which improves the statistics that was lacking at SPS).

Whereas a larger suppression of the quarkonia was expected at RHIC due to a higher QGP initial temperature and density, the data actually led to a surprising equivalent J/ψ suppression at RHIC and SPS for mid rapidities (see figure II.11). This was the first observation of the so-called "suppression of the suppression"[47]. The popular explanation is the balance at RHIC between an initially larger suppression and a final statistical recombination. In figure II.12, one can see a comparison between different kinematic regions for the J/ψ suppression at RHIC. As expected from recombinations but not from the shadowing, the J/ψ states measured at forward rapidity are more suppressed than at mid-rapidity (see left panel). The trans-

[47] When one observes less suppression than expected.

port models quite well describe both these suppressions (as shown in figure II.15). The J/ψ states measured at low transverse momentum p_T are more suppressed than at high p_T (see right panel). At first sight, this could seem a bit curious as one would expect less suppression at low p_T from the statistical recombinations. The high p_T data (red dots) are not well described by transport models whereas the low p_T data (black open circles) are reasonably well described by the statistical hadronisation model [132]. At high p_T, the observed plateau for $170 \lesssim N_{\rm part} \lesssim 320$ can be seen as a sign of sequential suppression. The suppression difference between the low and high p_T regions could be explained by the more important screening, shadowing and cold energy loss effects expected at low p_T, assuming that the recombination is negligible. Finally, note that there is not yet data at RHIC for other charmonium states (such as the ψ').

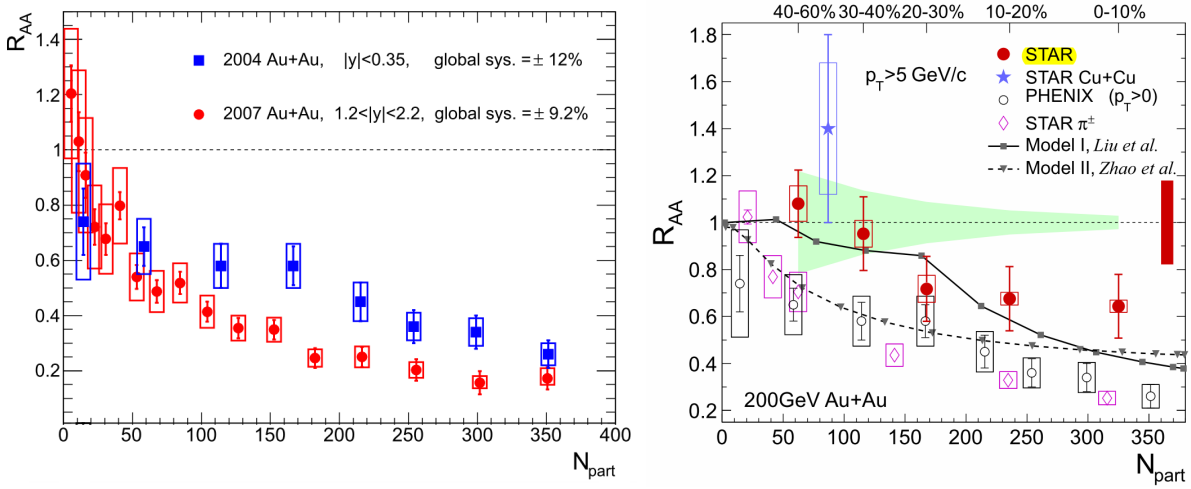

Figure II.12: R_{AA} data for the J/ψ as a function of centrality. *Left:* Comparison between mid and forward rapidities for low p_T inclusive J/ψ suppression [133]. *Right:* Comparison between low $p_T < 5$ GeV/c (black open circles) and high $5 < p_T < 14$ GeV/c (red dots) inclusive J/ψ suppression at mid rapidity ($|y| < 0.35$ and $|y| < 1$ respectively). The high p_T J/ψ suppression is compared with TAMU and THU transport models [134].

In figure II.13, the elliptic flow v_2 of the J/ψ is compared with the v_2 of lighter hadrons and various theoretical models. It is compatible with zero for $p_T > 2$ GeV/c, showing that intermediate p_T J/ψ do not thermalise with the medium, whereas very low p_T J/ψ shows some signs of thermalisation. The agreement between the data and the different model calculations is quite poor, and tends to show that the final recombination should be moderate (but nevertheless finite) to be compatible with a non flow situation for $p_T > 2$ GeV/c.

For bottomonium states, the R_{AA} of the $\Upsilon(1S)$ state as a function of centrality are shown in figure II.14. The $\Upsilon(1S)$ is quite strongly suppressed for central collisions but less than the J/ψ. Furthermore, its suppression starts at higher centralities than the J/ψ (i.e. at higher densities and temperatures). Both these observations support the sequential suppression point of view. Nevertheless, none of the theoretical models presented here fits the data. The $\Upsilon(2S + 3S)$ data are unfortunately

not yet exploitable due to large systematic errors [135].

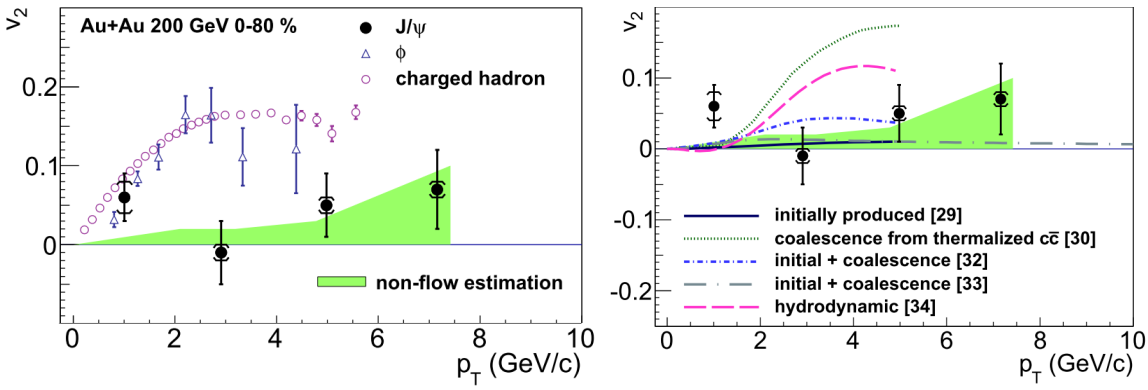

Figure II.13: *Left:* Elliptic flow v_2 of the J/ψ and charged hadrons at mid rapidity in 0-80% central events. *Right:* Elliptic flow v_2 of the J/ψ compared with different theoretical model calculations ([29] and [33] are from THU transport model; [30] and [32] from TAMU transport model) [136].

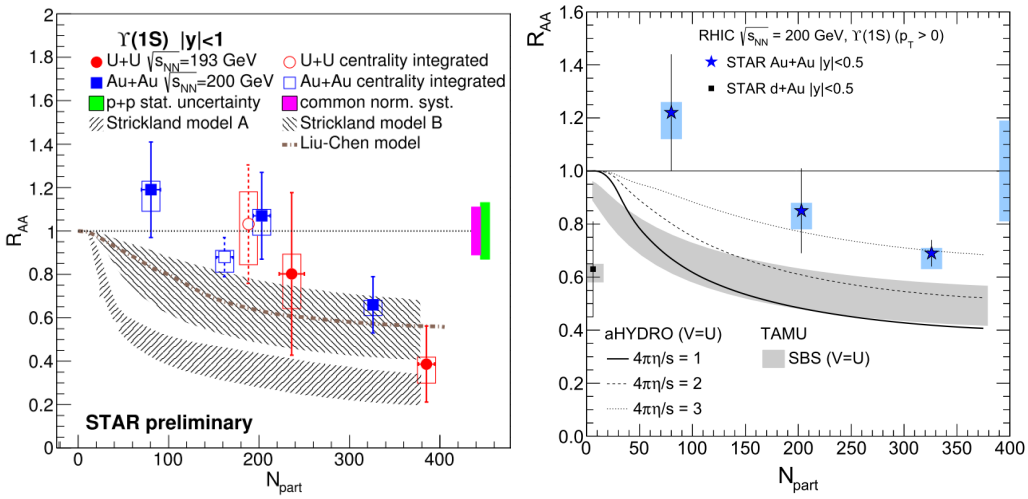

Figure II.14: R_{AA} data for the $\Upsilon(1S)$ as a function of centrality compared to various theoretical models [135].

II.3.3 LHC

With a collision energy ($\sqrt{s_{NN}} = 2.76$ TeV) more than ten times larger than at the RHIC (history repeats itself...), the Large Hadron Collider (LHC) and its ALICE and CMS detectors study heavy ion collisions (Pb-Pb). At this energy, theory predicts the production of a QGP with a maximum initial temperature of few times the critical temperature T_c, a longer life-time and a larger production of $Q\bar{Q}$ pairs with a better access to bottomonia than at RHIC.

As shown in figure II.15, the J/ψ states with low transverse momentum p_T are less suppressed at LHC than at RHIC for both mid and forward rapidities. This

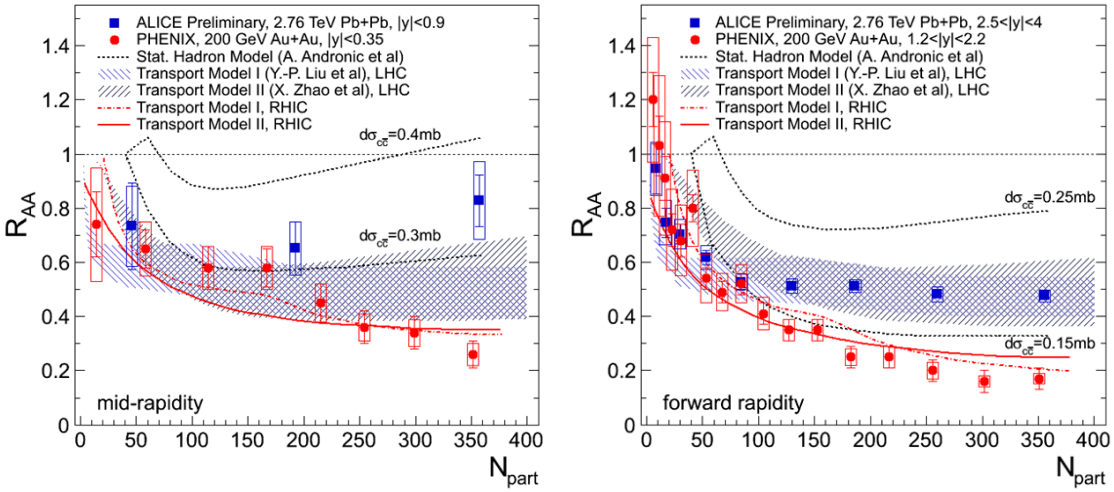

Figure II.15: R_{AA} data for the inclusive **low** p_T J/ψ as a function of centrality, compared with various model calculations [137]. *Left:* Comparison between RHIC and LHC results at mid rapidity and $p_T > 0$ (dominated by low p_T J/ψ). *Right:* Comparison between RHIC and LHC results at forward rapidity and for $p_T > 0$ and $0 < p_T < 8$ GeV/c respectively.

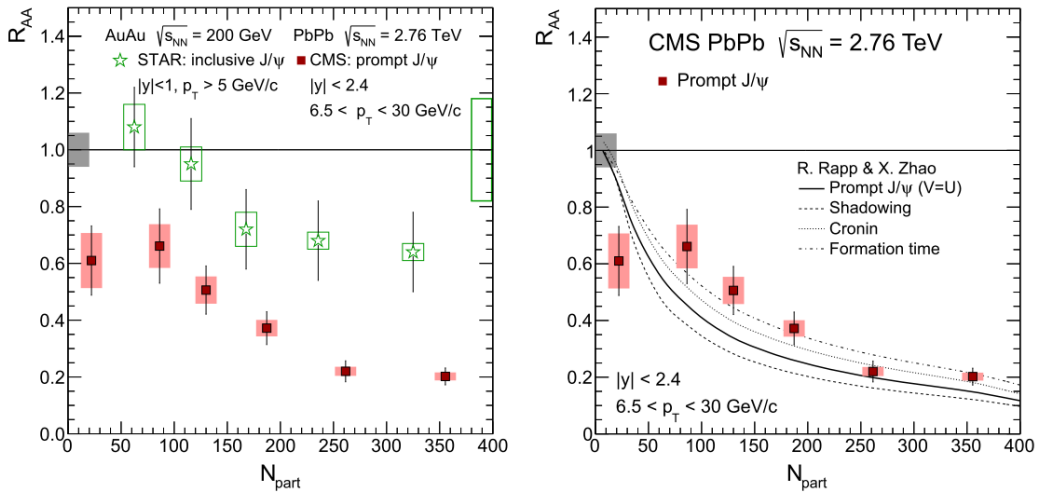

Figure II.16: *Left:* R_{AA} data for the **high** p_T J/ψ at mid rapidity as a function of centrality. Comparison between RHIC and LHC results for inclusive and prompt J/ψ respectively (no big differences between prompt and inclusive R_{AA}) [138]. *Right:* Comparison with TAMU transport model predictions.

is once again a "suppression of the suppression". Its most probable explanation is once again the statistical recombination, leaving open the question whether all $c\bar{c}$ pairs melt at the LHC. Transport models which include a significant recombination component indeed give a reasonable agreement with the forward rapidity data but overestimate the suppression at mid rapidity. At the opposite, the J/ψ states with high transverse momentum p_T are more suppressed at LHC than at RHIC and more suppressed than at low p_T (see left panel in figure II.16). One observes a smooth increase of the suppression towards a probable plateau at $R_{AA} \sim 0.2$ for most central

collisions. It does not correspond to any sequentially suppressed feed-downs contributions. This is nevertheless compatible with a more important color screening due to higher temperatures/densities and a negligible recombination contribution (which is less and less probable with increasing p_T). With these ingredients, the transport model shown in the right panel roughly describes the data. In contrast, the shadowing or energy loss calculations[48] alone have led to a clear disagreement with the data [19].

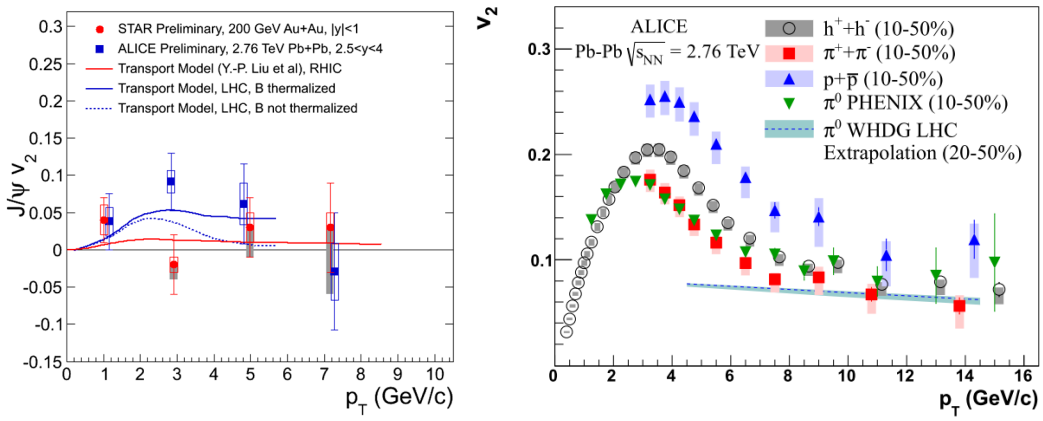

Figure II.17: *Left:* Comparison of the elliptic flow v_2 of the J/ψ at LHC for forward rapidity and at RHIC for mid rapidity [139]. One can note that an equivalent elliptic flow is also observed by CMS at mid-rapidity [140]. *Right:* To compare, the elliptic flow v_2 of the charged hadrons at LHC for mid rapidity [141].

The J/ψ elliptic flow v_2 at forward rapidity is shown in figure II.17 (left panel) and compared to transport models, and charged hadrons v_2 at mid rapidity (right panel). Whereas the elliptic flow was consistent with zero at RHIC, a positive v_2 is obtained at LHC for intermediate $2 < p_T < 6$ GeV/c. This elliptic flow might result from a partial thermalisation of both recombined ($p_T \lesssim 2.5$ GeV/c) and primordial ($p_T \gtrsim 2.5$ GeV/c) J/ψ contributions. It favours scenarios with an important fraction of J/ψ coming from recombination (as single heavy quarks interact much more that "neutral" bound states) or with a partial thermalisation of the $c\bar{c}$ pairs in the medium. Both transport models - which include a significant fraction of recombination - shown here give a reasonable agreement with the data.

The comparison between the ratio of ψ' to J/ψ in Pb-Pb collisions and the one in p-p collisions is shown in figure II.18 (left panel). An important difference appears between two kinematic regions. As one could expect from sequential suppression (ψ' more suppressed than J/ψ), at midrapidity and high p_T the ratio of ψ' to J/ψ in Pb-Pb collisions is smaller than in p-p collisions. However, at forward rapidity and intermediate/high p_T, the ψ' to J/ψ ratio is surprisingly larger in Pb-Pb than in pp, i.e the ψ' is less suppressed than J/ψ, which is in total contradiction with the

[48]Note that as the $R_{AA}(p_T)$ distributions of the heavy flavours [137, 138] are really different from light flavours (discussed in the introduction I.2.3.2), it shows that the energy loss processes act very differently on quarkonia if they undergo any.

sequential suppression and other effects too ! Neither the statistical hadronisation nor the transport models are able to explain such a behaviour (right panel) [142]. This effect is not observed in pA collisions [91] and should therefore not originate from shadowing or energy loss. For now, the only model which seems to be able to give such an inversion is the comover model (with dissociation and recombination) [143].

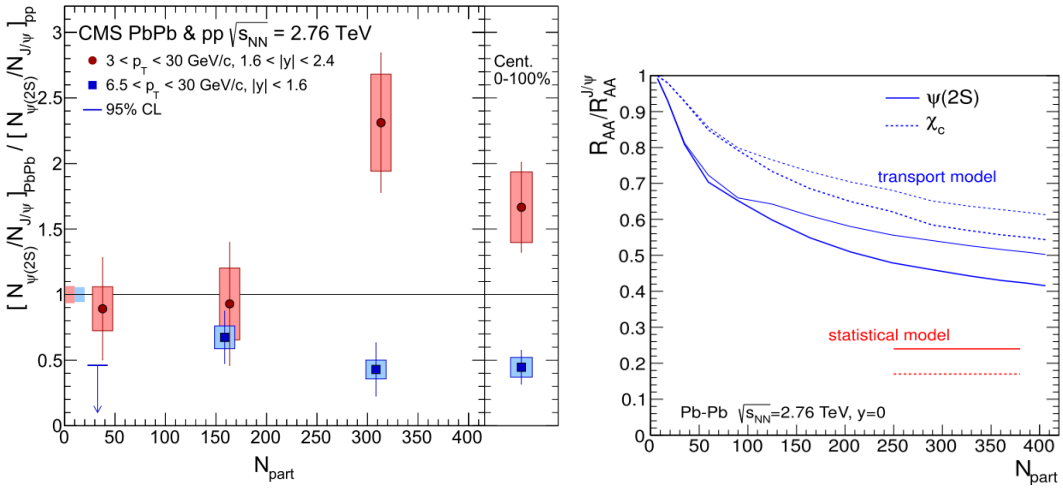

Figure II.18: *Left:* Double ratio of measured prompt yields $(N_{\psi'}/N_{J/\psi})_{PbPb} / (N_{\psi'}/N_{J/\psi})_{pp}$ as a function of centrality, for the mid rapidity (blue squares) and forward rapidity (red circles) [144]. *Right:* Transport and statistical hadronisation models corresponding predictions.[142]

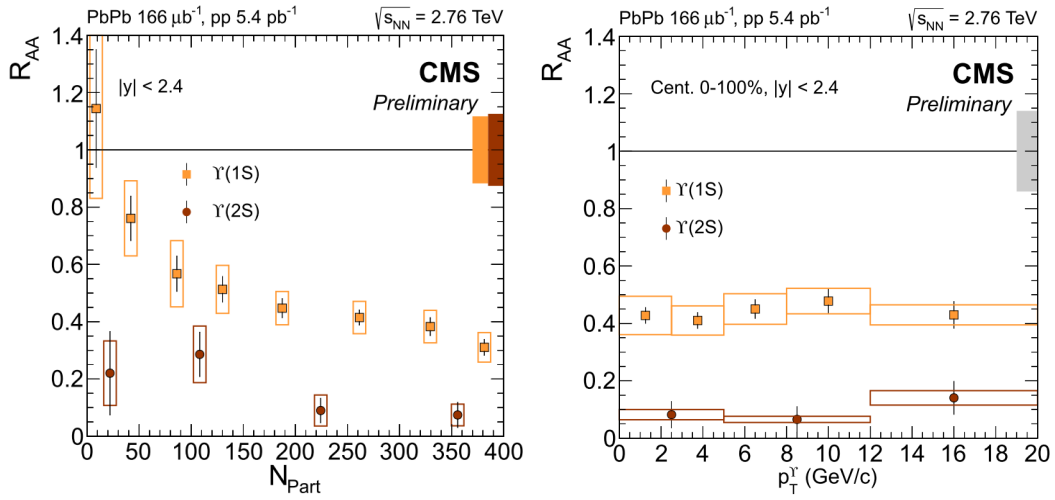

Figure II.19: R_{AA} data for the $\Upsilon(1S)$ and $\Upsilon(2S)$ as a function of centrality (*left*) and transverse momentum (*right*) [145].

As shown in figure II.19, the bottomonia are more suppressed at LHC than at RHIC. In the vein of the sequential suppression, the $\Upsilon(2S)$ state is more suppressed

than $\Upsilon(1S)$ and gets almost entirely melted starting from a certain centrality. Moreover, both states seem to reach a plateau from a certain centrality. Finally, the $\Upsilon(3S)$ state is so strongly suppressed that only an upper limit of $R_{AA}(\Upsilon(3S)) < 0.10$ with a 95% confidence level could be estimated [145]. As shown in figure II.20, the transport models (with a small recombination contribution) and the anisotropic hydrodynamics[49] can describe pretty well $\Upsilon(1S)$ data, but fail for $\Upsilon(2S)$. Moreover, the statistical hadronisation model clearly underestimates the suppression (figure II.21). The R_{AA} dependence on transverse momentum (and rapidity) is interestingly flat for both states (see the right panel of figure II.19). It shows that their suppression process is not quite sensitive to their velocity and direction of propagation.

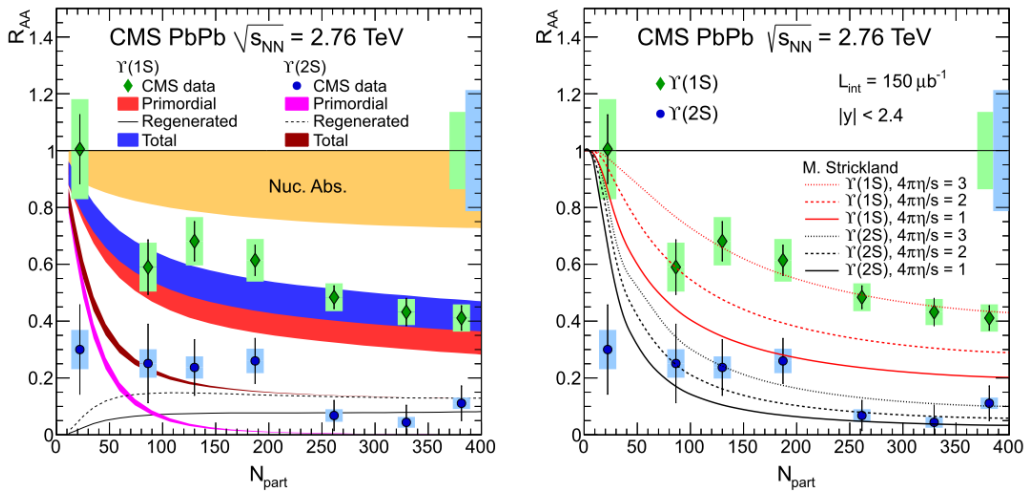

Figure II.20: R_{AA} data for the $\Upsilon(1S)$ and $\Upsilon(2S)$ as a function of the centrality compared with TAMU transport model (*left*) and aHYDRO model calculations (see section IV.2.1.1) (*right*) [19].

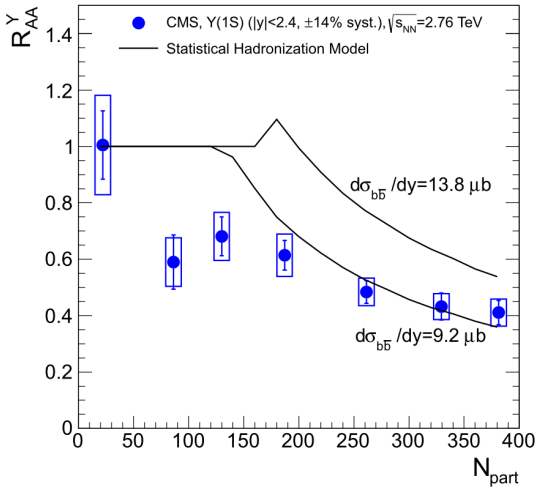

Figure II.21: R_{AA} data for the $\Upsilon(1S)$ as a function of the centrality compared with statistical hadronisation model [146].

[49] See section IV.2.1.1

II.4 Problematics, motivations and perspectives

We now wish to discuss the motivations for the present work. To this end, we first briefly sum up the irregular description of the data given by the common models and point out their questionable assumptions. As an answer, we then introduce the basic ideas of our model and its perspectives.

II.4.1 The main models: an irregular description of the data and criticisms

We have seen in section II.3 that the different models suffer from an irregular description of the data...

1) The sequential suppression is a priori not observed for the charmonia R_{AA} - exception made of some light "plateaus" - but may be masked by other effects such as recombination and cold nuclear matter effects. Furthermore, the observation of a ratio "$R_{AA}(\psi'/J/\psi)$" > 1 at forward rapidity is in total contradiction with its predictions. Nevertheless, a sequential like suppression is observed for the bottomonia, which are much less sensitive to other effects. Indeed, at RHIC the suppression of the $\Upsilon(1S)$ begins from a relatively large centrality. At LHC, a plateau at $R_{AA} \sim 0.4$ indicates that only the direct $\Upsilon(1S)$ survive and that the excited states (and their feed-downs) are almost entirely melted (as confirmed by the $\Upsilon(2S)$ and $\Upsilon(3S)$ data which are small but not null).

2) The statistical hadronisation model leads to a rather good description of the J/ψ suppressions at SPS, RHIC and LHC, nevertheless tarnished by large uncertainty bands. At the opposite, there is a clear disagreement between its predictions and the observed R_{AA} for the $\psi'/J/\psi$ ratio and the $\Upsilon(1S)$ at LHC.

3) The transport models are irregular with the J/ψ suppression in the different kinematic ranges at RHIC and LHC. Moreover, they are unable to describe the $\psi'/J/\psi$ ratio at forward rapidity. Finally, the bottomonia suppression is correctly described at LHC but not at RHIC.

... which still leaves room for theoretical improvements. Furthermore, these models are based on some questionable assumptions:

1) The sequential suppression assumes that the fate of the quarkonia is entirely decided in a very early stationary QGP. If a state is melted ($T_{\rm QGP}^{\rm max} > T_d$), the corresponding Q and $\bar{Q}$ are assumed to move freely inside the QGP until the hadronisation where they hadronise into open mesons. In other words, the $Q\bar{Q}$ pair is assumed to decorrelate very quickly and entirely, which might only be valid in a weakly-coupled QGP. It is nevertheless far from being obvious in a strongly-coupled QGP - as it is nowadays pictured - where their propagation should be very different. At the opposite, if a state can form ($T_{\rm QGP}^{\rm max} < T_d$), the evolution of the corresponding quarkonia in the medium is assumed to be completely adiabatic: no dissociation nor transitions to other states are

possible. Though, the evaluation of the dissociation and formation rates from hard inelastic scatterings (see II.2.1.3) and the recent lQCD studies on the finite life time of bound states in a deconfined medium [121, 122, 123] tend to show the nonadiabaticity of the evolution. Furthermore, the J/ψ elliptic flow measurement suggests that both recombined ($p_T \lesssim 2.5$ GeV/c) and primordial ($p_T \gtrsim 2.5$ GeV/c) J/ψ partially thermalise [139]. In a "quasi-stationary" version of the sequential pattern, the formation time of the states in the vacuum are taken into account by comparing the dissociation temperature with the local temperature $T_{\rm QGP}(\tau_f, \vec{x})$. Unfortunately, as already discussed, both the determinations of the dissociation temperatures and of the formation times are not obvious (see figure II.4 and section II.1 respectively).

2) The statistical hadronisation model assumes on the contrary that the fate of the quarkonia is entirely decided at a quasi-stationary phase boundary. Indeed, the initial $Q\bar{Q}$ pairs are first assumed to be fully dissociated in the deconfined QGP, then to equilibrate with the medium and finally to hadronise into open hadrons or quarkonia according to their statistical weight and mass. However, the full decorrelation of the initial $Q\bar{Q}$ pairs is far from being obvious according to lQCD calculations (static potentials and spectral functions) and especially if the tight and small bound states (such as J/ψ and $\Upsilon(1S)$) form before the deconfinement. Furthermore, because of their large inertia and small cross sections with the medium [147], it is not obvious that the heavy flavours get thermally equilibrated (and without any delay) with the very dynamic QGP created in heavy ion collisions. Moreover, the elliptic flow measurement of the J/ψ rather shows a partial thermalisation only.

3) The transport models correspond to a more dynamical view of the dissociation/formation processes. As in the quasi-stationary sequential suppression model, a state is initially melted if $T_{\rm medium}(\tau_f) > T_d$ and the corresponding $Q\bar{Q}$ pairs fully decorrelated. But if a state is initially formed, the corresponding $Q\bar{Q}$ pairs can still be dissociated or recombined during the evolution through inelastic collisions. As discussed in sections II.2.1.3 and II.2.2.2, the dissociation/formation rates are evaluated from inelastic cross section calculations. Though the criticism of the transport models is beyond the scope of this thesis, at first sight it could seem curious i) to use a cross section approach in a situation where one cannot assume the in and out states to be defined asymptotically, though one of its basic postulate [5]; ii) to use a perturbative approximation [106] for a non perturbative problem; iii) that the multipartonic effect is neglected during a single $q/g + \Phi$ interaction ("stationary" assumption).

II.4.2 The need for a real-time quantum treatment

As shown in the previous section, there is not yet a perfect theoretical description of the observables and some of the basic assumptions of the models are unjustified (or might be even ruled out by the observations). Furthermore, some observables can not be easily explained by the models, e.g. the suppression of the J/ψ suppression or the $\psi'/J/\psi$ ratio at forward rapidity. **Instead of assuming any (quasi-)stationary**

media/quarkonia, formation times, full decorrelation, or adiabaticity... one can go back to the "reality": nothing is instantaneous, nothing is stationary, nothing is adiabatic and nothing is fully (de)coupled. Basically, one can say that the $Q\bar{Q}$ pairs are produced before the QGP formation, propagate and interact continuously inside a deconfined and dense medium which is expanding and cooling down very rapidly. Whether the $Q\bar{Q}$ pairs emerge as bound quarkonia or as open hadrons is only resolved at the end of the evolution, and **one should then beware of the quantum coherence/correlation during the whole evolution** (see figure II.22 for illustration) [148, 149, 150]. In simpler words, as Young and Shuryak write [2]: "In a nutshell, the main issue is how small is the separation in the $[Q\bar{Q}]$ pair when the QGP is over, not in which particular states they have been during this time". Unfortunately, the description of this real-time dynamics requires to solve a very complicated quantum field theory problem at finite temperature $T(t)$. Even if solving this full problem is out of reach of the present theoretical methods, one can identify some effective models preserving most of the quantum features. They should lead to a dynamical and continuous picture of the dissociation, recombination, energy exchanges and possible transitions to other bound states, instead of the usual "coupled or decoupled" binary picture.

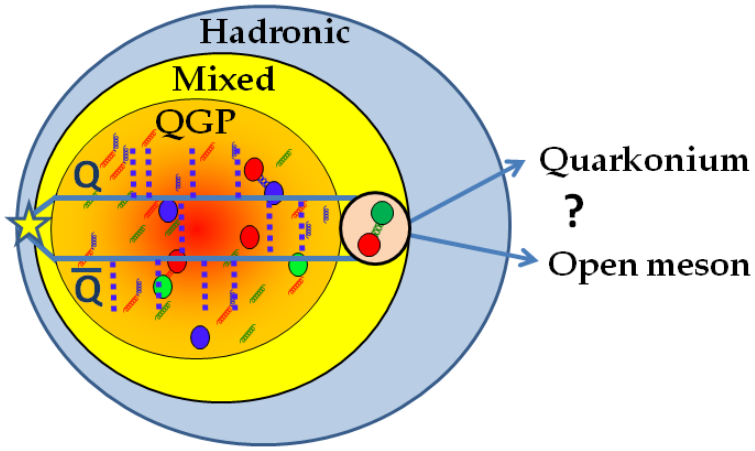

Figure II.22: Schematic drawing of the $Q\bar{Q}$ life and propagation inside the fireball.

To do so, **the basic idea of our approach is to study the $Q\bar{Q}$ pairs as open quantum systems continuously interacting with a thermal QGP background**. More explicitly, the continuous interaction between the medium and the internal degrees of freedom of a $Q\bar{Q}$ dipole is obtained through 1) a $Q\bar{Q}$ mutual interaction screened by color charges in its vicinity and 2) a fluctuation/dissipation mechanism reflecting the continuous hard elastic collisions $Q\bar{Q} + p \leftrightarrow (Q\bar{Q})^* + p$. Both ingredients possibly lead to transitions between bound quantum states or between bound and free states. The basic ideas of our approach are illustrated in the figure II.23.

The study has been proposed with the implicit hopes and perspectives to:

– Study the relative motion of the correlated heavy quark and antiquark in a

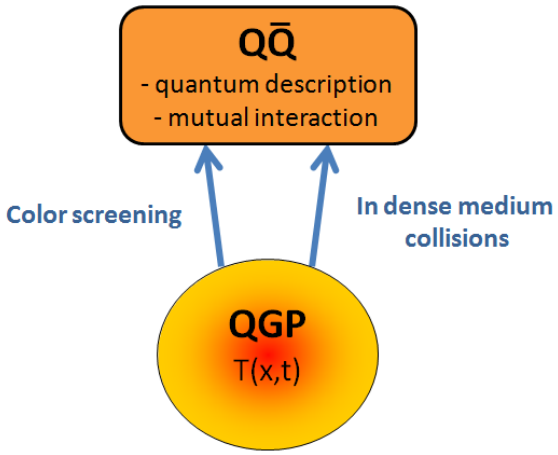

Figure II.23: Illustration of our approach through its basic ingredients and interactions between the $Q\bar{Q}$ and QGP systems.

cooling deconfined medium and deduce the real-time quarkonia content of the $Q\bar{Q}$ pair (in the quantum mechanical sense).

– Observe if the "suppression of the suppression" could be explained by a thermal effect. Indeed, the diffusive evolution of the relative distance between the Q and $\bar{Q}$ in a thermal medium is proportional to $\sqrt{D_S t}$ for Brownian particles [151] (where D_S is the spatial diffusion coefficient). It is expected to be slower than its ballistic evolution in the vacuum, which is $\propto t$ for the free spreading of a gaussian wavepacket [152]. Furthermore, because D_S is expected to be inversely proportional to the QGP temperature (see sections IV.1.1 and V.2.1 for more details), the diffusive evolution should be slower as the medium temperature increases with the collision energy. A smaller inter-quark distance could then lead to an enhancement of the J/ψ population.

– Make a phenomenological use of the drag and diffusion coefficients calculated for single heavy quarks - obtained from either microscopic calculations or lQCD results (see section V.2.1) - while insuring the quantum nature of the $Q\bar{Q}$ system.

– Find a connection between the main ideas of the sequential suppression (i.e. the decorrelation from a T-dependent color screening) and the statistical hadronisation (i.e. the thermalisation of the states) without making any of their unjustified assumptions. See the schematic view of the quarkonia suppression/enhancement models in hot media in figure II.24.

– Measure the medium temperatures above the critical temperature T_c, and not only the initial temperature (sequential suppression) or T_c (statistical hadronisation). The quarkonia could then be seen as a quantum continuous thermometer.

– Find a formalism which is effective enough to be introduced in a transport code in order to make phenomenological predictions.

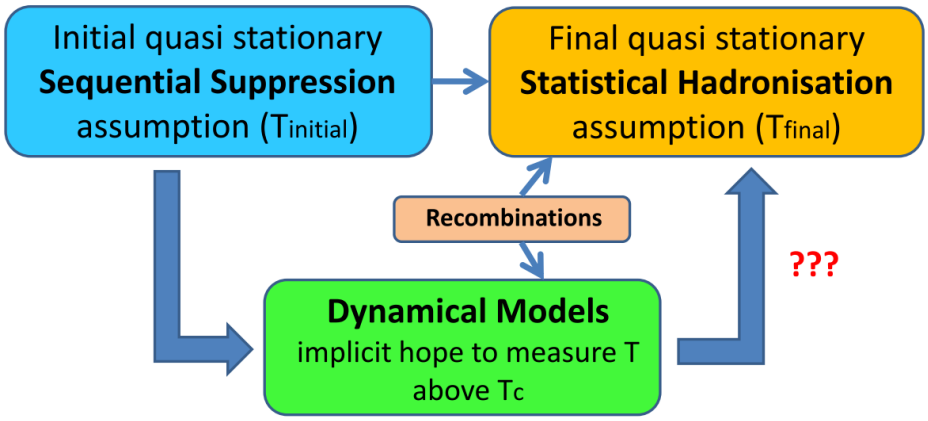

Figure II.24: Schematic view of quarkonia suppression/enhancement models in hot media. The dynamical models (among which the transport models) attempt to connect the ideas of the sequential suppression with the ones of the statistical hadronisation model. A thin arrow from a first model to another model means that some of the ideas of the first model are used by the other model.

Main ideas and transition

We have therefore shown the limits of the common models in both their data description and assumptions. We have also discussed the puzzling evolution of the experimental observations from SPS to LHC energies and highlighted some tricky issues such as the saturation of quarkonia suppression, the elliptic flow and the $\psi'/J/\psi$ ratio. As an answer to some of these issues, we have proposed to deal with the quarkonia as open quantum systems in continuous interaction with the deconfined medium. Before focusing on the possible fluctuation/dissipation mechanisms (in part IV), we study in the next part the "ballistic" dynamics of a $Q\bar{Q}$ pair with a color screened self-interaction only.

Part III

Mean field dynamics

In this part, we focus on the quantum dynamics of the internal degrees of freedom (d.o.f.) of a non-relativistic $Q\bar{Q}$ pair, self-interacting via the strong interaction and color screened by color charges in its vicinity. The pair is assumed to be immersed in an infinite homogeneous QGP at thermal equilibrium and the motion of its center-of-mass is not considered. By exploring the "ballistic" evolution of the relative $Q\bar{Q}$ motion without the effects of the direct collisions with the medium, we aim to evaluate the evolution of their relative distance and their transitions to free and other bound states. It is a first attempt to measure in what extent the assumptions of fast/full decorrelation or adiabatic evolution made by the sequential suppression (and statistical hadronisation model for the former) are justified. To this end, we therefore study the actual $Q\bar{Q}$ dynamics and do not just assume one. Our approach within this part is illustrated in figure III.1.

For a start, we progressively introduce in section III.1 the basic concepts and ingredients of the mean field approach, such as the screened potentials, temperature evolutions, possible initial states, equation of evolution and observables. To distinguish among the different components of the model, in section III.2 we focus on the basic evolutions of the $Q\bar{Q}$ pair obtained with the free and vacuum potentials corresponding respectively to the limit $T \to \infty$ and $T = 0$. Including the color screening effects, we then study the evolutions obtained with the weak (section III.3) and strong potentials (section III.4) at constant temperatures and with RHIC and LHC temperature scenarios. Finally, in section III.5 we discuss these evolutions regarding to other models, sum up the values obtained at the chemical freeze out and compare them to some extent to the data.

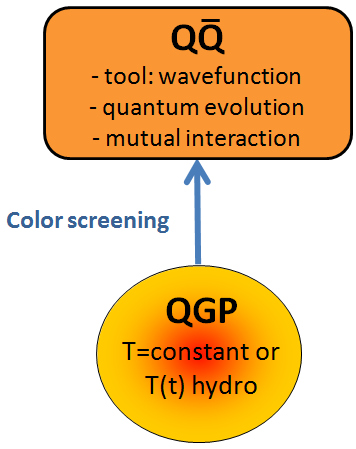

Figure III.1: Illustration of our approach within this part through its basic ingredients and interactions between the $Q\bar{Q}$ and QGP systems.

III.1 The ingredients of the mean field model

All along this part, the quantum state of the considered $Q\bar{Q}$ pair is described by a wavefunction $\psi(\vec{r}, t)$, where $\vec{r}$ is the relative three-vector between the two particles. The evolution of the $Q\bar{Q}$ wavefunction is given by the time dependent non-relativistic Schrödinger equation. We focus only on the S states allowing to reduce the full 3D analysis to a 1D radial situation without any approximation. Indeed, the evolution given by the Schrödinger equation in spherical coordinates does not lead to any transitions between states of different orbital momenta [153].

III.1.1 Color potentials and eigenstates

III.1.1.1 Justification of the potential approach

Because of their color charges, the heavy quark and antiquark of a pair interact with each other via the strong interaction (the so called self/mutual interaction). Unlike the light quarks, a simplified description of this interaction through a binding potential is possible in place of the unsolvable non-perturbative quantum field theory framework [154, 155, 156]. Indeed, because the heavy quark masses are much larger than the typical QCD scale $\Lambda_{\rm QCD} \sim 200$ MeV 1) their renormalised and current masses are almost equivalent implying that their running masses can be replaced by fixed masses, and 2) the binding energies are much smaller than their rest masses implying that relativistic corrections and sea quarks can be neglected.

III.1.1.2 The vacuum potential

In the vacuum, the usual basic binding potential is the so-called Cornell potential [154] which writes as a sum of two terms:

$$V(r) = \sigma\, r - \frac{\alpha}{r} \tag{III.20}$$

where the first term $\sigma\, r$ describes the long distance non-perturbative confinement whereas the second term $-\frac{\alpha}{r}$ a short distance, perturbative, Coulombian like interaction. As in [156], one can use the string tension coefficient $\sigma = (1.65 - \pi/12)/r_0^2$ (where $r_0 = 0.5$ fm) and the "Coulombian" coefficient $\alpha = \pi/12$ that were determined by [157] through a fit to lattice results. Additionally, one can include a third term $-0.8\sigma/(m_Q^2 r)$ which originates from independent relativistic effects of the quark spins [158]. Finally, to obtain a more complete description of the binding, one should also take care of the quarkonium instabilities through strong decays [159], also called string breaking. Indeed, as discussed in I.1.2, the gluonic flux tube can break into a quark/antiquark pair as the heavy quark/antiquark move away from each other. This fragmentation occurs spontaneously for charmonium states whose energies are above ~ 3.7 GeV (the $c\bar{c}$ threshold) and for bottomonium states above ~ 10.35 GeV (the $b\bar{b}$ threshold). A possible way to translate this instability in a

potential model, is to saturate the potential to a certain value V_{sat}, in order to "free" the $Q\bar{Q}$ pairs with higher energies. The saturation value should correspond to the energy difference between the maximum quarkonium energies and the bare mass of two quarks: $V_{\text{sat}} = 3.7 - 2 * 1.25 = 10.35 - 2 * 4.575 = 1.2$ GeV for charmonia and bottomonia. The resulting binding potential for a $c\bar{c}$ pair is shown in figure III.2. Note that this potential is close to what is obtained from lQCD calculations at the limit $T \to 0$ (see sections III.1.1.5 and III.1.1.5).

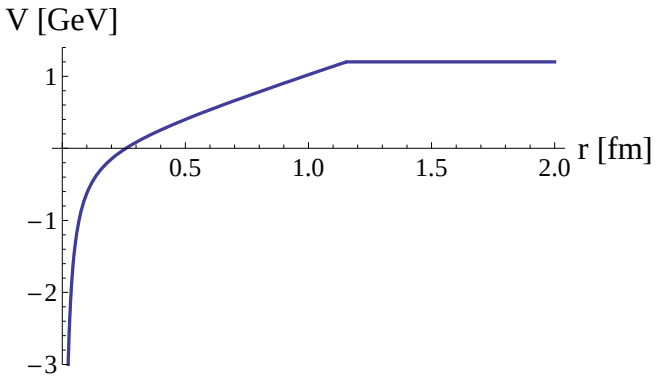

Figure III.2: The binding potential of a $c\bar{c}$ pair in the vacuum from strong interaction. It corresponds to the Cornell potential given by III.20 plus a term for the relativistic spin effects and a possibility of string breaking.

III.1.1.3 Basics of color screened potentials

In this part, the only interaction between the deconfined medium and the $Q\bar{Q}$ pair is the "Debye-like" color screening of the $Q\bar{Q}$ mutual interaction due to the presence of color charges in its vicinity. Within the potential approach, the mutual interaction and the Debye screening of the $Q\bar{Q}$ pair can be described through a modified potential. Historically, the basic ideas on screened potentials came from the study of electrically ionized fluids by Debye and Hückel [160]. They found that the usual Coulomb potential $\propto -1/r$ between two electrical charges was modified by the screening through an exponential damping term $\exp(-r/\lambda_D)$, where λ_D is the Debye-Hückel length. Hence, the interaction between two charges gets weaker at shorter distances. For color charges, the behaviour of the color screening is pretty much equivalent and leads to a temperature dependent lowering of the potential asymptotic value $V(r \to \infty)$. In this way, the decrease of the $Q\bar{Q}$ binding energy facilitates its access to free quantum states.

The potential of a $Q\bar{Q}$ pair in a deconfined medium at temperature T is usually derived from lQCD calculations. Actually, there are different possible potentials corresponding to different thermodynamic situations. From the lattice, one can directly evaluate the free energy $F(r, T)$, which corresponds to a static situation where the $Q\bar{Q}$ pair has an infinite time to exchange a maximum of reversible and irreversible (heat) energy with the medium. In parallel, one can also evaluate the entropy term

TS which corresponds to the maximum amount of irreversible energy that can be dissipated during this process. Then, if one considers an "adiabatically slow" evolution of the $Q\bar{Q}$ pair corresponding to a maximum heat exchange, its screened potential should be taken as the free energy $F(r,T)$. At the opposite "fast" limit, the internal energy $U(r,T)$ is defined by the process where no irreversible energy is exchanged with the environment. In practice, the internal energy is evaluated indirectly by "giving back" to the free energy F the maximum dissipated energy TS, i.e. with the thermodynamic relation $U(r,T) = F(r,T) + TS(r,T)$. To sum up, the free energy corresponds to a maximum heat exchange between the $Q\bar{Q}$ pair and the medium whereas the internal energy to no heat exchange.

To choose whether a $Q\bar{Q}$ pair should exchange a maximum, an intermediate or a null amount of irreversible energy with the medium is not obvious. Within our model, we will consider two kinds of potential: an intermediate heat exchange situation $F < V < U$ and the internal energy U. Below, we will see that they lead respectively to a weak and strong binding of the $Q\bar{Q}$ pair and their corresponding potentials are subsequently called weak and strong. In principle, the use of the weak potential $F < V < U$ might be more consistent in this part, where we do not consider any other energy exchange mechanism. At the opposite, the use of the strong potential U might be more consistent in the parts V and VII in order to avoid redundancies between energy exchange mechanisms. Below, we briefly overview the weak and strong potentials and corresponding state spectra that we use in practice, but note that an extensive discussion of their features can be found in [109].

III.1.1.4 Color singlet and color octet

The screened interaction also depends on the color state of the $Q\bar{Q}$ pair. As discussed in I.1.4.2, before potentially binding into a color neutral quarkonium state, a $Q\bar{Q}$ pair is initially produced either as a color singlet or octet state with a statistical ratio of the order of 1:8. It is thus most probable that in the deconfined medium the $Q\bar{Q}$ pair exists alternatively as a color singlet state or a color octet state in the course of its color exchanges with the medium. As shown in figure III.3, the binding potentials obtained from lQCD for the color singlet and octet channels are very different: while the singlet potential "V_1" is quite attractive over the typical quarkonia size ($\lesssim 1$ fm), the octet potential "V_8" is almost independent of $|\vec{r}|$ indicating a weak attraction/repulsion. Note also that they become equal beyond the typical quarkonia size. If one assumes the color states to be at thermal equilibrium, the probability to be in a color octet state is given by $\propto \exp(-(V_8 - V_1)/T)$. Young and Shuryak [2] then pointed out that as the ratio $(V_8 - V_1)/T$ is quite large (~ 10) over the typical quarkonia size, the color octet channel is suppressed by an order of magnitude and its contribution to the full dynamics is consequently almost negligible. All along the present work, we will therefore not consider the color octet contribution and assume the $Q\bar{Q}$ to be in a color singlet state.

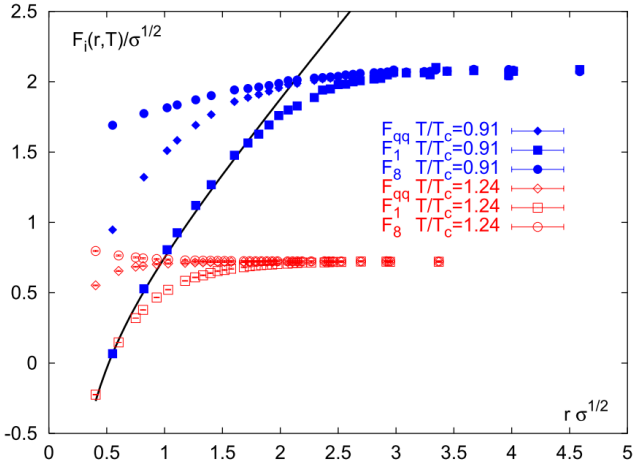

Figure III.3: Comparison between the color singlet $V_1 = F_1$ and color octet $V_8 = F_8$ free energies as a function of the relative distance at two different temperatures [155].

III.1.1.5 At finite T: the weak potential $F < V(T) < U$

The "weak" potential $F < V(T) < U$ considered here has been evaluated by Mocsy and Petreczky [156] from lQCD calculations, as an intermediate potential between the color singlet free energy $F(r,T)$ and the color singlet internal energy $U(r,T)$. As explained above, it corresponds to a screened situation where the pair exchanges some heat with the medium. In practice, we use a version of the weak potential which has been reparametrised by Gossiaux as follows. It is divided into three areas: the short distance potential V_0 that coincides with the zero temperature potential (III.20), the intermediate distance potential $V_{\rm int}$ taken with the parametrisation proposed in [161], and the exponentially damped long distance potential V_1. The weak potential then writes

$$V_{\rm weak}(r,T) = \begin{cases} V_0(r) & \text{for} \quad r < \frac{0.43\,\text{fm}}{T_{\rm red}} = r_0 \\ V_{\rm int}(r,T) & \text{for} \quad r_0 < r < r_1 \\ V_1(r,T) & \text{for} \quad r > \frac{1.25\,\text{fm}}{T_{\rm red}} = r_1 \end{cases} \qquad \text{with} \qquad \text{(III.21)}$$

$$V_0(r) = -\frac{\alpha}{r} + \sigma r - 0.8\frac{\sigma}{m_Q^2 r}, \qquad \text{(III.22)}$$

$$V_{\rm int}(r,T) = \frac{\text{V0} + g_1(r-r_0) + g_2(r-r_0)^2}{1 + g_3(r-r_0) + g_4(r-r_0)^2}\,, \text{ where V0} = V_0(r_0),$$

$$V_1(r,T) = V_\infty - \frac{4}{3}\frac{\alpha_1}{r}e^{-\sqrt{4\pi\ \tilde{\alpha}_1}Tr}, \text{ where } V_\infty = \sigma r_0.$$

The running coupling parameters $\alpha_1(T_{\rm red})$ and $\tilde{\alpha}_1(T_{\rm red})$ are determined in [162] from lattice results. The T-dependent parameters g_1, g_2, g_3 and g_4 permit to achieve a smooth connection between V_0 and V_1 for each $T_{\rm red}$. The reduced temperature is defined by $T_{\rm red} \equiv T/T_c$ where the QGP critical temperature is taken to $T_c = 0.165$

Gev. The corresponding potential is shown in figure III.4 for different values of the temperature.

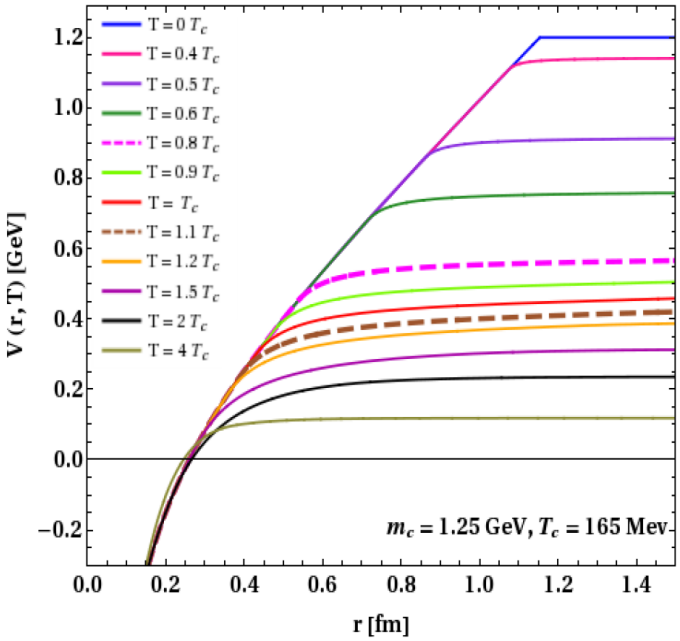

Figure III.4: The weak potential at different finite temperatures in the charmonium case [109].

III.1.1.6 At finite T: the strong potential $U(T)$

As an alternative at finite temperatures, we will also consider the "strong" potential $U(T)$, i.e. the color singlet internal energy, which has been evaluated from the lattice by Kaczmarek and Zantow in [104]. Once again, we use in practice a version coming from a reparametrisation by Gossiaux:

$$V_{\text{strong}} \equiv U(r,T) = \Big(-\frac{\alpha}{r} + \sigma r - \frac{0.8\sigma}{m_Q^2 r} \Big) \times e^{-(\mu r)^2} + V_0 \times \Big(1 - e^{-(\mu r)^2} \Big), \quad \text{(III.23)}$$

where the parameters σ, μ and V_0 have been determined to fit the results of [104]. The corresponding potential is shown in figure III.5 for different values of the temperature. As one can already notice from figures III.4 and III.5, the weak and strong potentials exhibit a very different behaviour near the critical temperature T_c. As shown in figure III.6, whereas the asymptotic value of the weak potential is smoothly decreasing with T (one has $V_{\text{weak}}(r \to \infty, T) \propto 1/T$), the asymptotic value of the strong potential exhibits an important peak around T_c and is generally larger when $T > T_c$. Therefore, it requires more energy to dissociate a $Q\bar{Q}$ pair in the strong potential than in the weak. Moreover, the charmonium states melt at larger temperatures (see table III.5).

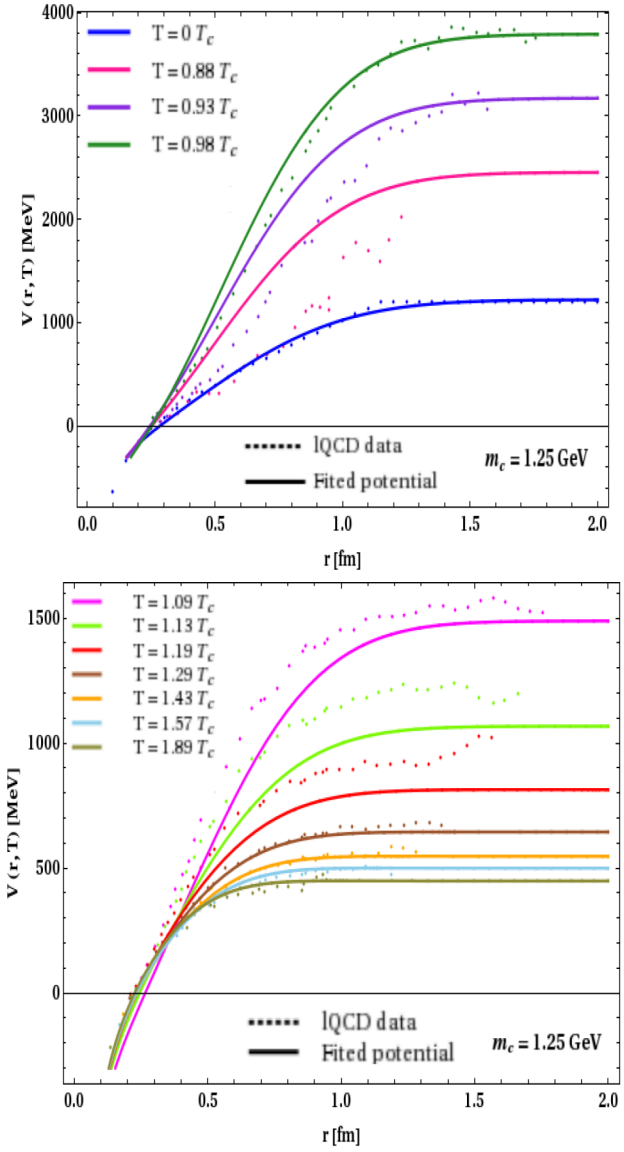

Figure III.5: The strong potential at different finite temperatures below (top panel) and above (bottom panel) T_c in the charmonium case [109].

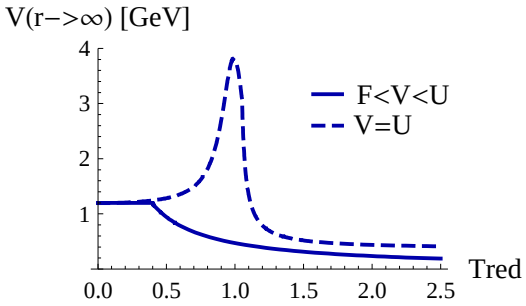

Figure III.6: A comparison of the asymptotic values of the weak and strong potentials $V(r \to \infty)$ as a function of temperature.

III.1.1.7 Eigenstates and dissociation temperatures

To obtain the state $\{\psi_{n,l}\}_{l=0\ldots}^{n=0\ldots}$ and energy $\{E_{n,l}\}_{l=0\ldots}^{n=0\ldots}$ spectra of these potentials, one needs to solve the time independent Schrödinger equation:

$$H\psi_{n,l} = E_{n,l}\,\psi_{n,l}, \tag{III.24}$$

where the Hamiltonian of a two particle system in the $Q\bar{Q}$ pair center of mass frame is given by [153]

$$H = 2m_Q - \frac{(\hbar c)^2}{m_Q}\nabla^2 + V(r, T_{\rm red}). \tag{III.25}$$

In spherical coordinates, the Schrödinger equation (III.24) and the decomposition of the wavefunction in radial $R(r)$ and angular $Y(\theta,\phi)$ components lead to an independent equation for the radial part,

$$\left\{\frac{\partial^2}{\partial r^2} - \frac{l(l+1)}{r^2} + \frac{m_Q}{(\hbar c)^2}\left(E_{n,l} - V(r) - 2m_Q\right)\right\} u_{n,l}(r) = 0, \tag{III.26}$$

where one has introduced the reduced radial wavefunction $u_{n,l}(r) \equiv r\,R_{n,l}(r)$ to simplify the calculation of the radial part of the nabla operator in spherical coordinates:

$$\nabla^2 R_{n,l}(r,t) = \frac{1}{r}\frac{\partial^2 u_{n,l}(r,t)}{\partial r^2}. \tag{III.27}$$

This differential equation (III.26) can be solved numerically from an iterative method described in [161]. In figure III.7, one can see for instance the vacuum charmonium radial wavefunctions obtained with the binding potential at the zero temperature limit (or equivalently with the finite temperature potentials at $T_{\rm red} \leq 0.4$). The corresponding energy spectra of the charmonia and bottomonia (table III.4) are close to the experimental values.

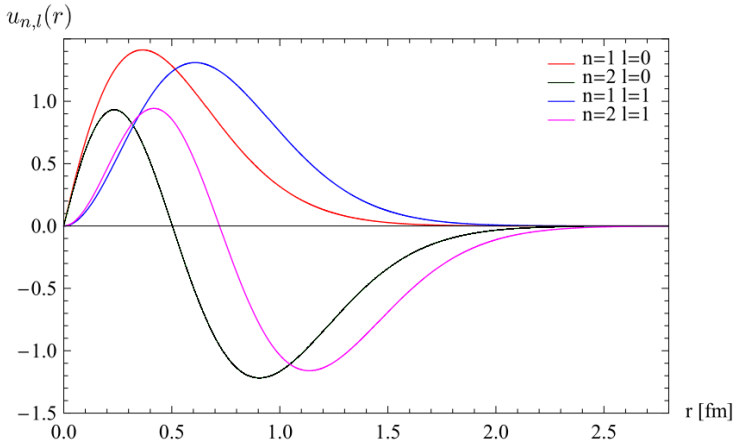

Figure III.7: The reduced radial wavefunctions for the charmonia in the "vacuum" obtained with either the vacuum, weak or strong potential at $T_{\rm red} < 0.4$ [161].

	State	$\langle r^2\rangle^{1/2}$ [fm]	$E_{n,l}$ [MeV]	Experimental energies [MeV]
Charmonia	J/ψ	0.46	3062	3097
	χ_c	0.74	3480	3511
	ψ'	0.96	3674	3686
Bottomonia	$\Upsilon(1S)$	0.27	9396	9460
	$\Upsilon(2S)$	0.54	9869	10023
	$\Upsilon(3S)$	0.78	10211	10355

Table III.4: Root mean square radius $\langle r^2\rangle^{1/2}$ [fm] and energy spectrum $E_{n,l}$ [MeV] for the quarkonium states obtained with the vacuum potential. The latter are compared with the experimental data for quarkonium energies (masses); see tables I.2 and I.3. The heavy quark masses are taken to $m_c = 1.25$ GeV and $m_b = 4.575$ GeV.

At larger temperatures, these states are modified by the potential variations: they tend to spread with increasing temperature (see for instance figure III.8) while their dissociation energies $E_{\rm diss}(T) = V(r \to \infty, T) - (E_{n,l}(T) - 2m_Q)$ get reduced (see figure III.9). Finally, the dissociation temperatures of the quarkonium states, given by $E_{\rm diss}(T_{\rm diss}) = 0$, are summed up in table III.5 and clearly show that the strong potential implies a stronger binding.

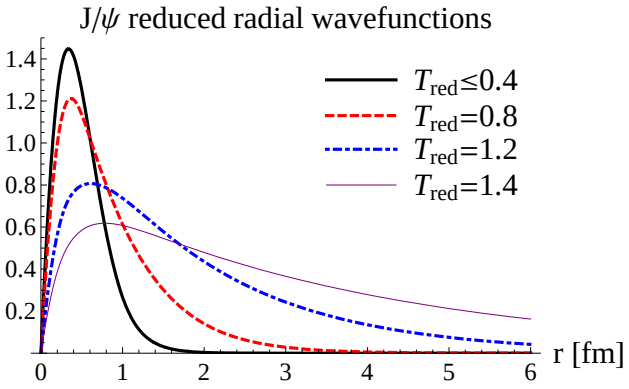

Figure III.8: The reduced radial wavefunctions of the J/ψ obtained with the weak potential $F < V < U$ at different temperatures. The thick curve corresponds to $T_{\rm red} \leq 0.4$, the thick dashed curve to $T_{red} = 0.8$, the thick dot-dashed curve to $T_{red} = 1.2$, the thin curve to $T_{red} = 1.4$ (at the limit of dissociation).

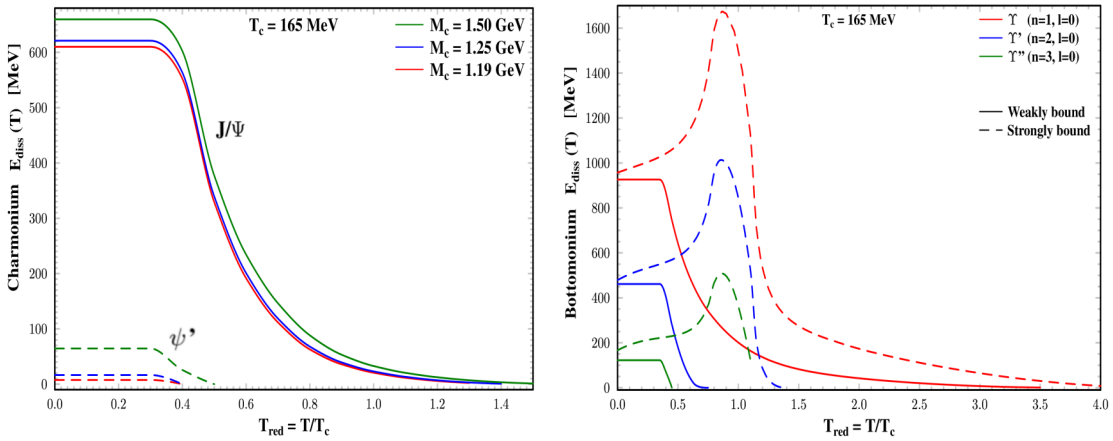

Figure III.9: The dissociation energies of the charmonium (*left panel*) and bottomonium (*right panel*) states as a function of the temperature obtained with the weak potential (*left panel*) or with the weak and strong potentials (*right panel*) [109].

— Dissociation temperatures —			
	State	$F < V < U$	$V = U$
Charmonia	J/ψ	1.45 T_c	1.85 T_c
	χ_c	0.48 T_c	1.2 T_c
	ψ'	0.4 T_c	1.1 T_c
Bottomonia	$\Upsilon(1S)$	3.55 T_c	4.45 T_c
	$\Upsilon(2S)$	0.8 T_c	1.45 T_c
	$\Upsilon(3S)$	0.5 T_c	1.2 T_c

Table III.5: Temperature of dissociations of the charmonium and bottomonium states obtained with the weak $F < V < U$ and strong $V = U$ potentials [109]. The heavy quark masses are taken to $m_c = 1.25$ GeV and $m_b = 4.575$ GeV.

III.1.2 Medium temperature evolutions

In section I.2.2, we have discussed the typical pattern of heavy-ion collisions. In a few words, 1) a pre-equilibrated anisotropic medium, with a quickly increasing temperature, promptly forms from the initial and successive parton scatterings and rapidly thermalises to a QGP after $t \lesssim 1$ fm/c, 2) the QGP phase cools down ($T > T_c$) and expands during $1 \lesssim t \lesssim 5 - 10$ fm/c, 3) once the crossover reached ($T \sim T_c$), the QGP turns into a mixed phase where the partons hadronise gradually 4) the resulting hadrons scatter inelastically until the chemical freeze out and the medium keeps expanding ($T < T_c$), 5) the final hadrons scatter elastically until the kinetic freeze out.

In this first approach, we choose the space-time temperature distribution derived by Kolb and Heinz [62]. It corresponds to a hydrodynamic evolution of an initial

thermalised state. The ideal hydrodynamic theory of the QGP tells us that the evolution of the transverse temperature distribution $T(\vec{r}_T, \tau)$ may be computed from the conservation of total entropy as the ideal fluid expands radially driven by transverse pressure gradients. On one hand, as the volume of QGP first grows linearly with time (Bjorken like expansion), the initial evolution of the entropy density s is inversely proportional to time: $s \propto \tau^{-\alpha}$, where $\alpha = 1$. As time increases, the volume of ideal fluid grows faster, such that the parameter α increases smoothly from 1 to 3 (see figure III.10). On another hand, as the QGP is described by an ideal gas of massless particles, its entropy density is also proportional to the cube of the temperature: $s \propto T^3$. Consequently, above the critical temperature, the temperature evolution is $T \propto \tau^{-\alpha/3}$.

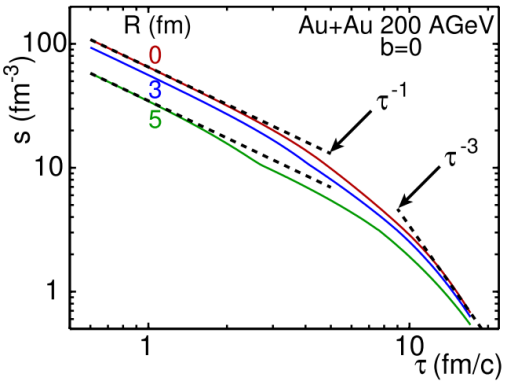

Figure III.10: Evolution of the entropy density as a function of time at three different distances from the center of the fireball (0, 3 and 5 fm) [62].

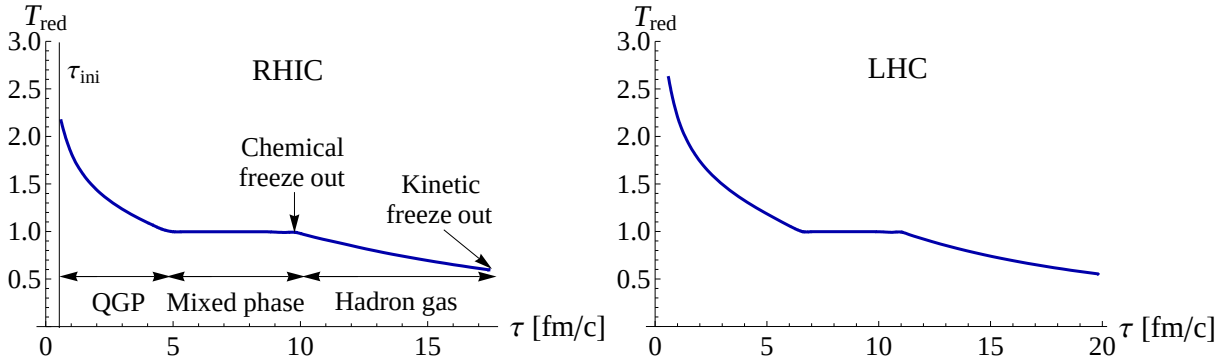

Figure III.11: Time evolution of the reduced temperature $T_{red}(t) = T/T_c$ at the center of the hydrodynamic fireball at RHIC $\sqrt{s_{NN}} = 200$ GeV (*left*) and LHC $\sqrt{s_{NN}} = 2.76$ TeV (*right*). When $T_{red} > 1$ the medium is a QGP phase, at $T_{red} = 1$ the medium is a mixed parton/hadron phase and when $T_{red} < 1$ the medium is a hadron gas.

As the pre-equilibrium phase is still poorly understood, the choice of the initial thermalised state is not obvious. Nevertheless, the initial transverse temperature distribution $T_{ini}(\vec{r}_T, \tau)$ can be derived from the density distributions of participating nuclei, given by the Glauber model [44]. The lapse of time required to reach a

thermalized initial state, from which the hydrodynamic evolution takes place, is given by $\tau_{ini} \sim \hbar c/T_{ini}$ ($\tau_{ini} \approx 0.6$ fm/c at RHIC and $\tau_{ini} \approx 0.5$ fm/c at LHC, in practice both taken to $\tau_{ini} = 0.6$ fm/c). The temperature distribution of the QGP phase is then given by:

$$T(\vec{r}_T, \tau) \approx T_{ini}(\vec{r}_T) \times \left(\frac{\tau_{ini}(\vec{r}_T)}{\tau} \right)^{\alpha/3}, \qquad \text{for } \tau \geq \tau_{ini}. \tag{III.28}$$

In this hydrodynamic model, the phase transition between the QGP and the final hadronic phase is a strong first order transition at $T = T_c = 165$ MeV where the medium is a mixed parton/hadron phase until the chemical freeze out. It contradicts the lattice QCD results (illustrated in the QCD phase diagram I.11) which rather show either a very weakly first order transition or a crossover. Nevertheless, the impact of this sharp transition on our dynamic should be small. After this transition, the temperature evolution corresponds to the hydrodynamics of a noninteracting hadron gas. Finally, the evolution ends at the kinetic freeze out ($T \sim 100$ MeV) when the hadron medium becomes so diluted that local thermal equilibrium can no longer be assumed.

Although in this hydrodynamic model the temperature distribution is spatially dependent, the $Q\bar{Q}$ pair will be assumed, for the purpose of simplification, to be immersed in a homogeneous medium whose *temperature evolution is taken at the center of the fireball and for a central collision.* The corresponding temperature evolutions at RHIC ($\sqrt{s_{NN}} = 200$ GeV) and LHC ($\sqrt{s_{NN}} = 2.76$ TeV) are shown in figure III.11.

III.1.3 Initial states

As discussed in section II.1, the $Q\bar{Q}$ pairs are produced at the very beginning of the collision and clearly before the formation of any deconfined medium. However, to know if their bound states form before the deconfined medium is not obvious and is subject to debate (especially for the charmonia). Within our model, we make few assumptions on the initial medium and $Q\bar{Q}$ states. First, we assume the evolution of the $Q\bar{Q}$ system to begin with the hydrodynamic QGP phase, i.e. we do not consider the strongly anisotropic pre-equilibrium phase. Consequently, *note that* the initial time $t = 0$ of the $Q\bar{Q}$ evolution corresponds to τ_{ini} of the medium evolution. Second, we assume the $Q\bar{Q}$ system at $t = 0$ to be either in a compact state (option 1) or already formed as a bound state (option 2).

If the pair is assumed to be in a compact state at the time of QGP formation (option 1), i.e. as it would be right after its production from the hard process, the initial radial wavefunction is chosen to be a general Gaussian wavepacket:

$$R(r, t = 0) = \sqrt{4\pi} \left(\frac{1}{\pi a^2} \right)^{3/4} e^{-\frac{r^2}{2a^2}} \tag{III.29}$$

where a is the initial Gaussian parameter taken to be equal to $a_c = 0.165$ fm and $a_b = 0.045$ fm for a $c\bar{c}$ and $b\bar{b}$ pair respectively. We normalise the radial wavefunction to unity, i.e. $\int |R(r)|^2 r^2 dr = 1$ as $Y(\theta, \phi) = 1//\sqrt{4\pi}$ for S states. The initial

Gaussian parameter can be estimated by applying the uncertainty principle to the intermediate quark of the Feynman diagrams for the $Q\bar{Q}$ production (leading order u or t channel, see figure I.9): $\Delta r \sim \hbar c/m_Q$. These values can also be fixed from experimental results in pp collisions: by analyzing open charmed p_T distributions or ratio of the direct ψ' to J/ψ cross-sections. The value $\sigma^D_{\psi'}/\sigma^D_{J/\psi} \sim 0.21$ in pp experiments [163, 164] is indeed close to the ratio of the corresponding initial populations $W_{\psi'}(t=0)/W_{J/\psi}(t=0) = 0.12/0.46 = 0.26$ in our model (see section III.2.1). Option 1 corresponds to the view that the $Q\bar{Q}$ pair interacts with the medium constituents as soon as it is created. The issue is then to determine in what extent the pairs form bound states when the plasma cools down and not whether the bound states "survive".

If the pair is assumed to be already formed as a bound state at the time of QGP formation (option 2), the initial radial wavefunction is chosen to be one of the vacuum radial eigenstates determined from the binding potential at $T = 0$.

III.1.4 Evolution with the Schrödinger equation and numerical resolution

As $m_Q \gg \Lambda_{\rm QCD}$, the $Q\bar{Q}$ system can be studied within the frame of non relativistic dynamics with the time dependent Schrödinger equation to describe their relative motion. The $Q\bar{Q}$ pair is described by the (reduced) radial wavefunction $R_{Q\bar{Q}}(r,t)$ ($u_{Q\bar{Q}}(r,t) \equiv rR_{Q\bar{Q}}(r,t)$). For numerical purposes, the time dependent Schrödinger equation for the radial part can easily be re-written as:

$$R_{Q\bar{Q}}(r, t+\Delta t) = e^{-i\frac{H}{\hbar}\Delta t}\, R_{Q\bar{Q}}(r,t), \tag{III.30}$$

and then expanded to the first order to the Crank-Nicolson scheme:

$$O_1^+\, R_{Q\bar{Q}}(r, t+\Delta t) = O_1^-\, R_{Q\bar{Q}}(r,t), \qquad \text{where} \quad O_1^\pm \equiv I \pm i\frac{H}{2\hbar}\Delta t \tag{III.31}$$

where I is the identity operator and Δt is the numerical time step. Because the $O_1^\pm$ operators are tridiagonal matrices in a discretised space approximation, equation III.31 can be numerically solved with the Thomas algorithm. The boundary conditions are given by:

$$\Big(\text{finite}\, R_{Q\bar{Q}}(0)\,,\; R_{Q\bar{Q}}(L) = 0\Big) \qquad \longleftrightarrow \qquad \Big(u_{Q\bar{Q}}(0) = 0\,,\; u_{Q\bar{Q}}(L) = 0\Big). \tag{III.32}$$

III.1.5 Weight and survivance observables

The real-time dynamics of the $Q\bar{Q}$ pair can be studied through different possible observables, such as the mean square position $\langle r^2\rangle = \langle\psi_{Q\bar{Q}}|\hat{r}^2|\psi_{Q\bar{Q}}\rangle$ and momentum $\langle p^2\rangle = \langle\psi_{Q\bar{Q}}|\hat{p}^2|\psi_{Q\bar{Q}}\rangle$, the probability density $\rho(r) = |\psi_{Q\bar{Q}}(r)|^2$, the quarkonium state occupation weights (see below), the mean energy of the pair $\langle E\rangle = \langle\psi_{Q\bar{Q}}|H|\psi_{Q\bar{Q}}\rangle$...

In the present work, we will mainly focus on the *quarkonia content* of a $Q\bar{Q}$ pair to study the quarkonia suppression. In our model, the population/*weight* W_i of a S

state i at t is defined as the projection of the $Q\bar{Q}$ wavefunction at t on the *vacuum* quarkonium states:

$$W_i(t) \equiv |\langle \psi_{n=i,l=0} | \psi_{Q\bar{Q}}(t) \rangle|^2 = \left(\int_0^\infty u_{Q\bar{Q}}(r,t) \times u^*_{i,0}(r, T_{\rm red} \leq 0.4)\, dr \right)^2 . \quad \text{(III.33)}$$

The weight $W_i(t)$ can be seen as the real-time population of a vacuum quarkonium state i at t, or in other words to the proportion of the $Q\bar{Q}$ pair that would instantaneously hadronise into a vacuum quarkonium state i if the QGP would extinguish at time t. At a temperature $T > 0.4$, there is then a mismatch between the Hamiltonian states (the instantaneous eigenstates at T) and the projection basis. Nevertheless, defined with the vacuum states, the quarkonia content allows us to study the real-time dynamics of a $Q\bar{Q}$ pair in a fixed basis all along its evolution (and especially of its bound component). As we assume an instantaneous transition between the $Q\bar{Q}$ components and the vacuum states at the chemical freeze-out (see below), it is only at this stage that the quarkonia content recovers all its physical meaning. We also define the *normed weight* or "*survivance*" S_i of a state i by

$$S_i \equiv \frac{W_i(t)}{W_i(t=0)}. \quad \text{(III.34)}$$

If the initial state of the $Q\bar{Q}$ pair is chosen to be a quarkonium state i (option 2), the survivance S_i (which is then equal to W_i) represents the probability for the state i to survive in the medium relatively to pp collision. In this case, one has $S_i(t) \leq 1$ and one really deals with the usual suppression. However, if one wishes to obtain the actual content on a state i, one would need to sum over its contributions from the different initial quarkonium states (weighted by their initial abundances). If the initial state is a Gaussian wavepacket (option 1), the initial $Q\bar{Q}$ pair can be seen as a weighted mix of quarkonium states and one can really probe its quarkonia content from $t = 0$ through the weights $W_i(t)$. Indeed, each $W_i(t)$ already includes the contributions obtained from the different initial bound states, i.e. the transitions between quarkonium states. The survivance $S_i(t)$, which is now possibly larger than unity, represents the gain or loss of this content inside the medium relatively to pp collision. Indeed, in pp collisions, the $Q\bar{Q}$ pair undergoes the vacuum potential. Then, the weights remain constant over the evolution and the survivances are equal to unity (as will be confirmed in section III.2.2). The survivance values in our model are therefore given relatively to pp collisions. Furthermore, as in the vacuum case the quarkonia content is fixed from $t = 0$, one can note that option 1 contradicts the common belief that some "formation times" are required for the quarkonia to emerge out of the $Q\bar{Q}$ pair.

III.1.6 Freeze out

To give the final predictions of our model, one needs to stop the evolution of the $Q\bar{Q}$ pair at some point. At first sight, the hydrodynamic evolution stops at the kinetic freeze out and the lQCD potentials have been evaluated down to $T = 0$. However, the particle abundance is usually thought to be fixed at the chemical freeze

out (see section I.2.3.1). In Kolb and Heinz's hydrodynamic model, the chemical freeze out occurs at the end of the first order transition, i.e. at time $t = 9.4$ fm/c at RHIC and $t = 10.4$ fm/c at LHC, at a temperature $T = T_c$. The latter reasonably agrees with numerous studies which evaluate the temperature of the chemical freeze out to be close to the critical temperature [165, 166]. As transitions between bound states are still possible in our model between the chemical and kinetic freeze-out, we therefore need to assume the inner dynamics of the $Q\bar{Q}$ pair to stop at the chemical freeze-out and assume an instantaneous transition to the vacuum states. The former assumption is also motivated by the future use of a drag parameter for dissipative evolutions, which has been calculated from partonic microscopic calculations and is therefore not valid if the quarkonia are in a hadron gas. The quarkonia content of the $Q\bar{Q}$ pair is thus fixed at the chemical freeze-out for our predictions (summed up in tables in section III.5) and we neglect the state formation times.

III.2 Evolutions with the free and vacuum potentials

III.2.1 Free case: $V(r) = 0$

III.2.1.1 Evolution of the $Q\bar{Q}$ pair

The free case can be seen in a first approximation to an evolution of the $Q\bar{Q}$ pair in a very weakly coupled QGP where the partons are fully deconfined (i.e. the $T \to \infty$ limit). The $Q\bar{Q}$ pair is then free of its binding potential, i.e. $V(r) = 0$, and one can consider the free expansion of its wavefunction. In this situation, the analytic solution of the Schrödinger equation can easily be derived by applying the time evolution operator to the initial Gaussian wavepacket in momentum space (V.60):

$$R_{Q\bar{Q}}(p_r, t) = R_{Q\bar{Q}}(p_r, 0)\, e^{-i\frac{H}{\hbar}\Delta t}, \qquad H = 2m_q + \frac{(\hbar c)^2}{m_q} p_r^2 \tag{III.35}$$

which inverse Fourier transform yields the time dependent Gaussian wavepacket:

$$R_{Q\bar{Q}}(r, t) = \sqrt{4\pi}\left(\frac{a^2}{\pi}\right)^{3/4}\left(\frac{1}{a^2 + 2i\hbar c^2 t/m_Q}\right)^{3/2} e^{-\frac{2ia^2 m_Q t/\hbar - 4c^2t^2 + r^2/2}{a^2 + 2i\hbar c^2 t/m_Q}} \tag{III.36}$$

r and t are respectively studied in fm and fm/c, and the unit factor is $\hbar c = 0.197$ GeV fm.

In this section, we focus on the evolution of a $c\bar{c}$ pair but the ideas for a $b\bar{b}$ pair are the same. As one can see in figure III.12 (left panel), the Gaussian probability density spreads out over space as time increases. The heavy quarks move therefore away from each other. As shown in figure III.12 (right panel), the relative motion

follows a "ballistic" evolution, i.e. $\sqrt{\langle r^2 \rangle} \propto t$ after a transient phase. As expected, the more narrow is the initial state in position space, the larger it is in momentum space, the higher is the ballistic velocity.

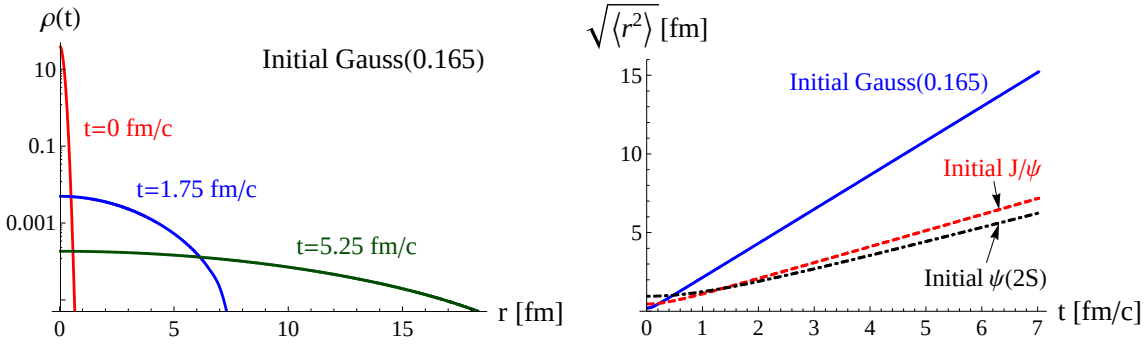

Figure III.12: *Left :* Evolution of the probability density for the $c\bar{c}$ pair in the free case from an initial Gaussian state. *Right :* Evolution of the root mean square radius from initial Gaussian ($a_c = 0.165$ fm), J/ψ and ψ' states: one obtains $\sqrt{\langle r^2 \rangle} \propto t$ after a transient phase.

To probe the accuracy of the numerical solver, one can compare the numerical and analytical results. We observe a difference proportional to Δt and Δr^2, i.e. less than 1% with the chosen grid. This difference is expected from the numerical scheme: the first order time expansion in (III.31) gives a first order accuracy and the spatial second derivative in (III.27) gives a second order accuracy with the use of the central difference approximation.

III.2.1.2 Projection on S states

The evolution of the charmonium (S state) weights[50] from an initial Gaussian state (option 1) and initial S states (option 2) are shown in figures III.13 and III.14, respectively.

For an initial Gaussian wavepacket (option 1), note that the initial weights are ~ 0.46 and ~ 0.12 for the J/ψ and ψ' state, respectively. For the bottomonia (not shown here), the initial weights are ~ 0.085, ~ 0.06 and ~ 0.04 for the $\Upsilon(1S)$, $\Upsilon(2S)$ and $\Upsilon(3S)$, respectively. As explained in section III.1.5, within our model these initial weights are the proportion of the $c\bar{c}$ pair that would promptly hadronise into the corresponding bound states in pp collisions. The ballistic evolution of the relative $c\bar{c}$ motion leads to strong suppressions of the bound components. Less than 1% (7%) of the J/ψ (ψ') survives after 3 fm/c, which is consistent with the suppression picture. Furthermore, from any initial state the ψ' component gets relatively less suppressed than the J/ψ component at some fixed time. This is a first indication that even though the bound states are fully melted for a certain time, the continuous consideration of the $Q\bar{Q}$ correlations could lead to a smaller

[50] As defined by relation III.33.

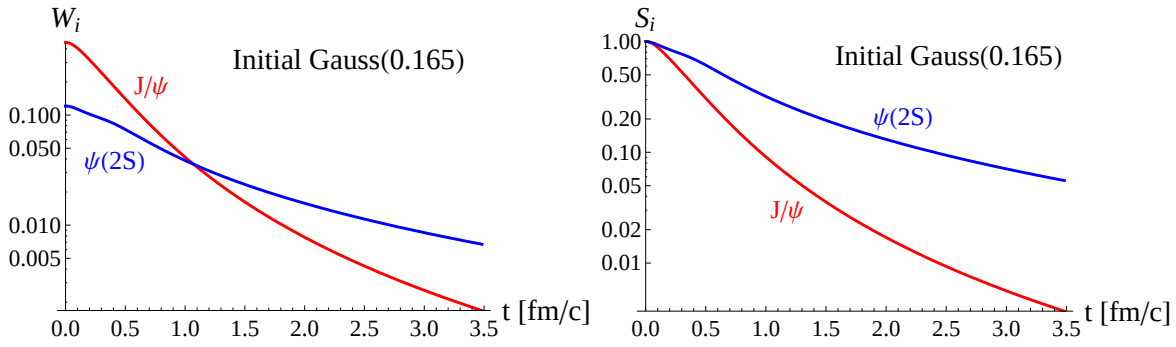

Figure III.13: Time evolution of the J/ψ and ψ' weights W_i (*left*) and survivances S_i (*right*) in the free case from an initial Gaussian wavepacket $a_c = 0.165$ fm (option 1).

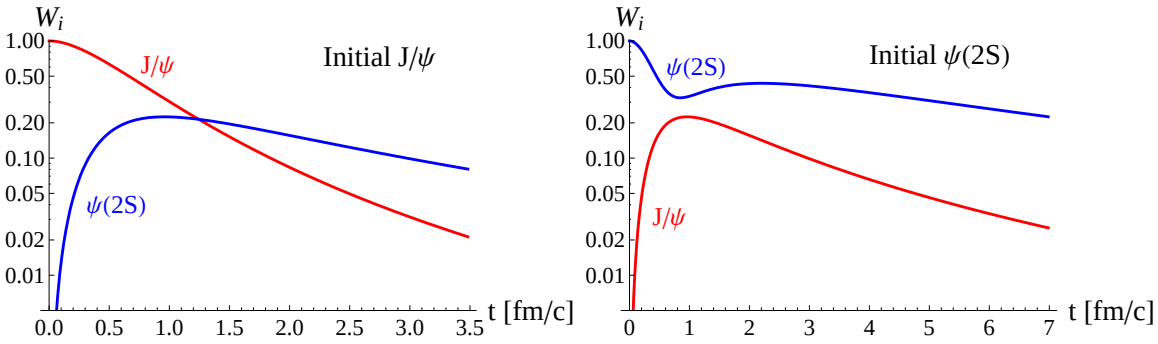

Figure III.14: Time evolution of the J/ψ and ψ' weights W_i in the free case from an initial J/ψ (*left*) and ψ' (*right*) state.

suppression for ψ' than for J/ψ at the phase boundary. This might provide some hint for a possible explanation of the experimental "$R_{AA}(\psi'/J/\psi) > 1$" ratio observed by the CMS collaboration at forward rapidity (see II.3.3). As expected, the suppression values and decreasing rates depend on the initial state: the narrower the latter is, the larger are the decreasing rates, the smaller the weights are at some fixed time. As a consequence, from an initial ψ' state, the survival probability of the ψ' state only slowly evolves and remains quite large over the typical QGP lifetime. Note finally, that the decorrelation of a state tends to populate the other states for a certain time. This effect is not considered in the sequential suppression picture.

Considering the quantum correlations of a $Q\bar{Q}$ pair immersed in a fully deconfined medium leads thus to some suppression patterns which are already quite far from the fast and full decorrelation picture.

III.2.2 Color potential in the zero temperature limit

We now consider the evolution of a $Q\bar{Q}$ pair self-interacting through its vacuum potential (as defined in III.1.1.2), i.e. at the limit $T = 0$. As shown in figure III.15 (left panel), the relative motion follows once again a ballistic evolution but logically with a smaller velocity than in the free case as the bound component of the $c\bar{c}$ wavefunction remains inside the potential well. As shown in the right panel, the charmonium weights remain constant. It is an obvious property of a hermitian

Hamiltonian when the basis of projection $\{\psi_i\}_{i=1...}$ corresponds to the potential and is mainly provided as a check of the numerical accuracy.

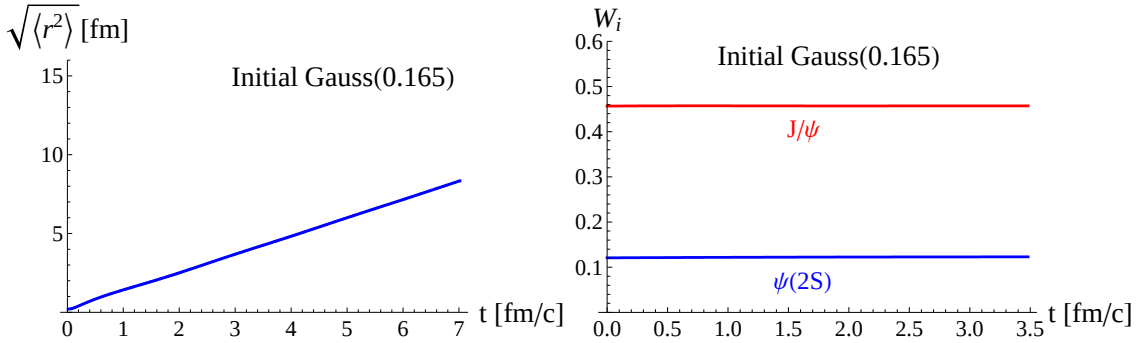

Figure III.15: From an initial Gaussian wavepacket; *Left :* Evolution of the root mean square radius for the $c\bar{c}$ pair with the vaccum potential: one obtains $\sqrt{\langle r^2 \rangle} \propto t$. *Right :* The J/ψ and ψ' weights as a function of time.

III.3 Evolution with the weak potential V_{weak}

To offer an actual alternative to the sequential suppression picture and verify its assumptions, one needs to study the $Q\bar{Q}$ correlation with a more realistic color screened self-interaction. To this end, we now focus on the weak potential V_{weak}, defined in section III.1.1.5, which includes a temperature dependent color screening. We first observe the behaviour of a $Q\bar{Q}$ pair immersed in a stationary medium at some constant temperatures. Then, to get closer to the heavy-ion collisions at RHIC and LHC, we include the temperature scenarios that we discussed in section III.1.2. They correspond to the temperature evolutions at the center of the fireball in a central collision obtained from an ideal hydrodynamic model.

III.3.1 At constant temperatures

We first consider for the initial state the Gaussian wavepacket (option 1). As shown in figure III.16, the evolution of the $Q\bar{Q}$ pair and of the charmonium weights strongly depends on the medium temperature. For the J/ψ component, the typical decorrelation time from its initial weight to its approximative final weight is relatively small ($\lesssim$ 4 fm/c) but not negligible. Furthermore, as shown in figure III.18, one can observe a smooth transition between the situation where the J/ψ component is not suppressed ($T_{\text{red}} \lesssim 0.6$) and the one where it is almost fully suppressed ($T_{\text{red}} \gtrsim 1.4 \approx T_{\text{diss}}^{J/\psi}$). It contrasts with the sequential suppression model which assumes an instantaneous and sharp transition at the dissociation temperature (see table III.5 for the dissociation temperatures corresponding to the weak potential).The picture is quite different for the ψ' component. Firstly, its decorrelation time varies from 4 to more than 30 fm/c (see figures III.16 and III.17). Secondly, it first undergoes a sharp transition to its "full" suppression at the dissociation temperature $T_{\text{red}} \sim 0.4 \approx T_{\text{diss}}^{\psi'}$, but then gets repopulated at higher temperatures $0.6 < T_{\text{red}} < 1.7$. The latter originates from the depopulation of the J/ψ

component. The behaviour of the ψ' component is therefore in strong disagreement with the sequential suppression picture and shows the importance of the possible transitions between bound states even if $T_{\rm red} > T_{\rm diss}$.

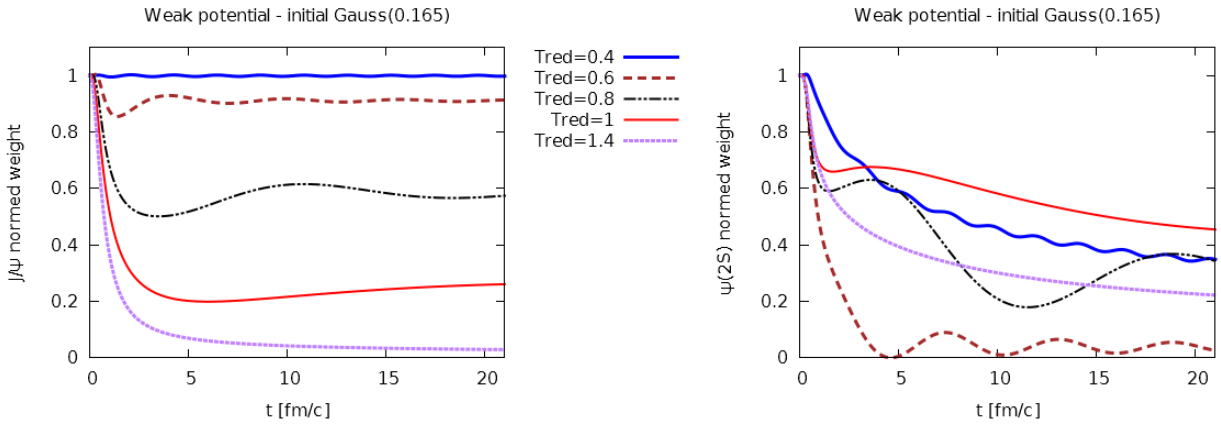

Figure III.16: *Left:* The evolution of the J/ψ survivance S_1 at different reduced temperatures T_{red} from the initial Gaussian wavepacket. *Right:* Same for the ψ' component.

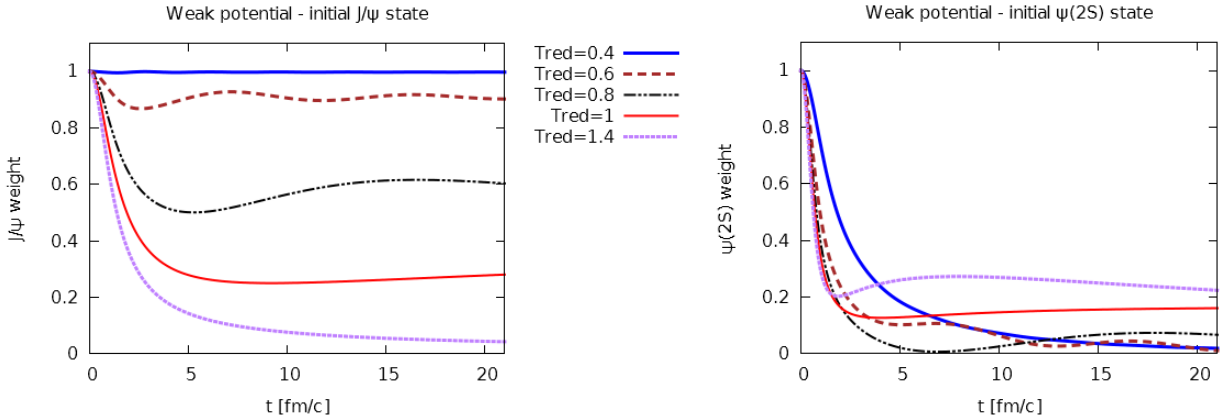

Figure III.17: *Left:* The evolution of the J/ψ survivance S_1 at different reduced temperatures T_{red} from an initial J/ψ state. *Right:* Same for the ψ' component from an initial ψ' state.

We now consider for the initial states the corresponding S states (option 2). First, one can notice that the evolutions of the J/ψ component from an initial Gaussian wavepacket and from an initial J/ψ state are quite close after the transient phase for this range of temperatures (see figure III.17). At the opposite, the ψ' component is clearly more suppressed from an initial ψ' state, which supports the idea that the ψ' component can get repopulated from the J/ψ depopulation in our model.

For the bottomonium states, one observes the same kind of evolutions with an even more progressive transition toward full suppression for the $\Upsilon(1S)$ state (see figure III.18 (right panel)).

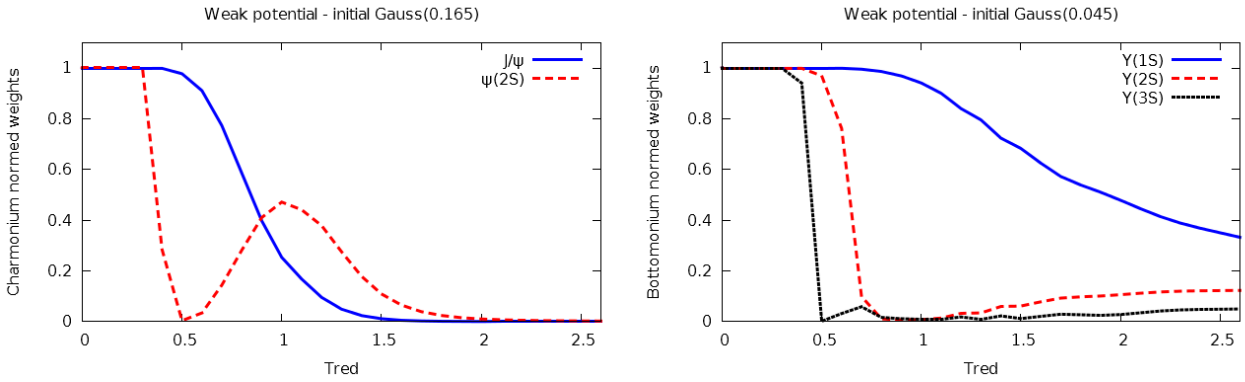

Figure III.18: From the initial Gaussian wavepackets. *Left:* The J/ψ ($T_{\rm diss} = 1.45\,T_c$) and ψ' ($T_{\rm diss} = 0.4\,T_c$) survivance values at $t \to \infty$ as a function of the reduced temperature. *Right:* Same for the bottomonium components $\Upsilon(1S)$ ($T_{\rm diss} = 3.55\,T_c$), $\Upsilon(2S)$ ($T_{\rm diss} = 0.8\,T_c$) and $\Upsilon(3S)$ ($T_{\rm diss} = 0.5\,T_c$).

We have therefore observed that our dynamical picture of the $Q\bar{Q}$ evolution leads to important differences with the sequential suppression: 1) the typical decorrelation times are not negligible (as compared to the QGP lifetime) and vary much with the situation, 2) for the 1S states the transition from null to full suppressions are not sharp but progressive, and 3) the excited components can be repopulated from the lower state depopulations.

III.3.2 At RHIC

To get closer to reality, we now include the hydrodynamic cooling obtained for RHIC heavy ion collisions, as defined in III.1.2. The evolution of the charmonium and bottomonium weights from initial Gaussian wavepackets (left panels) or corresponding quarkonium states (right panels) are shown in figures III.19 and III.20 respectively. One can first notice than the typical time for the weights to decorrelate is $\sim 3-6$ fm/c. In a more realistic scenario (i.e. including the motion of the $Q\bar{Q}$ center of mass and an inhomogeneous temperature), it would lead to an important difference in the suppressions of $Q\bar{Q}$ pairs reaching the phase boundary at different times.

As the variation of the weak potential is relatively small for $T_{red} \geq 1.4$, the main evolution of the weights, which occurs for $t < 4$ fm/c, is logically close to the results at $T_{red} = 1.4$ in figures III.16 and III.17. For $4 \lesssim t \lesssim 10$ fm/c, i.e. during the phase transition where $T \sim T_c$, the potential and the weights vary only a little. After the chemical freeze-out $t \gtrsim 10$ fm/c, we recall that the evolutions obtained with the potential approach make less sense as the quarkonium content should be fixed at the chemical freeze-out.

When the initial state is a Gaussian wavepacket, the excited states get partially repopulated (at least for a certain time) from the depopulation of the 1S states. It results in a smaller suppression of the ψ' component relatively to the J/ψ, whereas it does not affect the bottomonia for $t > 4$ fm/c. Furthermore, one can observe that the 1S components are clearly less suppressed if they are the initial state. As in the free

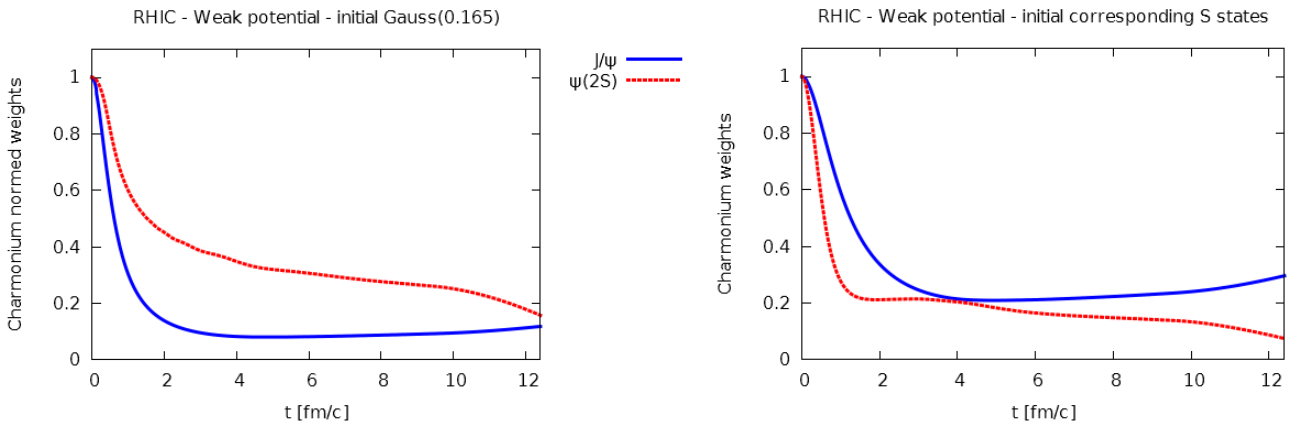

Figure III.19: *Left:* The evolution of the J/ψ and ψ' survivances S_i at RHIC from the initial Gaussian wavepacket (with $a_c = 0.165$). *Right:* Same but from initial J/ψ and ψ' states respectively.

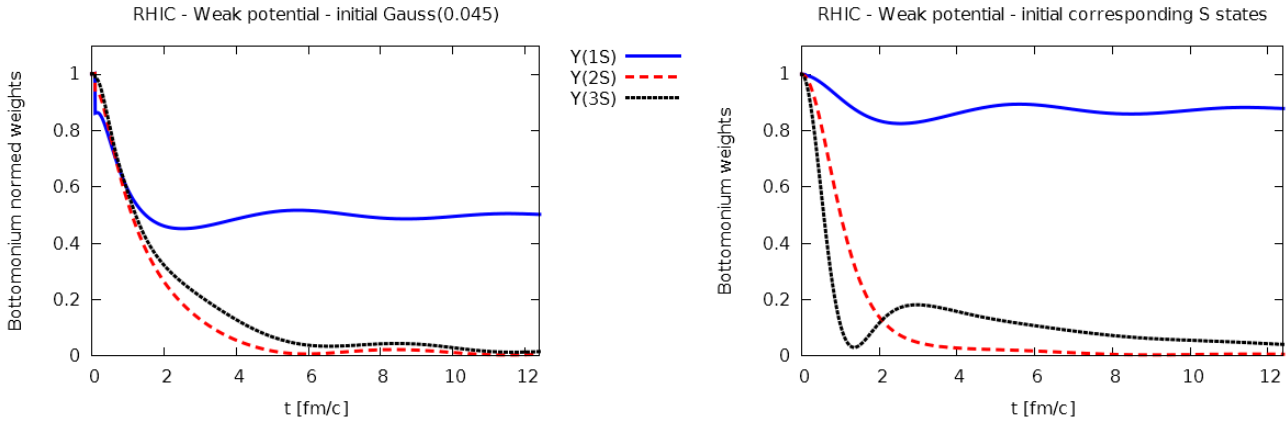

Figure III.20: *Left:* The evolution of the $\Upsilon(1S)$, $\Upsilon(2S)$ and $\Upsilon(3S)$ survivances S_i at RHIC from the initial Gaussian wavepacket (with $a_b = 0.045$). *Right:* Same but from corresponding initial bottomonium states.

case, it should be due to the smaller size of the quarkonium initial wavefunctions in momentum space, resulting to slower ballistic evolutions. The values of the normed weights at the chemical freeze-out ($t = 9.4$ fm/c) are summed up in table III.6 and show 1) an intermediate suppression of the J/ψ and ψ' states with a possible enhancement of the $\psi'/J/\psi$ ratio in heavy ion collision, 2) a partial suppression of the $\Upsilon(1S)$ state and strong suppressions of the $\Upsilon(2S)$ and $\Upsilon(3S)$ states.

III.3.3 At LHC

Despite of the $\sim$ 80 MeV difference in the initial temperature, the evolution of the weights are quite similar at RHIC and LHC, especially for the bottomonia. The charmonia are slightly more suppressed at LHC and the ratio $\psi'/J/\psi$ is clearly above or close to unity at the chemical freeze-out ($t = 10.4$ fm/c).

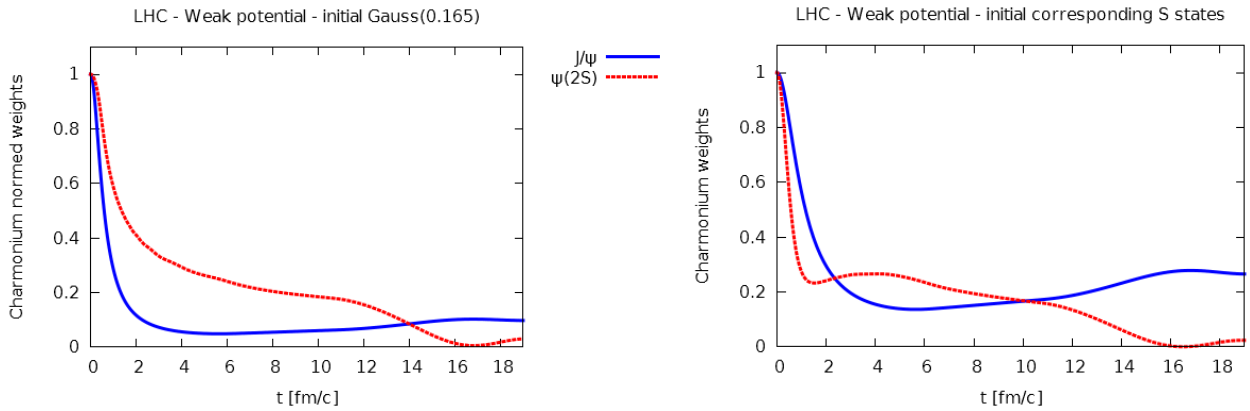

Figure III.21: *Left:* The evolution of the J/ψ and ψ' survivances S_i at LHC from the initial Gaussian wavepacket (with $a_c = 0.165$). *Right:* Same but from initial J/ψ and ψ' states respectively..

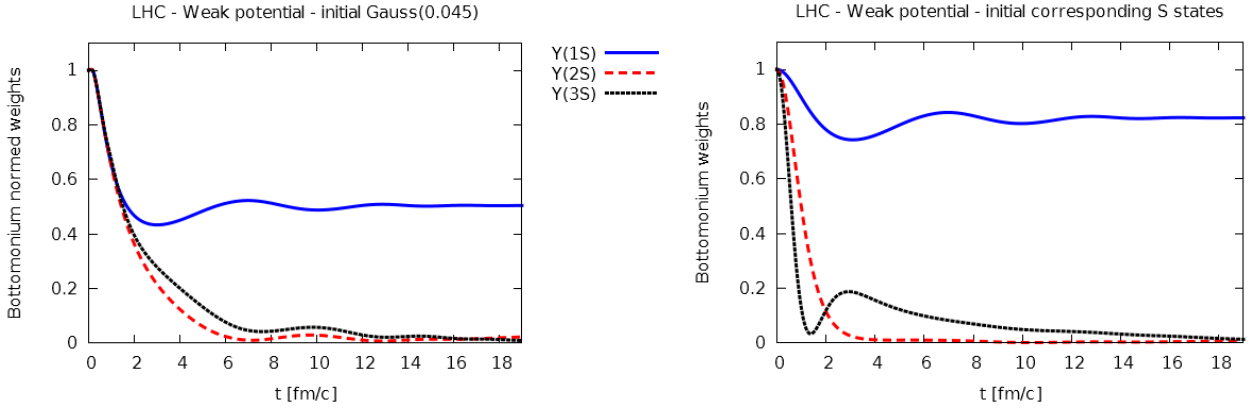

Figure III.22: *Left:* The evolution of the $\Upsilon(1S)$, $\Upsilon(2S)$ and $\Upsilon(3S)$ survivances S_i at LHC from the initial Gaussian wavepacket (with $a_b = 0.045$). *Right:* Same but from corresponding initial bottomonium states.

We have thus observed that at RHIC and LHC there is no early coupling/decoupling for the evolution of various quarkonia in the equilibrated medium. In the pre-equilibium phase, as the potential should vary very quickly from its vacuum to its high temperature form, option 1 should then be privileged until one provides a strong argument in favor of the coherence at very early times.

III.4 Evolutions with the strong potential $U(T)$

We now focus on the strong potential $V = U$, equal to the internal energy. As discussed in section III.1.1.6, the strong potential exhibits an important peak of its asymptotic values $U(r \to \infty, T)$ centered on T_c. If one does not include any additional thermal mechanisms, the strong potential corresponds to a fully adiabatic evolution of the $Q\bar{Q}$ pair in the deconfined medium.

III.4.1 At constant temperatures

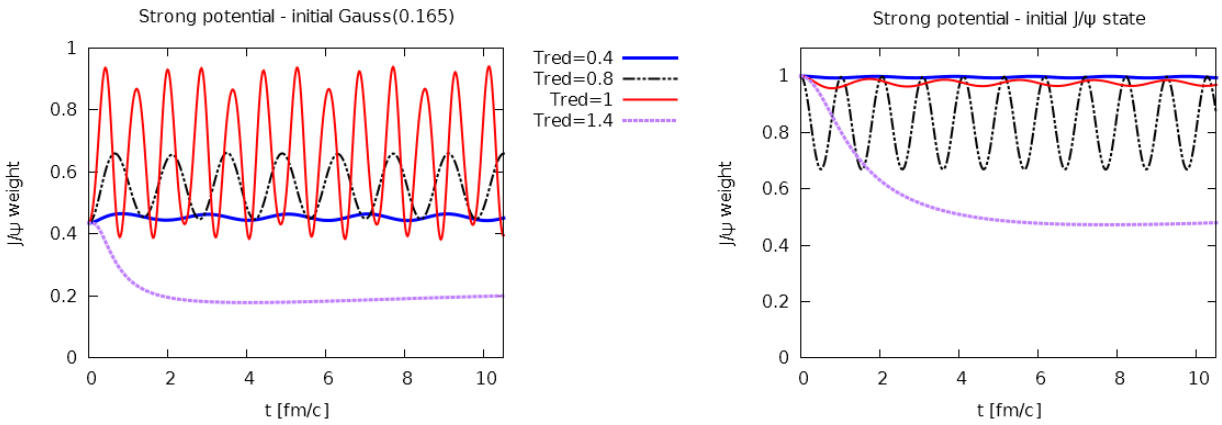

Figure III.23: *Left:* The evolution of the J/ψ weight at different reduced temperatures T_{red} from the initial Gaussian wavepacket. *Right:* Same but from J/ψ initial state.

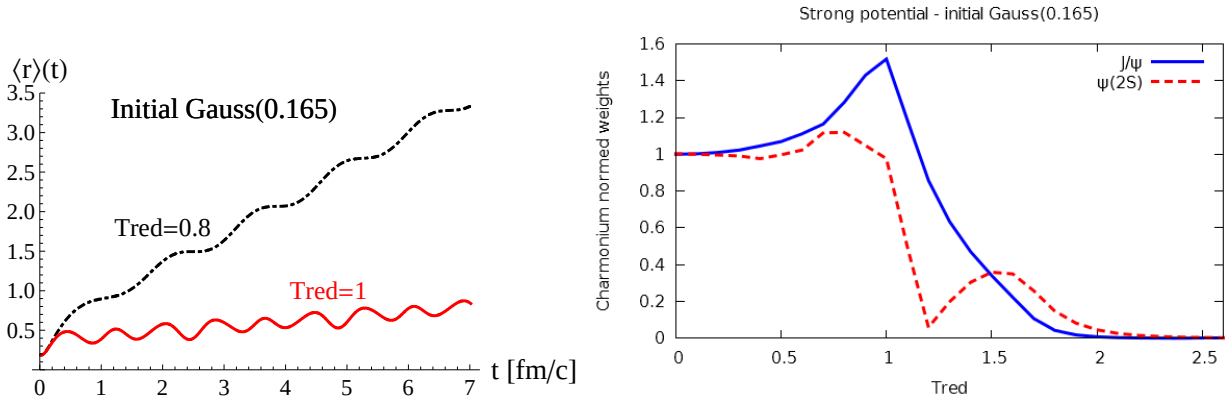

Figure III.24: From the initial Gaussian wavepacket. *Left:* Evolution of the average position [fm] for the $c\bar{c}$ pair. *Right:* The J/ψ ($T_{\text{diss}} = 1.85\,T_c$) and ψ' ($T_{\text{diss}} = 1.1\,T_c$) survivance values at $t \to \infty$ as a function of the reduced temperature.

As shown in figures III.23, the evolution of the quarkonium weights at constant temperatures are quite different with the strong potential when $T \sim T_c$. One observes strong oscillations of the weights with some repeated patterns. In figure III.24 (left panel), the oscillations of the mean radius around the usual ballistic evolution reveal the oscillatory motion of the wavepacket trapped in the potential. This motion is caused by the important change in the potential features when $T \sim T_c$. Outside of this temperature range, the evolutions are similar to the weak potential case but with smaller suppressions (as expected from $U(r \to \infty, T) > V^{\text{weak}}(r \to \infty, T)$). Because of the weight oscillations, it is difficult to define a large time behaviour when $T \sim T_c$. Even so, outside $T \sim T_c$, note that the suppression at large time shows similar behaviours to what we discussed in section III.3 (see III.24 right panel).

III.4.2 At RHIC

We now include the hydrodynamic cooling at RHIC energy as defined in III.1.2. The evolutions of the charmonium and bottomonium weights from the initial Gaussian wavepackets (left panels) or corresponding quarkonium states (right panels) are shown in figures III.25 and III.26 respectively.

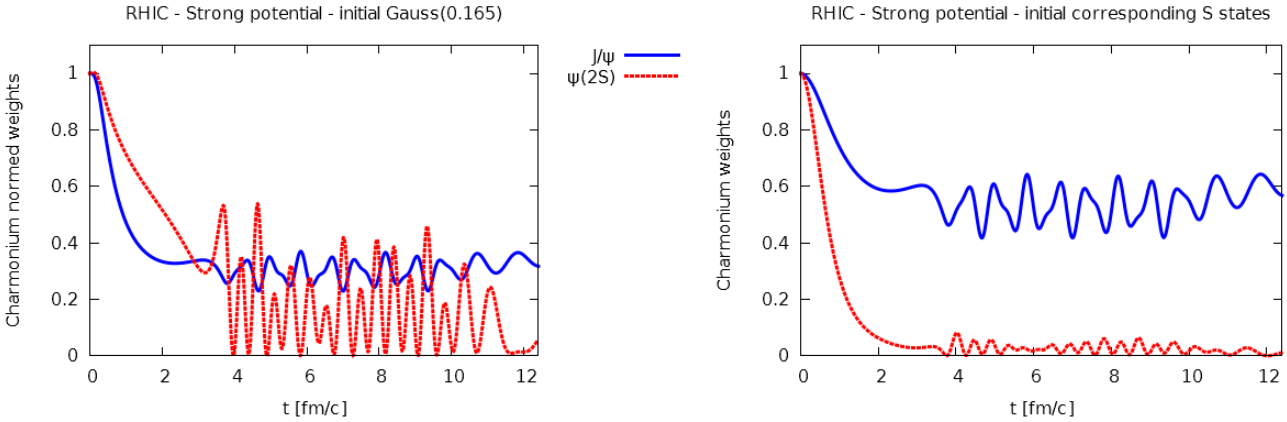

Figure III.25: *Left:* The evolution of the J/ψ and ψ' survivances S_i at RHIC from the initial Gaussian wavepacket (with $a_c = 0.165$). *Right:* Same but from J/ψ and ψ' initial bound states respectively.

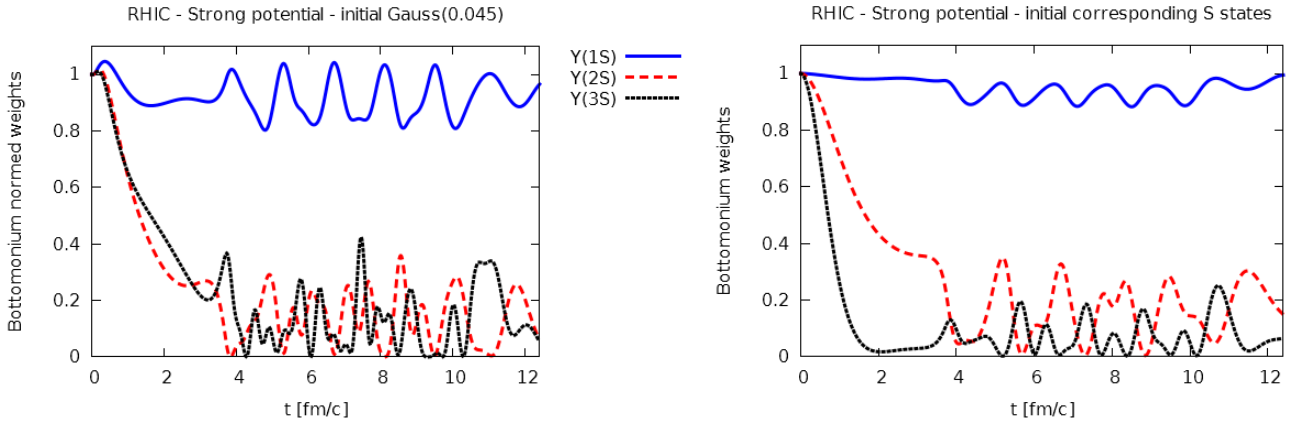

Figure III.26: *Left:* The evolution of the $\Upsilon(1S)$, $\Upsilon(2S)$ and $\Upsilon(3S)$ survivances S_i at RHIC from the initial Gaussian wavepacket (with $a_b = 0.045$). *Right:* Same but from corresponding initial bound states.

As expected from the previous section, the general evolution of the weights is a smooth decrease until the medium temperature reaches $T \sim T_c$ at $t \sim 4$ fm/c. The weights then oscillates until $T_{\rm red} \lesssim 0.8$, i.e. for $4 \lesssim t \lesssim 11$ fm/c. As expected from a stronger binding, the different quarkonium states are less suppressed than with the weak potential, exception made of the ψ' component. With the strong potential, the latter is indeed less repopulated from the smaller J/ψ depopulation. At the chemical freeze-out ($t = 9.4$ fm/c), the fully adiabatic evolution of the $Q\bar{Q}$ pair

at RHIC leads to intermediate and relatively strong suppressions of the J/ψ and ψ' states, respectively, a very small suppression of the $\Upsilon(1S)$ state and relatively strong suppressions of the $\Upsilon(2S)$ and $\Upsilon(3S)$ states. There is therefore a quite strong influence of the potential, as in other approaches.

III.4.3 At LHC

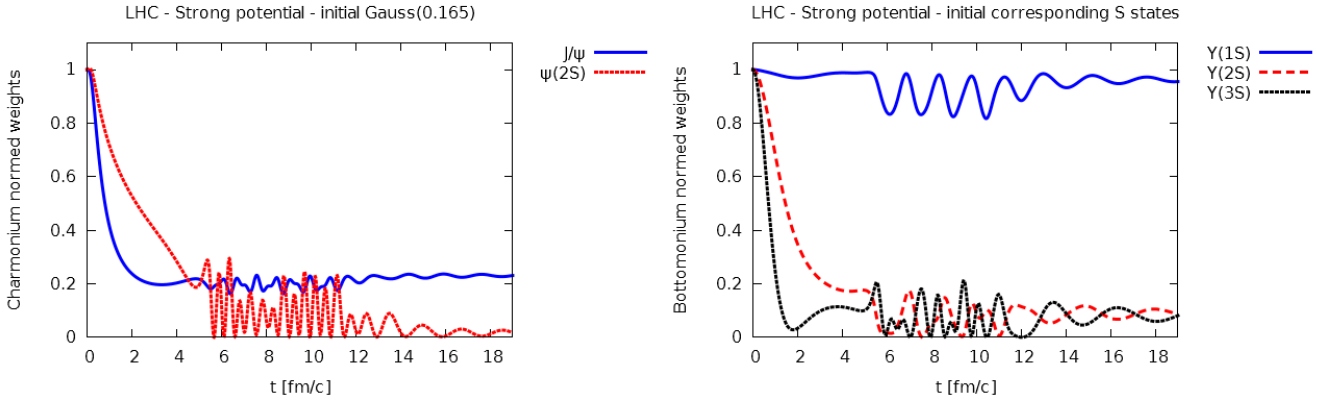

Figure III.27: *Left:* The evolution of the J/ψ and ψ' survivances S_i at LHC from the initial Gaussian wavepacket (with $a_c = 0.165$). *Right:* The evolution of the $\Upsilon(1S)$, $\Upsilon(2S)$ and $\Upsilon(3S)$ survivances at LHC from the corresponding initial bound states.

Like in the weak potential case, RHIC and LHC temperature scenarios lead to equivalent evolutions of the weights, with a little more suppression at LHC (see figures III.27).

III.5 Values at the chemical freeze-out and discussion

The values of the J/ψ, ψ', $\Upsilon(1S)$ and $\Upsilon(2S)$ survivances at the chemical freeze-out at RHIC ($t = 9.4$ fm/c) and LHC ($t = 10.4$ fm/c) are summed up respectively in table III.6 and III.7. However, note that to remove the strong influence of the upper limit on t in the strong potential case, we perform instead an averaging over the oscillations during the phase transition $T = T_c$.

For the charmonia, contrasting with the sequential suppression picture, one obtains rich suppression patterns which lead to intermediate suppressions at both RHIC and LHC. Furthermore, as a possible explanation of the $(N_{\psi'}/N_{J/\psi})_{PbPb}\,/\,(N_{\psi'}/N_{J/\psi})_{pp} > 1$ ratio observed at LHC at forward rapidity, our model can lead to larger survivances of the ψ' component than the J/ψ. It originates from important transitions between the two components which are completely untreated within common suppression models.

For the bottomonia, the $\Upsilon(1S)$ state is only weakly suppressed whereas the $\Upsilon(2S)$ and $\Upsilon(3S)$ states are strongly suppressed. At these energies, our "ordered"

State survivance at RHIC			R_{AA} data	
State \ Potential	V_{weak}	V=U	Low p_T	High p_T
J/ψ from initial J/ψ	0.24	0.52	0.26 ± 0.05	0.64 ± 0.14
J/ψ from init. Gauss(0.165)	0.09	0.30		
ψ' from initial ψ'	0.14	0.03	None	None
ψ' from init. Gauss(0.165)	0.26	0.17		
$\Upsilon(1S)$ from initial $\Upsilon(1S)$	0.88	0.93	0.66 ± 0.13	
$\Upsilon(1S)$ from init. Gauss(0.045)	0.49	0.91		
$\Upsilon(2S)$ from initial $\Upsilon(2S)$	0.005	0.16	None	
$\Upsilon(2S)$ from init. Gauss(0.045)	0.02	0.15		

Table III.6: Values of the J/ψ, ψ', $\Upsilon(1S)$ and $\Upsilon(2S)$ survivances at the chemical freeze-out at RHIC. Experimental most central R_{AA} data at RHIC in AuAu $\sqrt{S_{NN}} = 200$ GeV collisions: 1) high p_T STAR data [134] (inclusive (prompt and non prompt) J/ψ, $5 < p_T < 14$ GeV/c, $|y| < 1$ and 0-10% centrality) and 2) low p_T PHENIX data [133] (inclusive J/ψ, $p_T < 5$ GeV/c, $|y| < 0.35$ and 0-5% centrality). The non prompt contribution is estimated to 10-25% of the inclusive production. For the $\Upsilon(1S)$: STAR data [167] ($p_T > 0$ GeV/c, $|y| < 1$ and 0-10% centrality).

State survivance at LHC			R_{AA} data	
State \ Potential	V_{weak}	V=U	Low p_T	High p_T
J/ψ from initial J/ψ	0.17	0.40	0.83 ± 0.14	0.20 ± 0.03
J/ψ from init. Gauss(0.165)	0.06	0.20		
ψ' from initial ψ'	0.16	0.03	None	0.13 ± 0.04
ψ' from init. Gauss(0.165)	0.18	0.10		
$\Upsilon(1S)$ from initial $\Upsilon(1S)$	0.80	0.90	0.41 ± 0.06	
$\Upsilon(1S)$ from init. Gauss(0.045)	0.49	0.84		
$\Upsilon(2S)$ from initial $\Upsilon(2S)$	0.001	0.07	0.11 ± 0.06	
$\Upsilon(2S)$ from init. Gauss(0.045)	0.03	0.17		

Table III.7: Values of the J/ψ, ψ', $\Upsilon(1S)$ and $\Upsilon(2S)$ survivances at the chemical freeze-out at LHC. Experimental R_{AA} data at LHC in PbPb $\sqrt{S_{NN}} = 2.76$ TeV collisions. For the J/ψ: 1) high p_T CMS data [138] (prompt J/ψ, $6.5 < p_T < 30$ GeV/c, $|y| < 2.4$ and 0-10% centrality) (inclusive J/ψ: $R_{AA} = 0.24 \pm 0.03$) and 2) low p_T ALICE data [137] (inclusive J/ψ, $0 < p_T < 8$ GeV/c, $|y| < 0.9$ and 0-10% centrality). For the ψ': high p_T CMS data [144] (prompt ψ', $6.5 < p_T < 30$ GeV/c, $|y| < 1.6$ and integrated centrality). For the $\Upsilon(1S)$ and $\Upsilon(2S)$: CMS data [168] ($p_T > 0$ GeV/c, $|y| < 2.4$ and 0-5% centrality).

results for the bottomonia are thus in a better agreement with the sequential suppression scheme. Furthermore, note that we obtain only a little more suppression at LHC than at RHIC and that the energy dissipation - which is implicitly included in the weak potential - tends to increase the suppression.

The corresponding experimental data for most central collisions - where the effects of the deconfined matter are maximal - are given on an indicative basis. A correct result-data comparison would require to refine our model with initial cold nuclear matter effects, statistical recombinations, feed downs from excited states (see table I.2 and figure I.10) and a more realistic heavy ion collision scenario (e.g. spatial distributions of the quarkonia and temperature). Because the bottomonia are much less subject to recombinations and initial cold nuclear matter effects (see section II.2.1), our results for the $\Upsilon(1S)$ state can reasonably be compared to the experimental data if one considers the feed down contributions. Like other particles, the $\Upsilon(1S)$ p_T spectrum is dominated by its low p_T range, so that one can assume the indirect production of $\Upsilon(1S)$ to be $\sim 30 - 40\%$ of its inclusive production in pp collisions (see figure I.10). As the excited states are strongly suppressed, their contribution is very small and one can thus reduce our predictions for the $\Upsilon(1S)$ state to $\sim 60 - 70\%$ of their values. If one reasonably assume that the $\Upsilon(1S)$ states form before the deconfined medium (see section II.1) and that the weak potential is more realistic, the values $S(\Upsilon(1S)) = 0.88$ at RHIC and $S(\Upsilon(1S)) = 0.80$ at LHC are the most probable. Then our actual prediction within this model should be around $R_{AA} \sim 0.6$ at RHIC and $R_{AA} \sim 0.5$ at LHC. These values should lead to a rather good agreement with the data by including the shadowing/antishadowing effects.

Main ideas and transition

Limiting our dynamical model to the effects of the Debye screening on the $Q\bar{Q}$ binding, we have studied its real-time dynamics and quarkonia content. We have observed some important transitions between bound quantum states and between bound and free states. As a result and especially for the charmonia, we have obtained rich suppression patterns, even at the high temperature limit, which already rule out the simple melting picture assumed by the sequential suppression. In particular, the evolution of the $Q\bar{Q}$ pair in a dynamic medium leads to neither full nor fast decorrelation of the "melted" states and to possible repopulation of excited states from lower states. We have also pointed out the strong influence of the $Q\bar{Q}$ initial state and of the potential. Nevertheless, a full description of the $Q\bar{Q}$ dynamics should also include the effects of the direct collisions between the heavy quarks and the thermal medium. Including them should lead to a diffusive evolution of the $Q\bar{Q}$ pair which might strongly modify the suppression patterns. To this end, we introduce in the next part the open quantum system framework and motivate our approach for the $Q\bar{Q}$/QGP direct interaction.

Part IV

Quarkonia and open quantum systems

Inside the deconfined matter, the $Q\bar{Q}$ pairs are subject to screening effects due to color charges in their vicinity and to multiple hard collisions with the medium particles. In this part, we discuss how these multiple collisions can be accounted for in general and how they could affect the internal degrees of freedom of a $Q\bar{Q}$ pair. To this end, we first introduce the general frameworks of classical and quantum open systems in section IV.1. These frameworks separate a global system into a relevant small subsystem (the $Q\bar{Q}$ pair) and an irrelevant large environment (QGP) whose detailed dynamics is insignificant. It results in some energy and momentum exchanges between the two systems without significantly affecting the environment. We then briefly review how these effects are described in the literature for the $Q\bar{Q}$/QGP system IV.2.1 and motivate our approach IV.2.2.

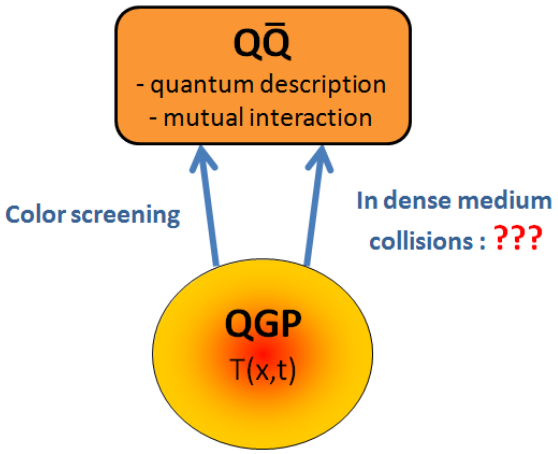

Figure IV.1: In this part, we discuss how to take into account the multiple direct interactions between the $Q\bar{Q}$ and QGP systems.

IV.1 Introduction to open quantum systems

IV.1.1 Classical Brownian motion

The Brownian motion refers to the erratic motion of Brownian particles - characterised by a heavy mass m - immersed in a thermal fluid and subject to permanent collisions with the fluid lighter particles (of mass m_f). The study of the Brownian motion usually assumes a clear separation between the different typical scales. The first time scale τ_{coll} corresponds to the typical microscopic interaction time between the bath components and the Brownian particle and leads to the fluctuations of the latter velocity. The second time scale corresponds to the typical time of the relaxation τ_{relax} of its average velocity. The mass hierarchy $m \gg m_f$ causes the relaxation to be much slower than the process of collisions, i.e. $\tau_{\text{coll}} \ll \tau_{\text{relax}}$. The dynamics of the Brownian motion is then usually considered on a time interval Δt in between these two time scales, i.e. $\tau_{\text{coll}} \ll \Delta t \ll \tau_{\text{relax}}$, in order to study its relaxation to equilibrium without focusing on each collision.

In classical mechanics, the Brownian motion is well described by the phenomenological Langevin equation within the Newtonian framework [151]. The subsystem evolution is obtained through the balance of two forces which generate irreversible energy exchanges between the two systems. These two forces, namely the friction force and the stochastic force, translate the two aspects of the collisions at the two described time scales. The Langevin equation in 1D writes,

$$m\frac{d^2x}{dt^2} = -mAv + F_R(t) + F_{\text{ext}} \tag{IV.37}$$

where x is the subsystem position, v its velocity, A the drag coefficient corresponding to the inverse relaxation time ($1/\tau_{\text{relax}}$), $F_R(t)$ the random/stochastic force and F_{ext} a possible external force. The first term of the RHS is the friction force proportional to the Brownian particle velocity. It translates its reduction in speed due the collisions if it propagates with a higher velocity than the medium particle. The second term is a fluctuating force which simulates the permanent collisions. This fluctuating force is generally taken as a homogeneous Gaussian noise, independent of the subsystem position and described by its mean and covariance function. As the direction of the collisions are completely random, the mean value of the noise is zero over many collisions: $\langle F_R(t)\rangle = 0$. The classical Langevin equation usually assumes no correlation between the successive collisions, so that the white noise covariance writes,

$$\langle F_R(t)F_R(t+\tau)\rangle = B\delta(\tau), \tag{IV.38}$$

where δ is the Dirac distribution and B the correlation strength. The classical fluctuation-dissipation relation,

$$B = 2mkT_{\text{bath}}A, \tag{IV.39}$$

where k is the Boltzmann factor and T_{bath} the bath temperature, gives the balance between the two forces (i.e. between the energy gain and loss). If the subsystem

is initially at a given velocity, the Brownian motion is characterised by a linear rise of the velocity variance $\sigma_v^2 = \langle [v(t) - \langle v \rangle]^2 \rangle \approx 2D_v t$ (when $t \ll \tau_{\text{relax}}$), where $D_v = B/(2m^2)$ is the diffusion coefficient in velocity space, before saturating to $\langle v^2 \rangle \approx D_v/A$ at thermal equilibrium ($t \gg \tau_{\text{relax}}$). Furthermore, at thermal equilibrium the variance of the position is given by $\langle x^2 \rangle \approx 2D_S t$, where $D_S = D_v/A^2$ is the spatial diffusion coefficient.

The Brownian motion can be equivalently described by the Fokker-Planck equation which focuses on the time evolution of the velocity density distribution $f(v,t)$ [151]. Without external force, the Fokker-Planck equation writes

$$\frac{\partial f}{\partial t} = \frac{\partial}{\partial v}(Avf) + \frac{\partial^2}{\partial v^2}(D_v f). \tag{IV.40}$$

The Fokker-Planck equation is usually derived from the Boltzmann equation[51] by expanding its collisional term to small momentum transfers (which is a consequence of the mass hierarchy). It can also be derived from the Kramers-Moyal expansion for stochastic process.

IV.1.2 Overview

The search for the description of quantum subsystems in contact with a heat bath has appeared to be crucial for the understanding of quantum fundamentals and in many branches of applied physics (where the quantum systems can never be isolated), such as in quantum diffusion and transport [169, 170, 171], quantum optics [172, 173, 174], low energy heavy ion scattering [175, 176], quantum computers and devices [177, 178, 179, 180], and of course high energy heavy ion collisions... Unfortunately, the Langevin dynamics - or more generally energy dissipation - cannot be introduced easily in the common quantum formalism, as no direct canonical quantization of an Hamiltonian can describe irreversible phenomena [181].

To solve this long standing problem, two main approaches have been proposed and have led to a description of quantum dissipation far from being unique.

1) In the most common approach, the subsystem plus bath is considered as a whole conservative system. By integrating out the bath degrees of freedom, one obtains the dissipative evolution of the subsystem only, given by a quantum master equation (QME) or equivalent [182, 183] (section IV.1.4). In a number of complex applications defining the bath and calculating the QME operators is rather complicated and some effective approaches are necessary [182, 184]. A simple model of the bath [172, 185, 186] - a thermal ensemble of oscillators linearly coupled to the subsystem - has proven to be a suitable framework to study Brownian motion (section IV.1.5).

2) Within the second category, many non-standard quantization procedures [187, 177, 188, 189] or new frameworks [190, 191, 192, 193, 194, 195, 196] have

[51] The Boltzmann equation is a kinetic equation which describes the dynamics of a particle in a classical diluted gas. It assumes that the time of one collision is much smaller than the typical time between two successive collisions.

been suggested to overcome the initial subsystem quantization difficulty (briefly discussed in section IV.1.6).

Generally, these evolutions are expected to lead the subsystem to a thermal equilibrium where the energy spectrum components of the subsystem are "Lamb" shifted and broadened [184, 197] (see section IV.1.7). These spectrum modifications are negligible at the weak coupling limit and one expects the thermal equilibrium predicted by statistical mechanics (the Gibbs state), i.e. Boltzmann distributions of the uncoupled subsystem energy states. One is at the *weak coupling limit* when the subsystem relaxation time τ_{relax} is much larger than the typical microscopic interaction time τ_{coll} and than the subsystem natural oscillation time. A Brownian subsystem usually corresponds to this situation.

IV.1.3 Pure and mixed states

In common quantum mechanics, one focuses on isolated systems with no interactions with their environment. The whole information about the system is encoded in a *well defined* state that evolves in a deterministic manner. The only probabilistic notion enters when one considers the result of an observable measurement such as the position, momentum... The state is then described by a *pure* normed vector $|\psi\rangle$, a single wavefunction or a Wigner distribution for instance.

In open quantum systems as in classical statistical mechanics, the study of the evolution and interactions of the whole system (subsystem of interest plus bath) is usually impossible and one needs to give a statistical nature to the bath-subsystem interaction. The subsystem must then be described by a *mixed state*, which includes not only the probabilistic information about the observable measurements *but also about the state itself* [198]. The common tool to describe a mixed state is the density matrix operator,

$$\rho(t) = \sum_{n,m=1}^{N} \rho_{nm}(t) |\psi_n\rangle\langle\psi_m| \,, \qquad \text{with } \sum_{n=1}^{N} \rho_{nn}(t) = 1, \tag{IV.41}$$

where $\{\rho_{nn}(t)\}_{n=1,\dots N}$ is the distribution of the weights of the accessible pure eigenstates $\{|\psi_n\rangle\}_{n=1,\dots N}$. Note that a diagonal term $\rho_{nn} = p_n$ is the probability - also called population or weight - for the system to be in a state $|\psi_n\rangle$, whereas the off-diagonal terms give information about the "coherences", i.e. the possible phase interferences between the different components of the system state. The expectation value of an observable operator $\hat{O}$ is then given by

$$\langle \hat{O} \rangle = \text{tr}(\rho \, \hat{O}). \tag{IV.42}$$

The evolution of the density matrix is deterministic and commonly given by a QME (see below).

If one considers instead a stochastic equation based on a pure state evolution[52], one needs to perform an average over a large sample of initially identical subsys-

[52] As for instance the Heisenberg-Langevin equation, the Schrödinger-Langevin equation or the stochastic Schrödinger equations as discussed later.

tems to recover the statistical notion implied by the mixed state [183, 199]. The expectation value of an observable operator $\hat{O}$ is then be given by

$$\Big\langle \langle\psi(t)|\hat{O}|\psi(t)\rangle \Big\rangle_{\text{stat}} = \lim_{n_{\text{stat}}\to\infty} \frac{1}{n_{\text{stat}}} \sum_{r=1}^{n_{\text{stat}}} \langle\psi^{(r)}(t)|\hat{O}|\psi^{(r)}(t)\rangle \,, \tag{IV.43}$$

where the pure state $|\psi^{(r)}(t)\rangle$ is given by the r$^{\text{th}}$ realisation of the stochastic evolution. Finally, a Wigner transform of the density matrix can also be used to describe mixed states.

IV.1.4 Quantum Master equations and equivalent

IV.1.4.1 Quantum Master equations

In the most common approach to open quantum systems [182], the subsystem plus bath is considered as a whole conservative system, in order to overcome the difficulty to treat the subsystem dissipation directly. The evolution of the density matrix operator ρ_{tot} of the global system in the total Hilbert space $\mathcal{H}_{\text{tot}} = \mathcal{H}_{\text{S}} \otimes \mathcal{H}_{\text{env}}$ is then given by the Liouville - von Neumann equation of motion,

$$\dot{\rho}_{\text{tot}} = -\frac{i}{\hbar}[H_{\text{tot}}, \rho_{\text{tot}}] \equiv \mathcal{L}_{\text{tot}}\, \rho_{\text{tot}} \tag{IV.44}$$

where H_{tot} is the Hamiltonian of the global system and $\mathcal{L}_{\text{tot}}$ is defined as the corresponding Liouville operator. Next, it is assumed that the global Hamiltonian and Liouvillian operators can be decomposed as:

$$H_{\text{tot}} = H_{\text{S}} + H_{\text{int}} + H_{\text{B}}; \qquad \mathcal{L}_{\text{tot}} = \mathcal{L}_{\text{S}} + \mathcal{L}_{\text{int}} + \mathcal{L}_{\text{B}}, \tag{IV.45}$$

where H_{S} is the "isolated" subsystem Hamiltonian (when the subsystem is not coupled with the bath), H_{int} the Hamiltonian describing the interactions between the bath and the environment and H_{B} the bath Hamiltonian. As one is only interested in the dynamics of the subsystem, one needs to trace out the bath degrees of freedom from the global density operator to obtain the "reduced" density operator ρ_{S} corresponding to the subsystem variables. To this end, one should employ a certain projection operator P, which contains the trace operation over the bath coordinates:

$$\rho_{\text{S}} = \text{tr}_{\text{B}}(\rho_{\text{tot}}) \equiv P\rho_{\text{tot}}. \tag{IV.46}$$

Applying these projections and decompositions to the equation of motion (IV.44) yields

$$\dot{\rho}_{\text{S}}(t) = P(\mathcal{L}_{\text{S}} + \mathcal{L}_{\text{int}})\rho_{\text{S}}(t) + \int_0^t dt' P\mathcal{L}_{\text{int}} e^{(1-P)\mathcal{L}_{\text{tot}}t'}(1-P)\mathcal{L}_{\text{int}}\, \rho_{\text{S}}(t-t'). \tag{IV.47}$$

The latter is the general time-retarded Nakajima-Zwanzig equation. The first term of the RHS describes the reversible unitary dynamics of the subsystem. The second term describes the possible transitions that the subsystem may undergo due to the interactions with the bath and corresponds to an irreversible non-unitary relaxation.

The second term is still too complicated for explicit evaluations, as it contains any power of $\mathcal{L}_{\rm int}$ and depends on the whole history of $\rho_{\rm S}$. To simplify it, one can perform the Born approximation, i.e. a truncation to the second order in $\mathcal{L}_{\rm int}$ corresponding to a weak coupling, and assumes the process to be Markovian (local in time), i.e. the bath has no memory of past events so that $\rho_{\rm S}(t-t')$ can be replaced by $\rho_{\rm S}(t)$, to derive from IV.47 the Born-Markov quantum master equation:

$$\dot{\rho}_{\rm S}(t) = P(\mathcal{L}_{\rm S}+\mathcal{L}_{\rm int})\rho_{\rm S}(t) + \int_0^t dt' P\mathcal{L}_{\rm int} e^{(1-P)(\mathcal{L}_{\rm S}+\mathcal{L}_{\rm B})t'}(1-P)\mathcal{L}_{\rm int}\rho_{\rm S}(t). \quad \text{(IV.48)}$$

In practice, the Born-Markov QME (IV.48) is transformed either into the Redeld equation in the eigenstate basis of H_S,

$$\dot{\rho}_{nm}(t) = -i\omega_{nm}\,\rho_{nm}(t) - \sum_{k,l} R_{nmkl}\rho_{kl}(t), \quad \text{(IV.49)}$$

where ω_{nm} are the transition frequencies and R the Redeld relaxation tensor, or into a QME with the Lindblad form [200],

$$\dot{\rho}_{\rm S}(t) = -\frac{i}{\hbar}[H_{\rm S}+H_{\rm LS},\rho_{\rm S}(t)] + \frac{1}{2}\sum_j \Big([L_j\rho_{\rm S}(t),L_j^\dagger] + [L_j^\dagger,\rho_{\rm S}(t)L_j]\Big), \quad \text{(IV.50)}$$

where $H_{\rm LS}$ is the Lamb-Stark Hamiltonian (discussed in IV.1.7) and L_j are the Lindblad operators which depend on the bath, subsystem and their coupling.

These QME have been successfully applied in different branches of applied physics such as in nuclear magnetic resonance [201] and optical spectroscopy [202].

IV.1.4.2 Stochastic Schrödinger equations

If N is the dimension of the subsystem Hilbert space, the computation of a QME scales with N^2 for the density matrix (see its definition IV.41) and N^4 for the relaxation tensor. As the dimension N is possibly very large, the numerical calculation can become rapidly nontrivial. As an alternative to QME when N is too large, one can use the so-called stochastic Schrödinger equations (SSE) [182, 183, 199, 203]. Because they are based on the evolution of the subsystem wavefunction $|\psi\rangle$, which scales to N, their calculation is considerably more favorable. The basic idea underlying these equations is a Markovian stochastic process designed such as to obtain $\rho_{\rm S}^{\rm QME}(t) = \langle|\psi\rangle\langle\psi|\rangle(t)$. Two main classes of SSE have been developed: the quantum state diffusion [199] and the quantum jump method [183, 203]. The first one is based on the solution of a nonlinear stochastic Schrödinger equation which includes the Lindblad operators. Within the second, the wavefunction is evolved step by step from the combination of a non-Hermitian Schrödinger equation (which also includes the Lindblad operators) and some random jumps to the other accessible states triggered by a Monte Carlo process. For both methods, there is in most cases[53] a direct correspondence between their solution and the solution of the QME (IV.50). Like the QME, they have been successfully applied in the last decade to simple model of systems [184, 197, 174, 203].

[53] Some differences have been observed [197].

IV.1.5 Heisenberg-Langevin equation from a bath of oscillators

Unfortunately, in a number of complex applications, defining the bath/interaction Hamiltonians and calculating the Lindblad operators is rather complicated. To disentangle the situation, some effective approaches are necessary [182, 184]. A simple model of the bath [172, 185, 186] - a thermal ensemble of harmonic oscillators linearly coupled to the subsystem - have proven to be a suitable framework to study Brownian motion.

The so-called Caldeira-Leggett model [185, 186, 182] consists of a Brownian particle linearly coupled to a large number of independent quantum oscillators. The Hamiltonian of the global system then writes,

$$H = \frac{p^2}{2m} + V(x) + \frac{1}{2}\sum_n^N \left(\frac{p_n^2}{m_n} + k_n(x_n - x)^2 \right), \tag{IV.51}$$

where $(x,\, p)$ and $(x_n,\, p_n)$ are the position and momentum operators in the Heisenberg picture of the Brownian particle and the n^{th} bath oscillator respectively, and $k_n = m_n\omega_n^2$ the n^{th} spring constant. The variables are required to obey the Heisenberg commutations

$$[x, p] = i\hbar \qquad and \qquad [x_j, p_k] = i\hbar\delta_{jk}. \tag{IV.52}$$

Using the Heisenberg equations of motion, performing a statistical average over the initial bath variables assumed to be at thermal equilibrium and going to the continuum for the oscillator frequencies lead to the so-called Heisenberg-Langevin (HL) equation for Heisenberg operators at the weak coupling limit:

$$\dot{p} = F(x) - A\,p + F_R(t), \tag{IV.53}$$

where $-A\,p$ is an Ohmic friction operator (A is then a Drag coefficient) and $F_R(t)$ a non-commutating stochastic operator satisfying the correlation

$$\langle F_R(t)F_R(t+\tau)\rangle = \frac{m}{\pi}\int_0^\infty \hbar\omega \left[\coth\left(\frac{\hbar\omega}{2kT_{\text{bath}}}\right)\cos(\omega\tau) + i\sin(\omega\tau)\right] A\, d\omega. \tag{IV.54}$$

The real part of the noise spectrum (IV.54) corresponds to the quantum fluctuation-dissipation theorem and is therefore independent of the bath model [182]. Furthermore, at the classical limit ($\hbar \to 0$) and at the high temperature limit ($T_{\text{bath}} \to \infty$) relation (IV.54) leads to the classical fluctuation-dissipation relation IV.39. Hence, the HL equation reduces to the classical Langevin equation at the classical limit. The properties of the quantum noise (IV.54) will be further discussed in part VI. Within this model, notice that even in the quantum realm the dynamics of a subsystem in interaction with a bath *can be reduced to two straightforward "classical" parameters*: the drag A (inverse relaxation time) and the bath temperature T_{bath}.

In general, the practical application of the HL equation is limited by its non-commutating operator nature. Although questionable [204], a common approximation [205, 206, 207, 208, 209, 210, 211] is to abandon its operator character and to replace the non-commutating q-number noise by a c-number noise while matching its covariance to the real part of the noise spectrum (IV.54):

$$\langle F_R(t)F_R(t+\tau)\rangle = \frac{m}{\pi}\int_0^\infty \hbar\omega \coth\left(\frac{\hbar\omega}{2kT_{\text{bath}}}\right)\cos(\omega\tau)A\,d\omega. \qquad \text{(IV.55)}$$

One then obtains the quasiclassical Langevin equation which leads to a reasonable description for subsystems which are nearly harmonic [205, 209] and to possible violations of the Heisenberg principle [204].

In part VI, we will explore in detail a possible counterpart of the Heisenberg-Langevin equation in the Schrödinger representation, the so-called Schrödinger-Langevin equation, which is more suited for our analysis.

IV.1.6 Other frameworks

Numerous other frameworks and non-standard quantization procedures have been proposed to overcome the initial subsystem quantization difficulty without considering the whole system. It includes for instance effective time dependent Hamiltonians [190, 191], stochastic mechanics quantization [177, 187], new variational principle for dissipative system [192], complex Hamiltonian [189], fluid interpretation of the Schrödinger equation[54] (Bohmian mechanics) [195, 196]... Though connections exist between them and with the QME, they have led to different equations of dissipative evolution...

IV.1.7 Long time behaviour and equilibrium

Generally, the equations of evolution that we have introduced in the previous sections IV.1.1, IV.1.4 and IV.1.5 are expected to bring the subsystem in thermal equilibrium with the heat bath.

In the classical realm, it can be shown that for a general potential the classical Langevin equation (IV.37) and equivalent Fokker-Planck equation lead the probability density for the subsystem position and momentum to the canonical (Maxwell-) Boltzmann density distribution[55] [212, 213],

$$F(x,p,T_{\text{bath}}) = \frac{1}{Z}\exp\left(-\frac{H(x,p)}{kT_{\text{bath}}}\right), \qquad \text{(IV.56)}$$

where $H(x,p) = p^2/2m + V(x)$ is the subsystem classical Hamiltonian and Z the partition function (a normalisation factor).

[54] Discussed in part VI

[55] If the process (x(t),p(t)) is Markovian and the probability density distribution $f(x,p,t)$ satisfies the Kramers equation, the unique stationary solution is the Maxwell Boltzmann distribution.

In the quantum realm where the energy states are quantified, the open quantum system framework predicts that the system-reservoir coupling can modify the energy spectrum of $H_{\rm S}$ [184, 197, 213]. Indeed, in equation (IV.50), the Lamb-Stark Hamiltonian $H_{\rm LS}$ induces small shifts of the unperturbed energy levels and the dissipative part induces a broadening of the spectral lines indicating a finite lifetime for the excited states due to the dissipation. At the weak coupling limit, these spectrum modifications are negligible and the subsystem density matrix at thermal equilibrium is expected to be,

$$\lim_{t\to\infty} \rho_{\rm S} = \frac{1}{Z} \exp\left(-\frac{H_S}{kT_{\rm bath}}\right) = \frac{1}{Z} \sum_{n=1}^{N} \exp\left(\frac{-E_n}{kT_{\rm bath}}\right) |\psi_n\rangle\langle\psi_n|, \qquad \text{(IV.57)}$$

where the $\{E_n\}_{n=1...N}$ and $\{\psi_n\}_{n=1...N}$ are the usual eigenenergies and states of the unperturbed subsystem Hamiltonian $H_{\rm S}$. The equilibrium density matrix (IV.57) is the general stationary solution of the quantum master equations at the weak coupling limit [184]. On its side, the ability of the Heisenberg-Langevin equation to bring a subsystem to the equilibrium distribution (IV.57) has only been demonstrated for the free and harmonic potential $V(x)$ [172, 212].

To conclude this brief discussion on open quantum systems, there is no universal description of quantum subsystems in interaction with a heat bath and the formalism should be adapted to each situation. If the interaction/bath can be defined and the trace operation performed without too many approximations, the framework of quantum master equations or stochastic Schrödinger equations should be the most rigorous. If not, more effective approaches are required and one can explore for instance the Heisenberg-Langevin framework.

IV.2 Quarkonia as classical and quantum dynamical systems

IV.2.1 Dynamical quarkonia suppression in the literature

The multiple direct interactions between the $Q\bar{Q}$ pairs and the medium particles are usually described through either a cross-section, an imaginary potential, a semi-classical or an open quantum system framework.

IV.2.1.1 Cross section and imaginary potential approaches

As already discussed in sections II.2.1.3 and II.4.2, the cross-section approach is based on the hard gluo-dissociation of the quarkonium states. The knowledge of the corresponding inelastic cross sections leads to the evaluation of the reaction rates for dissociation and formation which are commonly used by transport models to continuously flip between quarkonia and "free" $Q + \bar{Q}$ (see section II.2.2.2). However, the effects of the multiple (non-dissociative) interactions with the medium are not

considered.

From thermal field theory, Laine et al. [121] have derived a Schrödinger-type equation for the correlator of a decaying $Q\bar{Q}$ pair that takes into account the medium direct interaction with the quarkonia states. This Schrödinger-type equation exhibits an effective potential with a real part, for the usual Debye screening, and an imaginary part which translates the thermal effects. The temperature dependent imaginary part generates finite widths for the quarkonium states and thus their thermal decay in the plasma. An imaginary contribution to the potential has also been derived within other frameworks, such as non relativistic heavy quark effective theories (NRQCD at finite temperature) [214, 215] and lattice QCD [216]. The real and imaginary potential is commonly used within the anisotropic hydrodynamics model (aHYDRO) to describe quarkonia suppression [217, 218]. In this model, the quarkonia are assumed to be mainly influenced during their formation time (< 1 fm/c) and one therefore focuses on their propagation in the early-time strongly anisotropic QGP. In practice, the stationary 3D Schrödinger equation is solved to obtain the real and imaginary parts of the binding energy for each state. One then integrates the corresponding non-equilibrium decay rate over the lifetime of the state in the plasma as a function of its position and transverse momentum. Some aHYDRO predictions have already been presented in section II.3. Nevertheless, note that it assumes the bound states to be already formed, which is not obvious in such an early stage of the collision.

For both cross-section and imaginary approaches, the possible transitions between bound states are not considered although they might play a significant role as demonstrated in part III. Furthermore, as in the sequential suppression picture, the evolution of the quarkonia is assumed to be adiabatically slow, such that the $Q\bar{Q}$ pair remains in the corresponding bound state at whole time. This assumption may not hold if the binding potential evolves rapidly with the cooling QGP, leading to possible transitions between eigenstates [219]. In our view, a full dynamical description of the $Q\bar{Q}$ evolution - and not only of its bound states - is preferable. Finally, note that the imaginary part of the potential cannot be introduced in the Hamiltonian of our mean field model developed in part III. It would indeed lead to a non-unitary evolution of a pure state, i.e. to the disappearance of the $Q\bar{Q}$ pair.

IV.2.1.2 Semi-classic approaches

Because of their large mass, the heavy quark and antiquark of the pair can be seen as non-relativistic classical Brownian particles. Indeed, their typical De Broglie wavelength at thermal equilibrium, $\lambda \sim \frac{1}{\sqrt{M_Q T}}$, is smaller (but not much smaller) than the typical inter particle distance of the medium particles $\sim 1/T$. The heavy quarks might therefore be seen as classical particles. Furthermore, as $M_Q \gg T$ a collision between one of the heavy quarks and a medium particle leads to a change of its momentum $\Delta p_Q \sim T$ momentum, so that its change of velocity is $\Delta v_Q \sim T/M_Q \ll 1$. Hence, many collisions are required to change significantly

its velocity. It guarantees that the heavy quark relaxation time is much larger than the typical collision time and the clear separation between the different typical time scales required by the Langevin framework is satisfied (see IV.1.1). Finally, because the correlation length in the medium should be much smaller than the distance between the heavy quarks, the collisions on each heavy quark can be treated as uncorrelated [2]. One of the main difficulties that arises from the classical treatment of the $Q\bar{Q}$ pair is the connection between point-like Q and $\bar{Q}$ particles and the quantum nature of their bound states. In other words, how to translate the quantum properties of a bound state in a (semi-)classical formalism ?

To get around this problem, Young and Shuryak first proposed a semi-classical framework based on Wigner distributions [2]. In this framework, a collection of "test" particles is initially distributed according to a phase-space distribution given by the Wigner transformation of the $Q\bar{Q}$ initial state. The test particles are then evolved with the usual Langevin dynamics. Finally, to obtain the real-time population of the different bound states, the distribution of test particles is convoluted with the phase-space distributions of the bound states. This approach will be further discussed in part V and applied to our model. Very recently, Blaizot et al. have proposed a more elaborated Langevin dynamics where the friction and stochastic force depend explicitly on the configuration of the $Q\bar{Q}$ pair [220]. This dependence is derived from a subsystem plus reservoir development where the coupling between plasma light quark/antiquark fields (reservoir) and with the heavy quarks (subsystems) are Coulombic. The plasma degrees of freedom at thermal equilibrium are traced out through a path integral technique and some approximations at the weak coupling limit. One can note however that in this exploratory work, the connection between the classical particles and the quantum states is less sophisticated than in [2], i.e. restricted to some simple and imprecise criteria on binding energy and relative distance. As a possible pitfall for these semi-classical approaches, in part V we will see that the thermalisation of classical particles (given by IV.56) does not necessarily imply the thermalisation of quantum states (as given by IV.57).

IV.2.1.3 Open quantum systems

Because of the deep quantum nature of the $Q\bar{Q}$ states, one should look for a more appropriate framework. A correlated $Q\bar{Q}$ pair can be seen as a small quantum subsystem in interaction with the surrounding medium made of light quarks and gluons at thermal equilibrium. The latter can transfer energy and momentum to the $Q\bar{Q}$ pairs without being affected too significantly: it can be seen as a heat bath whose detailed dynamics is irrelevant. The open quantum systems, discussed in section IV.1, then provides a natural framework. Several approaches have been explored so far, namely 1) the reduced density matrix in path integral [221, 222], 2) the Pauli rate equation [223] and 3) the stochastic potential [224].

1) Young and Dusling have first used the Caldeira-Leggett Hamiltonian (IV.52) to determine the propagation of heavy quark/antiquark system coupled to a

bath of harmonic oscillators [221]. It leads to a reduced density matrix for the $Q\bar{Q}$ pair expressed as an imaginary-time path integral. Using the Cornell potential for the $Q\bar{Q}$ binding, the integral is solved numerically to show how dissipative effects could affect the correlators of quarkonium spectroscopy. However, the dynamics of the pair internal d.o.f is hardly accessible through this method. Recently, Akamatsu has proposed a more refined model based on first principles [222]. Similarly to Blaizot et al., the derivation of the reduced density matrix is carried out within a closed-time path integral formalism. He applies this formalism to thermal QCD at the leading-order in the non-relativistic and weak coupling limits. A correlator is derived and leads to the imaginary potential found by Laine et al. (see section IV.2.1.1). A master equation with the Lindblad form (IV.50) can also be derived [225]. The qualities of this work are undeniable (derivation from first principles, rigorous open quantum system framework...) but its actual application to quarkonia suppression seems entangled and might still require a lot of work (not tangible terms, large rank density matrix...).

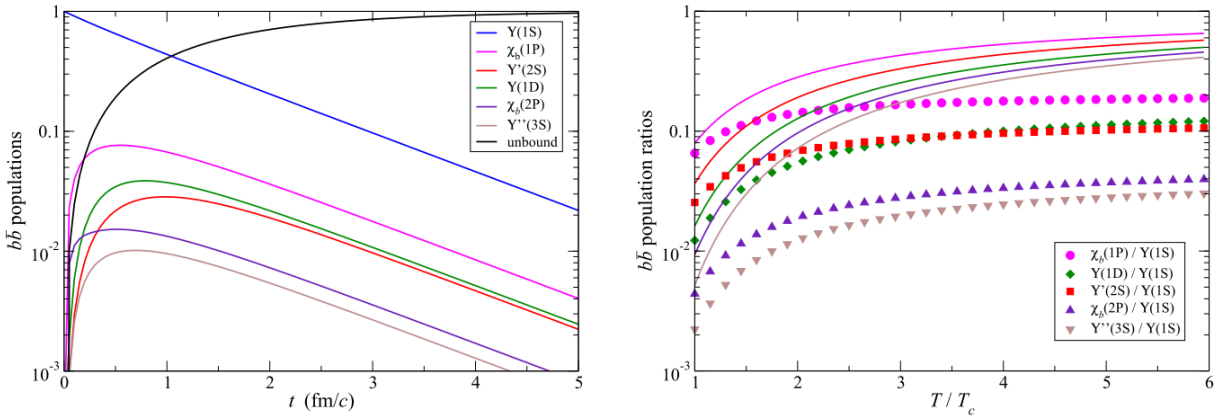

Figure IV.2: *Left*: Evolution of the bottomonium populations obtained with Borghini and Gombeau's Einstein master equation IV.58 in a thermal bath at $T = 5T_c$ with $T_c = 170$ MeV. *Right*: Comparison between the ratios of bottomomium populations as a function of temperature obtained with master equation IV.58 (symbols) and with expected Boltzmann behaviour (lines) [223].

2) Borghini and Gombeaud [223] have proposed an alternative phenomenological approach based on the Pauli (or Einstein) master equation,

$$\frac{d\rho^{\mathcal{S}}_{ii}}{dt}(t) = -\sum_{k\neq i} \Gamma_{i\to k}\, \rho^{\mathcal{S}}_{ii}(t) + \sum_{k\neq i} \Gamma_{k\to i}\, \rho^{\mathcal{S}}_{kk}(t) \tag{IV.58}$$

where $\rho^{\mathcal{S}}_{ii}$ is the population of the i^{th} quarkonium and $\Gamma_{i\to k}$ the transition rate from the state i to k. The set of transition rates is evaluated from Fermi's golden rule and a dipolar interaction between the $Q\bar{Q}$ and a gluonic vector field seen as a bath of oscillator at thermal equilibrium. The $Q\bar{Q}$ pair mutual interaction is taken as a vacuum Coulombic potential. At constant temperatures and after a transient phase, the populations are observed to decrease exponentially with a common decay rate (see left panel on figure IV.2). Furthermore,

as shown in the right panel, the quasi-equilibrium distributions obtained at some time t after the transient phase are not Boltzmann distributed (relation IV.57). This discrepancy originates from their difficulty in modeling the continuum of free states, whereas the correct transitions between bound and free states are necessary.

3) Akamatsu and Rothkopf have proposed a stochastic potential approach [224]. By including a white stochastic term in the usual unitary evolution operator, they derive a tractable master equation in which the spatial correlation of the stochastic term shows up as an imaginary potential. The presence of the noise term leads to spatial decoherence and exponential suppression of the ground states (see figure IV.3). Unfortunately, due to the absence of a friction term, this model is unable to thermalise the states and leads to a linearly increasing energy and to uniform state populations after a transient phase.

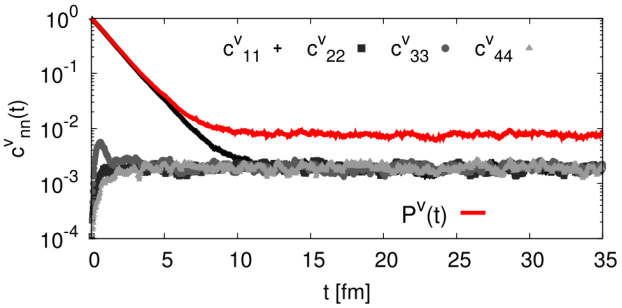

Figure IV.3: Populations of quarkonium states (c^v_{nn}) obtained with the vacuum potential and the stochastic model based on lattice QCD parameters [224].

The descriptions of quarkonia as open quantum systems developed so far are thus either rigorous but hardly applicable to phenomenology or more effective but unable to thermalise the inner dynamics. This quest is therefore quite recent and still open to new ideas.

IV.2.2 Langevin-like approaches and overview of the next parts

In this section, we wish to justify and discuss the approach that we have chosen to follow in the next parts. Because of the quantum nature of the bound states, a quantum description of the $Q\bar{Q}$ pair is necessary in our view. The open quantum system framework should then be appropriate to study its real-time dynamics. Unfortunately, its rigorous derivation within the subsystem plus bath approach is quite entangled[56] - due to the complexity of the QGP/quarkonia interaction and of the dynamic QGP itself - and hardly applicable to the quarkonia phenomenology. As a result, we have looked instead for an effective approach suitable for phenomenology: easy to implement in a realistic collision scenario, which guaranties the transitions

[56]The recent developments from Akamatsu discussed in IV.2.1.3 could nevertheless rule against this opinion.

between bound states and with the free states, and capable to thermalise the $Q\bar{Q}$ internal d.o.f. Motivated by the non-relativistic Brownian nature of the heavy quarks in a pair[57] and by the availability of Drag coefficients for single heavy quarks diffusion[58] (see section V.2.1), we have headed toward some semi-classical and quantum Langevin-like approaches at the weak coupling limit. One could then obtain a unified description of the $Q\bar{Q}$ pair inner dynamics and single heavy quarks propagation. The quantum $Q\bar{Q}$ pair can then be seen as subject to three forces: i) the drag force which accounts for energy dissipation, (ii) the stochastic force which mocks the dense collisions with the medium and (iii) the screened mutual interaction of the $Q\bar{Q}$ pair as in part III. Inspired by Young and Shuryak work IV.2.1.2, we have first focused on a semi-classical approach based on classical Langevin evolution of Wigner distributions (next part V). Nevertheless, its severe limitations urged us to look for a full dynamical quantum approach. We have then focused on a Langevin-like extension of the fundamental Schrödinger equation, the so-called Schrödinger-Langevin equation, which can be seen as the counterpart of the Heisenberg-Langevin equation (see section IV.1.5) in the Schrödinger representation. We have first studied its general properties as a sanity check (part VI) and then applied it to the $Q\bar{Q}$/QGP system within a simplified model (part VII).

[57] See section IV.2.1.2.

[58] The knowledge of the Drag - for single heavy quarks diffusion in the QGP - allows to reduce the dissipative dynamics at a mesoscopic scale into a single parameter.

Part V

Semi-classic approach

As a first attempt to assess the effects of direct thermal forces, we investigate a semi-classical framework initially proposed by Young and Shuryak [2]. It is based on a Wigner description of the correlated $Q\bar{Q}$ pair and the classical Langevin dynamics. As for the mean field case (part III), we only consider the internal degrees of freedom of the $Q\bar{Q}$ pair immersed in a homogeneous and infinite thermal QGP. Our approach within this part is illustrated in figure V.1. The semi-classical approach is first introduced without Langevin dynamics in section V.1.1. The related results are discussed in section V.1.2 and compared to the quantum results of part III. Next, in section V.2, the semi-classical approach with Langevin dynamics is introduced and the related results on direct J/ψ suppression at constant temperatures, or with RHIC and LHC scenarios, are presented. Note that these results have been published in a conference proceeding [226]. However, in section VI.1.2, we discuss their veracity through a critical review of the semi-classical formalism. Finally, in section V.3, we briefly discuss a related formalism that we have also explored, namely the Wigner-Moyal equations with quantum Fokker-Planck terms.

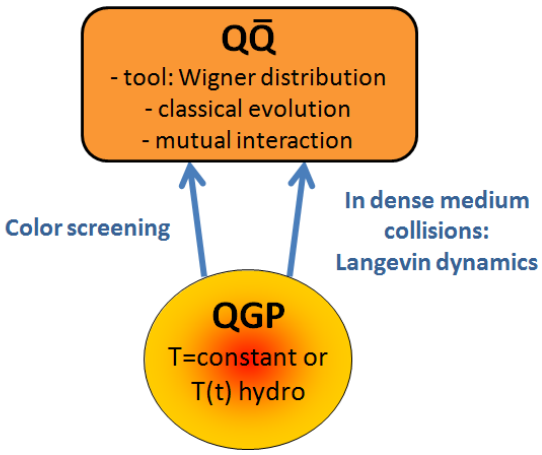

Figure V.1: Illustration of our approach within this part through its basic ingredients and interactions between the $Q\bar{Q}$ and QGP systems.

"Only the one who does not question is safe from making a mistake."
— Albert Einstein[59] —

[59]From a letter to Gustav Bucky, 1945. AEA 037462

V.1 The semi-classical model without Langevin dynamics

V.1.1 Wigner transformation and Wigner-Moyal equation

In usual quantum mechanics, the $Q\bar{Q}$ pair probabilistic information is described by a wavefunction Ψ, whose evolution is given by the Schrödinger equation. Equivalently the $Q\bar{Q}$ pair can be described by a phase space distribution called the Wigner distribution $F_{Q\bar{Q}}\left(\vec{r},\vec{p},t\right)$, derived from the Wigner transformation of the wavefunction [227]:

$$F_{Q\bar{Q}}\left(\vec{r},\vec{p},t\right)=\int e^{\frac{i\vec{p}\cdot\vec{r'}}{\hbar}}\psi^{*}_{Q\bar{Q}}\left(\vec{r}+\frac{\vec{r'}}{2}\right)\psi_{Q\bar{Q}}\left(\vec{r}-\frac{\vec{r'}}{2}\right)d\vec{r'}. \tag{V.59}$$

For instance, the radial Gaussian wavefunction

$$R_{Q\bar{Q}}(r,t=0)=\left(\frac{1}{\pi\sigma^{2}}\right)^{3/4}e^{-\frac{r^{2}}{2\sigma^{2}}}, \tag{V.60}$$

becomes the Gaussian Wigner distribution in both radial position and radial momentum space,

$$F_{Q\bar{Q}}(r,p,t=0)\propto e^{-\frac{r^{2}}{2(\frac{\sigma}{\sqrt{2}})^{2}}}e^{-\frac{p^{2}}{2(\frac{\hbar c}{\sqrt{2}\,\sigma})^{2}}} \tag{V.61}$$

where one can define the Gaussian parameters of the Wigner distribution: $\sigma_{r}^{WT}=\frac{\sigma}{\sqrt{2}}$ for the position part and $\sigma_{p}^{WT}=\frac{\hbar c}{\sqrt{2}\,\sigma}$ for the momentum part.

The evolution of the Wigner distribution is given by the Wigner transformation of the Schrödinger equation called the Wigner-Moyal equation (in relative coordinates) [227]:

$$\left[\left(\frac{\partial}{\partial t}+\frac{\vec{p}}{m}\cdot\frac{\partial}{\partial\vec{r}}\right)-\frac{2}{\hbar}\sin\left(\frac{\hbar}{2}\frac{\partial}{\partial\vec{p}}\cdot\frac{\partial}{\partial\vec{r}}\right)V\left(\vec{r}\right)\right]F_{Q\bar{Q}}\left(\vec{r},\vec{p},t\right)=0, \tag{V.62}$$

where m is the reduced mass and the spatial derivative in the sine term acts only on the mean field potential $V\left(\vec{r}\right)$ only. The Wigner-Moyal equation has two main advantages over the usual Schrödinger equation. First, one can easily include some thermal terms by analogy with the Fokker-Planck equation (see section V.2). Second, the connection between classical and quantum mechanics is more comprehensible. Indeed at the (semi-)classical limit, i.e. $\hbar\to 0$, one obtains the classical Wigner Moyal equation (V.63), equivalent to the Liouville equation, by expanding the sine term to the first order in $\hbar$.

$$\left[\left(\frac{\partial}{\partial t}+\frac{\vec{p}}{m}\frac{\partial}{\partial\vec{r}}\right)-\frac{\partial}{\partial\vec{p}}\frac{\partial}{\partial\vec{r}}V\left(\vec{r}\right)\right]F_{Q\bar{Q}}\left(\vec{r},\vec{p},t\right)=0. \tag{V.63}$$

To evaluate the probability of the $Q\bar{Q}$ pair to bind as a specific quarkonium state at hadronisation, one needs to project its Wigner distribution onto the corresponding

quarkonium Wigner distribution. For instance, in the case of the J/ψ state, the projection writes:

$$W_{J/\psi}(t) = \int F_{Q\bar{Q}}\left(\vec{r},\vec{p},t\right) F_{J/\psi}\left(\vec{r},\vec{p}\right) \frac{d^3\vec{p}d^3\vec{r}}{\left(\hbar c\right)^3}., \tag{V.64}$$

with both distributions normalized to unity.

The semi-classical formalism therefore includes the quantum Wigner distribution (equation V.59) of the $Q\bar{Q}$ pair, which is evolved with the classical Wigner-Moyal equation (V.63), and projected onto the vacuum quarkonium states at hadronisation (equation V.64). This semi-classical approach allows an easy access to numerical simulations through the practical use of the test particles method. In the latter, one reproduces the 3D Wigner distribution with a large set of N test particles which are sampled according to equation (V.61) at initial time and which are then evolved with Newton's laws (see [228] for more details). The projection on the vacuum quarkonium states is then given by

$$P_{J/\Psi}(t) = \frac{1}{N}\sum_{i=1}^{N} F_{J/\Psi}\left(r_i(t),p_i(t)\right), \tag{V.65}$$

the test particles version of (V.64), where $r_i(t)$ and $p_i(t)$ are, respectively, the instantaneous position and momentum of the i^{th} test particle. In the following sections, we focus on the normed weight $P_{J/\Psi}(t)/P_{J/\Psi}(0)$, equal to the survivance defined in the mean field part III (which corresponds to a R_{AA}-like value at hadronisation). For the numerical resolution, we use the Runge-Kutta fourth-order method which has proven to be reliable for these evolutions.

Because in this study we are only interested in S states, the $\psi_{Q\bar{Q}}(\vec{r},0)$ initial wave-function can be reduced to its radial part. As in part III, the initial radial wave-function is taken as a Gaussian wavepacket with Gaussian parameter $\sigma = 0.165$ fm. The corresponding parameters for the initial Wigner distribution are $\sigma_r^{WT} = 0.1167$ fm and $\sigma_p^{WT} = 0.844$ GeV/c. For the screened $Q\bar{Q}$ mutual interaction, we mainly choose the strong potential $U(\vec{r},T)$ (see section III.1.1 for more details). The internal energy is indeed better suited for this study as it does not include any energy exchange between the pair and the medium: a redundancy with the thermal forces is thus avoided. The results with the weak potential V_{weak} are also given for comparison.

V.1.2 Mean field evolutions with the semi-classical and quantum models

In order to check the limits of the semi-classical approximation without Langevin dynamics (i.e. only with color screened binding potentials), we compare the evolutions obtained from the semi-classical approach and the time-dependent Schrödinger equation (which leads to the correct evolutions already described in part III). As shown in figure V.2, in the free case (i.e. $V = 0$), the J/ψ weights are identical.

It is expected from the Erhenfest theorem which states that classical and quantum observables are similar when the potential changes slowly in comparison to the wavefunction size [229].

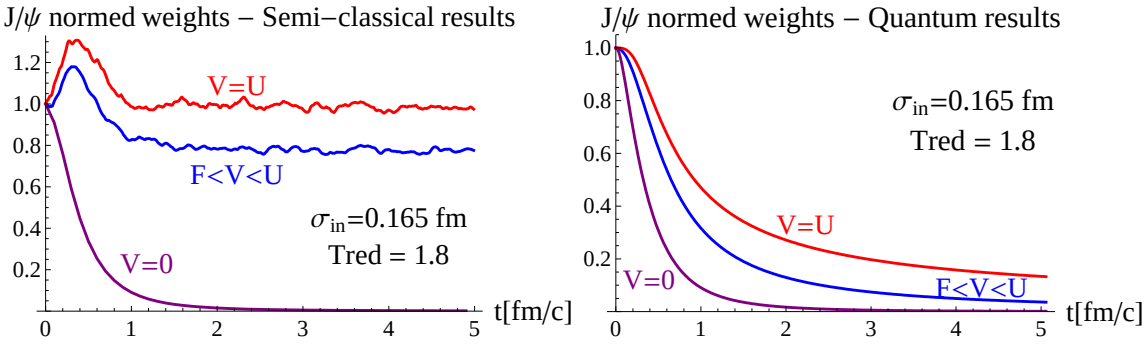

Figure V.2: *Left*: Semi-classical results for the J/ψ weights function of time at a fixed temperature $T_{\rm red} = 1.8$ ($T = 297$ MeV). *Right*: Quantum results for the same situation.

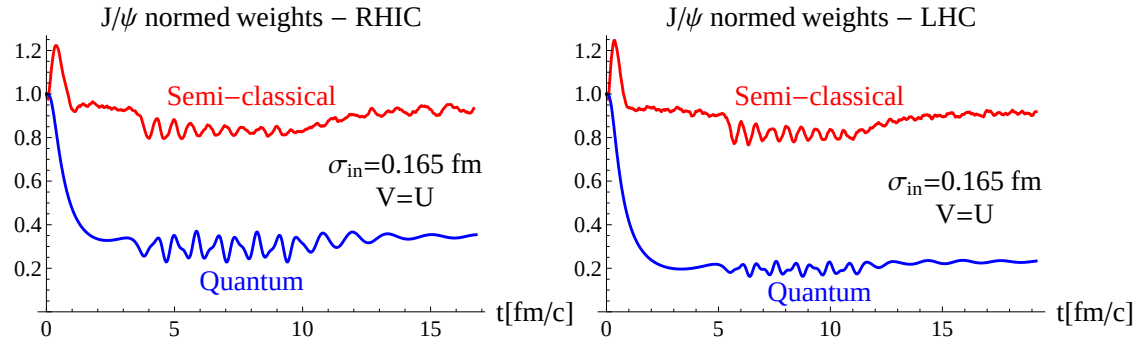

Figure V.3: Semi-classical and quantum results for the J/ψ weights function of time with RHIC (*left*) and LHC (*right*) temperature scenarios (see III.1.2).

However, as illustrated in figures V.2 and V.3, and expected from the Erhenfest theorem statement, important discrepancies appear with a binding potential: With the semi-classical approach, one observes some overshoot for $t < 1$ fm/c and a difficulty to reach the continuum (the J/ψ normed weight remains close to unity) at larger times. Note that in [2], the overshoot was explained by a rapid narrowing of the distribution in momentum space due to 1) a drag coefficient larger than the diffusion coefficient and 2) an initial momentum distribution larger than the thermal momentum distribution[60]. Because it is also observed without Langevin dynamics, their explanation is partly mistaken. The observation of the test particle paths in phase space rather shows that it is due to their momentum loss while climbing the potential barrier (which makes some of them enter the "J/ψ phase space zone"). As a positive point, note also that the semi-classical formalism partly reproduces the oscillations between eigenstates observed with the quantum formalism[61]. Note

[60] In other words, because the drag is much larger than the diffusion coefficient, the test particles are first slowed down to reach thermal velocities, which increases the J/ψ weight, and then diffuse spatially, which decreases the J/ψ weight.

[61] These oscillations are due to the high asymptotic values of the potential when $5 \lesssim t \lesssim 12$ fm/c. See section III.4 for more details.

finally that despite a difference of temperature of around 80 MeV between RHIC and LHC scenarios, the semi-classical formalism gives similar results for both. Consequently, if the Langevin dynamics does not drive the evolution, the validity of the semi-classical results with Langevin dynamics (section V.2 and [2]) is clearly questionable.

V.2 The semi-classical model with Langevin dynamics

V.2.1 Additional Fokker-Planck terms

A phenomenological way to take into account the thermalisation of the $Q\bar{Q}$ pair in this dynamical model is to consider the random interactions between the $Q\bar{Q}$ pair and the QGP constituents. By analogy with the Fokker-Planck equation of motion in momentum space (equivalent to Langevin forces), we introduce additional stochastic terms in the Wigner Moyal equation:

$$\left[\left(\frac{\partial}{\partial t}+\frac{\vec{p}}{m}\cdot\frac{\partial}{\partial\vec{r}}\right)-\frac{2}{\hbar}\sin\left(\frac{\hbar}{2}\frac{\partial}{\partial\vec{p}}\cdot\frac{\partial}{\partial\vec{r}}\right)V\left(\vec{r}\right)\right]F_{Q\bar{Q}}\left(\vec{r},\vec{p},t\right)=\vec{\nabla}_p\left(A\vec{p}F_{Q\bar{Q}}+\vec{\nabla}_p(D_vF_{Q\bar{Q}})\right), \tag{V.66}$$

where A and D_v are parameters described below. In the limit $\hbar\to 0$, this equation is equivalent to the approach adopted in [2]. Within the frame of the test particle method, the right-hand side of equation (V.66) is then equivalent to additional Langevin forces introduced in Newton's equation of motion:

$$\frac{d\vec{p}}{dt}=-\vec{\nabla}V(\vec{r})-A\,\vec{p}+\vec{\xi}(\vec{r},t) \tag{V.67}$$

The stochastic force $\vec{\xi}$ is defined by $\langle\vec{\xi}\rangle$=0 and $\langle\xi_i(t)\xi_j(t')\rangle = B\delta_{i,j}\delta$(t-t') (fluctuations are uncorrelated over time). The friction/dissipative term is $-A\,\vec{p}$ where A is the well known drag coefficient. The Einstein relation can then be deduced from quadratic and average momentum calculations [230], and the momentum diffusion coefficient D_v related to B (see section IV.1.1):

$$D_v=\frac{B}{2}=mTA \tag{V.68}$$

For the purpose of comparison, we present the results obtained from equation (V.66) in the $\hbar\to 0$ limit, both with the drags for single heavy quarks propagation from Gossiaux and Aichelin A[c/fm] $\cong 2(1.5T[\text{GeV}]+1.25T^2)$ [231] and from Young and Shuryak $A=4\pi T^2/(3\hbar cm)$ [2, 118] (see figure V.4). They originate from calculations of collisional energy loss of a single heavy quark in a partonic medium. The former drag has been evaluated through microscopic $2\to 2$ processes and a fit to experimental D-meson R_{AA} and v_2 data (which gives the factor 2). Note that diffusion coefficients have also been evaluated from lQCD [232, 233] and DQPM[62] [234].

[62]Dynamical Quasiparticle Model.

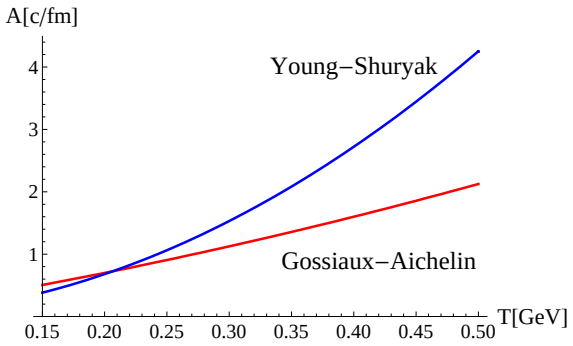

Figure V.4: Comparison between Gossiaux and Aichelin [231] and Young and Shuryak [2, 118] drag dependences on the temperature.

V.2.2 Evolutions at constant temperatures

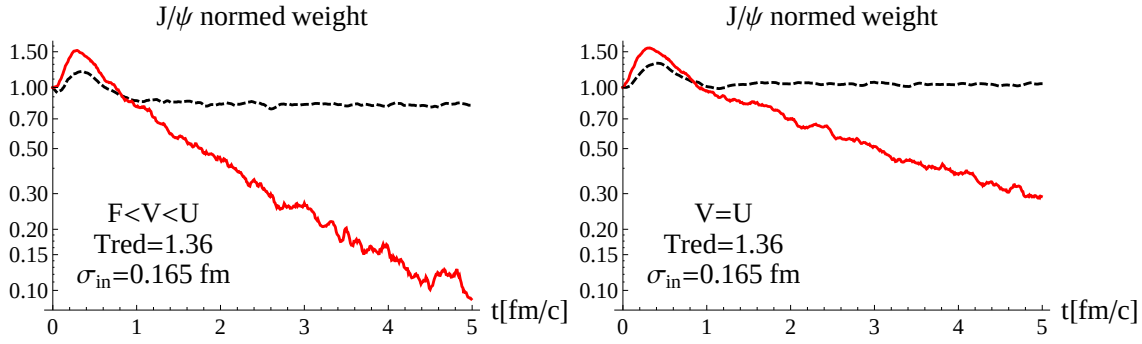

Figure V.5: Semi-classical results for the J/ψ weights function of time at a fixed temperature $T_{\rm red} = 1.36$ ($T = 225$ MeV) with the Langevin dynamics (drag coefficient from Gossiaux and Aichelin). *Left*: with the weak potential $F < V < U$ and *right*: with the strong potential $V = U$. Dashed lines: results without Langevin dynamics.

As shown in Fig.V.5, the additional Langevin dynamics leads to an actual evolution of the J/ψ weights that was missing in section V.1.2. On the one hand, one observes an enhancement of the overshoot for $t < 1$ fm/c, indeed explained this time by the rapid "thermalisation" of the distribution in momentum space (see explanation provided in section V.1.2). On the other hand, it helps the test particles to reach the continuum, i.e. to escape the range of the binding potential. The J/ψ weight indeed decreases exponentially from $t \gtrsim 1$ fm/c on, showing the continuous decay of the bound component[63] of the $c\bar{c}$ pair. The continuous decay originates from the spatial diffusion of the distribution towards large distances due to the Langevin dynamics. The decay rate is observed to increase with the temperature and is logically larger with the weak potential than with the strong potential (for which the binding energy is larger).

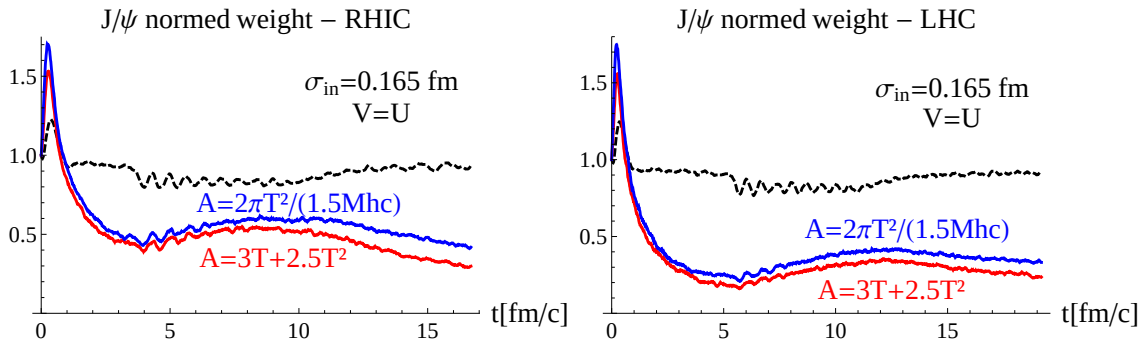

Figure V.6: *Left*: Semi-classical results for the J/ψ weights function of time with RHIC temperature scenario, $V = U$, and Langevin dynamics (plain lines); dashed line: same without Langevin dynamics. *Right*: Same but with LHC temperature scenario.

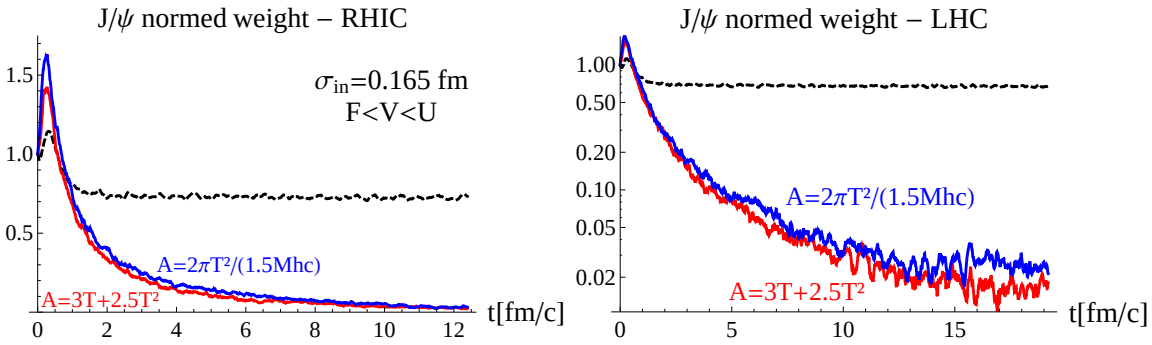

Figure V.7: *Left*: Semi-classical results for the J/ψ weights function of time with RHIC temperature scenario, $F < V_{\text{Weak}} < U$, and Langevin dynamics (plain lines); dashed line: same without Langevin dynamics. *Right*: Same but with LHC temperature scenario (semi-log plot).

V.2.3 Evolutions at RHIC and LHC

We now include in the model the hydrodynamic scenarios of temperature at RHIC and LHC as described in section III.1.2. The evolutions of the J/ψ weight with the weak and strong potentials are shown in figures V.6 and V.7 respectively. The first thing to notice is that one obtains an actual dynamical evolution: The $c\bar{c}$ pair is clearly not decorrelated instantaneously and the evolution is strongly non-adiabatic. One can then observe that the suppression is more important at LHC than at RHIC. The higher temperature at LHC indeed leads to a larger diffusion coefficient and to a more important screening. Next, one can note that from $t \gtrsim 5$ fm/c, the light J/ψ weight variations follow the important variations of the strong potential asymptotic value $U(r \to \infty, t)$ (see figure III.6): high asymptotic values lead to a narrowing of the spatial distribution whereas low asymptotic values to its spatial diffusion. The features of the weak potential screening logically induces a larger diffusion of the $c\bar{c}$ distribution resulting to a continuously shrinking exponential decay rate as the QGP cools down. Last, the two drag coefficients give similar evolutions with a difference

[63] By bound component of the $c\bar{c}$ pair we mean the component of the distribution that remains inside the phase space area of the bound states

of ~ 0.1 at the freeze out with the strong potential and negligible with the weak potential. As a robustness test, a variation of the initial wavepacket parameter of ± 0.01 fm/c (12%) leads to a maximum normed J/ψ weight deviation of 0.03 (8%) at the freeze out.

All together, this shows that the stochastic forces have a significant role both for stationary and for dynamical QGP.

V.2.4 Comparison with data

The survivances of the J/ψ component at the chemical freeze out with the semi-classical formalism and strong potential are summed up in table V.8, and compared to some extent to pure quantum results and experimental data. Of course the comparison to data may not be taken too seriously as we have not considered other effects such as cold nuclear matter effects (see II.2.1.1), feed downs from other quarkonia (see figure I.10)... Because of a small possible statistical recombination at RHIC (see II.3), the color-screening effects for charmonia are expected to be relatively more important there. Then, at RHIC our predicted value (0.5) should be compared to the low p_T data (0.26) where most of the charmonia are detected. Including the other effects would mostly lower our results in general and have thus a rather positive impact on our prediction at RHIC as we overestimate it. Note that Young and Shuryak [2] also found a suppression of 0.5 with a different parametrisation. At LHC, as the statistical recombination should be important at low p_T one should compare our result (0.32) to the high p_T data (0.20). Once again, including the other effects should therefore have a positive impact on our prediction at LHC.

	Semi-classical		Quantum		Experimental R_{AA}	
Langevin dynamics ? $\rightarrow$	No	Yes	No	Yes	high p_T	low p_T
RHIC	0.83	0.52	0.3	?	0.64 $\pm$0.14	0.26 $\pm$0.05
LHC	0.81	0.32	0.19	?	0.20 $\pm$0.03	0.83 $\pm$0.14

Table V.8: J/ψ normed weights at the chemical freeze out (or average over the mixed phase if weight oscillations) obtained at RHIC and LHC with the strong potential $V = U$. — RHIC AuAu $\sqrt{S_{NN}} = 200$ GeV collisions: 1) high p_T STAR data [134] (inclusive (prompt and non prompt) J/ψ, $5 < p_T < 14$ GeV/c, $|y| < 1$ and 0-10% centrality) and 2) low p_T PHENIX data [133] (inclusive J/ψ, $p_T < 5$ GeV/c, $|y| < 0.35$ and 0-5% centrality). The non prompt contribution is estimated to 10-25% of the inclusive production. — LHC PbPb $\sqrt{S_{NN}} = 2.76$ TeV collisions: 1) high p_T CMS data [138] (prompt J/ψ, $6.5 < p_T < 30$ GeV/c, $|y| < 2.4$ and 0-10% centrality) (inclusive J/ψ: $R_{AA} = 0.24 \pm 0.03$) and 2) low p_T ALICE data [137] (inclusive J/ψ, $0 < p_T < 8$ GeV/c, $|y| < 0.9$ and 0-10% centrality).

V.2.5 A critical post-review of the semi-classical results

We would like now to discuss the reliability of the results obtained with the semi-classical formalism as done so far by [2] and us (in [226] as well as in this manuscript).

In section V.1.2, we first pointed out that the "ballistic" evolutions given by the semi-classical formalism without the Langevin dynamics and the Schrödinger equation are very different. Nevertheless, if the diffusion is the leading ingredient of the full evolution (what seems to be the case for the $c\bar{c}$ pairs), it is likely that the effects of these discrepancies are finally small. However, later investigations brought us to question the semi-classical formalism even more:

• It is important to note that we have never tested whether the bound components of the $c\bar{c}$ pair actually thermalises with the bath. To do so, one should perform an evolution of the $c\bar{c}$ pair distribution at constant temperature T, project at a certain $t \gg \tau_{\rm relax}$ the distribution onto several bound states (J/ψ, ψ', ψ''...) and check if the resulting distribution of weights corresponds to a Boltzmann distribution with the bath temperature T. In their paper [2], Young and Shuryak did not investigate this question either. In order to add the feed-down contributions to the J/ψ yield, they just assumed (from experimental observations at SPS) that the ratio between bound states is proportional to $\exp(-\Delta m/T)$, where Δm is the mass difference between considered states.

• We have nevertheless investigated the properties of the semi-classical formalism in a simpler situation: the 1D harmonic oscillator. In this case, one can actually show [235] that the Wigner-Moyal equation (V.62) is identical to the classical Wigner-Moyal equation (V.63). For this specific potential, one has thus the possibility to test the "exact" equation (V.66) by applying the semi-classical method obtained by taking the $\hbar \to 0$ limit in this equation. We have investigated this model in figure V.8 (left panel). In most cases we have observed the thermal relaxation of the subsystem toward a certain equilibrium. The distributions of eigenstate weights p_n at equilibrium were roughly Boltzmannian (i.e. $p_n(t \gg \tau_{\rm relax}) \propto \exp(-E_n/T_{\rm sub})$) but the subsystem temperatures $T_{\rm sub}$ did not correspond to the bath temperatures T. This shows that equation (V.66) does not lead to the expected thermalisation of the $c\bar{c}$ bound states. Furthermore, as shown in figures V.9, we have observed an important violation of the Heisenberg principle when $B \ll A$ (i.e. $T \ll E_0$)[64], which in turn mechanically induces negative eigenstates weights for odd states (see the right panel of figure V.8).

To conclude: As the LHS of (V.66) corresponds to a genuine quantum evolution, this violation can only result from the classical Fokker-Planck/Langevin terms (RHS). Note that similar behaviours can be found within other semi-classical approaches, such as the quasi-classical Heisenberg-Langevin equation (see section IV.1.5). It is then quite likely that, for arbitrary potentials, both equation (V.66) as well as its $\hbar \to 0$ limit used previously in this section as well as in [2] are not appropriate to deal with the quantum evolution of $c\bar{c}$ pairs, especially at $T \sim T_c \ll E_{J/\psi} \sim 600$ MeV (where $B/A \sim 0.4$). A possible way to solve these issues - at least for the 1D harmonic oscillator - might be to add permanently the contribution of

[64] This can be explained noticing that the asymptotic distribution of equation (V.66) in the $\hbar \to 0$ limit is $\propto \exp(-H_{\rm cl}(\vec{r},\vec{p})/T)$, where $H_{\rm cl}$ is the classical Hamiltonian, implying that $\Delta r\, \Delta p$ can be arbitrarily small.

the quantum zero-point fluctuations through the use of a temperature dependent force correlation (such as relation VI.101) instead of the classical correlation (V.68) (see section VI.2.2.1).

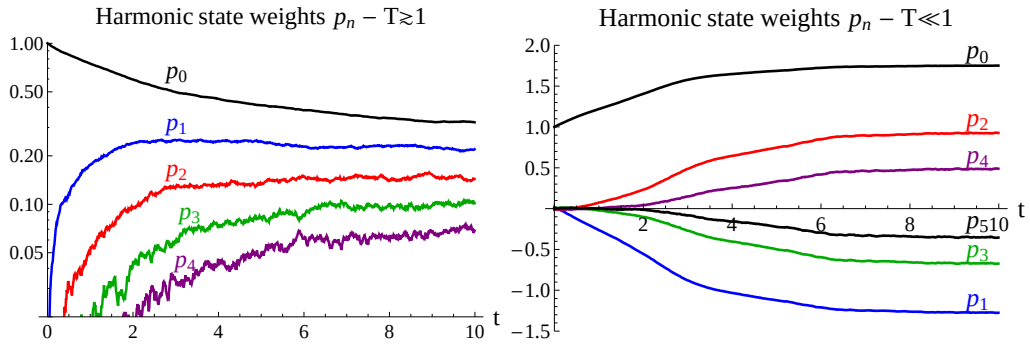

Figure V.8: Evolutions of the eigenstate weights with a 1D harmonic potential and a bath at $T \gtrsim E_0$ (*left*) and $T \ll E_0$ (*right*).

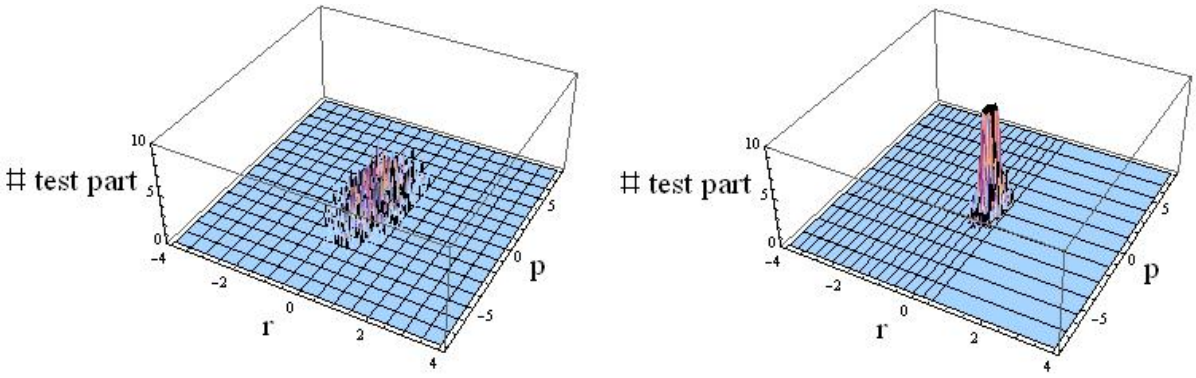

Figure V.9: Phase space distributions of the test particles with a 1D harmonic potential and a bath at $T \ll E_0$. *Left*: initial fundamental state (equal to the squeezed state for which $\Delta r\,\Delta p = \hbar/2$). *Right*: The final state distribution is peaked and therefore the Heisenberg principle is violated ($\Delta r\,\Delta p < \hbar/2$).

V.3 Brief discussion on quantum Fokker-Planck terms

To circumvent the violation of the Heisenberg principle, brought by the classical Fokker-Planck terms, we have also investigated a quantum version of the Fokker-Planck equation ([236] and references therein). The latter has been derived from the Caldeira-Leggett model (IV.1.5) in the limit that $2kT \gtrsim \hbar\omega_0$, where ω_0 is the frequency of the fundamental state. The RHS of (V.66) becomes (in the general case):

$$B\Delta_p F + \vec{\nabla}_p A\vec{p}F_{Q\bar{Q}} + 2D_{px}\vec{\nabla}_x \cdot \vec{\nabla}_p F_{Q\bar{Q}} + D_{xx}\Delta_x F_{Q\bar{Q}} \qquad \text{(V.69)}$$

where B, A are the classical coefficients, and $D_{px}(\Omega, T, A)$ and $D_{xx}(T, A)$ are new coefficients. Ω is the cut-off frequency of the reservoir oscillators. The effect of this

new RHS has been studied in the harmonic potential frame and shows no violation of the Heisenberg Principle at low temperatures (and therefore no negative state weights). However, at low temperatures $T \leq \hbar\omega_0$, the equilibrium state (distribution (3.21) in [236]) tends to spread over the phase space. As a result, the state weights become none Boltzmannian (see the solid curves of the figure V.10).

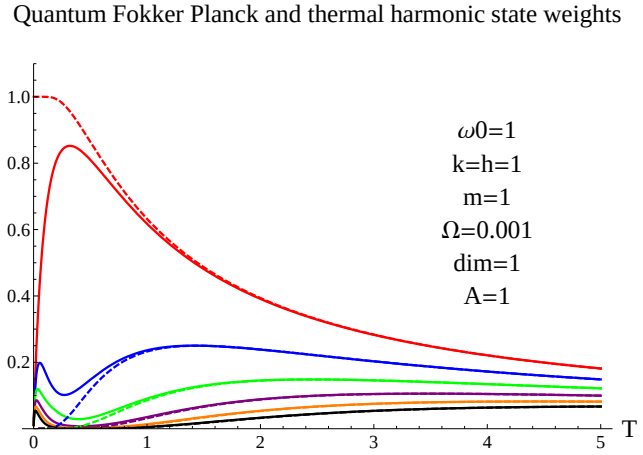

Figure V.10: Temperature dependence of the projection of the equilibrium state onto the harmonic states (in natural units). The solid curves correspond to the results obtained from the quantum Fokker-Planck approach [236] and are compared to what is expected from statistical quantum mechanics (dashed lines) [237]. The uppest curve correspond to the fundamental harmonic state, the one below to the first excited state...

The latter behavior at low temperature is incompatible with what is expected from quantum thermal theory. Indeed statistical quantum mechanics [237] shows that the thermal Wigner distribution for an harmonic oscillator should be (see the dashed curves of the figure V.10):

$$F(p,r) = 2\,\tanh(R)\,e^{-2/(\hbar\omega_0)\tanh(R)\,H} \tag{V.70}$$

where $H = \frac{p^2}{2m} + \frac{m\omega_0^2\,r^2}{2}$ is the harmonic Hamiltonian and $R = \frac{\hbar\omega/2}{kT}$ the ratio between the ground state energy and the thermal energy. Roughly, when $kT \ll \hbar\omega_0/2$ then $\tanh(R) \simeq 1$ and one gets the harmonic ground state as an asymptote. Whereas, when $kT \geq \hbar\omega_0/2$ then $\tanh(R) \propto 1/T$ and one gets Boltzmann distributions.

Because $T \sim T_c \ll E_{J/\psi} \sim 600$ MeV, the Wigner-Moyal equation plus quantum Fokker-Planck terms is thus not suited for our quantum study of the $Q\bar{Q}$ system.

Main ideas and transition

As a first attempt to observe the effects of direct thermal forces, we have investigated a semi-classical framework initially proposed by Young and Shuryak [2]. The formalism, i.e. the classical Langevin evolution of a $Q\bar{Q}$ quantum Wigner distribution, has been chosen as a convenient way to introduce a classical thermalisation process - which reflects the permanent collisions between the pair and the medium - while keeping accessible the full 3D situation without approximation. We focused exclusively on the J/ψ weight. We have first compared the evolutions given by the quantum and semi-classical equations without Langevin dynamics and observed important (expected) discrepancies. But these discrepancies might have a relatively small impact on the full evolution if the Langevin dynamics is the leading ingredient of the evolution (which seems to be the case here). We have then explored the full formalism and first observed relevant exponential decays of the J/ψ weight at constant temperatures after some transient phase. Including RHIC and LHC temperature scenarios (from hydrodynamics calculations), led to rich suppression patterns that might rule out the unjustified assumption of the fast/full decorrelation of $Q\bar{Q}$ pairs originating from melted states (made by both sequential suppression and statistical hadronisation models (see II.2.1.2 and II.2.2.1)). Finally, we severely questioned the accuracy of these results - and more generally the ones given by classical Fokker-Planck terms - by pointing out two important pitfalls: the violation of the Heisenberg principle at low temperatures $T \ll E_0$ and the actual "wrong" thermalisation of the eigenstate weights. All these faults urged us to look for a full dynamical quantum approach.

Part VI

The Schrödinger-Langevin equation: generalities and equilibration

VI.1 Introduction

In the last part, we have observed the limits of the semi-classical framework. To obtain a description of the $Q\bar{Q}$ pair which is compatible with quantum mechanics, one needs instead a "full" quantum treatment. To this end, in this part we introduce and study the general properties of a possible Langevin-like extension of the fundamental Schrödinger equation, the so called Schrödinger-Langevin ("SL") equation. After this general sanity check, the SL framework will be applied to the $Q\bar{Q}$/QGP system in the next part VII. Explicitly, the SL equation writes

$$i\hbar\frac{\partial\psi(\vec{x},t)}{\partial t} = \left[H_0 + \hbar A\Big(S(\vec{x},t) - \int \psi^* S(\vec{x},t)\,\psi\; d^3x\Big) - \vec{x}.\vec{F}_R(t)\right]\psi \quad \text{(VI.71)}$$

where A is a drag coefficient (inverse relaxation time), S the real phase of the wavefunction and $\vec{F}_R$ a stochastic force. The right hand side of the SL equation includes 1) the usual isolated Hamiltonian operator,

$$H_0 = -(\hbar^2/2m)\nabla^2 + V(\vec{x},t), \quad \text{(VI.72)}$$

where $V(\vec{x},t)$ is the mean field potential, 2) a nonlinear dissipative potential,

$$\hbar A(S - \langle S\rangle_{\vec{x}}) \quad \text{(VI.73)}$$

and 3) a fluctuating operator,

$$\vec{x}.\vec{F}_R(t). \quad \text{(VI.74)}$$

The dissipative and fluctuating terms are discussed respectively in sections VI.2.1 and VI.2.2. Because of its phenomenological aspect - only the drag A and bath temperature T_{bath} are necessary - and its numerical simplicity, the SL equation can be considered as a solid candidate for effective description of complex open quantum systems hardly accessible to quantum master equations or equivalent. In section VI.1.1, we first discuss two of its various derivations from the different approaches introduced in part IV. We then describe its basic properties in section VI.1.2. Before considering any actual applications to phenomenology, we show in section VI.1.3 that some questions and issues remain to be explored about its solutions and thermal relaxation. Finally, in sections VI.3 and VI.4, the thermal relaxation given by the SL equation will be studied with the harmonic and linear 1D potentials and with white and colored noises. The harmonic potential is a well-known base to study the properties of an open quantum system formalism, whereas the linear potential allows us to test an anharmonic situation which is closer to the $Q\bar{Q}$ binding potential.

N.B.: This part aims thus to study the properties of the SL equation within the general context of open quantum systems and is mostly inspired by the paper "The Schrödinger-Langevin equation with and without thermal fluctuations" written by Katz and Gossiaux (which should be published in 2016 [238]).

VI.1.1 Derivations

The SL equation can be derived in many ways within the different approaches developed in sections IV.1.5 and IV.1.6. Within the common open quantum system framework, the SL equation has first been introduced by Kostin [3] from an identification with the Heisenberg-Langevin equation (see section VI.1.1.1 below). With or without its fluctuating term, the SL equation has also been derived within many other frameworks such as the Schrödinger method of quantisation to the generalized Hamilton-Jacobi equation [188], the fluid interpretation of the Schrödinger equation [195, 196] (see section VI.1.1.2 below), nonlinear gauge transformations [239], the quantisation through stochastic mechanics [177], the diagonal limit of the quantisation of general non-Hamiltonian system [193] and others [240, 241, 242]...

For now, there is no established connection between the SL equation and the standard quantum master equations, which makes it a different type of stochastic Schrödinger equation than other stochastic Schrödinger equations existing in the literature [183, 199] (see section IV.1.4.2).

VI.1.1.1 From the Heisenberg-Langevin equation [3]

One wishes to identify some dissipative $V_{\rm Diss}$ and random V_R potentials in the Schrödinger equation,

$$i\hbar\frac{\partial\psi(\vec{x},t)}{\partial t} \;=\; H_0\,\psi + V_{\rm Diss}\,\psi + V_R\,\psi, \tag{VI.75}$$

that would correspond to the dissipative and random operators of the Langevin equation for Heisenberg operators

$$\dot{P} = F_0(X) - A\,P + F_R(t) \qquad \text{and} \quad \dot{X} = P/m\,. \tag{VI.76}$$

We first limit ourselves to the 1D case. The random potential directly corresponds to the random force through the usual derivation,

$$F_R(t) = -\partial V_R(x,t)/\partial x, \tag{VI.77}$$

and as $F_R(t)$ is independent of the position one obtains,

$$V_R(x,t) = -xF_R(t). \tag{VI.78}$$

Less straightforward, the dissipative potential can be obtained from an expectation value analysis. One first needs to express the momentum operator (in Heisenberg representation) expectation value in terms of the momentum operator and wavefunction (in Schrödinger representation):

$$\langle P(t)\rangle \;=\; \langle\psi|P|\psi\rangle = \langle\psi|P\psi\rangle = \langle P\psi|\psi\rangle = \big(\,\langle\psi|P\psi\rangle + \langle P\psi|\psi\rangle\,\big)/2 \tag{VI.79}$$

$$\;=\; \frac{\hbar}{2i}\int\Big[\frac{\partial\psi(x,t)}{\partial x}\psi^*(x,t) - \frac{\partial\psi^*(x,t)}{\partial x}\psi(x,t)\Big]. \tag{VI.80}$$

as P is self-adjoint. Differentiating with respect to time yields,

$$\frac{d\langle P(t)\rangle}{dt} = \langle \partial\psi/\partial t | P\psi\rangle + \langle \psi | P\partial\psi/\partial t\rangle \tag{VI.81}$$

Then, substituting the Schrödinger equation (VI.75) into (VI.81) and combining with the expectation value of equation (VI.76) leads to,

$$\langle \partial V_{\text{Diss}}/\partial x\rangle = A\,\langle P(t)\rangle \tag{VI.82}$$

The relation obtained for $\langle \partial V_{\text{Diss}}/\partial x\rangle$ from inserting equation (VI.80) into equation (VI.82) is satisfied for all wavefunctions if

$$\begin{aligned}\frac{\partial V_{\text{Diss}}}{\partial x} &= \frac{\hbar A}{2i}\left([\psi(x,t)]^{-1}\frac{\partial\psi(x,t)}{\partial x} - [\psi^*(x,t)]^{-1}\frac{\partial\psi^*(x,t)}{\partial x}\right) \\ &= \frac{\hbar A}{2i}\frac{\partial}{\partial x}\ln[\psi/\psi^*].\end{aligned} \tag{VI.83}$$

Integrating (VI.83) and choosing the integration constant such as to obtain an expectation value of the total energy equal to the one of the subsystem, one finally obtains the dissipative potential:

$$V_{\text{Diss}} = \frac{\hbar A}{2i}\Big(\ln[\psi/\psi^*] - \int \psi^*\ln[\psi/\psi^*]\,\psi\;dx\Big) \tag{VI.84}$$

In equation (VI.84), the dissipative term is written under its "logarithmic" formulation. One can obtain the equivalent "hydrodynamic" formulation back (equation $VI.71$) by employing the polar/Madelung transformation of the wavefunction,

$$\psi(x,t) = R(x,t)e^{iS(x,t)} \qquad \Rightarrow \qquad \ln[\psi/\psi^*] = 2iS \tag{VI.85}$$

where $R(x,t)$ and $S(x,t)$ are respectively the real amplitude and phase.

The generalisation to a three dimensional space is straightforward.

VI.1.1.2 From the quantum trajectory point of view [196]

The fluid dynamical (or quantum trajectories) interpretation of the Schrödinger equation is the easiest way to introduce and apprehend the dissipative term of the SL equation. Using the polar/Madelung transformation (VI.85) of the wavefunction, one can indeed re-write the Schrödinger equation as a system of two equations (real and imaginary part respectively):

$$\hbar\frac{\partial S}{\partial t} = -\frac{\hbar^2}{2m}\left(\frac{\partial S}{\partial x}\right)^2 - V(x,t) + \frac{\hbar^2}{2mR}\frac{\partial^2 R}{\partial x^2} \tag{VI.86}$$

$$\frac{\partial R}{\partial t} = -\frac{\hbar}{m}\frac{\partial R}{\partial x}\frac{\partial S}{\partial x} - \frac{\hbar}{2m}R\frac{\partial^2 S}{\partial x^2}. \tag{VI.87}$$

Relation (VI.87) is an equation of continuity for the wavefunction probability density, whereas relation (VI.86) makes the connection between quantum and classical mechanics when the phase S is associated with the quantum trajectory velocity:

$$p = \hbar \frac{\partial S}{\partial x}. \tag{VI.88}$$

This momentum can be seen as a hydrodynamic-like momentum in the probability space. The differentiation of equation (VI.86) yields:

$$\frac{\partial p}{\partial t} = -\frac{p}{m}\frac{\partial p}{\partial x} - \frac{\partial}{\partial x}\left(V(x,t) - \frac{\hbar^2}{2mR}\frac{\partial^2 R}{\partial x^2}\right) \tag{VI.89}$$

By analogy with Langevin forces in the classical Newtonian picture, one can introduce a friction term[65] that will act on the wavefunction "fluid":

$$\frac{\partial p}{\partial t} = -\frac{p}{m}\frac{\partial p}{\partial x} - \frac{\partial}{\partial x}\left(V(x,t) - \frac{\hbar^2}{2mR}\frac{\partial^2 R}{\partial x^2}\right) - Ap \tag{VI.90}$$

Finally, one obtains back the new Schrödinger equation with the new dissipative term:

$$i\hbar\frac{\partial \psi(x,t)}{\partial t} = \left(-\frac{1}{2m}\frac{\partial^2}{\partial x^2} + V(x,t) + \hbar A\big(S(x,t) - \langle S(x,t)\rangle_x\big)\right)\psi(x,t) \tag{VI.91}$$

where the total overall phase $\langle S(x,t)\rangle_x$ is subtracted for the evolution in order to ensure gauge invariance of the total energy.

VI.1.2 Properties

The SL equation exhibits some interesting properties:

- *Unitarity is preserved* at all times for the pure state [3, 196], i.e. the norm of the wavefunction remains constant. For a two particles system, like the quarkonia, unitarity means that the two particles and their correlations always exist and do not vanish while spreading over space. This feature is very different from what can be obtained with imaginary potentials (see IV.2.1.1) where the wavefunction, interpreted as the correlation between the two particles, vanishes during the evolution.

- *The uncertainty principle is always satisfied* [244, 245], i.e. the wavefunction always obeys the uncertainty inequality $\Delta x \Delta p \geq \hbar/2$. It can be opposed to other models such as the Caldirola-Kanai equation [190] without fluctuations (based on an effective time dependent Hamiltonian), the quasiclassical HL equation (see section IV.1.5) or the Wigner-Moyal equation with classical

[65] Usually the friction is well approximated by a linear and cubic forces. At low hydrodynamic velocity and not very far from the equilibrium, the cubic term becomes negligible [243].

Fokker-Planck terms (see section) where the uncertainty principle can be violated. Within the SL equation framework, the "narrowest" possible state is the fundamental state (also called zeropoint state) whatever the value of the dissipation strength A. Moreover, the thermal fluctuations (F_R) do not need to generate the quantum zeropoint fluctuations (which are required in other models like the Caldirola-Kanai equation).

- *The superposition principle is violated* due to the (logarithmic) nonlinear dependence of the dissipation upon the wavefunction. As we will see all along this part, this violation does not appear to be a problem per se for dissipative equations (as also advocated in [246, 247]).
- Even though the dissipation is nonlinearly dependent on the wavefunction, it still corresponds to an *ohmic friction*, i.e. proportional to the particle velocity. A nonlinear friction can still be obtained by extending the approach developed in section IV.1.5 to a nonlinear coupling [248, 249].
- As in the HL framework (IV.1.5), the thermal dynamics is mainly based on *two straightforward "classical" parameters*: the drag A and the bath temperature $T_{\rm bath}$. This simplicity makes the SL equation a solid candidate for effective description of complex open quantum systems hardly accessible to quantum master equations or equivalent.
- The use of *wavefunctions* is convenient as compared to density matrices, Wigner distributions or Heisenberg operators. Moreover, the evaluation of the state populations/weights is straightforward.
- The SL equation can *easily be implemented* numerically and especially in Monte-Carlo generator (used in some QGP transport codes). The numerical cost is proportional to the space-time grid size and to the number of realisations, i.e. to $n_{\rm space} \times n_{\rm time} \times n_{\rm stat}$ (where typically $n_{\rm space}$ is of the order of the hundreds, $n_{\rm time}$ and $n_{\rm stat}$ of the thousands). It remains quite reasonable in comparison to the common density matrix and quantum master equation approach where the numerical costs are highly expensive when the Hilbert space of the subsystem is large (see section IV.1.4). The mixed state observables are similarly defined within the SSE framework [183, 199].

VI.1.3 Solutions

The study of the solutions of the SL equation without its stochastic term has been carried in many specific cases. Analytically for a free particle [250, 251] and in uniform and harmonic potentials [196, 251, 195, 245, 252, 253]; numerically for the double well potential [196, 254], for interpenetrating waves and barrier penetration [250, 255] and for scattering and trapping [256]. The dissipation term is observed to decelerate and reduce the system toward its lowest energy state with an energy loss proportional to its classical kinetic energy [196]:

$$\frac{dE}{dt} = -A\frac{\langle p^2 \rangle}{m} \tag{VI.92}$$

Along these analysis, it has been advocated that the stationary eigenstates of H_0 are also stationary states of the equation [195, 252, 196]. At first sight, this behaviour is in contradiction with what is expected from damped quantum systems [172, 181, 185, 186]. As an answer to this expectation, we will show in section VI.2.1 how to obtain damping even with these states. The purely dissipative SL equation has already been applied in quantum chemistry [196] and heavy ion scattering [257, 258]

Very few studies of the SL equation solutions have however been carried with an additional driving or stochastic term. Kostin [3] first observed that for a free particle plane wave, the SL and HL equations lead to the same solution. Then, Messer [259] studied the evolution of a Gaussian wavefunction in the free and harmonic potentials. In the free case, he showed that the evolution differs from the Heisenberg-Langevin solution, highlighting that the SL and Heisenberg-Langevin equations are not strictly equivalent. In his calculation, Messer assumed that the SL equation led to the thermal equilibrium of statistical mechanics - which was not proven or tested - and used a white quantum noise for the stochastic force, which is questionable. The SL equation with the same assumptions has also been applied to atomic diffusion in solids [260]. On the numerical side, Sanin et al. [244, 261] extensively studied the evolution of an initial gaussian wavefunction in the harmonic and double well potentials, confined within infinite walls (the limits of the grid), and driven by non stochastic forces (sinusoidal, periodic pulses...).

In order to apply the full SL equation to phenomenology, a better understanding of its solutions and an exploration of its ability to lead a subsystem to thermal equilibrium are necessary. In sections VI.3 and VI.4, we study analytically and numerically the ability of the SL equation to bring different 1D subsystems to the thermal equilibrium of statistical mechanics using either a white or colored noise. To do so, we first introduce the dimensionless SL equation in section VI.1.4 and then discuss in more details the friction term and the quantum fluctuations in section VI.2.

VI.1.4 Dimensionless Schrödinger-Langevin equation

The behaviour of the SL equation will especially be studied with two external potentials: the harmonic $V = 1/2m\omega_0^2\, x^2$ and the linear $V = 1/2K_l\,|x|$. In all the following numerical studies, we use the SL equation with natural units, i.e. $\hbar = m = \omega_0 = K_l = k_{(B)} = 1$, and dimensionless variables x, t,...[66] Then, the characteristic energies are $E_0 = \hbar\omega_0/2 = 0.5$ and $\Delta E = E_1 - E_0 = 1$ ($E_0 \simeq 0.509$ and $\Delta E = E_1 - E_0 \simeq 0.66$) for the harmonic (linear) external potential. The dimensionless SL

[66] The dimensioned values of x, t, A, F_R and H_0 can be obtained by multiplying our dimensionless values respectively by $\sqrt{\hbar/m\omega_0}$, $1/\omega_0$, ω_0, $\sqrt{m\hbar\omega_0^3}$ and $\hbar\omega_0$ in the harmonic case or $(\hbar^2/mK_l)^{\frac{1}{3}}$, $(m\hbar/K_l^2)^{\frac{1}{3}}$, $(K_l^2/m\hbar)^{\frac{1}{3}}$, K_l and $(\hbar^2K_l^2/m)^{\frac{1}{3}}$ in the linear potential case.

equation, with the hydrodynamic formulation of the dissipative term, writes

$$i\frac{\partial\psi(x,t)}{\partial t} = \left[\frac{1}{2}\nabla^2\psi + V(x) + A\Big(S(x,t) - \langle S(x,t)\rangle\Big) - xF_R(t)\right]\psi, \quad \text{(VI.93)}$$

where the external potential is $V(x) = 1/2\,x^2$ or $V(x) = 1/2\,|x|$ within this study. The drag A and the stochastic process are thus the only parameters governing the generic evolution.

VI.2 Friction and quantum noises

VI.2.1 The friction non-linear term: a well defined prescription to obtain eigenstates damping

Though theoretically the fluctuation and dissipation aspects cannot be dissociated, it appears that in some specific studies only the damping is considered (quantum chemistry [196] and nuclear collisions [257, 258]). Unfortunately, the dissipative part of the SL equation (VI.71) suffers from ambiguities and needs some prescription to be defined properly. Its main non-linear term is the real phase $S(x,t)$, defined by the wavefunction decomposition

$$\psi(x,t) = R(x,t)e^{iS(x,t)}, \quad \text{(VI.94)}$$

where $R(x,t)$ is the real amplitude. $S(x,t)$ is indeterminate at the wavefunction nodes and multivalued (defined to a 2π modulo).

In the literature [196, 195, 252, 262], the phase $S(\psi)$ for real ψ corresponding to eigenstates is commonly prescribed to be zero (and thus continuous at the nodes of ψ) while $R(\psi)$ is taken as a real - *positive or negative* - function. This prescription has led to the conclusion that the stationary eigenstates of H_0 are also stationary states of the SL equation, as the dissipation term identically vanishes. For the sake of describing time-dependent situations, a corresponding prescription has however to be adopted for complex ψ as well. It is easily seen that such an analytical continuation unavoidably has one branch cut in each half complex-plane, both of them starting from the origin. Taking those branch cuts along the imaginary axis leads for instance to

$$S(\psi) = \arctan(\Im(\psi)/\Re(\psi)). \quad \text{(VI.95)}$$

with finite damping term in the SL equation. Therefore, a small modification of ψ (from real axis to complex plane) leads to a large variation of the associated damping of the quantum state, which is the sign of an ill-defined model.

We have proposed to use instead the "polar" or "Madelung" prescription, where one defines $R(x,t)$ as the module of the wavefunction, i.e. a real *positive* function. In practice, one could use the local argument of the wavefunction,

$$\mathrm{Arg}(\psi) = \mathrm{atan2}(\Im(\psi), \Re(\psi)), \quad \text{(VI.96)}$$

to determine $S(x,t)$, but the limitation of its values to a 2π interval illustrated in figure VI.1, would lead to discontinuities of the dissipative term with unphysical

effects[67]. To avoid these, we build the phase $S(x,t)$ on a spacial grid of step dx following the recursive law

$$S(x+dx) = S(x) + dS(x) \quad \text{where} \quad dS(x) = \text{Arg}[\psi(x+dx)/\psi(x)], \tag{VI.97}$$

starting from an arbitrary space point of reference "0" and get

$$S(j \times dx) = S(0) + \sum_{k=1}^{j} dS(k \times dx). \tag{VI.98}$$

The chosen value of the multivalued $S(0)$ is of no importance thanks to the regulator $-\langle S\rangle$, and can therefore be taken to $\text{Arg}[\psi(0)]$.

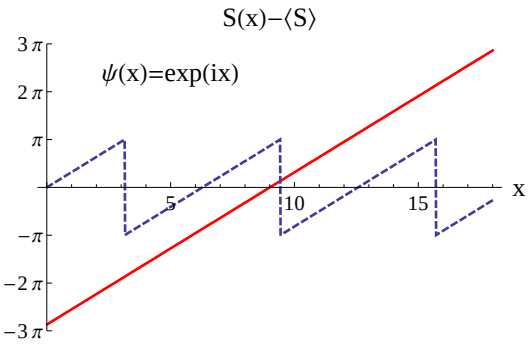

Figure VI.1: The dissipative term $S(x) - \langle S\rangle$ corresponding to the plane wave $\psi(x) = e^{ix}$ obtained with the argument function (dashed line) and with the recursive method (solid line).

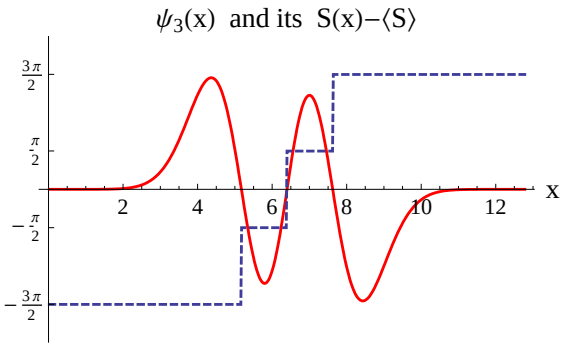

Figure VI.2: The real ψ_3 harmonic eigenstate (solid line, magnified for the plot sake) and its corresponding phase $S(x) - \langle S\rangle$ (dashed line) with the recursive method in the polar π prescription.

The polar prescription leads to singular phase shifts $+\pi$ at the wavefunction nodes as shown for instance in figure VI.2. Not only are these discontinuities theoretically allowed (thanks to the phase indeterminacy at the nodes), but they also have a convenient physical consequence: the stationary eigenstates of H_0 are not stationary states of the SL equation anymore. Indeed, for the excited eigenstates $\{\psi_n\}_{n\geq 1}$ of H_0 the friction term becomes a step potential which generates correlations between eigenstates and results in damping. To show the latter assertions, let us assume that an initial wavefunction $\psi = \sum c_n(0)\,\psi_n$ is equal to an eigenstate $\psi_{m\geq 1}$, i.e. with $c_n(0) = \delta_{nm}$. The SL equation without the thermal fluctuation term yields,

$$\begin{aligned} \dot{c}_n &= -\frac{i}{\hbar}\langle\psi_n|H_0|\psi\rangle - iA\,\langle\psi_n|(S-\langle S\rangle)|\psi\rangle \\ &= -\frac{i}{\hbar}E_n\,c_n - iA\sum_k c_k \int (S-\langle S\rangle)\psi_n^*\,\psi_k\,dx\,. \end{aligned} \tag{VI.99}$$

For symmetric external potentials for instance, one can show that if $\psi_{k=m}$ has an odd (even) parity, then the integral is finite and thus the transition $c_m \to c_n$ is allowed

[67]The invariance under the multiplication of the wavefunction by a simple phase factor would be broken.

at very small times for all ψ_n with even (odd) parities. Moreover, the smaller the difference $|n-m|$, the larger the transition rate, which is consistent with the Fermi Golden Rule. Last but not least, the transition rate to $n = m-1$ is larger than to $n = m+1$, which is consistent with damping. At larger times, these transitions and the damping can be observed numerically (see for instance figure VI.3).

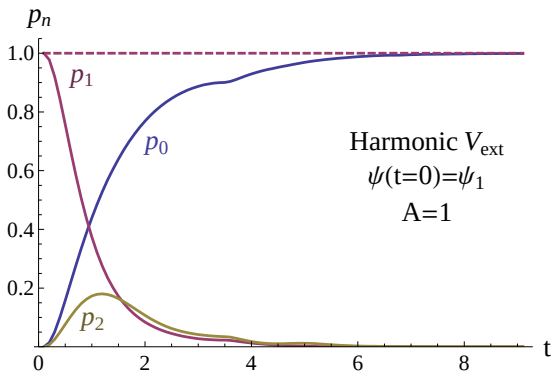

Figure VI.3: Evolution of the eigenstate weights $p_{n=0,1,2} = |\langle\psi_n|\psi(t)\rangle|^2$ with the dimensionless SL equation (relation (VI.93) without fluctuating term) from an initial first excited state, with the "polar" prescription (solid lines) and the "arctan" prescription (dashed lines).

Both the "arctan" and "polar" prescriptions are mathematically correct and the choice between them should be physically motivated. Unfortunately, though intuitively we expect the dissipation to act on any excited state, the stationarity of the H_0 eigenstates in the corresponding dissipative situation remains an open question within the open quantum system framework [263]. As illustrated in figure VI.3, thanks to the two prescriptions, the SL equation can reproduce both situations. From the common perspective of the quantum master equation [184], the Lamb shifted energy levels acquire finite lifetimes (finite widths), implying that the polar prescription is better suited for robust phenomenological studies. Let us finally stress that the choice of the prescription is of little importance when the fluctuations are considered, as they drive the state away from any given eigenstate.

VI.2.2 Thermal fluctuations and numerical implementation

VI.2.2.1 Quantum noises

All the Langevin-like equations include a noise term which simulates the many collisions (or couplings) that the subsystem undergoes with the particles of the bath. This noise is generally taken as a homogeneous Gaussian random process, independent of the subsystem position, and described by its average and covariance function. The random direction of the many collisions always yields a zero average. As seen in section IV.1.1, the classical Langevin equation usually assumes no correlation between these collisions, and the white noise covariance writes,

$$\langle F_R(t) F_R(t+\tau)\rangle = 2mkT_{\text{bath}} A\,\delta(\tau), \tag{VI.100}$$

where δ is the Dirac distribution and $T_{\rm bath}$ the bath temperature (input of the noise). The asymptotic solution of the (classical) Langevin equation is then the corresponding Boltzmann distribution of statistical mechanics.

In the quantum realm, the noise operator is built from the initial bath position and momentum operators whose non-commutative property leads to the main differences with the classical case. Senitzky [172] first proposed an HL equation - for a general bath linearly acting on a harmonic subsystem (with natural frequency ω_0) - where the noise operator is also described by a white noise covariance,

$$\langle F_R(t)F_R(t+\tau)\rangle = 2mA\left[\frac{\hbar\omega_0}{2} + \frac{\hbar\omega_0}{\exp(\hbar\omega_0/kT_{\rm bath})-1}\right]\delta(\tau), \qquad \text{(VI.101)}$$

leading to a markovian process. This covariance has been used by Messer [259] in its analytic comparison of the HL and SL solutions. The first term of the RHS bracket corresponds to the zero point fluctuations of the subsystem. This term is required within the HL framework for canonical commutations to hold at $T_{\rm bath} = 0$, as shown by equation (52) in [172]. However, within the SL framework, the zero point fluctuations appear naturally in the wavefunction such that they do not need to be included in the noise operator for the the canonical commutations to hold. Therefore, this term becomes unnecessary and the white quantum noise writes,

$$\langle F_R(t)F_R(t+\tau)\rangle = B\,\delta(\tau), \qquad \text{(VI.102)}$$

where

$$B = 2mA\,E_0\left[\coth\left(\frac{E_0}{kT_{\rm bath}}\right) - 1\right], \qquad \text{(VI.103)}$$

with $E_0 = \hbar\omega_0/2$, the zero point energy. In section VI.3, we will show that the fluctuation-dissipation relation (VI.103) indeed allows to reach an asymptotic thermal distribution of states when one uses a white noise and a harmonic external potential.

However, Li et al. [264] pointed out an important weakness in the derivation of (VI.101). They also claimed that the colored quantum noise (non-Markovian),

$$\langle F_R(t)F_R(t+\tau)\rangle = \frac{m}{\pi}\int_0^\infty \hbar\omega\left[\coth\left(\frac{\hbar\omega}{2kT_{\rm bath}}\right)\cos(\omega\tau) + i\sin(\omega\tau)\right]A\,d\omega, \qquad \text{(VI.104)}$$

first derived by Ford et al. [185], is the only one able to drive a general subsystem to the correct thermal equilibrium via the HL equation. For now, the latter assertion has only been demonstrated in a limited form [212, 213].

Actually, in order to get rid of the bath zero point fluctuations contribution - that was first judged physically unjustified -, Ford et al. first derived a quantum noise under the form of the normal product

$$\langle N[F_R(t)F_R(t+\tau)]\rangle = \frac{2mA}{\pi}\int_0^\infty \frac{\hbar\omega}{\exp(\hbar\omega/kT_{\rm bath})-1}\cos(\omega\tau)\,d\omega. \qquad \text{(VI.105)}$$

Both colored noises lead to a non-Markovian process even if the friction is memoryless. The spectra corresponding to these two colored noises, are shown in figure

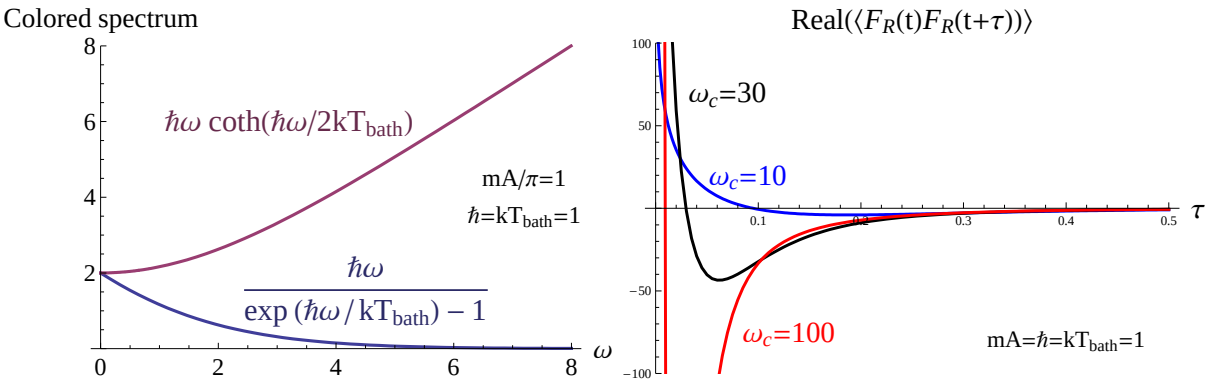

Figure VI.4: *Left*: The rising spectrum of the colored noise (VI.104) – which requires a frequency cut-off to be integrated – and the decreasing spectrum of (VI.105) at $T_{\text{bath}} = 1$. *Right*: The noise correlation (VI.104) strongly depends on the value of the frequency cut-off. The cut-off is here evaluated with a Lorentzian shape.

VI.4 (left). As pointed out by Gardiner [213], the correct choice of spectrum depends on what is actually measured to find it: e.g. in absorption measurements one gets the black body radiation Planck spectrum corresponding to (VI.105), whereas in Josephson junction noise current measurements [265] one gets the linearly rising spectrum at high frequencies corresponding to (VI.104). Within the SSE framework, the choice between white and colored noises is also intensively discussed, for instance to obtain the correct thermal equilibrium of a non-Markovian master equation [197] or the correct positivity property for the Bloch-Redfield master equation [266].

To use these correlations within the SL framework, one needs to assume that the noise operator can be taken as a commutating c-number (whereas it is a non-commutating q-number within the HL framework). Although questionable, this assumption was actually already implied in Kostin's derivation of the SL random potential [3] and is commonly made within the quasiclassical HL equation framework (see section IV.1.5). It does not lead to any violation of the Heisenberg relations [244, 245] as one obtains with the quasiclassical HL equation [182].

Though they are not fully justified (as explained above), we have focused on the white (VI.102) and colored (VI.105) noise correlations, in order to observe their ability to lead the subsystem toward the thermal equilibrium of statistical mechanics. Our choice not to explore (VI.104) within this work was motivated by the additional complications brought by the required high frequency cut-off and by the practical/conceptual problem arising from the correlation imaginary part. Indeed, as shown in figure VI.4 (right), the noise correlation (VI.104) strongly depends on the value of the high frequency cut-off - which evaluation is specific to each system - and on the choice of the cut-off shape (Lorentzian, exponential, sharp...).

Finally, whereas the white noise (VI.102) leads to an uncorrelated stochastic force, the colored quantum noise (VI.105) gives a stochastic force with a strong temperature dependence of its correlation time. The latter becomes really large at low temperatures ($\propto 1/T$) and the Brownian hierarchy/weak coupling limit - the

typical relaxation time ($\propto 1/A$) should be much larger than the stochastic force correlation time - is broken when $A \gtrsim T$.

VI.2.2.2 Numerical implementation

Here we describe a numerical method to generate stochastic stationary Gaussian variables characterized by an autocorrelation $\langle F_R(t)F_R(t+\tau)\rangle = C(\tau)$. To build these variables numerically, we first define a set of uncorrelated Gaussian random variables $\hat{r}_j$ with zero average and correlation $\langle \hat{r}_j\, \hat{r}_{j'}\rangle = \Delta t\, \delta_{jj'}$, where Δt is the time step of the numerical scheme. We build the Gaussian random force $\hat{F}$ at a time t_i – and assumed to be constant over the time step $[t_i, t_i + \Delta t]$ – from the weighted sum

$$\hat{F}_i = \sum_{j=-\infty}^{+\infty} W_{i-j}\, \hat{r}_j\,, \tag{VI.106}$$

where the weights W_{i-j} depend only on the difference $i-j$ to guarantee the stationarity of the process. Then, the average of $\hat{F}_i$ is null and its covariance is given by

$$\left\langle \hat{F}_i\, \hat{F}_{i'} \right\rangle = \sum_{j,j'=-\infty}^{+\infty} W_{i-j} W_{i'-j'} \langle \hat{r}_j\, \hat{r}_{j'}\rangle = \sum_{j=-\infty}^{+\infty} W_{i-j} W_{i'-j} \Delta t\,, \tag{VI.107}$$

which, in the continuous limit $\Delta t \to 0$, becomes

$$\langle F_R(t)F_R(t')\rangle = \int_{-\infty}^{+\infty} \mathcal{W}(t-t'')\, \mathcal{W}(t'-t'')\, dt''\,, \tag{VI.108}$$

with $W_i = \mathcal{W}(t_i)$ for a given time step Δt. Then, one easily shows that the Fourier transform of $\mathcal{W}$ is just the square root of the power spectrum $P(\omega)$ of the retained noises, i.e.

$$P(\omega) \;=\; |\tilde{\mathcal{W}}(\omega)|^2 \tag{VI.109}$$

with

$$P(\omega) \;=\; 2mA\, \frac{\hbar\omega}{\exp(\hbar\omega/kT_{\rm bath}) - 1}\,, \tag{VI.110}$$

for the colored quantum noise (VI.105) and

$$P(\omega) \;=\; \lim_{\sigma\to 0}\; B\, \exp\left(-\frac{1}{2}\sigma^2\omega^2 \right), \tag{VI.111}$$

for the white quantum noise (VI.102). For the latter, the flat spectrum is obtained when $\sigma \to 0$, but in practice it is sufficient to take $\sigma \ll \tau$, where τ is the typical time of the subsystem evolution. Then, one gets explicitly

$$\mathcal{W}(\tau) = \frac{1}{\pi} \int_0^\infty \sqrt{P(\omega)}\, \cos(\omega\tau) d\omega\,. \tag{VI.112}$$

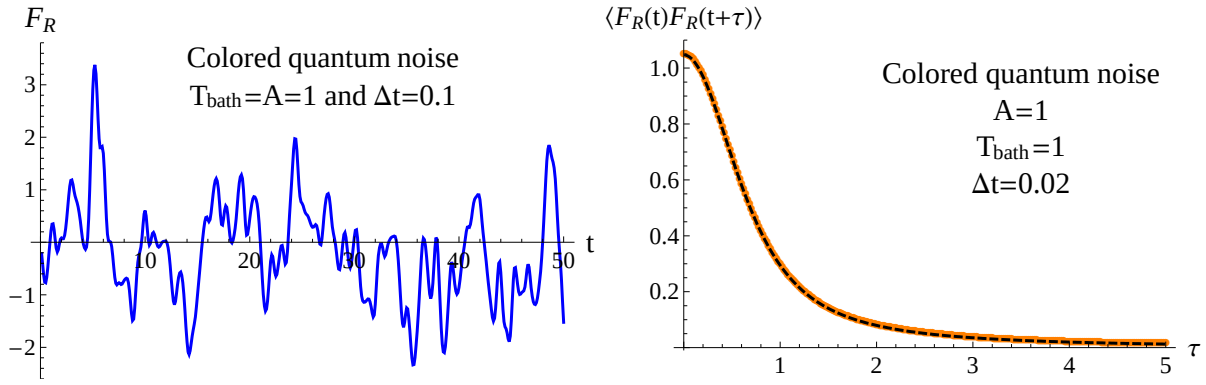

Figure VI.5: *Left*: Example of one colored quantum noise (VI.105) realisation obtained with the described numerical method. *Right*: Corresponding analytical (dashed black curve) vs. numerical (orange dots) covariances over time.

and then the stochastic variables $\{\hat{F}_i\}$ through equation (VI.106).

In figure VI.5 (left), an example of a colored noise (VI.105) realisation obtained with the described numerical method is shown. In figure VI.5 (right), the corresponding numerical time correlation is successfully compared to the analytical expectation,

$$\langle F_R(t)F_R(t+\tau)\rangle = \frac{A}{\pi}\left(\frac{1}{\tau^2} - \pi^2 T_{\text{bath}}^2\,\text{Csch}^2[\pi T_{\text{bath}}\tau]\right). \tag{VI.113}$$

Besides, one can easily show that the variables defined in this way are Gaussian. Similar algorithms can be found in the literature and have been successfully used in SSE and other formalisms (see [197] and references therein).

VI.3 Equilibration with a harmonic potential

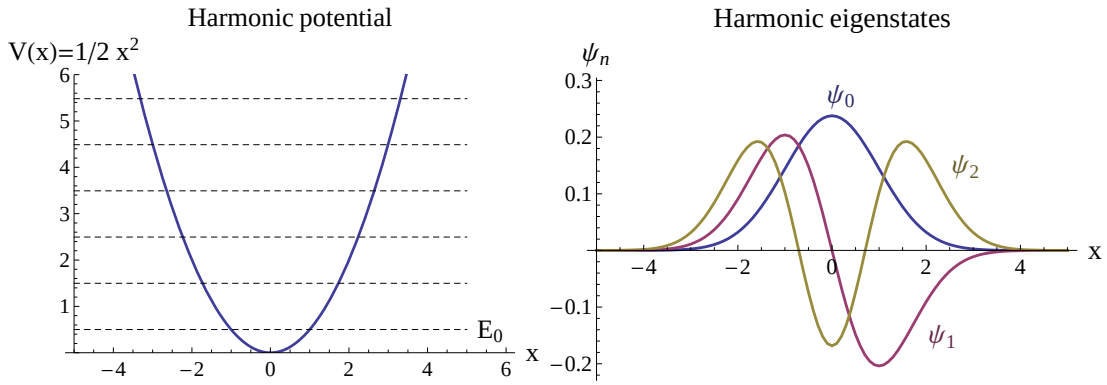

Figure VI.6: *Left*: The harmonic potential under study (thick line) and its corresponding eigenenergies (dashed lines). *Right*: The corresponding three lower eigenstates.

VI.3.1 Analytic solutions with a white noise and Gaussian wavepackets as initial conditions (and asymptotic states)

We first assume a general Gaussian wavepacket,

$$\psi(x,t) = e^{\frac{i}{\hbar}\left(\alpha(t)[x-x_{\rm cl}(t)]^2+p_{\rm cl}(t)[x-x_{\rm cl}(t)]+\gamma(t)\right)}, \tag{VI.114}$$

where $\alpha(t)$ is a complex number related to the wavepacket width ($\mathrm{Im}(\alpha(t=0))>0$), $\gamma(t)$ a complex phase, and $x_{\rm cl}$ and $p_{\rm cl}$ are the position and momentum Gaussian centroids (central values). Inserting (VI.114) in the SL equation leads to four ordinary differential equations for α, $x_{\rm cl}$, $p_{\rm cl}$ and γ, including:

$$\dot{\alpha} + A\mathrm{Re}(\alpha) + \frac{2}{m}\alpha^2 + \frac{m\omega_0^2}{2} = 0 \tag{VI.115}$$

and

$$\dot{p}_{\rm cl} = -m\omega_0^2\, x_{\rm cl} - Ap_{\rm cl} + F_R\,, \qquad \dot{x}_{\rm cl} = \frac{p_{\rm cl}}{m} \tag{VI.116}$$

From any $\mathrm{Im}(\alpha(t=0))>0$, the solution of equation (VI.115) tends asymptotically to $\alpha(t\to\infty) = im\omega_0/2$, which corresponds to the width of the ground state $\sqrt{\hbar/m\omega_0}$. After some initial relaxation, the general solution from any initial state (VI.114) is thus the ground state displaced in space with a trajectory obeying the classical equations of motion (VI.116). For a free wavepacket, the solution of equation (VI.116) is then $p_{\rm cl}(t) = p_{\rm cl}(t=0)\exp(-At)$ showing that A is indeed the drag coefficient.

We now want to show that the distribution of the eigenstate weights is the Boltzmann distribution $\propto e^{-E_n/T_{\rm sub}}$ with $T_{\rm sub} = T_{\rm bath}$ (where $T_{\rm sub}$ is the subsystem temperature) provided that the fluctuation-dissipation relation (VI.103) is satisfied. In other terms, the subsystem equilibrates with the medium if (VI.103) is satisfied. In the following sections VI.3.2 and VI.3.3.2, we will show numerically that these results are universal, i.e. independent of the chosen initial state, drag and temperature.

As determined above, for asymptotic times the wavefunction writes,

$$\psi \propto e^{-\frac{(x-x_{\rm cl}(t))^2}{2a^2}+ip_{\rm cl}(t)x}\,, \tag{VI.117}$$

where the square width is $a^2 = \frac{1}{m\omega_0}$. We would like to know what is the weight of the different H_0 eigenstates

$$\psi_n = \frac{H_n(\xi)e^{-\frac{\xi^2}{2}}}{\sqrt{2^n n!\sqrt{\pi}}}\,, \tag{VI.118}$$

where $\xi = \frac{x}{a}$. We first reformulate (VI.117) as

$$\psi \propto e^{-\frac{\xi^2}{2}+2\mu\xi-\frac{(x_{\rm cl}/a)^2}{2}}\,, \tag{VI.119}$$

where we have set $\mu = \frac{\frac{x_{\rm cl}}{a} + i p_{\rm cl} a}{2}$. Using the identity

$$e^{2\mu\xi - \mu^2} = \sum_{n=0}^{+\infty} \frac{\mu^n}{n!} H_n(\xi)\,, \tag{VI.120}$$

then yields

$$\psi \;\propto\; e^{-\frac{(x_{\rm cl}/a)^2}{4} - \frac{(p_{\rm cl} a)^2}{4} + i\frac{p_{\rm cl} x_{\rm cl}}{2}} \sum_{n=0}^{+\infty} \frac{\sqrt{2^n}\mu^n}{\sqrt{n!}} \psi_n(\xi). \tag{VI.121}$$

We thus deduce that the eigenstate weight $p_n(x_{\rm cl}, p_{\rm cl})$ for a given realisation of the stochastic noise is given by

$$p_n(x_{\rm cl}, p_{\rm cl}) \;\propto\; \frac{2^n |\mu|^{2n}}{n!}\; e^{-\frac{(x_{\rm cl}/a)^2}{2} - \frac{(p_{\rm cl} a)^2}{2}} \;\propto\; \frac{\left((x_{\rm cl}/a)^2 + (p_{\rm cl} a)^2\right)^n}{2^n n!}\; e^{-\frac{(x_{\rm cl}/a)^2}{2} - \frac{(p_{\rm cl} a)^2}{2}} \tag{VI.122}$$

and one has exactly $\sum p_n = 1$. Above, we showed that the position $x_{\rm cl}$ and momentum $p_{\rm cl}$ centroïds satisfy the classical stochastic equation of motion (VI.116). When the stochastic force correlation is of the form $\langle F_R(t) F_R(t+\tau)\rangle = B\,\delta(\tau)$ (white noise) it is known that the distribution of the trajectories ($x_{\rm cl}$, $p_{\rm cl}$) is

$$W(x_{\rm cl}, p_{\rm cl}) \propto e^{-\frac{\frac{m\omega_0^2 x_{\rm cl}^2}{2} + \frac{p_{\rm cl}^2}{2m}}{kT_{\rm cl}}}, \tag{VI.123}$$

where $T_{\rm cl} := \frac{B}{2mA}$, A is the drag and B the force autocorrelation. The eigenstate weight, averaged over the fluctuations, will then be given by

$$p_n = \int W(x_{\rm cl}, p_{\rm cl}) p_n(x_{\rm cl}, p_{\rm cl}) dx_{\rm cl} dp_{\rm cl}\,. \tag{VI.124}$$

To determine (VI.124), we use the relation

$$p_n(x_{\rm cl}, p_{\rm cl}) = \frac{(-1)^n}{n!} \frac{\partial^n}{\partial \eta^n}\; e^{-\eta\left(\frac{(x_{\rm cl}/a)^2}{2} + \frac{(p_{\rm cl} a)^2}{2}\right)}\Bigg|_{\eta=1}. \tag{VI.125}$$

After some trivial integration on $x_{\rm cl}$ and $p_{\rm cl}$, one gets that

$$\int W(x_{\rm cl}, p_{\rm cl}) e^{-\eta\left(\frac{(x_{\rm cl}/a)^2}{2} + \frac{(p_{\rm cl} a)^2}{2}\right)} dx_{\rm cl} dp_{\rm cl} = \frac{\frac{\hbar\omega_0}{kT_{\rm cl}}}{\eta + \frac{\hbar\omega_0}{kT_{\rm cl}}}\,, \tag{VI.126}$$

where the numerators guarantees that for $\eta = 0$, one has $\int W(x_{\rm cl}, p_{\rm cl}) dx_{\rm cl} dp_{\rm cl} = 1$. Differentiating n times (VI.126) with respect to η yields

$$p_n = \frac{\frac{\hbar\omega_0}{kT_{\rm cl}}}{\left(1 + \frac{\hbar\omega_0}{kT_{\rm cl}}\right)^n} \tag{VI.127}$$

We thus have

$$p_n \propto e^{-n\ln\left(1 + \frac{\hbar\omega_0}{kT_{\rm cl}}\right)}\,. \tag{VI.128}$$

Setting

$$\ln\left(1+\frac{\hbar\omega_0}{kT_{\rm cl}}\right)=\frac{\hbar\omega_0}{kT_{\rm sub}}\quad\Leftrightarrow\quad kT_{\rm cl}=\frac{\hbar\omega_0}{e^{\frac{\hbar\omega}{kT_{\rm sub}}}-1}\,, \tag{VI.129}$$

one obtains $p_n \propto e^{-n\frac{\hbar\omega_0}{kT_{\rm sub}}}$ which shows that the distribution of states follows a Boltzmann distribution with a temperature $T_{\rm sub}$. Recalling the expression of $T_{\rm cl}$ in terms of A and B, one gets the condition relating A, B and $T_{\rm sub}$:

$$\frac{B}{2mA}=\frac{\hbar\omega_0}{2}\left[\coth\left(\frac{\hbar\omega_0}{2kT_{\rm sub}}\right)-1\right], \tag{VI.130}$$

which is the relation (VI.103) for the white quantum noise and shows that $T_{\rm sub} = T_{\rm bath}$ the bath temperature. Reciprocally, we have proven that the distribution of the state weights is Boltzmannian if one uses a white noise with the relation (VI.103). This reasoning can be easily extended to three dimensions.

VI.3.2 Wavefunction pattern during one stochastic realisation

From numerical observations, we first confirm that after some initial relaxation, the general solution from initial state is the ground state displaced in space with a stochastic trajectory. Indeed with any noises, drags, potentials and initial states, a common wavefunction evolution pattern emerges during a noise realisation (see for instance figure VI.7 and VI.8). First, as in section VI.3.1, the shape of the wavefunction evolves toward the ground state shape. In parallel, if one starts from an initial excited eigenstate, the phase "breaks" at the nodes and evolves toward a linear phase in the region where the wavefunction takes non negligible values (see the $t = 17$ panel in figure VI.8 for instance). In parallel and until the end of the evolution, the centroïd oscillates around the potential minimum following a stochastic trajectory along the space axis. Some discrepancies to this pattern, coming from numerical instabilities, appear when $A \ll T$ and when $T \gg 1$.

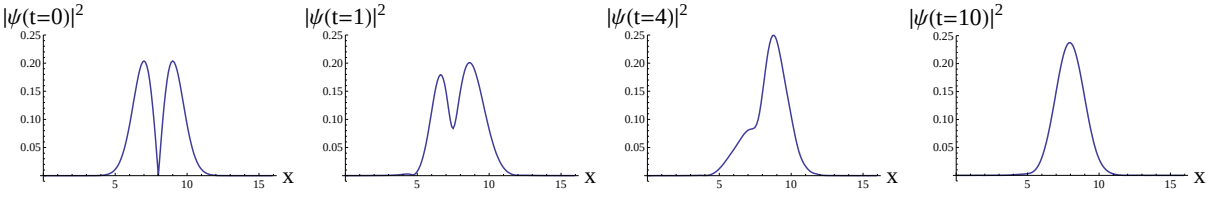

Figure VI.7: Typical wavefunction shape/module evolution toward the ground state shape/module during one noise realisation.

VI.3.3 With the white noise

We now want to generalise numerically the results we obtained in section VI.3.1 for any initial states, drags and temperatures.

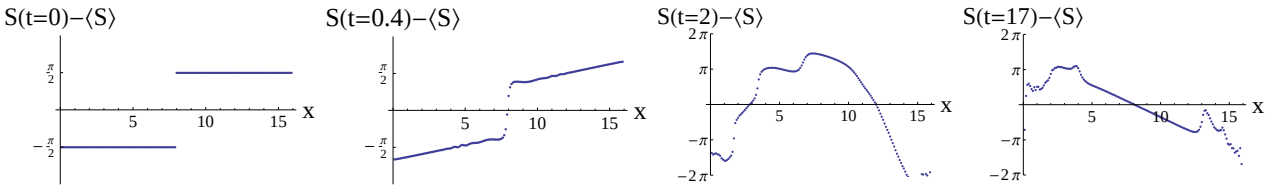

Figure VI.8: Typical wavefunction phase evolution towards linearity (where the wavefunction takes significant values) during one noise realisation.

VI.3.3.1 Energy and weight evolutions

To illustrate the SL equation ability to bring a subsystem to thermal equilibrium, we choose to evolve the initial ground state ψ_0 in a bath at temperature $T_{\text{bath}} = 1$. The noise parameter is taken to $\sigma = 0.03$ and the grid steps as $\Delta x = 0.1$, $\Delta t = 0.01$.

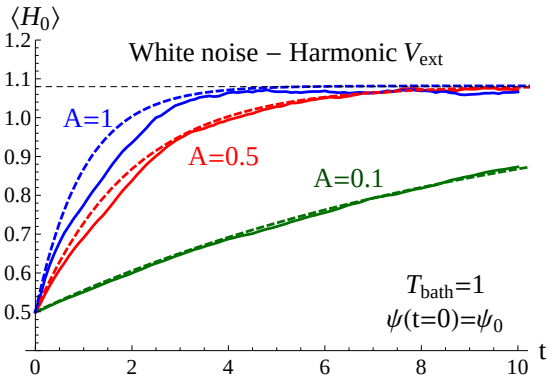

Figure VI.9: *Solid curves*: Numerical $\langle H_0 \rangle$ average energy evolutions for different drags A. *Dashed horizontal line*: Corresponding theoretical asymptotic value given by the exact relation (VI.131). *Dashed curves*: Corresponding theoretical evolutions given by (VI.132).

We first focus on the average energy $\left\langle \langle H_0 \rangle \right\rangle_{\text{stat}}$ as given by (IV.43); we will just write $\langle H_0 \rangle$ for simplification. Three average energy evolutions with drags corresponding to weak $A = 0.1$, intermediate $A = 0.5$ and strong $A = 1$ couplings (weak coupling if $A \ll \omega_0 = 1$ and $A \ll \sigma^{-1}$) are shown in figure VI.9. The theoretical asymptotic value for a thermal quantum harmonic oscillator is given by,

$$\langle H_0 \rangle (t \to \infty) = E_0 \coth \left(\frac{E_0}{k T_{\text{bath}}} \right), \tag{VI.131}$$

and corresponds to our value $\langle H_0 \rangle (t \to \infty) \simeq 1.07$ when $T_{\text{bath}} \simeq 1$. The average energy evolution rate predicted by Senitzsky [172] within the HL equation framework,

$$\langle H_0 \rangle (t) = E_0 \, e^{-At} + \langle H_0 \rangle (t \to \infty) \Big(1 - e^{-At} \Big), \tag{VI.132}$$

fits our numerical evolution in the weak coupling case (where Senitzsky's HL equation actually applies) as shown in figure VI.9.

The second interesting observable is the distribution of the eigenstate weights (populations) $p_n(t)$, as given by (IV.43) with the projection operator $O_n = |\psi_n\rangle\langle\psi_n|$.

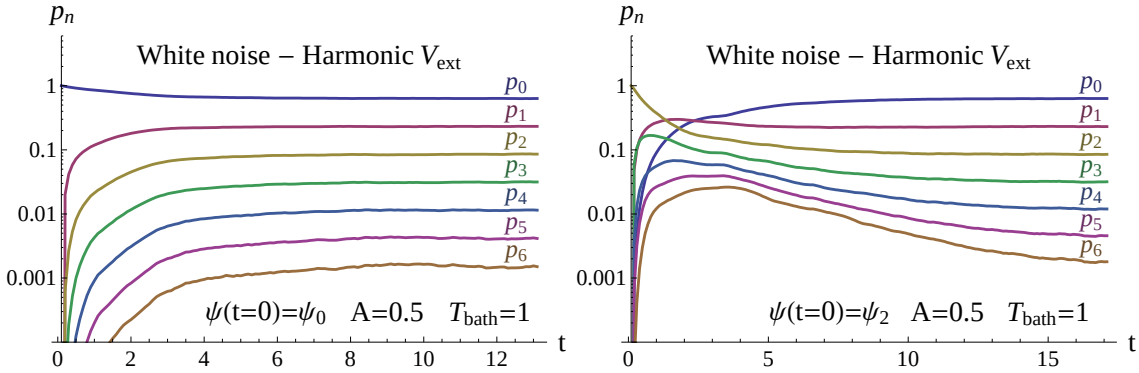

Figure VI.10: Evolutions of the eigenstate weights $p_{n=0,...6}(t)$ from the initial ground state (*left*) and 2nd excited state (*right*) for a drag corresponding to an intermediate coupling.

As shown in figure VI.10, their evolutions during the transient phase follow the general expectation that the main transitions occur between neighbouring energy levels, a feature also found in the transition elements of the Fermi Golden Rule. Moreover, they lead to a reshuffling of the weights, such as $p_n > p_{n+1}$, reached after a lapse of time proportional to the relaxation time $1/A$.

VI.3.3.2 Asymptotic behaviour

As shown for instance in figure VI.11, the asymptotic distribution of the weights is independent of the chosen initial state and perfectly fits a Boltzmann like distribution. One can determine the *actual temperature reached by the subsystem, called* T_{sub}, by fitting the Boltzmann line $\propto e^{-E/T_{sub}}$ to the asymptotic $p_{n=0,...10}(E_n)$ values. For the previous example, one finds that $T_{sub} = 0.99 \simeq T_{bath}$.

In figure VI.12, we compare the temperature actually reached by our subsystem T_{sub} to the bath temperature T_{bath} used as input of the noise. For a large range of temperatures and independently of the drag A and initial state, we observe that $T_{sub} \simeq T_{bath}$ and that the asymptotic distributions of the weights are Boltzmannian. One can thus conclude that the subsystem correctly thermalises when one uses the white noise (VI.102) with (VI.103).

The total uncertainty on the asymptotic values, for a statistic of a few thousands of realisations, grows with the temperature from $\sim 2\%$ at $T_{bath} = 0.1$ to $\sim 10\%$ at $T_{bath} = 5$. Indeed, a higher temperature implies larger wavefunction oscillations along the space axis and numerical instabilities, which imply larger weight oscillations at each noise realisation and for the mixed state observables. An additional averaging over a time range $\Delta t'$ once the equilibrium is reached, leads to more reliable results. The accuracy then follows the common statistical law $\propto 1/\sqrt{n_{stat} \times \Delta t'}$. When $T_{bath} \ll 1$, the distributions exhibit an alternating pattern at really small weights ($\sim 10^{-20}$). It is most probably due to numerical issues, associated for instance to the discretization scheme or the spectrum approximation (partly due to the "infinite walls" at the grid limits [261]).

We have therefore generalised the analytic results obtained in section VI.3.1

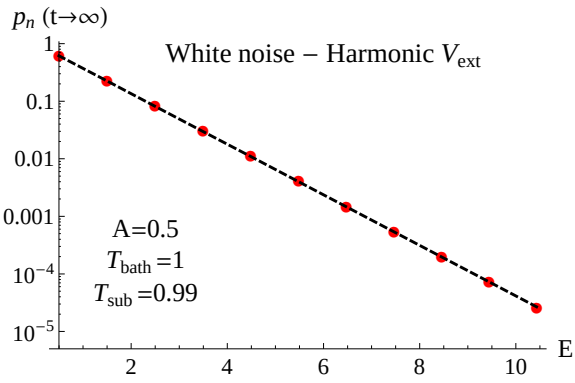

Figure VI.11: The asymptotic distribution of the eigenstate weights $p_{n=0,...10}$ (red dots), obtained with $A = 0.5$ and $T_{\rm bath} = 1$, function of the corresponding eigenenergies $E_{n=0,...10}$. It fits the Boltzmann distribution ($\propto e^{-E/T_{\rm sub}}$) with $T_{\rm sub} = 0.99$ (dashed line).

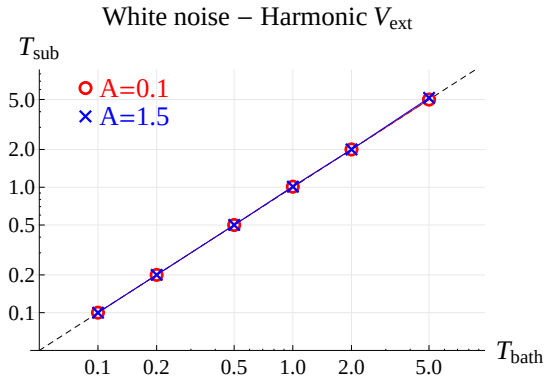

Figure VI.12: Asymptotic subsystem temperature $T_{\rm sub}$ as a function of the bath temperature $T_{\rm bath}$ for two different drags: $A = 0.1$ (red circles) and $A = 1.5$ (blue crosses) corresponding respectively to a weak and strong coupling. The dashed line corresponds to the ideal case $T_{\rm sub} = T_{\rm bath}$.

with an initial Gaussian wavepacket to some other initial states. We can thus conjecture that the SL equation, within the case of a harmonic external potential and the white noise (VI.102 and VI.103), universally leads to the thermal equilibrium of statistical mechanics. Moreover, though only expected at the weak coupling limit (as explained in the introduction), it is also reached in the intermediate and strong regimes. Finally, the observed behaviour fits Senitzky's point of view that initial correlations should be suppressed and replaced by some universal thermal correlations.

VI.3.3.3 Decoherence of the reconstructed density matrix

If a coherent quantum system undergoes many "classical" collisions, it is commonly thought to loose its coherences towards a reduced "classical" state [267]. In our study, one can explicitly check the decoherence from the coherent state to the classical correlations. The coherences correspond to the off-diagonal terms of the density matrix, as seen in section IV.1.3. The density matrix can be reconstructed from the statistical mixed state through

$$\rho_{mn}(t) = \lim_{n_{\rm stat}\to\infty} \frac{1}{n_{\rm stat}} \sum_{r=1}^{n_{\rm stat}} \langle\psi_m|\psi^{(r)}(t)\rangle\langle\psi^{(r)}(t)|\psi_n\rangle \,. \tag{VI.133}$$

For instance, starting from the full coherent state $\psi(t=0) = (\psi_0+\psi_1+\psi_2)/\sqrt{3}$, i.e. from the density matrix,

$$\rho(t=0) = \begin{pmatrix} 1/3 & 1/3 & 1/3 \\ 1/3 & 1/3 & 1/3 \\ 1/3 & 1/3 & 1/3 \end{pmatrix}, \tag{VI.134}$$

in the orthogonal basis (ψ_0, ψ_1, ψ_2), one obtains at equilibrium (for $A = 1$ and $T_{\text{bath}} = 0.9$),

$$\rho(t \gg \tau_{\text{relax}}) = \begin{pmatrix} 0.675 & 0.001 - 0.004i & 0.004 + 0.0008i \\ 0.001 + 0.004i & 0.222 & -0.0007 - 0.001i \\ 0.004 - 0.0008i & -0.0007 + 0.001i & 0.071 \end{pmatrix} \quad \text{(VI.135)}$$

At equilibrium, the off-diagonal terms (coherences) get much smaller than the diagonal terms, proof that some decoherence has occurred, and that the diagonal terms (weights or populations) get thermally distributed. One therefore obtains statistical "classical" correlations from a purely coherent state.

VI.3.4 With the colored noise

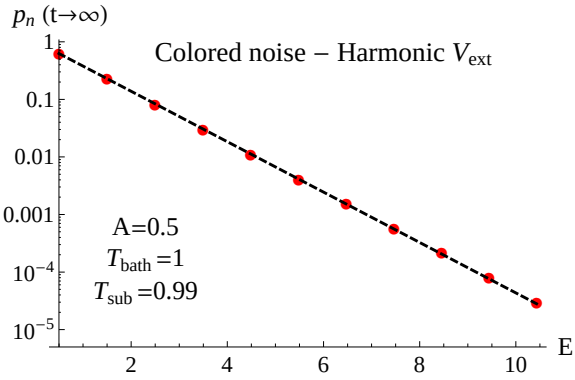

Figure VI.13: The asymptotic distribution of the eigenstate weights $p_{n=0,...10}$ (red dots), obtained with $\{A = 0.5, T_{\text{bath}} = 1\}$, function of the eigenenergies $E_{n=0,...10}$, in comparison to the Boltzmann distribution ($\propto e^{-E/T_{\text{sub}}}$) at $T_{\text{sub}} = 0.99$ (dashed line).

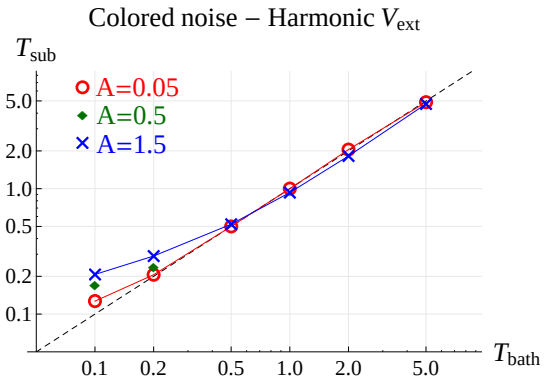

Figure VI.14: Asymptotic subsystem temperature T_{sub} as a function of the bath temperature T_{bath} for three different drags: $A = 0.05$ (red circles), $A = 0.5$ (green diamonds) and $A = 1.5$ (blue crosses) corresponding respectively to a weak, intermediate and strong coupling. The dashed line corresponds to the ideal case $T_{\text{sub}} = T_{\text{bath}}$.

The evolution of the $\langle H_0 \rangle$ average energy is close to the one obtained with the white noise (figure VI.9) and fits Senitzky's law (VI.132) in the weak coupling limit. The evolutions of the eigenstate weights are also close to the ones obtained with the white noise (figure VI.10). As illustrated in figure VI.13, the asymptotic distributions of the weights are Boltzmannian independently of the drag A and initial state, and all the observations made in section VI.3.3.2 apply here too. In figure VI.14, we compare the temperature actually reached by our subsystem T_{sub} to the bath temperature T_{bath} used as input of the noise. When $T_{\text{bath}} \gtrsim 0.5$, the subsystem correctly thermalises in a good approximation (we note a light drag dependence: The larger A the smaller T_{sub}). At lower temperatures, some important discrepancies

(T_{sub} "saturates") appear when $A \gtrsim T_{\text{bath}}$. These weight discrepancies must therefore originate from the Brownian hierarchy breaking as described in section VI.2.2.1.

VI.4 Equilibration with a linear potential

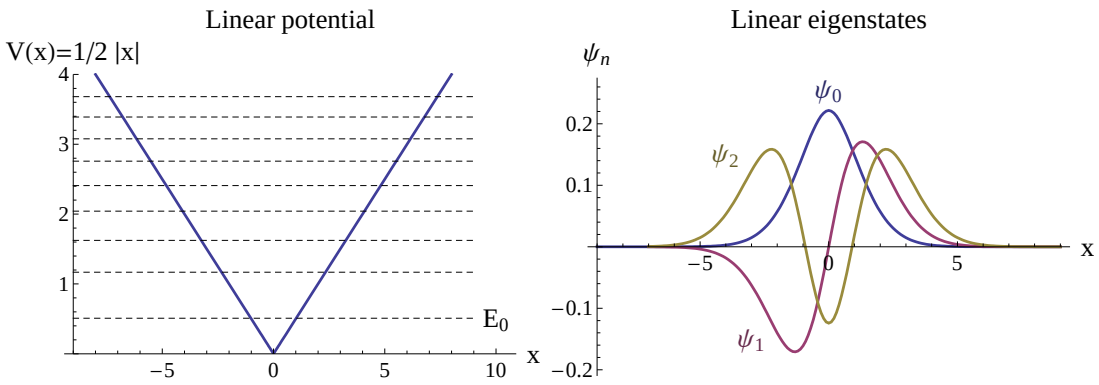

Figure VI.15: *Left*: The linear potential under study (thick line) and its corresponding eigenenergies (dashed lines). *Right*: The corresponding three lower eigenstates.

VI.4.1 With the white noise

As explained in section VI.2.2.1, the white quantum noise (VI.102) and (VI.103) was initially derived for a harmonic potential. In this section, we test its ability to be extended to other types of potentials through the example of the linear potential[68] $V = 1/2\,|x|$. In the white quantum noise expression (VI.103), we set E_0 to the value 0.509 equal to the ground state energy.

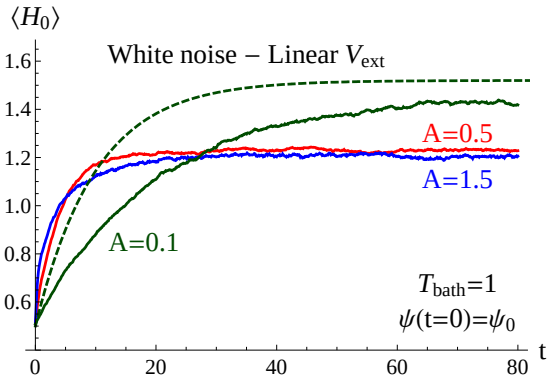

Figure VI.16: Numerical average energy $\langle H_0 \rangle$ evolutions for different drags A (solid curves) and the theoretical evolution given by (VI.132) with $\{T_{\text{bath}} = 1,\ \langle H_0 \rangle(t \to \infty) = 1.52,\ A = 0.1\}$ (dashed curve).

[68] The linear potential is close to the linearly rising quarkonia potential.

As shown in figure VI.16, the asymptotic value of the $\langle H_0 \rangle$ average energy exhibits a strong A-dependence and is not equal to the expected statistical average

$$\langle H_0 \rangle(t \to \infty) = \frac{\sum_i E_i \, e^{-E_i/T_{\text{bath}}}}{\sum_i e^{-E_i/T_{\text{bath}}}} \simeq 1.52 \,. \tag{VI.136}$$

At small drags ($A < 1$), the average energy evolutions are nevertheless in good agreement with the exponential rate (VI.132) when one takes the measured $\langle H_0 \rangle(t \to \infty)$ and effective $A_{\text{eff}} \simeq A/2$ values. Therefore, the energy variation remains proportional to the drag for both types of potentials in the weak coupling regime.

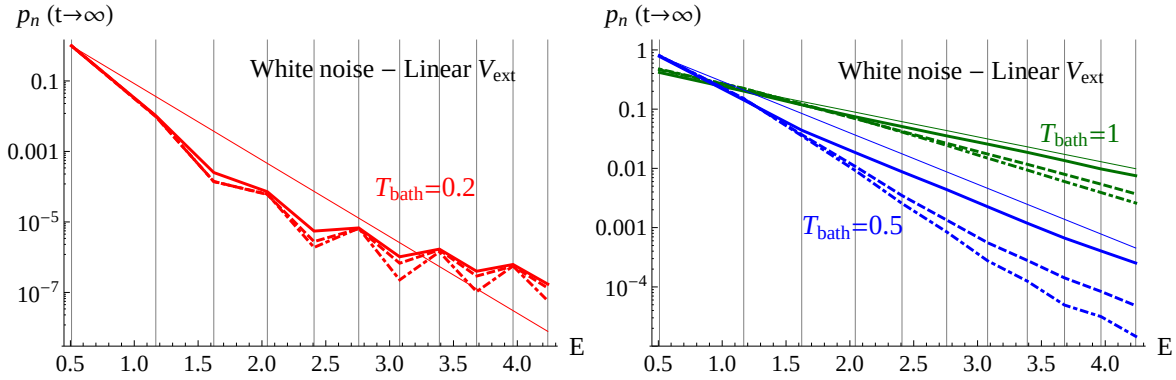

Figure VI.17: The asymptotic distributions of the eigenstate weights $p_{n=0,\ldots 10}$ (joined by lines) function of the eigenenergies $E_{n=0,\ldots 10}$ (vertical lines), obtained with different drags $A = 0.1$ (solid lines), $A = 0.5$ (dashed lines) and $A = 1.5$ (dot-dashed lines) and temperatures $T_{\text{bath}} = 0.2$ (*left*), $T_{\text{bath}} = 0.5$ and 1 (*right*). They are compared to the corresponding "ideal" Boltzmann distributions $\propto e^{-E/T_{\text{bath}}}$ (thin lines).

Independent of the initial state, the asymptotic distributions of the weights $p_{n=0,\ldots 10}$ are close to the Boltzmann distributions $\propto e^{-E/T_{\text{bath}}}$ only when $1 \lesssim T_{\text{bath}} \lesssim 3$ at weak couplings (see figure VI.17). At low temperatures strong discrepancies are observed: The higher excited states exceed the Boltzmann law, exhibit a alternating pattern and saturate at low weights. Moreover, a dependence on the drag value is observed from the 2^{nd} (4^{th}) excited state at low (medium) temperatures. The latter explains the $\langle H_0 \rangle$ dependence on the drag observed in figure VI.16: a smaller drag is observed to generate higher populations for the excited eigenstates and thus a higher average energy. At large temperatures $T \gtrsim 5$, the subsystem temperature T_{sub}, is difficult to evaluate because of statistical fluctuations and numerical scheme imperfections.

Given that the SL equation does not lead to proper Boltzmann distributions in this case, using the previous definition of the subsystem temperature T_{sub} could appear rather unjustified. Nevertheless, as one is often interested in the low lying eigenstates in phenomenology (the fundamental and few lower excited eigenstates), a T_{sub} can be defined for these states by tracing the effective Boltzmann lines $\propto e^{-E/T_{\text{sub}}}$ between the two first weights (p_0 and p_1) as a minimum. The numbers of low lying eigenstates which are then close to the effective Boltzmann lines are summed up in Tab. VI.9. The evaluation of T_{sub} vs. T_{bath}, showed in figure VI.18, exhibits clear discrepancies to the "ideal" $T_{\text{sub}} = T_{\text{bath}}$ line at low and high temperatures and for

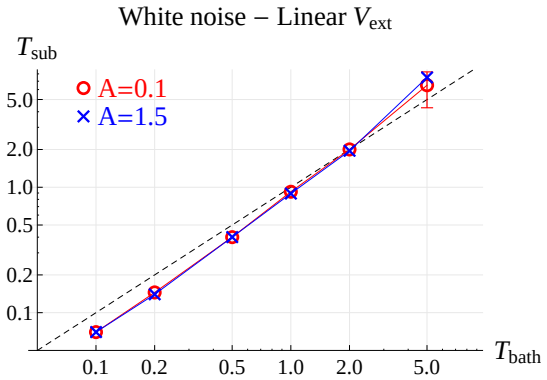

Figure VI.18: Asymptotic subsystem temperature $T_{\rm sub}$ as a function of the bath temperature $T_{\rm bath}$ for two different drags $A = 0.1$ (red circles) and $A = 1.5$ (blue crosses) corresponding respectively to weak and strong couplings. The dashed line corresponds to the ideal case $T_{\rm sub} = T_{\rm bath}$.

any drag value. At high temperatures our accuracy on $T_{\rm sub}$ is low due to a very large time required to reach the asymptotes and a large uncertainty as in section VI.3.3.2 (e.g. for $A = 0.1$, $T_{\rm sub} \in [4.3, 8.3]$ with an average of ~ 6.5).

— Number of weights close to $\propto e^{-E/T_{\rm sub}}$? —			
$T_{\rm bath}$ \ Coupling	Weak	Intermediate	Strong
Low ($T_{\rm bath} < 0.5$)	3	2	2
Medium ($0.5 < T_{\rm bath} < 2$)	5	5	4
High ($T_{\rm bath} > 2$)	10	9	8

Table VI.9: Approximate number of weights close to the corresponding Boltzmannian $\propto e^{-E/T_{\rm sub}}$. One can consider the agreement to be poor from 2 to 4 weights, good from 5 to 7 and very good from 8 to 11. A better agreement is obtained toward the weak coupling and/or high temperature regimes.

In view of these elements, we conclude that the white quantum noise (VI.102) is not quite suitable to obtain an acceptable thermal equilibrium (in the sense of $p_n \propto e^{-E_n/T_{\rm bath}}$) with other external potentials than the harmonic one. Nevertheless, if one is interested in a limited number of low lying eigenstates (see Tab. VI.9), this formalism could be used for phenomenological purposes by performing a rescaling in the noise expression (VI.103): either by changing the value of E_0 (to 0.33 here) or by choosing the input $\tilde{T}_{\rm bath}$ such as to obtain the desired $T_{\rm sub} = T_{\rm bath}$. Conversely, this study confirms the very specific nature of the harmonic potential upon which general conclusions should not be drawn as regards the applicability of any scheme aiming at describing the thermalisation of quantum subsystem.

VI.4.2 With the colored noise

Unlike the white noise, the colored noise (VI.105) was derived without assumptions on the external potential. In this section, we test its ability to be extended to other potentials through the example of the linear potential.

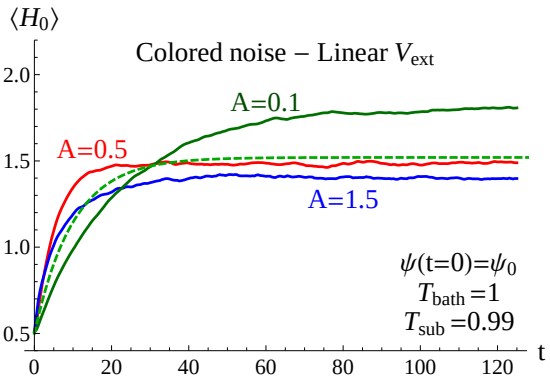

Figure VI.19: Numerical average energy $\langle H_0 \rangle$ evolutions for different drags A (solid curves) and the theoretical evolution given by (VI.132) with $\{T_{\text{bath}} = 1,\ \langle H_0 \rangle (t \to \infty) = 1.52,\ A = 0.1\}$ (dashed curve).

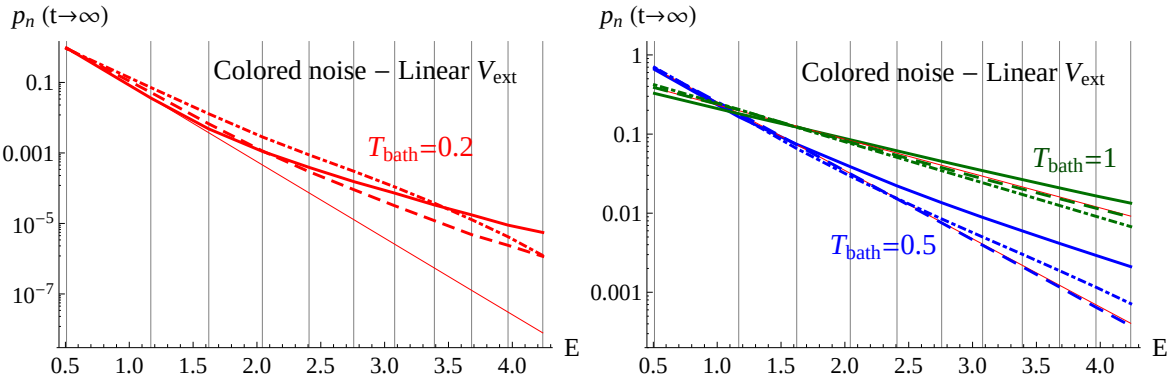

Figure VI.20: The asymptotic distributions of the eigenstate weights $p_{n=0,\dots 10}$ (joined by lines) function of the eigenenergies $E_{n=0,\dots 10}$ (vertical lines), obtained with different drags $A = 0.1$ (solid lines), $A = 0.5$ (dashed lines) and $A = 1.5$ (dot-dashed lines) and temperatures $T_{\text{bath}} = 0.2$ (*left*), $T_{\text{bath}} = 0.5$ and 1 (*right*). They are compared to the corresponding "ideal" Boltzmann distributions $\propto e^{-E/T_{\text{bath}}}$ (thin lines).

As shown in figure VI.19 (left), the $\langle H_0 \rangle$ average energies are similar to the ones obtained with the white noise (figure VI.16). As shown in figure VI.20, the asymptotic distributions of the weights are observed to be independent of the initial state and close to the Boltzmann distributions $\propto e^{-E/T_{\text{bath}}}$ for a limited numbers of low lying eigenstates at the weak coupling limit and at strong couplings when $T_{\text{bath}} \gtrsim A$. At intermediate couplings, the distributions are observed to be "perfectly" Boltzmannian when $T_{\text{bath}} \gtrsim A$. When $T_{\text{bath}} < 0.2$, we observe a similar alternating pattern behaviour than in the white quantum noise case (see figure VI.17) with however lighter oscillations. Despite these discrepancies, the relation T_{sub} vs. T_{bath}

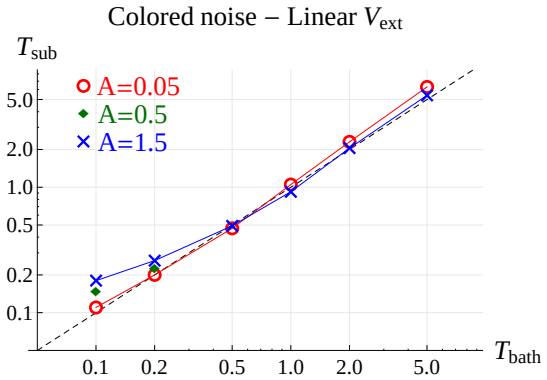

Figure VI.21: Asymptotic subsystem temperature $T_{\rm sub}$ as a function of the bath temperature $T_{\rm bath}$ for three different drags: $A = 0.05$ (red circles), $A = 0.5$ (green diamonds) and $A = 1.5$ (blue crosses) corresponding respectively to a weak, intermediate and strong coupling. The dashed line corresponds to the ideal case $T_{\rm sub} = T_{\rm bath}$.

(figure VI.21), obtained by focusing on the lowest excited states, is interestingly close to the one obtained with the harmonic potential, with the exception of the high temperature regime where one naturally recovers the white quantum noise results ($T_{\rm sub} > T_{\rm bath}$). These observations confirm the rather general nature of the colored noise (VI.105), which might thus be combined with a wider class of potentials and used in a good approximation for thermalisation studies in the weak coupling case.

Main ideas and transition

For the purpose of finding an effective formalism suitable to the thermalisation of quarkonia in a QGP, we have focused on the Schrödinger-Langevin (SL) equation (VI.71). It is a stochastic and non-linear quantum equation which allows a gradual evolution from pure to mixed states through statistic forces.

Its nonlinear friction term is commonly believed to maintain the stationarity of the excited states of the uncoupled Hamiltonian H_0. We have shown in Sec. VI.2.1 that the Madelung/polar transformation of the wavefunction leads to a nonzero damping for these states. In this way, we have reconciled the SL equation with the intuitive expectation that the dissipation process should act on any state in order to bring the subsystem to its ground state. We have then focused on the solutions of the SL equation with two different noise operators taken as c-numbers: the quantum noise (VI.102, VI.103) - which has been derived by Senitzky [172] and subtracted by its term of ground state fluctuations - and the colored noise (VI.105) derived by Ford, Kac and Mazur [185]. When the subsystem undergoes a harmonic potential, the SL equation has demonstrated its ability to bring any initial state to the thermal equilibrium of statistical mechanics (i.e. Boltzmann distributions of the uncoupled subsystem energy states) in the weak coupling limit with either noise, confirming the assumption made by Messer [259]. Though only expected at this limit (as explained in the introduction), the intermediate and strong regimes have also led to the same equilibrium with the white quantum noise and partially with the colored quantum noise. For this case, some disagreements between the subsystem temperature T_{sub} and the bath temperature T_{bath} (input of the noise) have been observed at low temperatures and attributed to the breaking of the Brownian hierarchy. When the subsystem is submitted to a linear potential, non-Boltzmannian behaviours and stronger drag dependences have been observed at low and medium temperatures for both kind of noises. Nevertheless, the colored quantum noise has led to better results in the sense of statistical mechanics (provided that the Brownian hierarchy is preserved), confirming its rather universal nature.

We have therefore observed that within our assumptions (semi-classical noise and negligible shifts of the energy spectrum), the SL equation does not universally lead a subsystem to the thermal equilibrium of statistical mechanics. The SL equation and the quasiclassical Langevin equation seem therefore to have a common difficulty in the description of dissipative evolutions outside the nearly harmonic, free potential cases and classical high temperature limit [182, 209, 204]. Nevertheless, if one focuses on phenomenological applications where only the lower states are considered (e.g. the quarkonia), the SL equation can be used in a good approximation as an effective open quantum system formalism. Dealing with the full hierarchy of states in the general case would possibly require either the use of the colored noise correlation (VI.104), of a q-number noise operator or of a more refined quantum treatment of the subsystem interactions with the heat bath. Another possibility would be to determine a fluctuation-dissipation theorem inherent to the SL equation (probably hardly accessible because of its non-linear nature).

To use the SL equation in practice, one must perform a rescaling of the noise - suited to each mean field potential - to rectify the observed differences between $T_{\rm sub}$ and $T_{\rm bath}$. One can indeed choose an effective heat-bath temperature $\tilde{T}_{\rm bath}$ such as to reach the desired subsystem temperature $T_{\rm sub} = T_{\rm bath}$. It just requires the proper knowledge of the $T_{\rm bath}(T_{\rm sub})$ function as displayed for instance in Fig. VI.18 and VI.21.

It should be noted that our analysis relies on the hypothesis that the asymptotic distribution of subsystem-eigenstates weights p_n must be Boltzmannian whatever the potential and the coupling strength to the rest of the system (the heat bath). To our knowledge, such an assumption has not been universally established from fundamental principles (i.e. starting from the distribution of the full-system eigenstates and tracing out the heat-bath degrees of freedom).

In the next part, we apply this formalism to the correlated $Q\bar{Q}$ pair immersed in a QGP bath at thermal equilibrium within a simplified model. Note finally that, as the drag coefficient for heavy quarks is proportional to T^c with $c \in [1, 2]$, we are a priori safe from the Brownian hierarchy breaking identified for the colored noise.

Part VII

The Schrödinger-Langevin approach to quarkonia suppression

In the previous part VI, we have studied the thermal relaxation - and its limitations - given by the Schrödinger-Langevin (SL) equation for various simple potentials and noises. In the present part, we apply this formalism to the correlated $Q\bar{Q}$ pair subsystem immersed in a QGP bath at thermal equilibrium. In the SL scheme, the time-dependent real potential implements the Debye-screening while the stochastic and dissipative terms express the (hard) interactions between the QGP and the $Q\bar{Q}$ pair, possibly leading to dissociation. The SL equation preserves unitarity and enables to treat the transitions between bound states and with the open states. It allows to consider a realistic compact initial state, made of a linear superposition of quarkonium eigenstates and to preserve the quantum nature of the $Q\bar{Q}$ pair in its time-evolution. The basic ingredients of this model - temperature dependent color screened potentials, temperature scenarios and initial states - are presented in the mean field section III.1. In the latter, the 3D Schrödinger equation in spherical coordinates was reduced to its radial part as transitions only occurred between states of equal orbital quantum number l (we studied there the S states given by $l = 0$). In section VII.1, we first show that the dissipative and fluctuating terms of the SL equation induce transitions between states of different l. A complete treatment of the $Q\bar{Q}$ pair subsystem in a QGP bath hence requires the full 3D SL equation in spherical coordinates. Unfortunately, this complete treatment is not easily accessible and some approximations are required. In the present part, we explore a simplified model where the situation is approximated to a 1D symmetrical linear screened potential (section VII.2). This model should contain the essential physics but is not aimed to reproduce the experimental data; we just wish to grasp the global trends. In section VII.3, we first study the $Q\bar{Q}$ pair dynamics in a QGP at constant temperatures and with the temperature evolutions at RHIC and LHC from Kolb and Heinz "reduced" model[69]. As in the previous parts, we mainly focus on its real-time quarkonia content. In section VII.4, we then carry out this study within a more realistic collision framework extracted from the state-of-the-art EPOS event generator: finite volume, inhomogeneous temperature and quarkonia position-momentum distributions. The predictions are finally compared to experimental data (to some extent) and other models.

[69]In this part, the pre-equilibrium phase before the QGP is considered and assumed to be at $T = T(\tau_{\rm ini})$ (see section III.1.2). As $\tau_{\rm ini} \ll \tau_{\rm relax}$, this modification does not lead to any significant change in the dynamics.

VII.1 The Schrödinger-Langevin equation in 3D spherical coordinates

The SL equation in spherical coordinates writes

$$i\hbar\frac{\partial\psi(\vec{r},t)}{\partial t} = \left[H_0 + \hbar A\Big(S(\vec{r},t) - \int \psi^*(\vec{r'},t)S(\vec{r'},t)\,\psi(\vec{r'},t)\;d^3\vec{r'}\Big) - \vec{r}.\vec{F_R}(t)\right]\psi\,, \quad \text{(VII.137)}$$

where the mean field Hamiltonian H_0 is

$$H_0 = -(\hbar^2/2m)\vec{\nabla}^2 + V(\vec{r}), \quad \text{(VII.138)}$$

m is the reduced mass and $\vec{r}$ the vector between the origin and the point of coordinates (r,θ,ϕ). The wavefunction can be decomposed in the (orthonormal) spherical harmonics basis [153],

$$Y_{l,m}(\theta,\phi) = (-1)^m\sqrt{\frac{(2l+1)}{4\pi}\frac{(l-m)!}{(l+m)!}}\,P_l^m(\cos\theta)\,e^{im\phi}, \quad \text{(VII.139)}$$

where the P_l^m are the associated Legendre polynomials. In this basis, the wavefunction then writes

$$\psi(r,\theta,\phi) = \sum_{l=0}^{L}\sum_{m=-l}^{l} R_{l,m}(r,t)\,Y_{l,m}(\theta,\phi). \quad \text{(VII.140)}$$

where L should be infinite, but can be taken to $L=2$ in practice to obtain from the equation (VII.137) a resolvable set of equations for the coefficients $R_{l,m}$. To do so, one projects equation (VII.137) onto each $Y_{l';m'}$:

$$\int_{\phi=0}^{2\pi}\int_{\theta=0}^{\pi} Y_{l',m'}(\theta,\phi)\,[\text{equation (VII.137)}]\,\sin(\theta)d\theta d\phi. \quad \text{(VII.141)}$$

Using

$$\int_{\phi=0}^{2\pi}\int_{\theta=0}^{\pi} Y_{l',m'}(\theta,\phi)\,Y_{l,m}(\theta,\phi)\,\sin(\theta)d\theta d\phi = \delta_{ll'}\delta_{mm'}, \quad \text{(VII.142)}$$

the equation (VII.137) with a radial potential and without the fluctuation/dissipation terms yields

$$i\hbar\frac{\partial R_{l',m'}(r,t)}{\partial t} = -\frac{\hbar^2}{2m}\left[\frac{1}{r^2}\frac{\partial}{\partial r}\left(r^2\frac{\partial R_{l',m'}}{\partial r}\right) - \frac{l'(l'+1)}{r^2}R_{l',m'}\right] + V(r)R_{l',m'}. \quad \text{(VII.143)}$$

The projection of the stochastic term requires to write the vector $\vec{r}$ in terms of the spherical harmonics,

$$\begin{aligned}\vec{r} &= r\sin\theta\cos\phi\,\vec{e}_x + r\sin\theta\sin\phi\,\vec{e}_y + r\cos\theta\,\vec{e}_z \quad \text{(VII.144)}\\ &= \sqrt{\frac{4\pi}{3}}\,r\,(Y_{1,-1}\,\vec{e}_{-1} + Y_{1,0}\,\vec{e}_0 + Y_{1,1}\,\vec{e}_1),\end{aligned}$$

where

$$\vec{e}_{-1} = \frac{\vec{e}_x + i\vec{e}_y}{\sqrt{2}}, \qquad \vec{e}_0 = \vec{e}_z \qquad \text{and} \qquad \vec{e}_1 = \frac{-\vec{e}_x + i\vec{e}_y}{\sqrt{2}}. \tag{VII.145}$$

In the latter basis, the stochastic force writes

$$\vec{F}_R(t) = \frac{F_x - iF_y}{\sqrt{2}}\,\vec{e}_{-1} + F_z\,\vec{e}_0 - \frac{F_x + iF_y}{\sqrt{2}}\,\vec{e_1} \equiv F_{-1}\,\vec{e}_{-1} + F_0\,\vec{e}_0 + F_1\,\vec{e}_1. \tag{VII.146}$$

The projected stochastic term is then

$$\begin{aligned} & \sum_{l,m} \int_{\phi=0}^{2\pi} \int_{\theta=0}^{\pi} Y^*_{l',m'}(\theta,\phi)\,\vec{r}.\vec{F}_R(t)\,R_{l,m}Y_{l,m}\,\sin(\theta)d\theta d\phi \qquad \text{(VII.147)} \\ = \; & \sqrt{\frac{4\pi}{3}}\,r \sum_{l,m} \sum_{m''=-1}^{1} R_{l,m}\,\vec{e_{m''}}.\vec{F}_R(t) \int_{\phi=0}^{2\pi} \int_{\theta=0}^{\pi} Y^*_{l',m'} Y_{1,m''} Y_{l,m} \sin(\theta)d\theta d\phi \\ = \; & \sqrt{\frac{4\pi}{3}}\,r \sum_{l,m} \Xi_{l,m,l',m'}(r,t) R_{l,m} \end{aligned}$$

where Ξ is a tensor. In appendix A (page 195), an explicit expression of the matrix resulting from the sum in equation (VII.147) is given in the limited case $L = 2$.

The projection of the dissipative term is

$$\hbar A \sum_{l,m} R_{l,m} \int_{\phi=0}^{2\pi} \int_{\theta=0}^{\pi} Y^*_{l',m'}(\theta,\phi) \Big(S(\psi) - \langle S(\psi) \rangle \Big) Y_{l,m}\,\sin(\theta)d\theta d\phi \tag{VII.148}$$

As $S(\psi)$ is non-linear, it cannot be decomposed in the spherical harmonics basis. Hence, one should determine the phase of the wavefunction numerically on each sphere of radius r and proceed to the integration both in the entire space for the regulator $\langle S(\psi) \rangle$ and on each sphere of radius r for the integral in (VII.148). If one calls $c_{l,m}$ the results of the main integrals in equation (VII.148), one should obtain a dissipative term of the form:

$$\hbar A \sum_{l,m} c_{l,m}(r,t)\,R_{l,m}. \tag{VII.149}$$

In the limited case $L = 2$, one finally obtains a set of 9 crossed equations as illustrated in appendix A (page 195). Each crossed equation includes terms with different values of l and m: the dissipative and fluctuating terms of the SL equation induce transitions between states of different orbital and magnetic quantum numbers. A complete treatment of the $Q\bar{Q}$ pair subsystem in a QGP bath hence requires the resolution of the 3D SL equation and cannot be reduced to its radial part as in part III. Unfortunately, the numerical resolution of a system of numerous crossed equations is not easily accessible (though feasible for $L = 2$). For now, we will rather explore a limited simplified 1D model.

VII.2 Generalities: simplified potential and noise rescaling

VII.2.1 1D simplified potentials

Within this simplified model, we approximate the $Q\bar{Q}$ self interaction in the vacuum to a 1D symmetrical linear potential $1/2\,K|x|$ saturated[70] at $V_{\max} = 1.2$ GeV, i.e.

$$V_{\text{lin}}(x, T=0) = \begin{cases} 1/2\,K|x| & \text{when} \quad 1/2\,K|x| < 1.2\,\text{GeV} \\ 1.2 & \text{when} \quad 1/2\,K|x| \geq 1.2\,\text{GeV} \end{cases} \tag{VII.150}$$

The color self binding potentials are indeed mainly linear around the considered eigenenergies. The string parameter K is chosen such as to obtain an energy difference between the first two even states given by $E_2 - E_0 = E(\psi') - E(J/\psi) = 589$ MeV for charmonia and $E_2 - E_0 = E(\Upsilon') - E(\Upsilon) = 563$ MeV for bottomonia. It leads[71] to $K = 1.54$ for charmonia and $K = 2.75$ for bottomonia.

The effect of the T-dependent Debye screening is taken into account by saturating the linear potential V_{lin} to the value of the weak or strong color potentials at large distances[72] $V(r \to \infty, T)$, i.e.

$$V_{\text{lin}}^{\text{weak}}(x, T) = \begin{cases} 1/2\,K|x| & \text{when} \quad 1/2\,K|x| < V_{\text{weak}}(r \to \infty, T) \\ V_{\text{weak}}(r \to \infty, T) & \text{when} \quad 1/2\,K|x| \geq V_{\text{weak}}(r \to \infty, T) \end{cases} \tag{VII.151}$$

and

$$V_{\text{lin}}^{U}(x, T) = \begin{cases} 1/2\,K|x| & \text{when} \quad 1/2\,K|x| < U(r \to \infty, T) \\ U(r \to \infty, T) & \text{when} \quad 1/2\,K|x| \geq U(r \to \infty, T) \end{cases} \tag{VII.152}$$

At $T = 0$, note that $V_{\text{lin}}^{\text{weak}}$ and V_{lin}^{U} are both equivalent to the vacuum linear potential, i.e. $V_{\text{lin}}^{\text{weak}}(T=0) = V_{\text{lin}}^{U}(T=0) = V_{\text{lin}}(T=0)$. The potential $V_{\text{lin}}^{\text{weak}}$ is illustrated in figure VII.1 for different temperatures. The number of bound states (i.e. such as $E_n \leq V(r \to \infty, T)$) as a function of the temperature then follows the evolution of the much different weak and strong saturations (see figure III.6 and VII.2). As discussed in section III.1.1, the strong potential is determined without irreversible exchange of energy between the quarkonia and the bath, as opposed to the weak potential. The saturation given by the strong potential might therefore be more suited to a formalism, such as the SL equation, where the thermal exchanges are provided explicitly[73]. Within the $V_{\text{lin}}^{\text{weak}}$ model especially, the $\Upsilon(3S)$-like state is not bound ($E_4 > 1.2$ GeV) whereas it should be in reality. We therefore do not expect relevant results for this state and its results are given on an indicative basis.

[70] For the string breaking; see section III.1.1.

[71] With $m_c = 1.25$ GeV and $m_b = 4.575$ GeV.

[72] See figure III.6 and section III.1.1.

[73] Though it remains an open question, as one could say that with the thermal forces we rather reproduce the imaginary part of the potential.

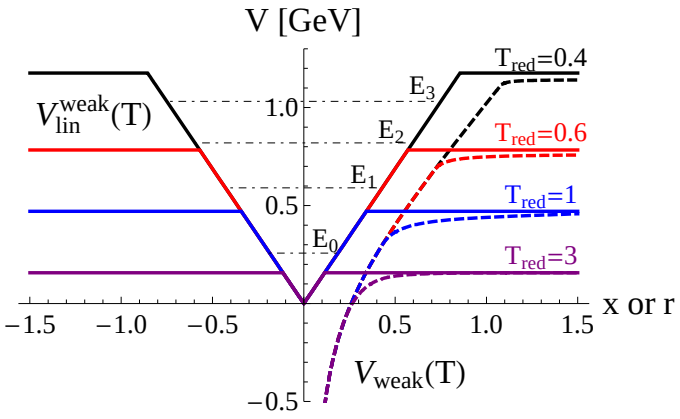

Figure VII.1: The 1D symmetrical linear potential $V_{\text{lin}}^{\text{weak}}(x,T)$ for a $b\bar{b}$ pair (solid lines) and the weak potential V_{weak} (dashed lines) at four different reduced temperatures ($T_{\text{red}} = T/T_c$ where $T_c = 0.165$ GeV). The eigenenergies of the vacuum potential V_{lin} are represented by dot-dashed horizontal lines: E_0, E_1, E_2, E_3 respectively correspond to the $\Upsilon(1S)$-like, χ_b-like, $\Upsilon(2S)$-like, χ_b'-like states. Obtained by removing the saturation, the eigenenergy $E_4 \sim 1.22$ GeV corresponds to the $\Upsilon(3S)$-like state.

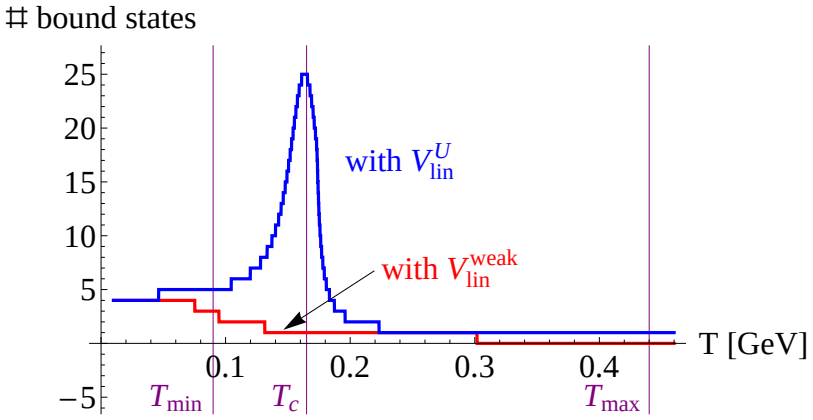

Figure VII.2: The number of bottomonium bound states as a function of T for $V_{\text{lin}}^{\text{weak}}$ and V_{lin}^{U}. The temperatures T_{min} and T_{max} correspond to the minimum and maximum values in Kolb and Heinz model at LHC.

Finally, one should note that, as in the previous parts, we only consider the vacuum eigenstates to evaluate the quarkonia content of a $Q\bar{Q}$ pair and not the instantaneous eigenstates (at T). There is therefore a mismatch between the Hamiltonian states and the projection basis. Nevertheless, as defined here, the quarkonia content allows us to study in a fixed basis the real-time dynamics of a $Q\bar{Q}$ pair all along its evolution (and especially of its bound component). As we assume an instantaneous transition to the vacuum states at the chemical freeze-out, it is only at this stage that the quarkonia content recovers all its physical meaning.

VII.2.2 Equilibration and rescaling

Conceptually, the effects of a thermal bath on the $Q\bar{Q}$ pair should be both a partial dissociation and a thermalisation of the bound component. Within our

wavefunction approach, the dissociation is related to the continuous "leakage" of the wavefunction out of the potential well due to the color screening/saturation and the thermal forces. The thermalisation of the bound component (i.e. what remains inside the potential well) is brought by a combination of dissipative and stochastic forces, and should lead to a re-equilibration of the populations as given by the Boltzmann distribution (IV.57).

As was observed and discussed in section VI.4 for the linear potential, the temperature of the subsystem[74] $T_{\rm sub}$ at equilibrium does not corresponds in most situations to the bath temperature[75] $T_{\rm bath}$ within the SL framework. One then needs to perform a rescaling of the noise correlation to obtain a better agreement between $T_{\rm sub}$ and $T_{\rm bath}$ at equilibrium. If one would choose to perform such a rescaling with the linear potential that includes the saturation/screening, most of the eigenstates would be unbound for the typical range of QGP temperatures, and one would not obtain the required Boltzmann-like distributions even for the lowest states. Therefore, we consider instead the linear potential without the saturation/screening (i.e. with $V_{\rm max} = \infty$) to deduce the rescaling law. We will see in the next section that one then obtains the correct thermalisation of the bound components even when the saturation/screening is turned back on.

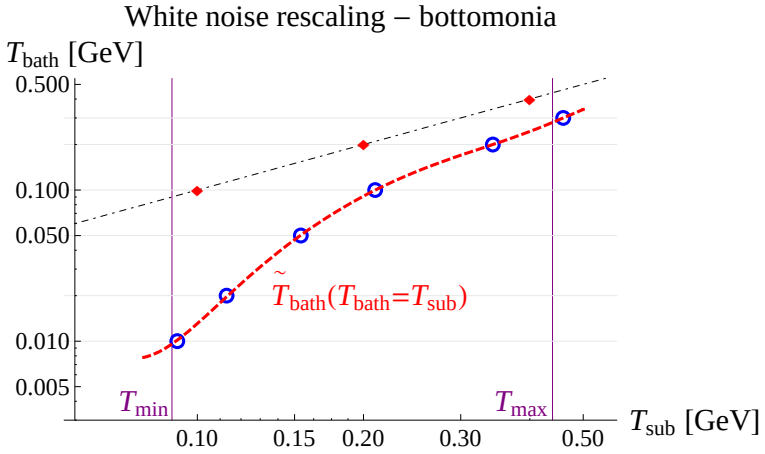

Figure VII.3: To obtain a rescaling of the white noise correlation for bottomonia, the measured $T_{\rm bath}(T_{\rm sub})$ distribution (circle points) is fitted to a polynomial function $\tilde{T}_{\rm bath}(T_{\rm bath})$ $(= 0.100266 - 2.89439T_{\rm bath} + 28.9901T_{\rm bath}^2 - 103.683T_{\rm bath}^3 + 170.61T_{\rm bath}^4 - 104.392T_{\rm bath}^5$ here) (dashed curve). The dot-dashed line corresponds to the ideal case $T_{\rm bath} = T_{\rm sub}$. The vertical lines correspond to the minimum and maximum temperatures in Kolb and Heinz model at LHC (see III.1.2). The red diamonds correspond to three $T_{\rm sub}$ measured at equilibrium while using the noise rescaling: the subsystem now correctly thermalises for the states of interest.

As introduced in section VI.4.2, the rescaling consists in the use of an effective bath temperature $\tilde{T}_{\rm bath}$ as input of the noise correlation such as to reach the desired

[74] $T_{\rm sub}$ is measured by tracing the effective Boltzmann lines $\propto e^{-E/T_{\rm sub}}$ between the two lowest weights.

[75] The bath temperature is used as an input of the noise correlation.

subsystem temperature $T_{\rm sub} = T_{\rm bath}$. It just requires to fit the $T_{\rm bath}(T_{\rm sub})$ function, obtained with the drag $A(T_{\rm bath})$, with a polynomial function as illustrated in figure VII.3 for bottomonia and the white noise. Then, if one desires to obtain the subsystem temperature $T_{\rm sub} = T_{\rm bath}$ at equilibrium, one chooses the corresponding $\tilde{T}_{\rm bath}(T_{\rm bath})$ value, given by the fit, as the new input of the noise correlation. Note that the color noise rescaling should be only weakly affected by the "saturation" effect observed in part VI (which appeared when the Brownian hierarchy was strongly broken) as $A(T) \propto T$ for the quarkonia.

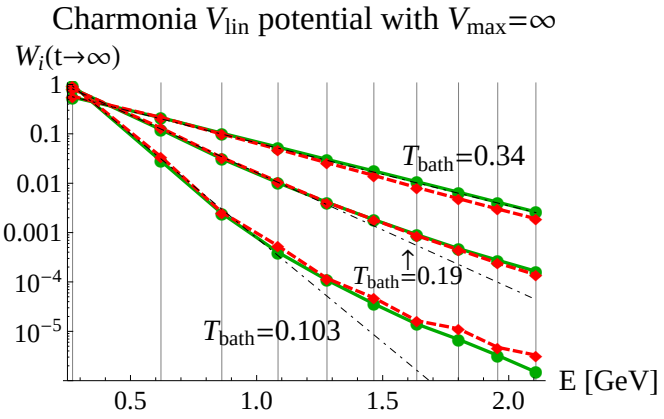

Figure VII.4: Comparison of the equilibrium distributions given by the rescaled white (dashed lines) and colored (solid lines) noises for three different bath temperatures [GeV].

Once rescaled, one should wonder whether the white or the colored noise is better suited for this model. As shown for instance in figure VII.4 for the charmonia, the equilibrium distributions of the weights obtained with the white and colored noises show no important differences for the typical temperature range of the QGP. Furthermore, for the lower states of main interest (J/ψ, χ_c and ψ'-like states for charmonia and $\Upsilon(1S)$, χ_b, $\Upsilon(2S)$ and $\Upsilon(3S)$-like states for bottomonia), the distributions are close to Boltzmannian. Finally, as the colored noise is more expensive numerically and as the white noise rescaling is independent of the drag value, the latter will be used preferentially for this model. *To simplify the notations*, in the following we will write T for $T_{\rm bath}$ (*exception* made with notation $V_{\rm lin}^{\rm weak}(T=0)$ which only means that we use the vacuum potential and not that the bath is at $T=0$).

VII.3 Evolutions at constant temperatures and with Kolb and Heinz model

VII.3.1 Charmonia results and analysis

We recall that for a $c\bar{c}$ pair in a QGP at temperature T, we use the drag coefficient given by $A(T)[\text{c/fm}] \cong 3T[\text{GeV}] + 2.5T^2$ (see section V.2.1). Different initial states are considered for the $c\bar{c}$ pair: the J/ψ-like and ψ'-like states if one considers that the quarkonia form before the deconfined phase or a Gaussian compact state of

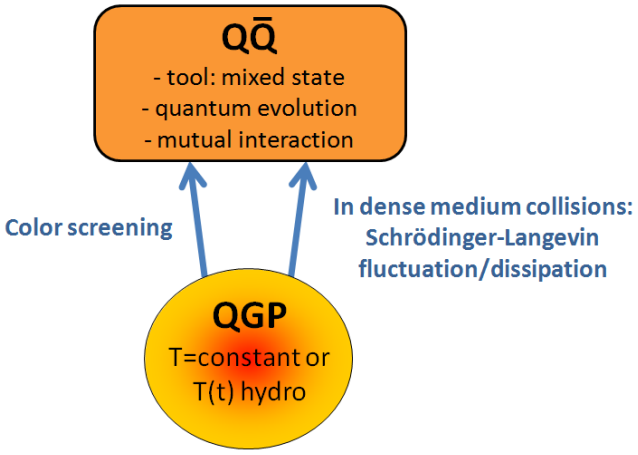

Figure VII.5: Illustration of our approach within the following section VII.3 through its basic ingredients and interactions between the $Q\bar{Q}$ and QGP systems.

parameter $a = 0.165$ fm if not (see section III.1.3). This will allow to evaluate the effect of the initial state on the survivances.

VII.3.1.1 At constant temperatures

In this section, we focus on the overall dynamics of the $c\bar{c}$ pair at some fixed temperatures. Several models are investigated to better observe the contributions of the mean field and thermal forces: the mean field only model "$V_{\rm lin}(T)$", the vacuum potential plus thermal forces model "$V_{\rm lin}(T=0)+$stocha" and the screened potential plus thermal forces model "$V_{\rm lin}(T)+$stocha".

a) Evolution of the charmonium-like weights.

The evolutions of the charmonium weights obtained with $V_{\rm lin}^{\rm weak}$ for different bath temperatures, initial states and models are shown in figures VII.6 and VII.7. First of all, one should notice that the evolutions obtained with the 1D linear *mean field only* (thin curves) are quantitatively very different from what we obtained with the 3D radial mean field in part III (compare figures III.17 and VII.6 for instance). With the mean field only, the 1D linear potentials lead to smaller suppressions than the 3D radial potentials.

We now focus on the models which *include the thermal forces* (thick or dashed curves). One first observes a re-equilibration of the charmonium weights during a transient phase $t \lesssim \tau_{\rm relax} \sim 5$ fm/c towards a "thermal" hierarchy (i.e. $W_i > W_{i+1}$). After this transient phase, the continuous leakage of the wavefunction out of the potential well leads to a universal decay of the $c\bar{c}$ pair system. The exponential decay rate Γ at large times is indeed common to all weights and is independent of the initial state (see example at $T = 0.3$ GeV). Qualitatively, the rate Γ is observed to increase with the temperature when there is no screening (dashed curves), whereas it saturates for intermediate temperatures $T \gtrsim 0.2$ GeV with the screening (thick curves). At large times $t \gg \tau_{\rm relax}$, note finally that the weights become al-

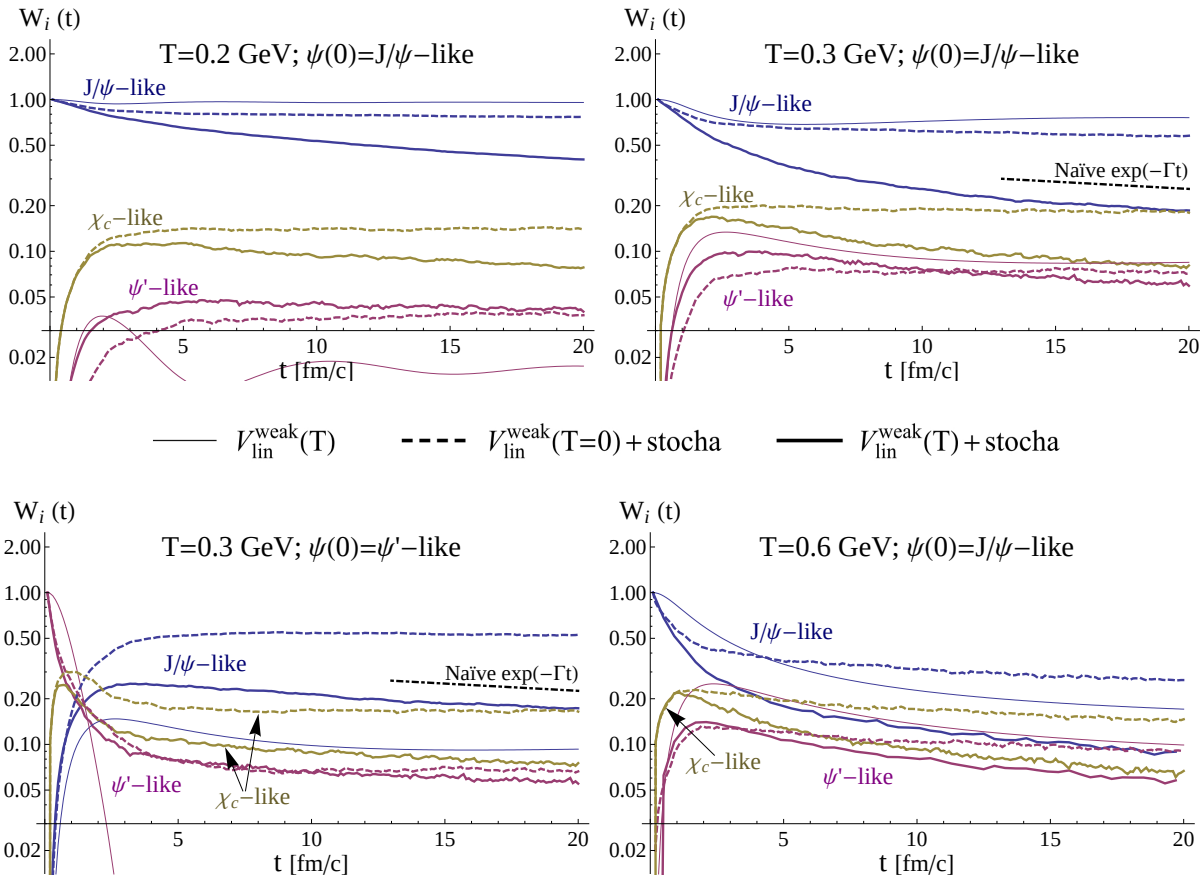

Figure VII.6: Evolutions of the charmonium weights obtained with $V_{\rm lin}^{\rm weak}$ for different bath temperatures and initial states. The thin curves are obtained with the color screening but without thermal forces (i.e. the "mean field" situation), the dashed curves with the thermal forces but without screening (i.e. the vacuum potential $V_{\rm lin}^{\rm weak}(T=0)$ which saturates at $V_{\rm max}=1.2$ GeV) and the thick curves with both features. See numerical version for colors.

most independent of the initial state (compare for instance the thick curves for the weights W_i at $T=0.3$ GeV from the initial J/ψ-like, ψ'-like and Gaussian states in figures VII.6 and VII.7). For the models including the thermal forces, the initial coherences are thus suppressed and replaced by locally equilibrated correlations[76]. One can qualitatively compare the evolutions of the J/ψ component obtained with the present 1D thermal model and the ones obtained within the 3D semi-classical framework of part V (compare for instance the J/ψ survivance S_i in figure VII.7 at $T=0.3$ and the one in V.5). They have in common the exponential decay after a transient phase. However, the transient phases are very different: we obtained an important "overshoot" in the semi-classical framework whereas it is very small or inexistent here (see J/ψ-like curves in figure VII.8). Furthermore, the decay rates were clearly larger in the semi-classical framework.

As expected, the *comparison between the models with and without color screen-*

[76] As also discussed in section VI.3.3.3.

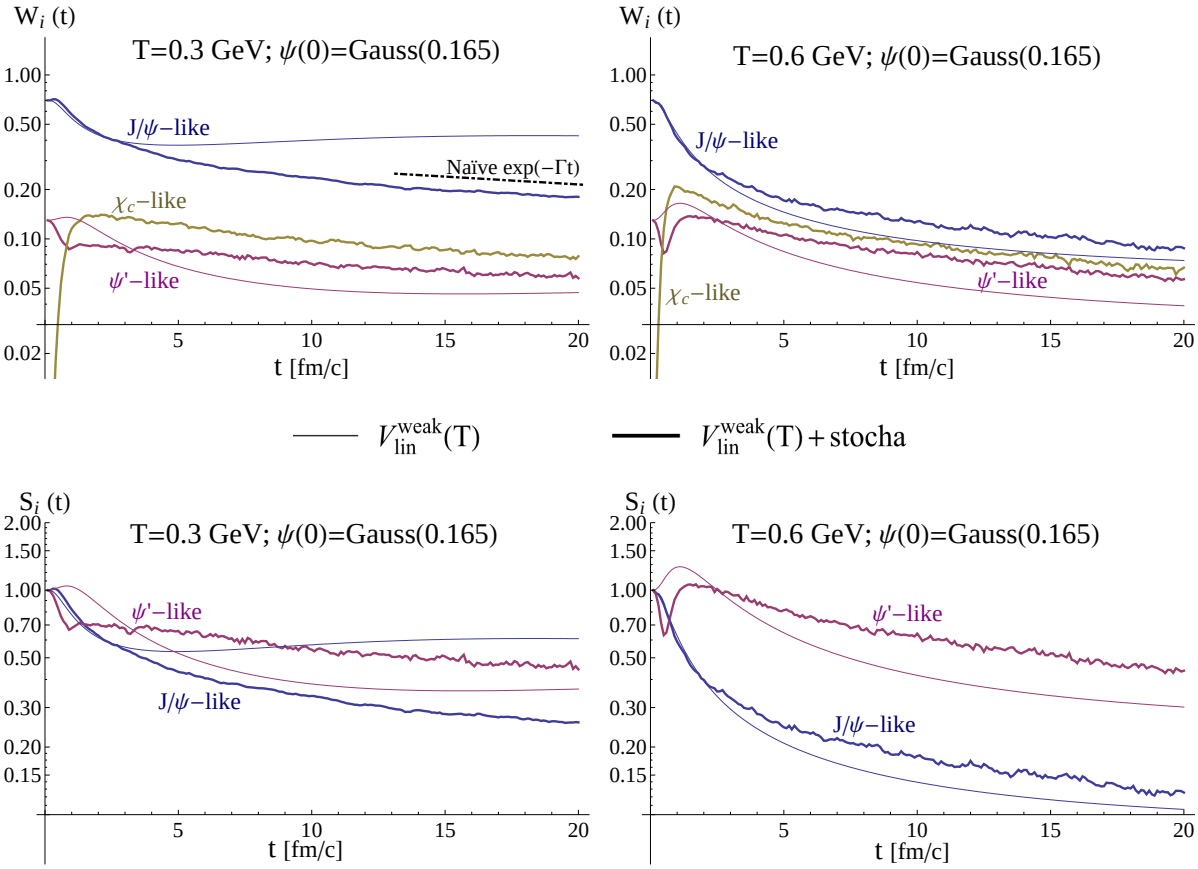

Figure VII.7: Evolutions of the charmonium weights (*top*) survivances (*bottom*) obtained with $V_{\rm lin}^{\rm weak}(T)$ from an initial Gaussian state for different bath temperatures. The thin curves are obtained with the color screening but without thermal forces (i.e. the mean field situation) and the thick curves with both features.

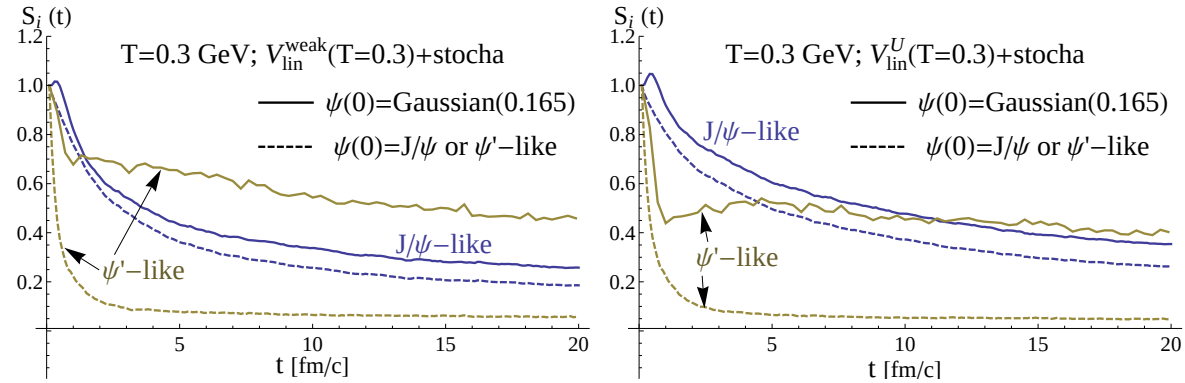

Figure VII.8: Evolutions of the charmonium survivances obtained with $V_{\rm lin}^{\rm weak}(T)$ (*left*) and $V_{\rm lin}^{U}(T)$ (*right*) from different initial states at a bath temperature $T = 0.3$ GeV. The thick curves correspond to an initial Gaussian state and the dashed curves from an initial J/ψ-like and ψ'-like states for the J/ψ-like and ψ'-like survivances respectively.

ing (thick and dashed curves respectively) shows that the screening leads to larger decay rates and suppressions at large times $t \gg \tau_{\rm relax}$. At intermediate times and

especially at low temperatures, the ψ' component can be less suppressed with the screening (see $T = 0.2$ in figure VII.6 for instance), repopulated transiently by the diffusion of the wavefunction. The *comparison between the models with and without thermal forces* (thick and thin curves, respectively) highlights the effect of the thermal forces on the wavefunction trajectory and on the weight distributions. Whereas the mean field situation is driven by ballistic trajectories, which lead to a strong dependence on the initial state, the thermal situation is driven by a thermal diffusion which suppresses this dependence at large times (see also figure VII.11). Including thermal forces can then lead to relatively more or less suppression than the pure mean field situation, depending on the initial state, the bath temperature and the considered component. Even so, we note that the thermal forces lead to larger decay rates and suppressions for the J/ψ component from an initial J/ψ-like state (figure VII.6), and to smaller suppressions at large temperatures ($T \gtrsim 0.5$ GeV) from an initial Gaussian state (figure VII.7 (top)). At high temperatures (and therefore large drags), the relative motion of the heavy quarks could therefore be slowed down in the diffusive regime relatively to its ballistic counterpart. Furthermore, from an initial Gaussian state, the survivance $S_i(t) = W_i(t)/W_i(t = 0)$ of the ψ'-like component is larger than the J/ψ-like one for temperatures above $T \gtrsim 0.25$ GeV (see figures VII.7 (bottom)). As we will see with the LHC temperature scenario, this effect could explain the puzzling observation made by the CMS collaboration that the ψ' is less suppressed than the J/ψ for certain kinematics[77]. In our opinion, this observation can only be fully understood by considering the quantum nature of the $c\bar{c}$ pair.

One of the main assumption of the sequential suppression model (see II.2.1.2) is the very fast and full decorrelation of melted states (a state for which the dissociation temperature is smaller than the bath temperature). Within our framework, this assumption is ruled out for several reasons. First, the evolution of the $c\bar{c}$ pair can lead to non-vanishing weights[78] at large times even for "melted" states (see figures for $T = 0.6$ GeV for instance). Second, thanks to the quantum correlations, the survivance of a state can strongly depend on the initial state, whereas within the sequential suppression model one should obtain the full suppression of the melted components whatever the initial state. Concrete consequence of these effects is illustrated in figure VII.8. Note finally in this figure the interest of the survivance evolutions obtained from the Gaussian initial state (which can be seen as a mix of quarkonium states): each component is a mix of contributions from its own depopulation (as obtained with the quarkonium initial state) and from its regeneration from the depopulations of other components. The survivance of a state i from the quarkonium initial state i gives thus only a partial information on its actual survivance[79].

[77] See section II.3.3.

[78] Assuming an instantaneous transition from the state of the pair at some large time to the quarkonium vacuum states.

[79] One should sum over the contributions obtained from each initial quarkonium states, to obtain its actual value.

b) Local equilibriums.

Because of the wavefunction continuous leakage out of the potential well, the system cannot reach a stable equilibrium - as obtained in part VI - but only local equilibriums at each $t \gg \tau_{\rm relax}$. The true equilibrium corresponds to the complete dissolution of the $c\bar{c}$ pair over infinite space[80]. As illustrated in figure VII.9 (left panel), even though the noise rescaling was performed without saturation and screening, one still obtains the correct thermal equilibrium for the relative weights of the bound and almost bound states despite the presence of the saturation/screening. Here we define a state i to be bound or almost bound if its energy is $E_i \lesssim V_{\rm lin}(x \to \infty, T)$. Note that the overall normalisation of these thermal distributions continuously shrinks with the wavefunction continuous leakage towards large distances. For the unbound states (i.e. $E_i > V_{\rm lin}(x \to \infty, T)$), one does not expect any thermalisation and the weights only reflect the density of the free $Q\bar{Q}$ component in the vicinity of the potential well (which overlaps with the unbound state wavefunctions). As shown in figure VII.9 (right panel), within our model, its leads to quite flat distributions of the unbound state weights.

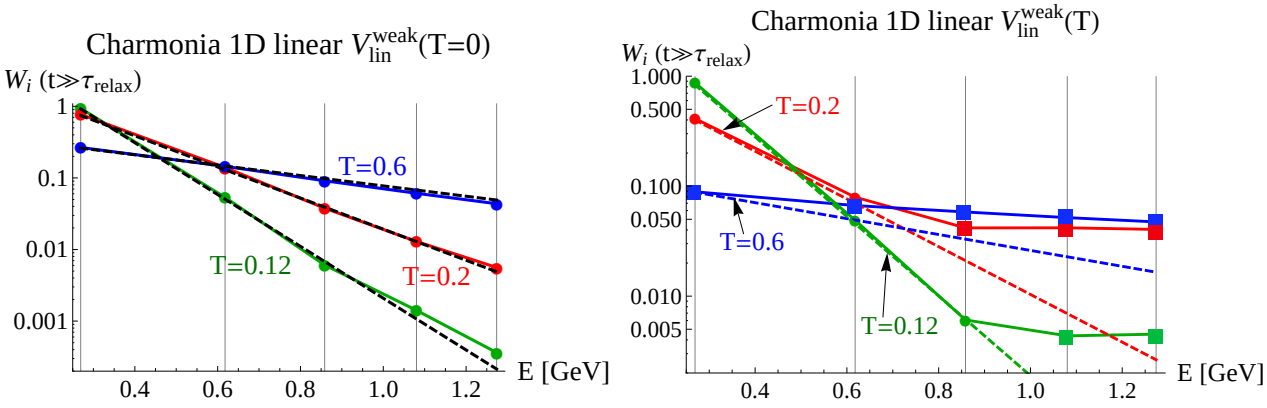

Figure VII.9: *Left*: The distributions of the charmonium weights when the subsystem is locally equilibrated at some $t \gg \tau_{\rm relax}$ (solid lines) obtained with the vacuum potential $V_{\rm lin}^{\rm weak}(T=0)$ (i.e. with four bound states and one "almost" bound ($\Upsilon(3S)$)) and for different bath temperatures. The dashed lines show the corresponding Boltzmann distributions. *Right*: Same but with the screened potential $V_{\rm lin}^{\rm weak}(T)$. One has zero, two and three bound (or almost bound) states at $T = 0.6$, $T = 0.2$ and $T = 0.12$ GeV respectively. The unbound states (for which one does expect a thermalisation) are indicated by squares.

In a stationary QGP, the SL equation therefore naturally leads to local distributions of the quarkonium states following correct relative statistical weights, which allows to make the connection with models based on the hypothesis of statistical recombination. This sanity check is a unique feature of our approach.

[80]The grid size has to be chosen such as the wavefunction reflexions on the grid boundaries to be small.

c) Mean squared position and probability density.

One can check the relative motion of the heavy quarks through the mean square position $\langle x^2 \rangle$ (see figure VII.10). As expected, with the thermal forces one obtain a diffusive evolution, i.e. $\langle x^2 \rangle \propto t$ after a transient phase [151], which contrasts with the ballistic evolution obtained with the mean field only (see part III).

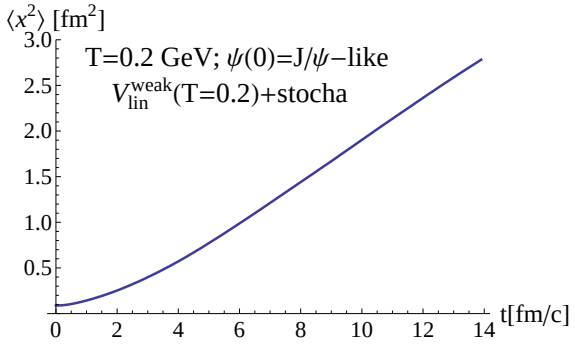

Figure VII.10: Evolution of the mean square radius from an initial J/ψ-like state with $V_{\rm lin}^{\rm weak}$ and the thermal forces at $T = 0.2$ GeV. One obtains $\langle x^2 \rangle \propto t$ after a transient phase.

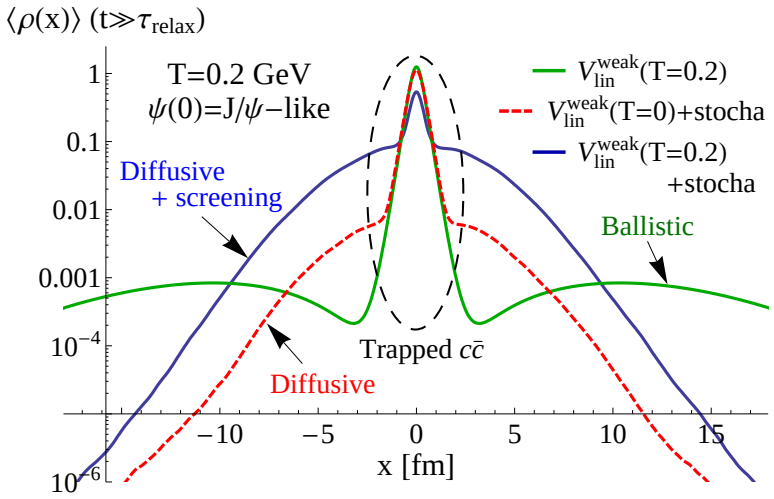

Figure VII.11: Probability density $\rho(x,t) = \langle |\psi(x,t)|^2 \rangle_{\rm stat}$ of the $c\bar{c}$ subsystem at local equilibrium (at a certain time $t \gg \tau_{\rm relax}$) in a bath at $T = 0.2$ GeV.

Another interesting observable is the probability density $\rho(x,t) = \langle |\psi(x,t)|^2 \rangle_{\rm stat}$. Three different regimes of wavefunction leakage can be observed in figure VII.11: a ballistic one when there is no thermal forces, a weakly diffusive one with the thermal forces and the vacuum potential, and a strongly diffusive one with the thermal forces and the screened potential. The ballistic regime is clearly converted into a diffusive regime with the thermal forces. The three regimes have in common that part of the $c\bar{c}$ subsystem remains trapped inside the potential "well" and populates the eigenstate weights. The observation of the probability density at large distances

is an excellent test to check the effect of the grid size. Indeed, if the latter is not large enough, one can observe important density oscillations and a lump near the grid limits. The latter occur when the wavefunction reflections on the grid wall are too important, which may also compromise the relevant central area.

d) Conclusion.

A similar dynamics is obtained with the "strong" potential $V_{\rm lin}^{U}$ and the discussions are equivalent to the one developed so far for the $V_{\rm lin}^{\rm weak}$ potential. We have therefore already observed non-trivial evolutions with a stationary medium at constant temperatures and showed that both the screening and the thermal forces have a strong influence. Moreover, the thermal diffusion replaces the ballistic evolution obtained with the mean fields only.

VII.3.1.2 At RHIC

We now include in the model the hydrodynamic temperature scenario at RHIC from Kolb and Heinz model as described in section III.1.2. The drag coefficient being only valid in the deconfined phase, the evolution for $T < T_c$ is given on an indicative basis. As shown in figure VII.12, one first observes a thermal re-equilibration of the eigenstate weights during a transient phase ($t \lesssim \tau_{\rm relax} \sim 5$ fm/c), along with an initial suppression due to the screening. Whereas this transient phase is similar to what we observed at constant temperatures, the evolution then behaves quite differently from the previous "universal" decay: the J/ψ component gets continuously repopulated whereas the χ_c and ψ' components keep on depopulating. These opposite tendencies originate in the the two main aspects of the thermal dynamics: 1) wavefunction diffusion toward large distances following the variations of the color screening and drag ($\propto T$) especially due to the stochastic term and 2) cooling toward lower states while the bath temperature decreases thanks to the friction term.

The comparison between the dashed and thick curves (i.e. without and with color screening) shows that the screening leads to larger suppressions (by a factor 2 or less) for the J/ψ component and smaller suppressions for the ψ' component. Similarly, the comparison between the thin and thick curves (i.e. without and with thermal forces) shows that the thermal forces mainly lead to larger or equivalent suppressions for the J/ψ component and to *smaller* suppressions for the ψ' component. The evolutions obtained with the weak and strong linear potentials are roughly similar, but the latter logically leads to less suppression for the typical QGP lifetime (~ 10 fm/c). Note that the strong linear potential does not reproduce the weight oscillations that we have observed with the genuine strong potential $V = U$ (see sections III.4 and V.1.2). From the different initial states, one obtains the same kind of evolutions after the transient phase and only a little difference for the weight values at large times (but not for the survivances). Indeed, while only $\sim 2-6\%$ of the ψ' survives from an initial ψ' state, more than $\sim 20-30\%$ does from an initial Gaussian state (see comparisons in figure VII.13). It shows that the ψ' found at the end of the QGP evolution are mostly the ones regenerated from J/ψ. One can finally notice that the J/ψ component gets also a contribution from the suppression

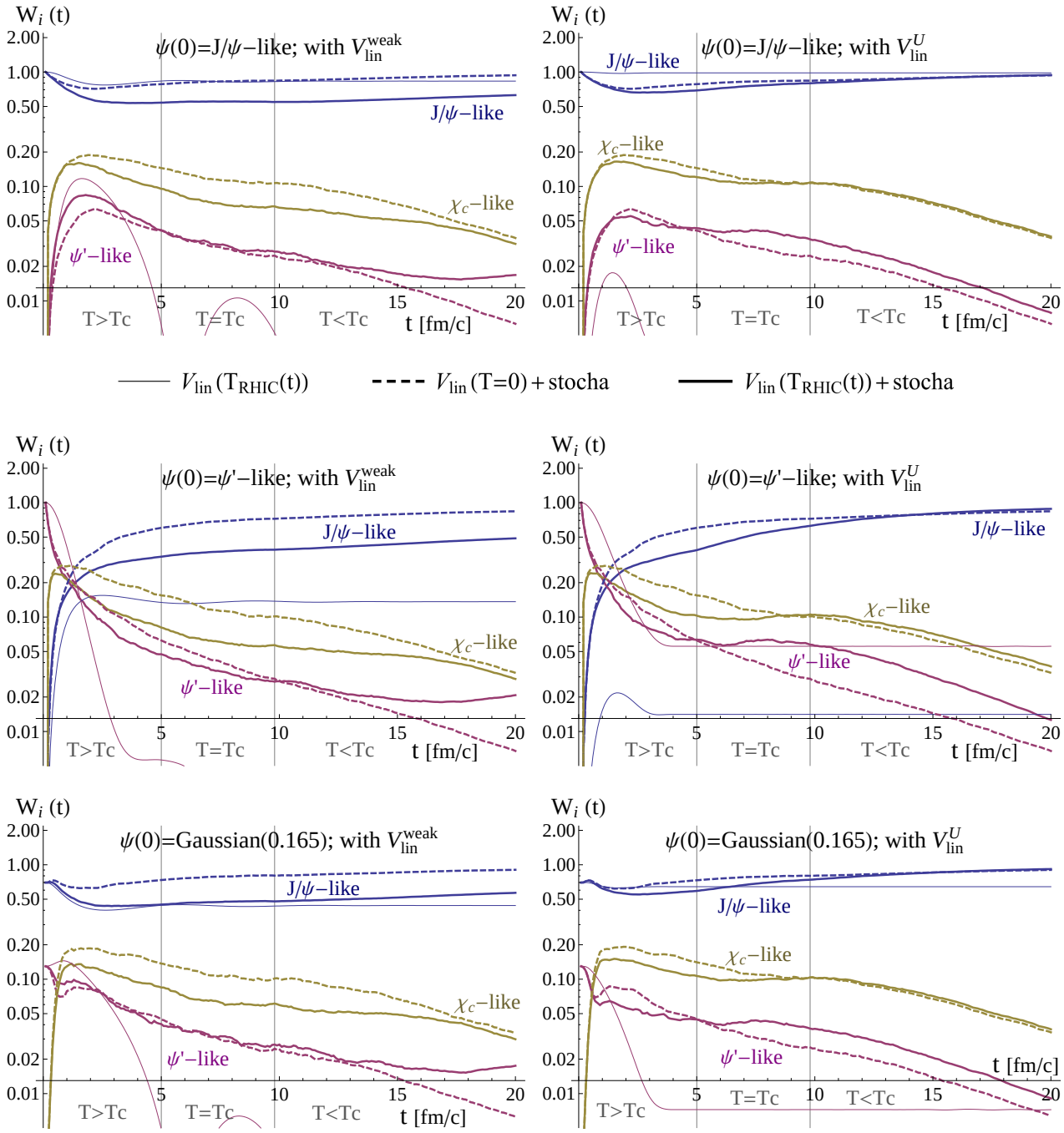

Figure VII.12: Evolutions of the charmonium weights from an initial J/ψ-like (*top*), ψ'-like (*center*) and gaussian (*bottom*) initial states, obtained with the $V_{\rm lin}^{\rm weak}$ (*left*) and $V_{\rm lin}^{U}$ (*right*) potentials for the RHIC temperature scenario. The thin curves corresponds to the mean field situation, the dashed curves is obtained with the thermal forces and the vacuum potential, and the thick curves with the thermal forces and the color screened potentials. See numerical version for colors.

of other higher components.

After the re-equilibration phase, the $c\bar{c}$ subsystem is not instantaneously at ther-

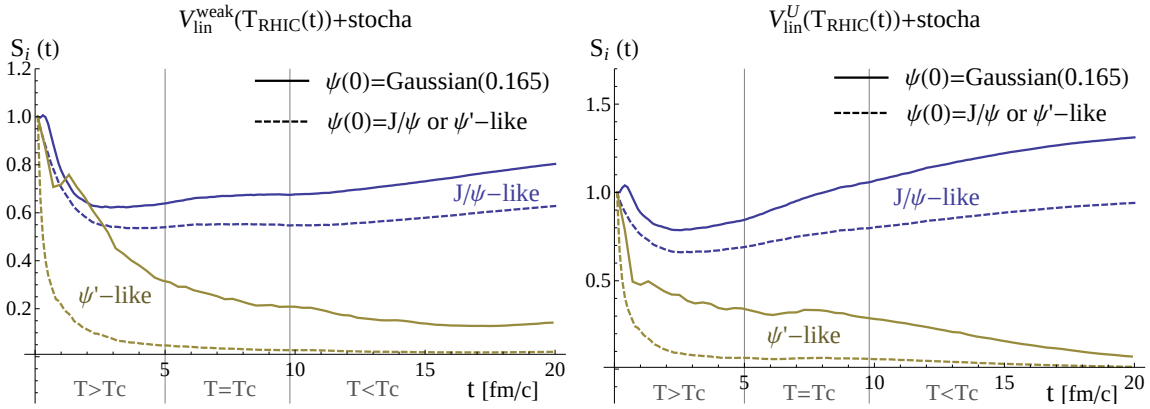

Figure VII.13: Evolutions of the charmonium survivances obtained with $V_{\rm lin}^{\rm weak}(T)$ (*left*) and $V_{\rm lin}^{U}(T)$ (*right*) from different initial states for the RHIC temperature scenario. The thick curves correspond to an initial Gaussian state and the dashed curves from an initial J/ψ-like and ψ'-like states for the J/ψ-like and ψ'-like survivances respectively.

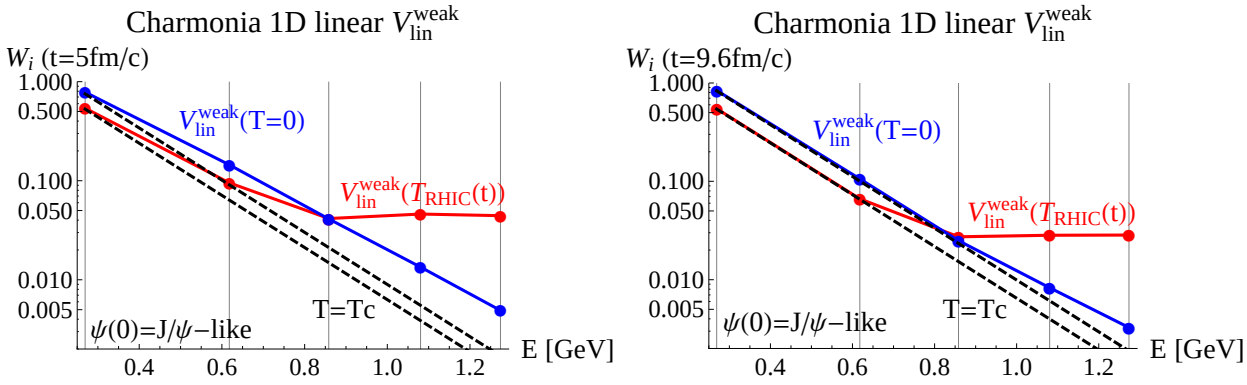

Figure VII.14: The distributions of the charmonium weights measured at $t = 5$ (*left*) and $t = 9.6$ fm/c (*right*) with the vacuum potential $V_{\rm lin}^{\rm weak}(T = 0)$ (blue) and the screened potential $V_{\rm lin}^{\rm weak}(T)$ (red) at RHIC. The dashed lines show the corresponding Boltzmann distributions at $T = T_c$.

mal equilibrium with the bath (see example in figure VII.14 (left)). There is a certain latency period for the subsystem to relax to the bath equilibrium. This latency can be observed for instance when the QGP temperature remains constant at $T = T_c$ (between 5 and 9.6 fm/c in the RHIC scenario): after few fm/c the subsystem equilibrates with the bath as shown in figures VII.14 (right). This latency highlights that, as a Brownian particle, the typical $c\bar{c}$ relaxation time is larger than any of the typical QGP times.

VII.3.1.3 At LHC

As shown in figures VII.27 (in appendix B) and VII.15, the evolutions obtained with the temperature scenario at LHC are quite similar to the ones at RHIC. One obtains more suppression for the J/ψ component at LHC than at RHIC with both potentials, and less suppression for the ψ' component. Furthermore, at intermediate times ($\sim 1 - 4$ fm/c) the ψ' component can be less suppressed that the J/ψ

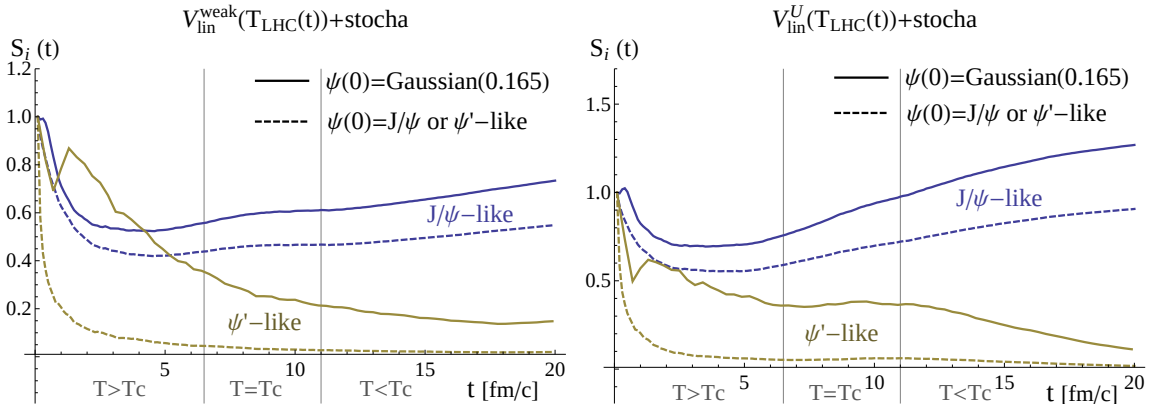

Figure VII.15: Same than figure VII.13 but with LHC temperature scenario.

component at LHC *but not* at RHIC (compare the left panels of figures VII.15 and **??**). These simple potentials combined with the SL equation seems therefore only weakly affected by the difference between RHIC and LHC scenarios.

VII.3.1.4 Sum up, values at the chemical freeze-out and data

The main conclusions for the $c\bar{c}$ evolution within this simplified 1D model are 1) both the color screening and the thermal forces cannot be neglected, 2) the thermal diffusion replaces the ballistic evolution, 3) the temperature difference between RHIC and LHC has little influence on the evolution, 4) relatively to the pure mean field situation, the thermal forces rather tend to increase the J/ψ suppression from a J/ψ initial state or have no effect from a gaussian initial state, and 5) decrease the ψ' suppression. So far, our study shows that the survivance of a state depends on the initial population, the deconfined medium life-time and temperature. We have observed the important contribution of the state regenerations from transitions between states. We have shown that for charmonia there is no fast decorrelation of the "melted states" as assumed by the sequential suppression model. Furthermore, we have observed a clear difference of time scales between the $c\bar{c}$ relaxation and the temperature evolution. In a more realistic scenario (with a crossover), it suggests that the thermal distribution of the $c\bar{c}$ components at the chemical freeze-out could not reflect the chemical freeze-out temperature. With our model, one could then extract the effective temperatures of the chemical freeze-out for quarkonia. As in the mean field part III, our framework possibly leads to a smaller suppression of the ψ' component relatively to the J/ψ at intermediate times at LHC but not at RHIC and therefore the recent result at LHC at forward rapidity[81] seems feasible. Finally, we have noticed that with this 1D linear model of the potential, the evolutions without thermal forces are very different from what we obtained with the radial charmonia potentials. Moreover, with the 1D linear potentials, the usual Gaussian parameters (for the initial Gaussian wavepacket) do not strictly lead to the same initial ratios as with the radial charmonia potentials. The 3D study seems necessary to obtain more reliable predictions.

[81] See section II.3.3

The values of the state survivances at the chemical freeze-out[82] at RHIC and LHC are summed up in tables VII.10 and VII.11 respectively. We obtain for the J/ψ component a moderate suppression which increases slightly with the collision energy. The ψ' component is more strongly suppressed (but still finite !) and its suppression decreases slightly with the collision energy.

State survivance at RHIC			R_{AA} data	
State \ Potential	$V_{\rm lin}^{\rm weak}$	$V_{\rm lin}^{U}$	Low p_T	High p_T
J/ψ from initial J/ψ	0.55	0.80	0.26 ± 0.05	0.64 ± 0.14
J/ψ from initial Gauss(0.165)	0.67	1.03		
ψ' from initial ψ'	0.028	0.06	None	None
ψ' from initial Gauss(0.165)	0.21	0.29		

Table VII.10: J/ψ and ψ' survivances $S_i(t) = W_i(t)/W_i(t=0)$ at the chemical freeze-out at RHIC ($t \approx 10$ fm/c). Experimental most central R_{AA} data at RHIC in AuAu $\sqrt{S_{NN}} = 200$ GeV collisions: 1) high p_T STAR data [134] (inclusive (prompt and non prompt) J/ψ, $5 < p_T < 14$ GeV/c, $|y| < 1$ and 0-10% centrality) and 2) low p_T PHENIX data [133] (inclusive J/ψ, $p_T < 5$ GeV/c, $|y| < 0.35$ and 0-5% centrality). The non prompt contribution is estimated to 10-25% of the inclusive production.

State survivance at LHC			R_{AA} data	
State \ Potential	$V_{\rm lin}^{\rm weak}$	$V_{\rm lin}^{U}$	Low p_T	High p_T
J/ψ from initial J/ψ	0.47	0.72	0.83 ± 0.14	0.20 ± 0.03
J/ψ from initial Gauss(0.165)	0.60	0.97		
ψ' from initial ψ'	0.022	0.06	None	0.13 ± 0.04
ψ' from initial Gauss(0.165)	0.27	0.37		

Table VII.11: J/ψ and ψ' survivances at the chemical freeze-out at LHC ($t \approx 11$ fm/c). Experimental R_{AA} data at LHC in PbPb $\sqrt{S_{NN}} = 2.76$ TeV collisions. For the J/ψ: 1) high p_T CMS data [138] (prompt J/ψ, $6.5 < p_T < 30$ GeV/c, $|y| < 2.4$ and 0-10% centrality) (inclusive J/ψ (prompt and non-prompt): $R_{AA} = 0.24 \pm 0.03$) and 2) low p_T ALICE data [137] (inclusive J/ψ, $0 < p_T < 8$ GeV/c, $|y| < 0.9$ and 0-10% centrality). For the ψ': high p_T CMS data [144] (prompt ψ', $6.5 < p_T < 30$ GeV/c, $|y| < 1.6$ and integrated centrality).

The corresponding experimental data for most central collisions - where the effects of the thermal deconfined matter are maximal - are given on an indicative basis. As in the mean field part III, a correct result-data comparison would require to refine our model with initial cold nuclear matter effects, feed downs from excited

[82] See section III.1.6.

states[83], recombinations from uncorrelated pairs and a more realistic heavy ion collision scenario (e.g. spatial distributions of the quarkonia and temperature). In the low p_T regime, we clearly underestimate the charmonia suppression at RHIC (but the mean field discrepancy might possibly explain it). At LHC, where the low p_T data might be dominated by uncorrelated pair recombinations, our results go in the right direction by overestimating the suppression. Finally, this simple dynamical model does not give an explanation of the J/ψ ordering (the "suppression of the suppression") at low p_T between RHIC and LHC.

VII.3.2 Bottomonia results and analysis

The study of the bottomonia suppression is also of a great interest for our analysis. Indeed, as they are much less subject to the recombination process - much fewer $b\bar{b}$ in the medium - and to shadowing effects - $b\bar{b}$ pairs are produced from gluons with larger momentum fraction x -, their experimental data are cleaner for a direct comparison with our dynamical model. For a $b\bar{b}$ pair in a QGP at temperature T, we use the drag coefficient given by $A(T)[\mathrm{c/fm}] \cong 0.92\,T[\mathrm{GeV}] + 0.64\,T^2$ [231].

VII.3.2.1 At constant temperatures

For the bottomonia, we now focus on the three lower S states - i.e. the $\Upsilon(1S)$-like, $\Upsilon(2S)$-like and $\Upsilon(3S)$-like states - but as the latter is always an unbound state with the $V_{\mathrm{lin}}^{\mathrm{weak}}$ potential (see figure VII.2) it is more given on an indicative basis in this case. As shown in figures VII.16, the behaviours of the $b\bar{b}$ and $c\bar{c}$ pairs are quite similar within this model (see section VII.3.1.1 for the discussion). There are nevertheless two main differences: a larger relaxation time and the thermal distributions are shifted toward smaller weights. Both originate from the smaller value of the drag parameter, which implies a larger relaxation time and a larger thermal diffusion fr bottomonia.

These evolutions can be roughly[84] compared to Borghini and Gombeaud's results from Einstein master equation (see figure IV.2). Both formalisms lead to a "universal" exponential decay of the bottomonium populations after a transient phase during which the populations get re-equilibrated. However, whereas they seem unable[85] to obtain a thermalisation of the bound states at local (in time) equilibriums, the Schrödinger-Langevin framework can within this simple model (as shown in figure VII.9).

[83] See table I.2 and I.10

[84] They study a 3D situation with a coulomb potential whereas we study a 1D situation with a screened linear potential.

[85] Because of some missing transitions between bound and open states (see section IV.2.1.3).

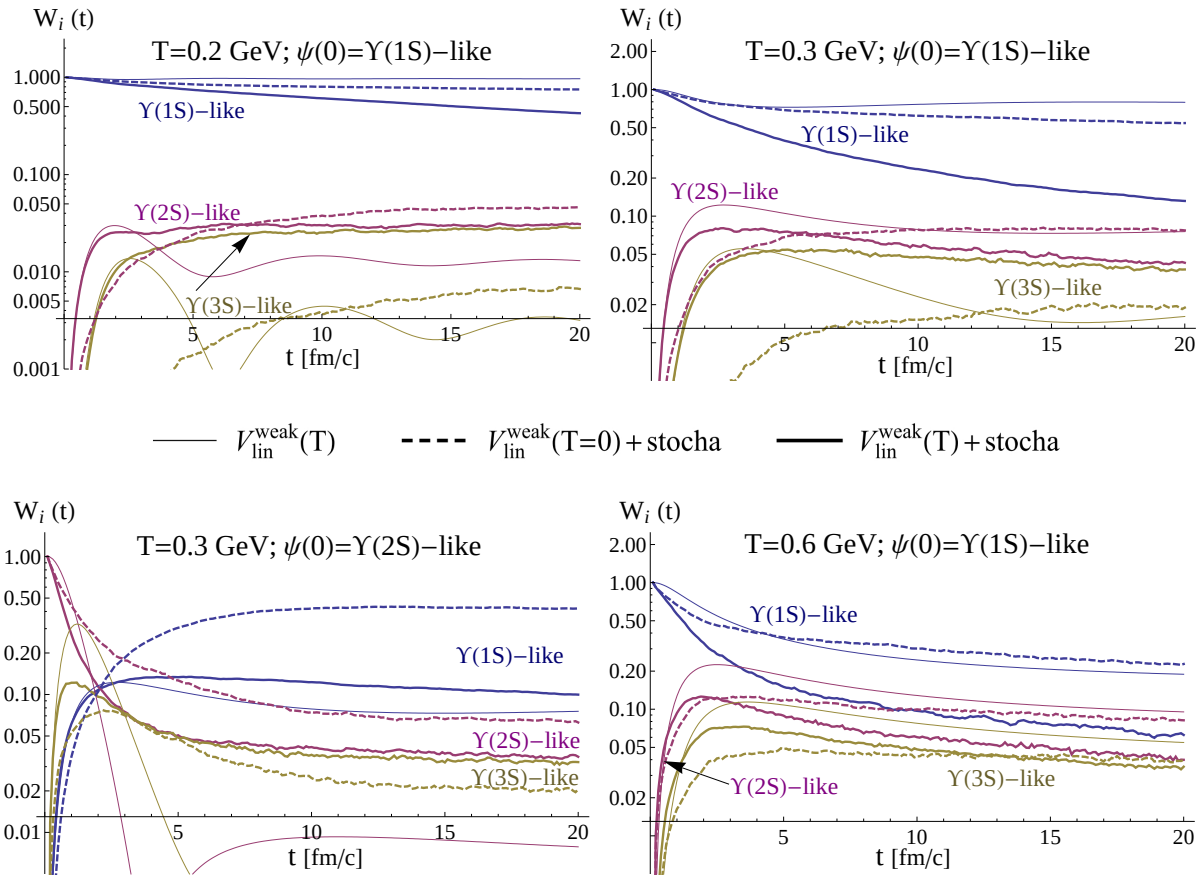

Figure VII.16: Evolutions of the bottomonium weights obtained with $V_{\rm lin}^{\rm weak}$ for different bath temperatures and initial states. The thin curves are obtained with the color screening but without thermal forces (i.e. the "mean field" situation), the dashed curves with the thermal forces but without screening (i.e. the vacuum potential $V_{\rm lin}^{\rm weak}(T=0)$ which saturates at $V_{\rm max}=1.2$ GeV) and the thick curves with both features. See numerical version for colors.

VII.3.2.2 At RHIC

By comparing figures VII.18 and VII.17 with VII.13 and VII.12, the behaviours of the $b\bar{b}$ and $c\bar{c}$ pairs are also very similar with an additional temperature scenario (see section VII.3.1.2 for the discussion). The comparison between the dashed and thick curves (i.e. without and with color screening) shows that the screening leads to equal or less suppressions for the $\Upsilon(3S)$ component (at the opposite from the $\Upsilon(1S)$ and $\Upsilon(2S)$ states). The additional diffusion coming from the screening indeed benefits to higher excited states. This effect becomes so strong with the weak potential $V_{\rm lin}^{\rm weak}$ that one can even observe a population inversion between the $\Upsilon(2S)$ and $\Upsilon(3S)$ components at intermediate times. Further investigations would be required to explain this effect.

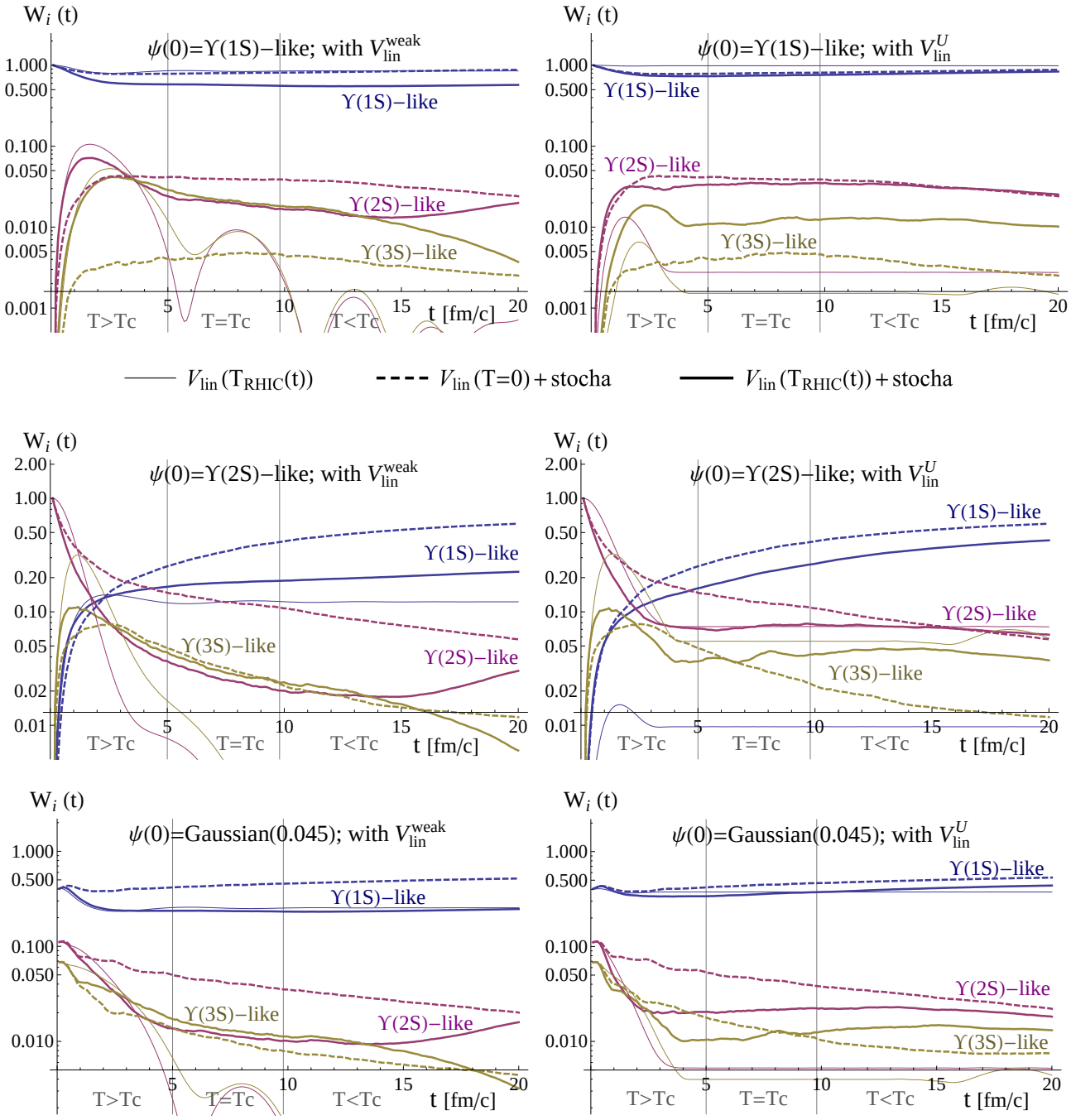

Figure VII.17: Evolutions of the bottomonium weights from the $\Upsilon(1S)$-like (*top*), $\Upsilon(2S)$-like (*center*) and gaussian (*bottom*) initial states, obtained with the $V_{\rm lin}^{\rm weak}$ (left) and $V_{\rm lin}^{U}$ (right) potentials for the RHIC temperature scenario. The thin curves corresponds to the mean field situation, the dashed curves is obtained with the thermal forces and the vacuum potential, and the thick curves with the thermal forces and the color screened potentials. See numerical version for colors.

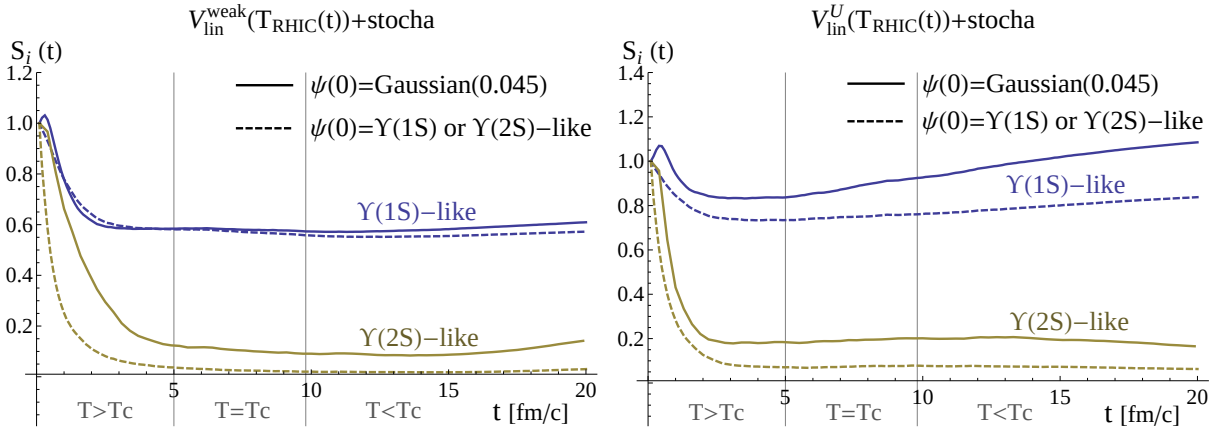

Figure VII.18: Evolutions of the bottomonium survivances obtained with $V_{\text{lin}}^{\text{weak}}(T)$ (*left*) and $V_{\text{lin}}^{U}(T)$ (*right*) from different initial states for the RHIC temperature scenario. The thick curves correspond to an initial Gaussian state and the dashed curves from an initial $\Upsilon(1S)$-like and $\Upsilon(2S)$-like states for the $\Upsilon(1S)$-like and $\Upsilon(2S)$-like survivances respectively.

VII.3.2.3 At LHC

As shown in figures VII.28 (in appendix B) and VII.19, the evolutions obtained with the temperature scenario at LHC are very similar to the ones at RHIC. One obtains more suppression for the $\Upsilon(1S)$ component at LHC than at RHIC with both potentials, and less suppression for the $\Upsilon(2S)$ and $\Upsilon(3S)$ components.

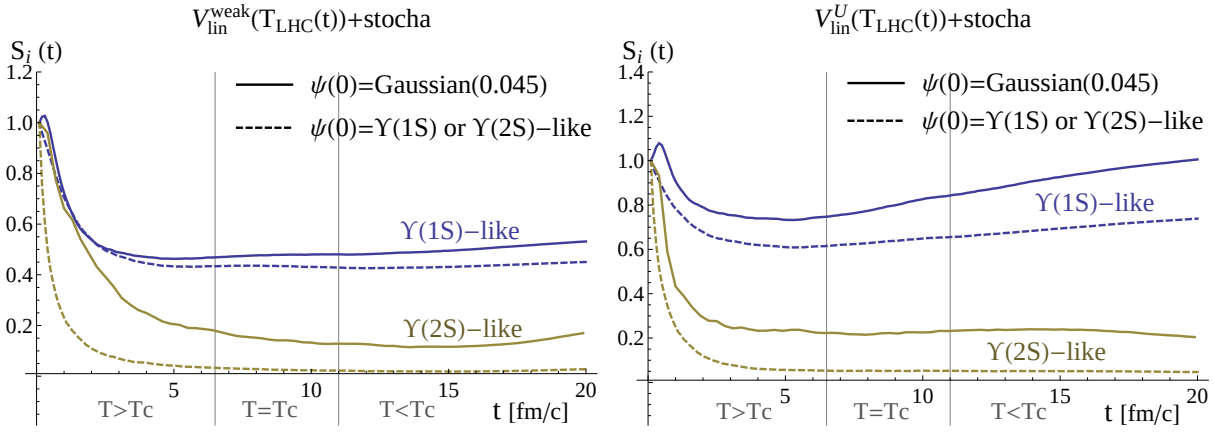

Figure VII.19: Evolutions of the bottomonium survivances obtained with $V_{\text{lin}}^{\text{weak}}(T)$ (*left*) and $V_{\text{lin}}^{U}(T)$ (*right*) from different initial states for the LHC temperature scenario. The thick curves correspond to an initial Gaussian state and the dashed curves from an initial $\Upsilon(1S)$-like and $\Upsilon(2S)$-like states for the $\Upsilon(1S)$-like and $\Upsilon(2S)$-like survivances respectively.

VII.3.2.4 Values at the chemical freeze-out and data

The bottomonium survivances at the chemical freeze-out at RHIC and LHC are summed up in tables VII.12 and VII.13 respectively. Similarly to the charmonia, we obtain for the $\Upsilon(1S)$ component a moderate suppression which increases with the collision energy and a more strongly suppressed $\Upsilon(2S)$ component which suppression decreases slightly with the collision energy. These results can reasonably be compared to the experimental data as both the recombination and the effect of shadowing are small (see section II.2.1). At first sight, both the $\Upsilon(1S)$ and $\Upsilon(2S)$ components are overestimated. However, adding the contributions of the suppressed feed downs from excited states (see figure I.10) should reduce these values (as done for instance in section III.5). The population inversion between the $\Upsilon(2S)$ and $\Upsilon(3S)$ components obtained with the $V_{\text{lin}}^{\text{weak}}$ seems unphysical, and does not appear a priori in the data (in which $\Upsilon(3S)$ is the most suppressed of the three states [168]).

State survivance at RHIC			R_{AA} data
State \ Potential	$V_{\text{lin}}^{\text{weak}}$	V_{lin}^{U}	
$\Upsilon(1S)$ from initial $\Upsilon(1S)$	0.57	0.76	0.66 ± 0.13
$\Upsilon(1S)$ from initial Gauss(0.045)	0.58	0.92	
$\Upsilon(2S)$ from initial $\Upsilon(2S)$	0.02	0.08	None
$\Upsilon(2S)$ from initial Gauss(0.045)	0.09	0.20	

Table VII.12: $\Upsilon(1S)$ and $\Upsilon(2S)$ survivances at the chemical freeze-out at RHIC ($t \approx 10$ fm/c). Experimental most central R_{AA} data at RHIC in AuAu $\sqrt{S_{NN}} = 200$ GeV collisions: STAR data [167] ($p_T > 0$ GeV/c, $|y| < 1$ and 0-10% centrality).

State survivance at LHC			R_{AA} data	
State \ Potential	$V_{\text{lin}}^{\text{weak}}$	V_{lin}^{U}	Mid y	Forward y
$\Upsilon(1S)$ from initial $\Upsilon(1S)$	0.43	0.64	0.41 ± 0.06	0.22 ± 0.05
$\Upsilon(1S)$ from initial Gauss(0.045)	0.48	0.83		
$\Upsilon(2S)$ from initial $\Upsilon(2S)$	0.02	0.05	0.11 ± 0.06	None
$\Upsilon(2S)$ from initial Gauss(0.045)	0.13	0.22		

Table VII.13: $\Upsilon(1S)$ and $\Upsilon(2S)$ survivances at the chemical freeze-out at LHC ($t \approx 11$ fm/c). Experimental R_{AA} data at LHC in PbPb $\sqrt{S_{NN}} = 2.76$ TeV collisions. For the mid rapidity: CMS data [168] ($p_T > 0$ GeV/c (one can note that the bottomonia suppression is almost independent of p_T [145]), $|y| < 2.4$ and 0-5% centrality) and for the forward rapidity: ALICE data [268] ($p_T > 0$ GeV/c, $2.5 < |y| < 4$ and 0-20% centrality).

VII.4 Evolutions with a more realistic collision framework from EPOS generator

In the previous sections, we have considered $Q\bar{Q}$ pairs standing at the center of a cooling fireball, i.e. of zero momentum. We now carry out the study for the bottomonia within a more realistic collision framework at LHC extracted from the "state-of-the-art" EPOS event generator. These more realistic collisions include a finite volume, an inhomogeneous temperature and some position-momentum distributions of the $b\bar{b}$ pairs.

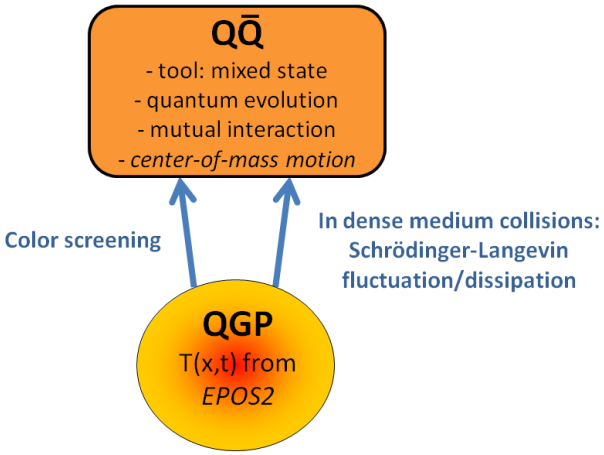

Figure VII.20: Illustration of our approach within this section through its basic ingredients and interactions between the $Q\bar{Q}$ and QGP systems.

VII.4.1 New ingredients

The temperature background $T(\vec{x}, t)$ is extracted from the EPOS2 event generator [269, 270]. It is a state of the art framework which attempts to describe pp, pA and AA collisions. In AA collisions, the initial 3D QGP state is generated from a Gribov-Regge multiple scattering approach where the particle production originates from cut pomerons (parton ladders). It leads to inhomogeneous density and temperature distributions (see figure VII.21). The evolution of the produced medium is then described by an ideal hydrodynamic expansion which is fitted to a lQCD equation of state [271]. Hence, the time evolution of the temperature at the phase transition corresponds to a crossover and not to a 1st order transition like in Kolb and Heinz model[86] (see figure VII.22). EPOS has proven to provide a good description of the light quark sector and is therefore suited for our analyses [272].

Within our model, the initial color singlet $b\bar{b}$ pairs are spatially distributed[87] in the QGP volume according to the Glauber model [44]. To each pair is then randomly associated a momentum value with an even probability for simplification. In section

[86] The model of Kolb and Heinz is described in section III.1.2

[87] Note that in EPOS3 the production of charm quarks has been implemented and one could use the corresponding position-momentum distributions as the initial state.

VII.4.2, we will see that the R_{AA} distributions are almost independent of p_T, so this simplification only has a negligible impact on our results. The pairs (center-of-mass) are then assumed to propagate along straight lines with no energy loss as in transport models. We assume that the static potentials evaluated from lQCD at zero momentum, that we have used so far, does not depend on the $b\bar{b}$ center-of-mass momentum. For their inner dynamics, each $b\bar{b}$ pair is evolved according to the Schrödinger-Langevin framework with one of the simplified linear 1D potentials ($V_{\rm lin}^{\rm weak}$ or $V_{\rm lin}^{U}$). At each time step t_i, the temperature T of the Debye-screening and fluctuation/dissipation mechanisms, is taken accordingly to the j^{th} pair position $\vec{x}_j$ in the EPOS background, i.e. $T = T(\vec{x}_j, t_i)$.

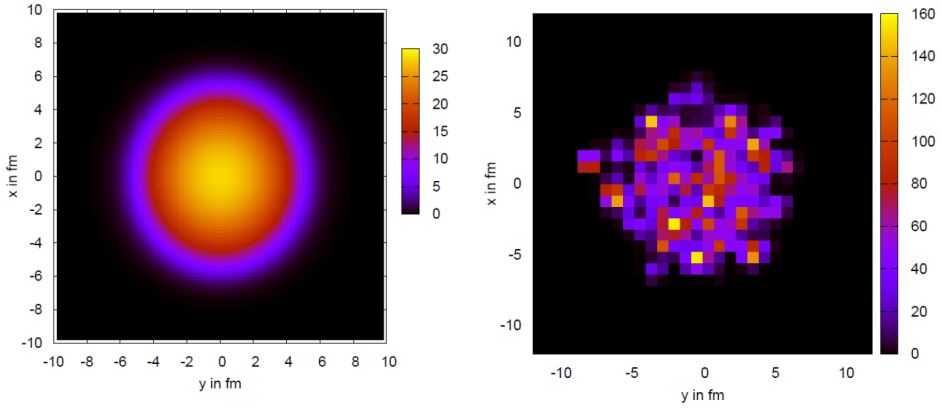

Figure VII.21: Spatial distributions of the energy density in a transverse plane obtained from Kolb and Heinz model (*left*) and from a realisation of EPOS2 (*right*) in most central collisions. Beware that the color scales are different.

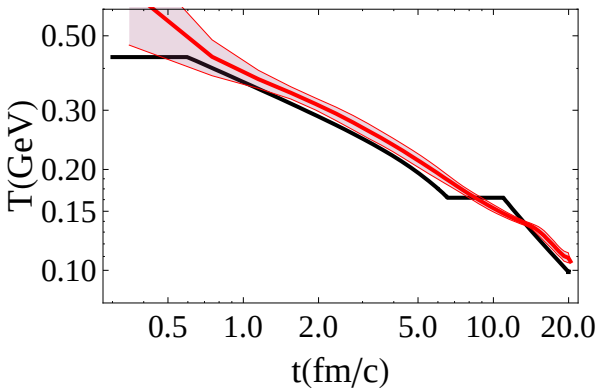

Figure VII.22: Time evolution of the temperature at the center of the fireball obtained from Kolb and Heinz model (black curve) and from a statistical average of EPOS2 predictions (red curve). The band corresponds to the typical fluctuations around the average value.

VII.4.2 Preliminary results and discussion

If not indicated, the initial state of the pairs is taken to be the Gaussian compact wavepacket. With this initial state, the survivances $S_i(t) = W_i(t)/W_i(t=0)$ can be seen as the experimental R_{AA}. Indeed, in this case all the transitions between bound states are included (see section VII.3), whereas one needs to sum over the different contributions if one starts from the initial bound states. *As we do not implement* the cold nuclear matter effects and the feed-downs, our R_{AA} results do not aim to reproduce experimental data, but just grasp the global trends. Our results are given for the full rapidity range.

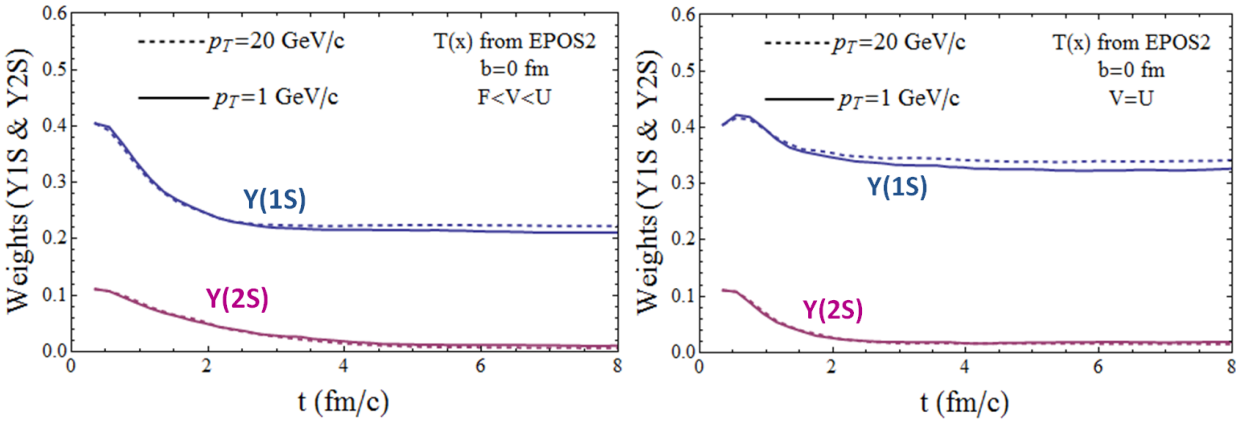

Figure VII.23: Evolutions of the bottomonium weights from the Gaussian state, obtained with the V_{lin}^{weak} (*left*) and V_{lin}^{U} (*right*) potentials for the space-time temperature distributions from EPOS2 in central collisions (b=0) at LHC.

In figure VII.23, we show the evolutions of the bottomonium weights obtained in central collisions (b=0) for two different transverse momenta p_T. First, one should note that these evolutions are very similar to what we obtained with Kolb and Heinz model at LHC (see figure VII.28). Second, we observe almost no dependence on the transverse momentum. Whatever their momentum, the $b\bar{b}$ pairs remain thus long enough in the medium to behave almost like they were standing at the center of the fireball. Kolb and Heinz model for a $b\bar{b}$ pair fixed at the center of the fireball (section VII.3) was therefore a good approximation for central collisions.

As one can see in figure VII.24, this very weak dependence on p_T is also true for semi-peripheral and peripheral collisions, with the exception of $\Upsilon(2S)$ in peripheral collisions. This flat p_T-dependence of the R_{AA} is a very promising result of our model as it perfectly agrees with the experimental observation at LHC shown in figure[88] VII.25. In figure VII.26, we show the results for the R_{AA} dependence on the number of participants (i.e. the centrality). At first sight, the distributions obtained with the weak linear potential seem in a better agreement with the experimental data (in figure VII.25), but including the feed down and cold nuclear matter contributions might rather indicate that the strong linear potential is in a better agreement. This analysis will be performed in a near future.

[88] Already shown in part II.

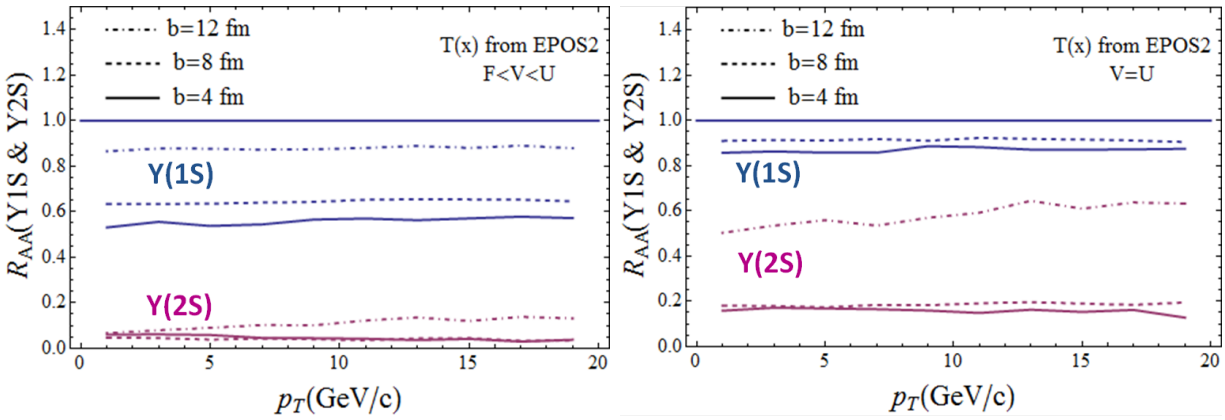

Figure VII.24: The p_T-dependence of the bottomonium survivances for three different impact parameters b, obtained with the initial Gaussian state, the $V_{\rm lin}^{weak}$ (*left*) and $V_{\rm lin}^{U}$ (*right*) potentials, and the space-time temperature distributions from EPOS2 at LHC.

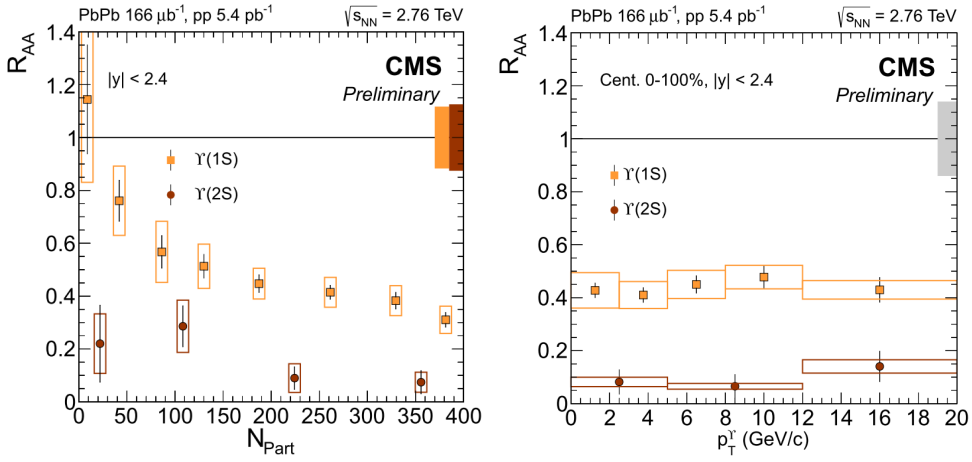

Figure VII.25: R_{AA} data for the $\Upsilon(1S)$ and $\Upsilon(2S)$ as a function of centrality (*left*) and transverse momentum (*right*) [145].

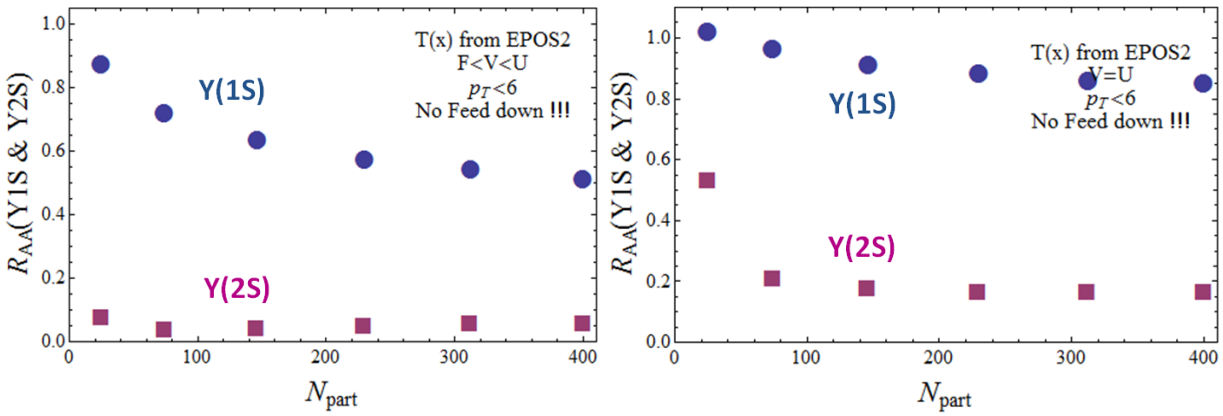

Figure VII.26: The $N_{\rm part}$-dependence of the bottomonium survivances, integrated on the impact parameter b and obtained with the initial Gaussian state, the $V_{\rm lin}^{weak}$ (*left*) and $V_{\rm lin}^{U}$ (*right*) potentials, and the space-time temperature distributions from EPOS2 at LHC.

Main ideas

In the Schrödinger-Langevin (SL) scheme, the time-dependent real potential implements the Debye-screening while the stochastic/dissipative forces express the (hard) interactions between the QGP and the $Q\bar{Q}$ pairs through two simple parameters (the drag and the temperature). It possibly leads to transitions between bound states and between bound and open quantum states, which are treated with more or less success resorting to master equations or imaginary potentials in other frameworks. The SL equation preserves unitarity for the pure state and leads for the mixed state to a correct thermalisation of the bound components within simple models. We have studied the real-time dynamics of $Q\bar{Q}$ pairs immersed in a QGP and bound by a simple 1D screened linear interaction. This model does not aim to reproduce the data but rather gives insights on the dynamics. We have mainly focused on the quarkonia content of the pairs and obtained rich suppression patterns. They rule out the basic assumptions of the sequential suppression model: there is no fast and full decorrelation of "melted" states and no adiabatic evolution of "formed" states. Furthermore, we have observed interesting transitions between bound states possibly leading to their regeneration (especially for the excited states). Our dynamical model creates a bridge between the main ideas of the sequential suppression model (the partial screening) and the statistical hadronisation model (thermalisation of the states). Our results suggest that the thermal distribution of the $Q\bar{Q}$ components at hadronisation may not reflect the QGP hadronisation temperature (due to its large inertia). Finally, we have applied our model to a more realistic collision framework at LHC. The resulting R_{AA} dependence[89] on p_T and $N_{\rm part}$ reasonably describes the data trends.

[89] These results have been recently discussed in a conference proceeding [273].

General conclusion

We have investigated the quarkonia suppression in a Quark Gluon Plasma from a dynamical point of view. Our approach is based on the real-time evolution of non-relativistic correlated $Q\bar{Q}$ pairs described as open quantum systems continuously interacting with a cooling QGP. This analysis implicitly aimed to 1) study the effects of the color screening and permanent collisions on the $Q\bar{Q}$ separation and quarkonia content, 2) observe if the ordering of the J/ψ suppression at RHIC and LHC could be explained by a thermal effect, 3) give a dynamical and continuous picture of the dissociation, recombination, energy exchange and possible transitions to other bound states, 4) create a connection between the sequential suppression and statistical hadronisation models which would permit to justify some of their assumptions, 5) measure the medium temperature above the critical temperature T_c, 6) describe the quarkonia nuclear modification factor at RHIC and LHC.

To this end, we have explored three approaches which combine the following ingredients: i) a correlated $Q\bar{Q}$ pair seen as a dipole in its center-of-mass frame and described by a pure wavefunction, a pure Wigner distribution or a mixed state, ii) a mutual interaction between the Q and $\bar{Q}$ partly screened by color charges in their vicinity iii) a cooling QGP either described by the hydrodynamic model from Kolb and Heinz or by the state-of-the-art EPOS2 event generator, iv) some classical or quantum Langevin-like mechanisms reflecting the continuous collisions between the Brownian $Q\bar{Q}$ pair and the thermal medium. We have first investigated a "ballistic" evolution of the $Q\bar{Q}$ pair based on the Schrödinger equation including the mean field potential only. We focused on the S state weights allowing to reduce the full 3D analysis to a radial 1D situation without approximations. Then, as a first attempt to include a thermal mechanism to obtain a "diffusive" evolution, we have explored a semi-classical approach where the $Q\bar{Q}$ pair was described by the Wigner-Moyal equation supplemented by a classical Langevin dynamics. We have finally investigated the full quantum evolution given by the so-called Schrödinger-Langevin equation within a simplified 1D model.

Through the results of various simulations we have shown that:

- The basic assumptions of the sequential suppression model are unjustified.
- The semi-classical frameworks exhibit important pitfalls and might not be suited for this analysis.
- The Schrödinger-Langevin equation leads to thermal relaxation, with however some limitations.
- It is mandatory to consider both the screening and thermal effects.
- Transitions between bound and open quantum states and between bound quantum states play a crucial role. The former lead to dissociation and recombination phenomena, whereas the second to significant regeneration of quarkonium states.

– The system exhibits different time scales between the $Q\bar{Q}$ relaxation and the evolution of the QGP temperature. It suggests that the possible thermal distribution of the quarkonium states at the end of the evolution might not reflect the chemical freeze out temperature.

– This framework may provide a possible explanation for the unusual $\psi'/J/\psi$ ratio measured by the CMS collaboration at LHC.

– Within our models, the thermal effect cannot explain the ordering of the J/ψ suppression at RHIC and LHC. To take into account the recombinations of uncorrelated pairs at low p_T seems therefore necessary.

In further investigations, one could extend the Schrödinger-Langevin framework to the realistic 3D situation, include the color octet channels and implement important phenomena such as the feed downs, cold nuclear matter effects and recombinations of uncorrelated pairs. The results could then be compared to experimental data. One could then also proceed to a more systematic comparison with lQCD observables and other open quantum system approaches. It might allow to distinguish between the possible binding potentials, to obtain a relevant thermometer for the QGP and to unify the description of single and bound heavy flavours in a deconfined medium. An alternative approach might be the use of Stochastic Schrödinger equations to unravel the recently proposed master equations from first principles. Finally, we remain convinced that a dynamical approach of the "open quantum system" kind is the only framework which might provide an accurate description of quarkonia production in heavy-ion collisions.

Appendix A

The 3D Schrödinger-Langevin equation decomposed in the spherical harmonics basis for the limited case L=2

In the limited case of $L = 2$, the sum in VII.147 for the stochastic term is given by:

$$\sum_{l,m} \Xi_{l,m,l',m'}(r,t) R_{l,m} = \begin{bmatrix} \mathbf{0} & A_1 & \mathbf{0} \\ A_2 & \mathbf{0} & A_3 \\ \mathbf{0} & A_4 & \mathbf{0} \end{bmatrix},$$

where the matrices A_1, A_2, A_3 and A_4 are:

$$A_1 = \begin{bmatrix} \frac{-F_1 R_{0,0}}{\sqrt{\pi}} & \frac{F_0 R_{0,0}}{2\sqrt{\pi}} & \frac{-F_{-1} R_{0,0}}{\sqrt{\pi}} \end{bmatrix},$$

$$A_2 = \begin{bmatrix} \frac{F_{-1} R_{1,-1}}{\sqrt{\pi}} \\ \frac{F_0 R_{1,0}}{2\sqrt{\pi}} \\ \frac{F_1 R_{1,1}}{\sqrt{\pi}} \end{bmatrix},$$

$$A_3 = \begin{bmatrix} -\sqrt{\frac{6}{5\pi}} F_1 R_{1,-1} & \sqrt{\frac{3}{5\pi}} \frac{F_0 R_{1,-1}}{2} & -\frac{F_{-1} R_{1,-1}}{\sqrt{5\pi}} & 0 & 0 \\ 0 & -\sqrt{\frac{3}{5\pi}} F_1 R_{1,0} & \frac{F_0 R_{1,0}}{\sqrt{5\pi}} & -\sqrt{\frac{3}{5\pi}} F_{-1} R_{1,0} & 0 \\ 0 & 0 & -\frac{F_1 R_{1,1}}{\sqrt{5\pi}} & \sqrt{\frac{3}{5\pi}} \frac{F_0 R_{1,1}}{2} & -\sqrt{\frac{6}{5\pi}} F_{-1} R_{1,1} \end{bmatrix}$$

and

$$A_4 = \begin{bmatrix} \sqrt{\frac{6}{5\pi}} F_{-1} R_{2,-2} & 0 & 0 \\ \sqrt{\frac{3}{5\pi}} \frac{F_0 R_{2,-1}}{2} & \sqrt{\frac{3}{5\pi}} F_{-1} R_{2,-1} & 0 \\ \frac{F_1 R_{2,0}}{\sqrt{5\pi}} & \frac{F_0 R_{2,0}}{\sqrt{5\pi}} & \frac{F_{-1} R_{2,0}}{\sqrt{5\pi}} \\ 0 & \sqrt{\frac{3}{5\pi}} F_1 R_{2,1} & \sqrt{\frac{3}{5\pi}} \frac{F_0 R_{2,1}}{2} \\ 0 & 0 & \sqrt{\frac{6}{5\pi}} F_1 R_{2,2} \end{bmatrix}.$$

Finally, from the 3D Schrödinger-Langevin equation VII.137 one thus obtain a system of 9 crossed equations. Fore instance, the crossed equations for $l' = 0$ and $l' = 1$ are:

- $l' = 0, m' = 0$:

$$i\hbar\frac{\partial R_{0,0}(r,t)}{\partial t} = -\frac{\hbar^2}{2m}\frac{1}{r^2}\frac{\partial}{\partial r}\left(r^2\frac{\partial R_{0,0}}{\partial r}\right) + V(r)R_{0,0} \qquad \text{(VII.153)}$$
$$-\sqrt{\frac{1}{3}}\,r\left[2F_{-1}\,R_{1,-1} + F_0\,R_{1,0} + 2F_1\,R_{1,1}\right]$$
$$+\hbar A\sum_{l,m} c_{l,m}(r,t)\,R_{l,m}.$$

- $l' = 1, m' = -1$:

$$i\hbar\frac{\partial R_{1,-1}(r,t)}{\partial t} = -\frac{\hbar^2}{2m}\left[\frac{1}{r^2}\frac{\partial}{\partial r}\left(r^2\frac{\partial R_{1,-1}}{\partial r}\right) - \frac{2}{r^2}R_{1,-1}\right] + V(r)R_{1,-1} \qquad \text{(VII.154)}$$
$$-\sqrt{\frac{1}{3}}\,r\left[-2F_1\,R_{0,0} + 2\sqrt{\frac{6}{5}}F_{-1}\,R_{2,-2} + \sqrt{\frac{3}{5}}F_0\,R_{2,-1} + 2\frac{F_1\,R_{2,0}}{\sqrt{5}}\right]$$
$$+\hbar A\sum_{l,m} c_{l,m}(r,t)\,R_{l,m}.$$

- $l' = 1, m' = 0$:

$$i\hbar\frac{\partial R_{1,0}(r,t)}{\partial t} = -\frac{\hbar^2}{2m}\left[\frac{1}{r^2}\frac{\partial}{\partial r}\left(r^2\frac{\partial R_{1,0}}{\partial r}\right) - \frac{2}{r^2}R_{1,0}\right] + V(r)R_{1,0} \qquad \text{(VII.155)}$$
$$-\sqrt{\frac{1}{3}}\,r\left[F_0\,R_{0,0} + 2\sqrt{\frac{3}{5}}F_{-1}\,R_{2,-1} + \frac{2\,F_0\,R_{2,0}}{\sqrt{5}} + 2\sqrt{\frac{3}{5}}F_1\,R_{2,1}\right]$$
$$+\hbar A\sum_{l,m} c_{l,m}(r,t)\,R_{l,m}.$$

- $l' = 1, m' = 1$:

$$i\hbar\frac{\partial R_{1,1}(r,t)}{\partial t} = -\frac{\hbar^2}{2m}\left[\frac{1}{r^2}\frac{\partial}{\partial r}\left(r^2\frac{\partial R_{1,1}}{\partial r}\right) - \frac{2}{r^2}R_{1,1}\right] + V(r)R_{1,1} \qquad \text{(VII.156)}$$
$$-\sqrt{\frac{1}{3}}\,r\left[-2F_{-1}\,R_{0,0} + 2\frac{F_{-1}\,R_{2,0}}{\sqrt{5}} + \sqrt{\frac{3}{5}}F_0\,R_{2,1} + 2\sqrt{\frac{6}{5}}F_1\,R_{2,2}\right]$$
$$+\hbar A\sum_{l,m} c_{l,m}(r,t)\,R_{l,m}.$$

Appendix B

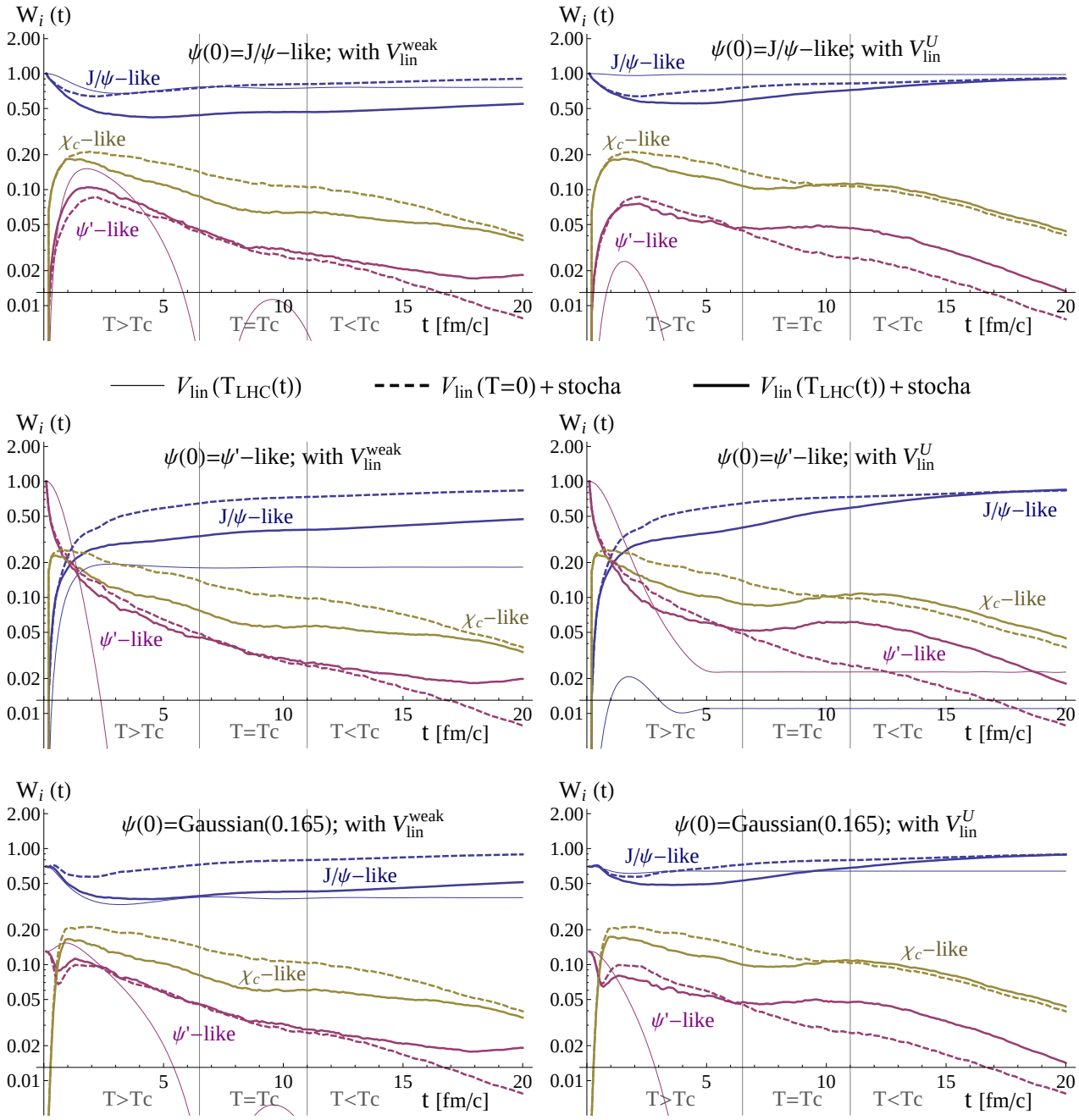

Figure VII.27: Evolutions of the charmonium weights from an initial J/ψ-like (top) and ψ'-like (bottom) states, obtained with the $V_{\rm lin}^{\rm weak}$ (*left*) and $V_{\rm lin}^{U}$ (*right*) potentials for the LHC temperature scenario (Kolb and Heinz). The thin curves corresponds to the mean field situation, the dashed curves is obtained with the thermal forces and the vacuum potential, and the thick curves with the thermal forces and the color screened potentials. See numerical version for colors.

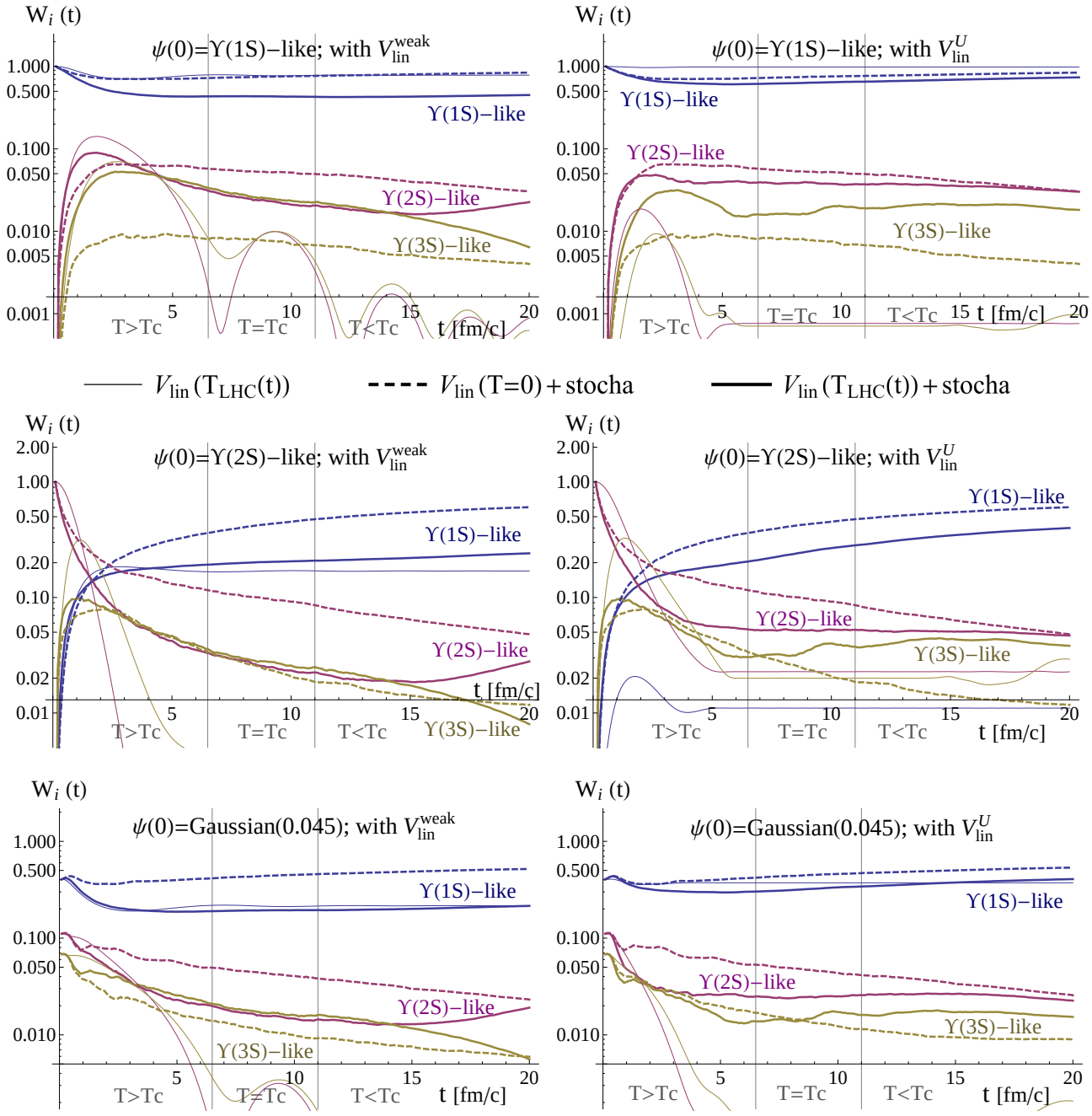

Figure VII.28: Evolutions of the bottomonium weights from different initial states, obtained with the $V_{\rm lin}^{\rm weak}$ (*left*) and $V_{\rm lin}^{U}$ (*right*) potentials for the LHC temperature scenario (Kolb and Heinz). The thin curves corresponds to the mean field situation, the dashed curves is obtained with the thermal forces and the vacuum potential, and the thick curves with the thermal forces and the color screened potentials. See numerical version for colors.

Résumé en français

Selon la théorie du Big Bang, les particules élémentaires qui composent notre univers seraient passées par un état extrêmement chaud ($\gtrsim 10^{12}$ K) et dense de Plasma de Quark et Gluon (PQG), avant de former des nucléons, des atomes, des molécules... Le PQG devrait être une étape clé pour comprendre comment la distribution homogène de matière originelle est devenue inhomogène, menant aux structures de matière actuellement observées dans l'espace. Le PQG consiste en un état dense et déconfiné de quarks et de gluons (appelés ensemble partons). Ces derniers sont les composants élémentaires de la matière nucléaire et sont, en conditions normales, confinés dans des systèmes composites (les "hadrons") tels que les protons et neutrons. Depuis les années 80, le PQG est au centre d'une intense investigation expérimentale et théorique ayant pour but de prouver son existence et de déterminer ses propriétés. Pour reproduire sur Terre les conditions extrêmes nécessaires à son obtention, une possibilité est de collisionner des ions lourds ultra-relativistes dans des collisionneurs géants tels que le RHIC et le LHC. Ainsi, on peut potentiellement produire de très petites ($\sim 10^{-14}$ m) "bulles" de PQG aux durées de vie extrêmement courtes ($\sim 10^{-21}$ s) et dont l'étude est un véritable défi. On ne peut en effet considérer que des observables indirectes résultantes de l'expansion et du refroidissement de ces bulles, c'est-à-dire les hadrons finalement produits. Une des observables possibles du PQG et de sa température est la "suppression des quarkonia". Cette observable correspond à une production inférieure d'états liés de quark/antiquark lourds ($Q\bar{Q}$) dans les collisions d'ions lourds relativement aux collisions proton-proton où le PQG ne peut être à priori créé. Cette suppression a en effet été observé expérimentalement mais ses intrigantes évolutions avec l'énergie de collision et les paramètres cinématiques ne correspondent pas systématiquement à ce qui était attendu, rendant nécessaire une meilleur compréhension théorique. Dans cette thèse, nous proposons une description dynamique des paires $Q\bar{Q}$ décrites comme des systèmes quantiques ouverts en interaction continue avec les partons du milieu déconfiné.

Le premier chapitre, intitulé "Du modèle standard aux collisions d'ions lourds", présente le cadre global dans lequel s'inscrit ce travail. Les bases du Modèle Standard de la physique des particules et de la chromodynamique quantique (QCD), la théorie de l'interaction forte, sont tout d'abord présentées. Les notions de constante de couplage, de liberté asymptotique, de confinement et d'hadron sont discutées. Une attention particulière est donnée à la physique des quarkonia: leurs propriétés, états excités, désintégrations et mécanismes de production sont décrits, ainsi que l'intérêt de leur étude en collisions proton-proton. Dans un second temps, le diagramme de phase de la matière nucléaire VII.29 et la nature des transitions entre matière hadronique et PQG sont discutés. Par la suite, les différentes étapes attendues lors d'une collision d'ions lourds sont détaillées (voir figure VII.30): des ions initiaux, en passant par l'évolution du PQG formant la boule de feu, jusqu'aux hadrons finaux. Les paramètres permettant de caractériser une collision d'ions lourds, tels que l'énergie dans le centre de masse $\sqrt{s_{NN}}$ et le nombre de nucléons participants à la collision $\langle N_{\rm part}\rangle$, sont définis. Pour finir, une brève revue des différentes observables

expérimentales du PQG est donnée: la multiplicité des hadrons légers, le flot hydrodynamique, la suppression des hadrons légers aux grands moments transverses...

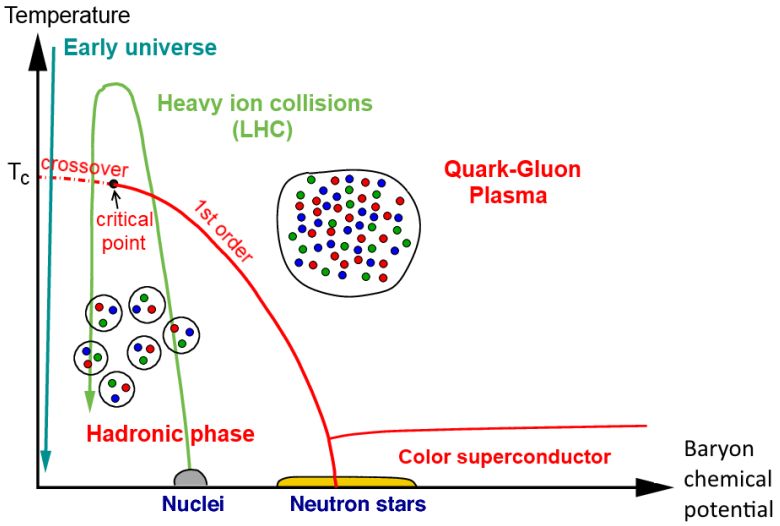

Figure VII.29: Schéma du diagramme de phase de la QCD présenté en fonction de la température et du potentiel chimique baryonique μ_B. La température critique entre matière hadronique et partonique est évaluée à $T_c \simeq 170 \pm 25$ MeV ($\sim 10^{12}$ Kelvin !) à $\mu_B \simeq 0$ [34].

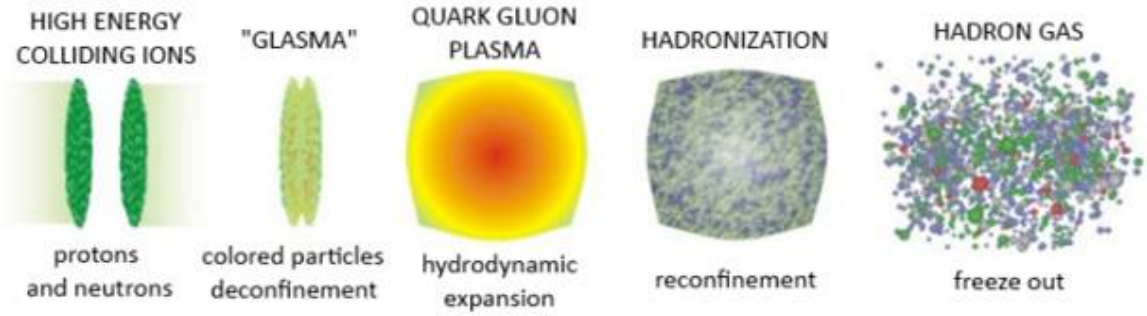

Figure VII.30: Représentation schématique des différentes étapes d'une collision d'ions lourds, des ions initiaux jusqu'aux nombreux hadrons observés au final dans les détecteurs.

Le second chapitre, intitulé "Une revue de la suppression des quarkonia", est une revue des modèles théoriques et des résultats expérimentaux concernant la suppression des quarkonia, l'observable sur laquelle cette thèse se concentre. L'intérêt des quarks lourds dans les collisions d'ions lourds est tout d'abord justifié. Étant produit dans les premiers instants de la collision en quantité plutôt bien maitrisée, les quarks lourds permettent en effet de sonder le milieu crée tout au long de son évolution. En particulier, les paires $Q\bar{Q}$ corrélées devraient être sensibles à la température du milieu déconfiné. Les différents modèles décrivant la production des quarkonia dans les collisions d'ions lourds sont ensuite revus en détail. Sont décrits par exemple les effets de la matière nucléaire froide, le modèle de suppression séquentielle propos par Matsui et Satz [1], les modèles d'hadronisation statistique [113, 114, 115] et de

transport [112, 63, 64, 124, 125, 126, 127]. En particulier, le modèle de suppression séquentielle se base sur les températures de dissociation des quarkonia: si la température maximale du PQG T_{PQG} est supérieure à la température de dissociation d'un état T_d, celui-ci est assumé dissocié pour toujours, à l'opposé si $T_{\mathrm{PQG}} < T_d$, l'état est supposé survivre sans être perturbé. Les résultats expérimentaux obtenus auprès du SPS, RHIC et LHC, à des énergies de collision allant de quelques dizaines de MeV à quelques TeV, sont ensuite discutés. Les limites et l'irrégularité de la description de ces données par les principaux modèles sont pointées. Une revue critique des hypothèses des principaux modèles nous permet enfin de justifier l'approche développée dans la présente thèse: étudier la dynamique en temps réel des paires $Q\bar{Q}$ corrélées, considérées comme des systèmes quantiques ouverts en interaction permanente avec un PQG en refroidissement. Explicitement, l'interaction continue entre le milieu et les degrés de liberté internes de la paire doit se manifester par 1) un écrantage de couleur dit "de Debye" dû à la présence de charges de couleur dans leur voisinage et 2) des mécanismes de fluctuation/dissipation qui reflètent les collisions permanentes avec les partons du milieu. Cette description devrait mener à une image dynamique et continue de la dissociation des quarkonia, de leur recombinaison et des transitions entre états liés. Les perspectives d'un tel modèle sont finalement explicitées.

Le troisième chapitre, intitulé "Dynamique de champ moyen", est consacré à l'évolution d'une paire $Q\bar{Q}$ fixée au centre de la boule de feu et évoluant dans un potentiel de liaison écranté par le champ de couleur environnant (l'aspect 1) ci-dessus). Dans un premier temps, sont présentés les différents ingrédients du modèle. Pour l'interaction mutuelle et écrantée des deux quarks lourds est considéré soit un potentiel "faiblement" liant déterminé par Mocsy et Petreczky [156] (voir figure VII.31) soit un potentiel "fortement" liant déterminé par Kaczmarek et Zantow [104]. Dérivés de résultats de QCD sur réseau (lQCD), ces deux potentiels correspondent à des régimes thermodynamiques différents: le premier à un régime intermédiaire entre énergie libre $F(T)$ et énergie interne $U(T)$ et le second à l'énergie interne. Les caractéristiques de leur dépendance en température et de leurs états propres sont ensuite présentées (formes des fonctions d'onde, énergies propres, températures de dissociation...). Les évolutions de la température du centre de la boule de feu au RHIC et au LHC sont données par le modèle d'évolution hydrodynamique de Kolb et Heinz [62] (voir par exemple figure VII.32). L'évolution "balistique" de la paire $Q\bar{Q}$ est déterminée avec l'équation de Schrödinger non relativiste en partant soit d'un paquet d'onde gaussien initial (hypothèse que la paire vient d'être produite) soit d'un état de quarkonium (hypothèse que l'état lié a eu le temps de se former). Ce choix d'état initial est motivé par la méconnaissance des temps de formation des états liés.

Afin d'observer le "contenu" en quarkonia (charmonia ou bottomonia) de la paire $Q\bar{Q}$ ($c\bar{c}$ ou $b\bar{b}$ respectivement), sa fonction d'onde est projetée à chaque instant sur les états propres du vide (déterminés avec les potentiels à $T = 0$). On obtient alors les évolutions des poids W_i des différents quarkonia, qui sont données et discutées pour les différentes configurations de potentiel et d'état initial pour différentes températures constantes ou pour les scénarios d'évolution de température du RHIC

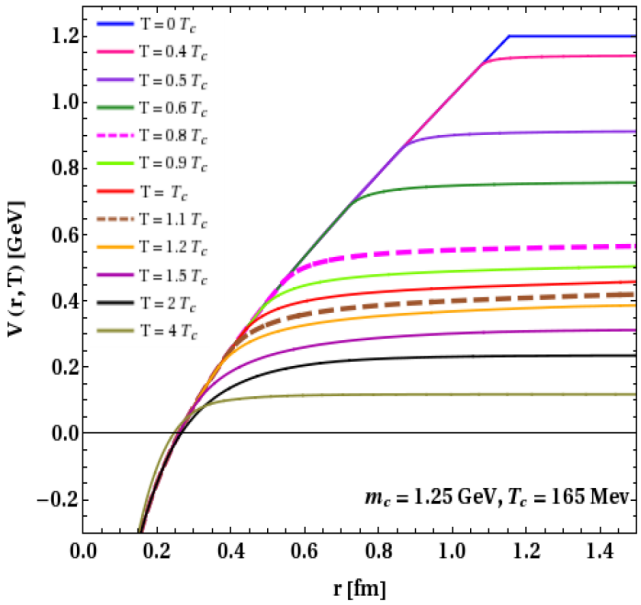

Figure VII.31: Le potentiel "faiblement" liant des charmonia à différentes températures [109].

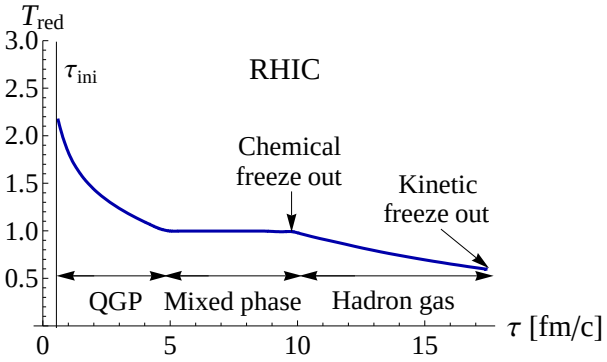

Figure VII.32: Évolution hydrodynamique de la température réduite $T_{red}(t) = T/T_c$ au centre de la "boule de feu" au RHIC $\sqrt{s_{NN}} = 200$ GeV. Quand $T_{red} > 1$ le milieu est un PQG, à $T_{red} = 1$ le mileu est une phase mixte parton/hadron et un gaz de hadron quand $T_{red} < 1$.

et du LHC (voir par exemple figure VII.33). La richesse des évolutions obtenues montre que le problème ne peut être réduit à de simples états couplés/découplés, que les temps de décorrélation ne sont pas petits comparés aux temps typiques du PQG et que d'importantes transitions entre états liés sont possibles (en particulier, l'état ψ' peut être fortement repeuplé lors de la décorrélation du J/ψ). Toutes ces observations tendent à écarter les hypothèses des modèles de suppression séquentielle et d'hadronisation statistique (rapide et complète décorrélation des paires provenant d'états dissociés ou de tous les états respectivement).

Le quatrième chapitre, intitulé "Quarkonia et systèmes quantiques ouverts", aborde l'aspect lié aux collisions multiples que subit la paire $Q\bar{Q}$ avec les partons du milieu. L'objectif de ce chapitre est d'identifier un (ou des) formalisme(s) per-

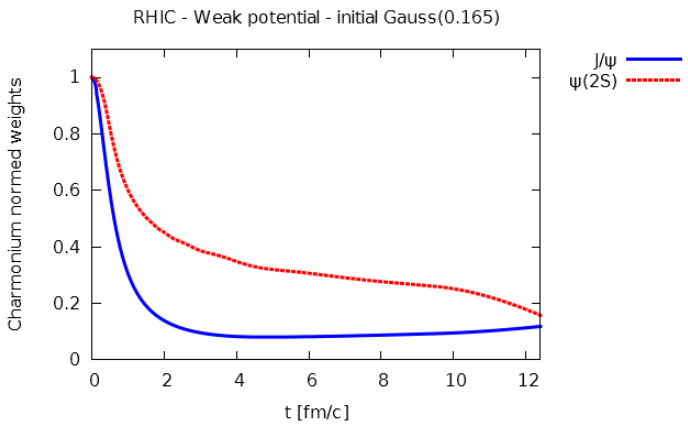

Figure VII.33: Évolution des poids normés $S_i = W_i(t)/W_i(t=0)$ des états de J/ψ et ψ' au RHIC à partir d'un état initial gaussien (de paramètre $a_c = 0.165$).

mettant d'aborder ces collisions dans le cadre de la thèorie des systèmes quantiques ouverts. Ce chapitre est divisé en deux parties: la première est une introduction à la théorie des systèmes classiques et quantiques ouverts et la seconde une revue de la littérature sur les applications de cette théorie au cas des quarkonia. Puisque les quarks lourds de la paire peuvent être vus dans le PQG comme des particules "brownienne", la première partie cherche en particulier à introduire les différentes approches envisagées dans la littérature pour des dynamiques de type brownienne, c'est-à-dire lorsque le temps de relaxation du sous-système d'intérêt est long par rapport aux temps typiques de collision et d'étude. Du coté classique [151], l'équation de Langevin (ou de façon équivalente l'équation de Fokker-Planck) permet de décrire la dynamique d'une particule brownienne classique à l'aide d'un terme de friction, inversement proportionnel à la vitesse de la particule et paramétré par le coefficient de friction, et d'une force stochastique simulant les multiples collisions avec le milieu. La balance de ces deux aspects, obtenue grâce à la relation d'Einstein, permet au sous-système d'intérêt d'atteindre l'équilibre thermique déterminé par la physique statistique (distributions de Boltzmann). Du coté quantique [182], la dynamique de Langevin ne peut être introduite trivialement dans le formalisme quantique commun (aucune quantification d'un Hamiltonien ne peut mener à des phénomènes irréversibles). Différentes approches ont été proposées pour surmonter cette difficulté, mais il n'existe pas de description universelle. L'approche la plus commune est de considérer le sous-système d'intérêt et le bain thermique comme un système global conservatif, puis en intégrant les degrés de liberté du bain et en procédant à quelques approximations, il est possible d'obtenir l'évolution dissipative du sous-système seule. Habituellement, l'équation d'évolution qui en dérive à la limite brownienne ("de faible couplage"), se présente sous la forme d'une équation maîtresse quantique [182, 200] pour la matrice densité ou alternativement d'une équation de Schrödinger stochastique [183, 199, 203]. Dans le cas d'applications complexes où il est difficile de définir l'hamiltonien d'interaction/du bain ou de calculer les opérateurs de Lindblad sans trop d'approximations, des approches effectives sont nécessaires (du type de Langevin par exemple). Un modèle simple de bain [172, 185, 186] - un ensemble d'oscillateurs harmoniques couplé linéairement

au sous-système - a prouvé être un cadre pertinent. Celui-ci mène, à la limite de faible couplage, à une équation de Langevin pour les opérateurs de Heisenberg, dénommée équation de Heisenberg-Langevin. L'application pratique de celle-ci est cependant limitée par la nature non-commutative de ces opérateurs. Comme pour le cas classique, l'équilibre thermal attendu à la limite de faible couplage est donné par les distributions de Boltzmann. Différentes approches ont été proposées afin de traiter des interactions multiples entre les quarkonia et le PQG: approches de type section efficace et potentiel imaginaire, approches semi-classiques et systèmes quantiques ouverts. L'approche semi-classique de Young et Shuryak [2] est explorée dans le chapitre 5. Les approches de types systèmes quantiques ouverts développées jusqu'à présent semblent être soit rigoureuses [222], mais difficilement applicables à la phénoménologie, ou plus effectives [224, 223], mais incapables d'amener à la thermalisation de la dynamique interne des paires $Q\bar{Q}$.

Le cinquième chapitre, intitulé "Une approche semi-classique", explore un cadre semi-classique initialement proposé par Young et Shuryak [2]. C'est une première tentative de notre part d'introduire les effets directs d'un PQG thermal sur les paires $Q\bar{Q}$. Le formalisme, c'est-à-dire l'évolution classique de Langevin de la distribution de Wigner d'une paire $Q\bar{Q}$, a été choisi comme moyen commode d'introduire un processus classique de thermalisation - qui reflète les collisions permanentes entre la paire et les partons du milieu - tout en gardant accessible l'analyse en 3D sans approximation. Nous nous sommes exclusivement concentrés sur l'évolution du poids en J/ψ. Nous avons tout d'abord comparé les évolutions obtenues avec les formalismes quantique et semi-classique sans dynamique de Langevin, et avons observé d'importantes différences (qui étaient attendues). Ces différences peuvent sembler problématiques au premier abord mais pourraient être en fait négligeables une fois la dynamique de Langevin incluse si cette dernière dominait l'évolution (ce qui semble être le cas ici). Nous avons ensuite exploré le formalisme complet et observé de pertinentes décroissances exponentielles du poids en J/ψ, après une période transitoire, à différentes températures constantes. Incluant les scénarios de

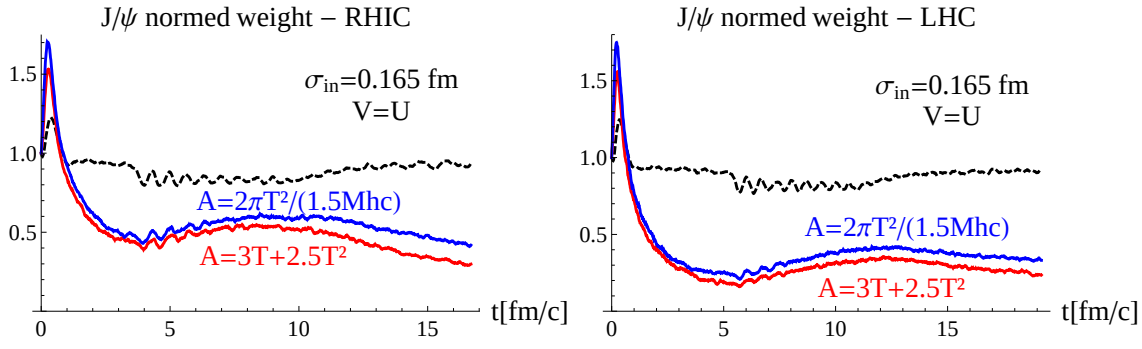

Figure VII.34: *Left*: Résultats du modèle semi-classique pour les poids du J/ψ en fonction du temps avec les scénarios de température du RHIC (gauche) et du LHC (droite), $V = U$ et la dynamique de Langevin (lignes pleines). Lignes pointillées: même cas mais sans dynamique de Langevin.

température du RHIC et du LHC, nous avons obtenu de riches schémas de sup-

pression (voir figure VII.34 par exemple) qui semblent écarter, encore une fois, les hypothèses injustifiées des modèles de suppression séquentielle et d'hadronisation statistique. Ces résultats ont été publiés dans un compte-rendu de conférence [226]. Finalement, nous avons sévèrement questionné la pertinence des résultats obtenus avec les méthodes semi-classiques (dont la notre), en pointant deux écueils important observés dans le cas trivial du potentiel harmonique: une violation du principe d'incertitude d'Heisenberg à basse température ($T \ll E_0$) et une mauvaise thermalisation des états propres. Tous ces défauts nous ont incité à chercher une approche entièrement quantique.

Dans le but de trouver un formalisme quantique effectif adapté à la thermalisation des quarkonia dans le PQG, dans le sixième chapitre, intitulé "L'équation de Schrödinger-Langevin: généralités et équilibration", nous nous sommes concentrés sur les propriétés de l'équation de Schrödinger-Langevin ("SL"). Explicitement, l'équation de SL s'écrit

$$i\hbar\frac{\partial\psi(\vec{x},t)}{\partial t} = \left[H_0 + \hbar A\Big(S(\vec{x},t) - \int \psi^* S(\vec{x},t)\,\psi\; d^3x\Big) - \vec{x}.\vec{F}_R(t)\right]\psi,$$

où A est le coefficient de friction (inverse du temps de relaxation), S la phase réelle de la fonction d'onde et $\vec{F}_R$ une force stochastique. Grâce à son aspect phénoménologique - seuls les paramètres de friction et de température sont nécessaires - et à sa simplicité numérique, l'équation de SL peut en effet être considérée comme un solide candidat pour des descriptions effectives de systèmes quantiques ouverts difficilement accessibles aux équations maîtresses ou équivalents. C'est une équation stochastique et non-linéaire qui permet une évolution graduelle d'un état pur à un état mixte grâce à une force stochastique (et donc à de larges statistiques) et à un terme dissipatif non-linéaire. Dans un premier temps, deux de ses dérivations possibles sont données: par identification avec l'équation de Heisenberg-Langevin [3] et dans le cadre de la théorie des trajectoires quantiques. Ses propriétés basiques sont ensuite discutées: l'unitarité est préservée pour l'état pur, le principe d'incertitude d'Heisenberg est toujours satisfait, le principe de superposition est violé par la non-linéarité... Afin de nous assurer de la pertinence de l'équation de SL (en vue d'applications phénoménologiques), il était nécessaire de répondre à certaines questions ouvertes relatives à ses solutions: la stationnarité des états excités de l'hamiltonien non couplé et la relaxation thermal. Il est communément pensé que le terme non-linéaire de friction maintient la stationnarité des états excités de l'hamiltonien non couplé. Au contraire, nous avons montré que la transformé de Madelung (ou polaire) de la fonction d'onde mène à une friction non nulle pour ces états. De cette manière, nous avons réconcilié l'équation de SL avec l'idée intuitive que la dissipation doit pouvoir agir sur n'importe quel état pour amener le sous-système à son état fondamental. Afin d'tudier la relaxation thermal, nous avons ensuite étudié les solutions de l'équation de SL en testant deux opérateurs de bruit pour la force stochastique (prise comme un nombre classique): un bruit blanc (VI.102, VI.103) [172] et un bruit coloré (VI.105) [185] inspirés de la littérature. L'analyse détaillée des évolutions du sous-système soumis à un potentiel harmonique ou linéaire 1D, montre que sous certaines conditions l'équation de SL permet de

conduire à l'équilibre thermique. Nous avons conclu que l'équation de SL peut être utilisée en phénoménologie lorsque seuls les états de basse énergie sont considérés (ce qui inclus les quarkonia). L'ensemble de ces résultats fait l'objet d'une publication [238].

Dans le septième et dernier chapitre, intitulé "Étude de la suppression des quarkonia avec l'approche de Schrödinger-Langevin", l'équation de SL est appliquée à l'évolution d'une paire $Q\bar{Q}$ corrélée plongée dans un PQG. Dans un premier temps, il est montré que l'équation de SL en coordonnées sphériques induit des transitions entre états de moments orbitaux différents. L'analyse ne peut alors plus se réduire à la partie radiale comme dans le troisième chapitre et requière un traitement complet en coordonnées sphériques 3D, qui est malheureusement difficilement accessible. Certaines approximations étant alors nécessaires, nous avons exploré pour cette thèse un modèle simplifié où la situation est approximée à un potentiel 1D linaire et symétrique. Ce modèle devrait contenir l'essentiel de la physique mais n'a pas pour but de reproduire les données expérimentales. Comme dans le troisième chapitre, la dynamique de la paire $Q\bar{Q}$ et de son contenu en quarkonia est tout d'abord étudiée à diverses températures constantes, où nous avons observ une thermalisation correcte des états et le caractère diffusif de l'évolution. Nous avons ensuite inclus les scénarios d'évolution hydrodynamique de la température au centre de la boule de feu au RHIC et au LHC. Nous avons obtenu de riches schémas de suppression (voir par exemple figure VII.35) qui, de même que dans les modèles précédent, tendent à écarter les hypothèses des modèles de suppression séquentielle et d'hadronisation statistique. De plus, nous avons observé d'intéressantes transitions entre états menant en particulier à une régénération du ψ' s'amplifiant avec l'énergie de collision. Ceci pourrait donner une piste d'explication à la surprenante et inexpliquée mesure, de la collaboration de CMS, d'un ratio de suppression $\psi'/J/\psi$ supérieur à 1 à grande rapidité. La comparaison des évolutions obtenues avec et sans forces thermales et avec et sans écrantage, montre qu'aucun de ces deux aspects ne peut être négligé. Enfin, nous avons appliqué notre modèle aux bottomonia dans un cadre plus réaliste de collision au LHC extrait du générateur d'événement EPOS: volume fini, distribution de température inhomogène et distributions des paires en position et moment. Les dépendances des R_{AA} obtenues en p_T et N_{part} (voir par exemple figure VII.36) décrivent raisonnablement les tendances des données. Ces premiers résultats sont présentés dans un compte-rendu de conférence [273].

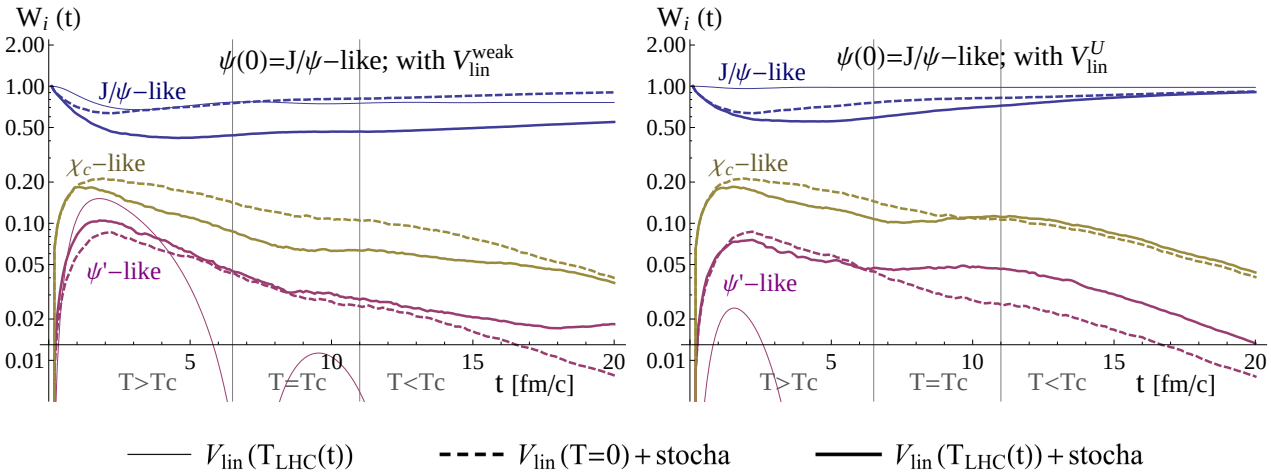

Figure VII.35: Évolutions des poids des charmonia en partant d'un état initial similaire au J/ψ, obtenues avec les potentiels $V_{\rm lin}^{\rm weak}$ (*gauche*) et $V_{\rm lin}^{U}$ (*droite*) pour le scénario de température du LHC (de Kolb et Heinz). Les courbes fines correspondent à la situation de champ moyen, les courbes pointillées sont obtenues avec les forces thermales et le potentiel du vide, et les courbes épaisses avec les forces thermales et les potentiels écrantés de couleur.

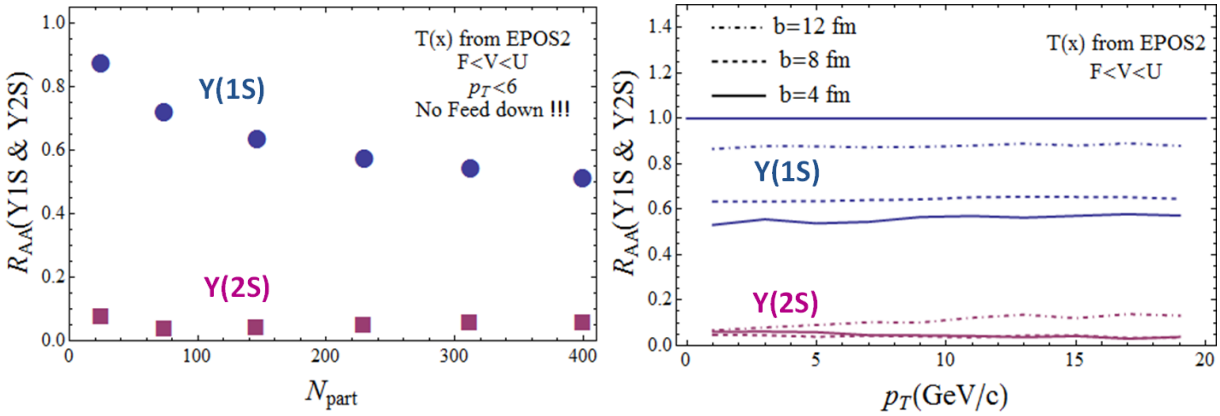

Figure VII.36: Dépendances en $N_{\rm part}$ (gauche) et p_T (droite) des poids normés des bottomonia pour trois paramètres d'impact b (droite) ou intégrées en b (gauche), obtenues avec l'état gaussien initial, le potentiel $V_{\rm lin}^{weak}$ et les distributions spatio-temporelles en température données par EPOS2 au LHC.

Bibliography

[1] T. Matsui and H. Satz, "J/ψ suppression by Quark-Gluon Plasma Formation," Phys. Lett. B **178** (1986) 416. (Cited on pages 7, 46, 50, 58, and 201.)

[2] C. Young and E. Shuryak, "Charmonium in strongly coupled quark-gluon plasma," Phys. Rev. C **79** (2009) 034907 [arXiv: 0803.2866] (Cited on pages 8, 67, 77, 114, 120, 123, 124, 125, 127, 128, 131, and 205.)

[3] M. D. Kostin, "On the Schrödinger-Langevin equation," J. Chem. Phys. **57** (1972) 3589. (Cited on pages 8, 135, 137, 139, 144, and 206.)

[4] E. D. Bloom, D. H. Coward, H. DeStaebler, J. Drees, G. Miller, L. W. Mo, R. E. Taylor, M. Breidenbach, J. I. Friedman, G. C. Hartmann and H. W. Kendall, Phys. Rev. Lett. **23** (1969) 930. (Cited on page 16.)

[5] M.E. Peskin and D.V. Schroeder, *An introduction to quantum field theory*. Advanced book classics. Addison-Wesley Publishing Company, (1995). (Cited on pages 17 and 66.)

[6] W. Greiner, S. Schramm and E. Stein, *Quantum Chromodynamics*. Springer, 3rd edition, (2007). (Cited on page 18.)

[7] S. Bethke, "Experimental tests of asymptotic freedom," Prog. Part. Nucl. Phys. **58** (2007) 351 [hep-ex/0606035]. (Cited on page 20.)

[8] B. Andersson, G. Gustafson, G. Ingelman and T. Sjöstrand, "Parton fragmentation and string dynamics," Phys. Rep., **97** (2-3) (1983) p31-145. (Cited on page 21.)

[9] Y. Nambu, "The confinement of quarks," Scientific American, **235** (5) (1976) p48-60. (Cited on page 21.)

[10] M. N. Chernodub, [arxiv: 1001.0570 [hep-ph]]. (Cited on page 21.)

[11] K. A. Olive *et al.* (Particle Data Group), Chin. Phys. C **38** (2014) 090001. See Quarkonia. See Quark masses. (Cited on pages 22 and 23.)

[12] G. T. Bodwin, E. Braaten and G. P. Lepage, Phys. Rev. D **51** (1995) 1125; Erratum-ibid. D **55** (1997) 5853. (Cited on page 24.)

[13] R. Baier and R. Rückl, Z. Phys. C **19** (1983) 251. (Cited on page 24.)

[14] B. Guberina, J. H. Kuhn, R. D. Peccei and R. Rückl, "Rare Decays Of The Z0," Nucl. Phys. B **174** (1980) 317. (Cited on page 24.)

[15] P. L. Cho and A. K. Leibovich, "Color octet quarkonia production," Phys. Rev. D **53** (1996) 150 [arXiv:hep-ph/9505329];
Phys. Rev. D **53** (1996) 6203 [arXiv:hep-ph/9511315]. (Cited on pages 24 and 25.)

[16] E. Braaten and S. Fleming, Phys. Rev. Lett. **74** (1995) 3327. (Cited on page 25.)

[17] G. T. Bodwin, E. Braaten and G. P. Lepage, Phys. Rev. D **51** (1995) 1125; Erratum-ibid. D **55** (1997) 5853. (Cited on page 25.)

[18] M. Butenschoen and B. A. Kniehl, "J/ψ polarisation at Tevatron and LHC: Nonrelativistic-QCD factorisation at the crossroads," (2012) [arXiv:hep-ph/1201.1872v1]. (Cited on page 25.)

[19] A. Andronic *et al.*, "Heavy-flavour and quarkonium production in the LHC era: from proton-proton to heavy-ion collisions," [arXiv:1506.03981 [nucl-ex]]. (Cited on pages 25, 45, 46, 47, 52, 55, 57, 62, and 64.)

[20] Z. Conesa del Valle, G. Corcella, F. Fleuret, E. G. Ferreiro, V. Kartvelishvili, B. Kopeliovich, J. P. Lansberg and C. Lourenco *et al.*, "Quarkonium production in high energy proton-proton and proton-nucleus collisions," Nucl. Phys. Proc. Suppl. **214** (2011) 3 [hep-ph/1105.4545]. (Cited on page 26.)

[21] V. Gribov and L. Lipatov, Sov. J. Nucl. Phys. **15** (1972) 438 and 675. L. Lipatov, Sov. J. Nucl. Phys. **20** (1975) 94. G. Altarelli and G. Parisi, Nucl. Phys. B **126** (1977) 298. Y. Dokshitser, Sov. Phys. JETP **46** (1977) 641. (Cited on page 26.)

[22] E. Kuraev, L. Lipatov and V. Fadin, Sov. Phys. JETP **44** (1976) 443. E. Kuraev, L. Lipatov and V. Fadin, Sov. Phys. JETP **45** (1977) 199. Y. Balitskii and L. Lipatov, Sov. J. Nucl. Phys. **28** (1978) 822. (Cited on page 26.)

[23] J. C. Collins and M. J. Perry, "Superdense Matter: neutrons or asymptotically free quarks ?", Phys. Rev. Lett. **34** (1975) 1353. (Cited on page 26.)

[24] E. Shuryak, "Quark-Gluon Plasma and Hadronic Production of Leptons, Photons and Pions Phys. Lett. B **78** (1978) 150. (Cited on page 26.)

[25] Uwe-Jens Wiese, Lecture: An introduction to lattice field theory (2009).
Marco Panero, Presentation: Introduction to lattice QCD (2010). (Cited on page 27.)

[26] F. Karsch, Lattice QCD at High Temperature and Density (2001) [arXiv:hep-lat/0106019v2]. (Cited on page 27.)

[27] A. Bazavov, T. Bhattacharya, M. Cheng, N.H. Christ, C. DeTar, *et al.*, "Equation of state and QCD transition at finite temperature," Phys. Rev. D**80** (2009) 014504. (Cited on page 28.)

[28] F. Beutler, Workshop on Quark-Gluon-Plasma and Cold Atomic Physics - SS 2008 "Thermodynamics of relativistic gases and the QGP" (2008). (Cited on page 28.)

[29] A. Chodos, R. L. Jaffe, K. Johnson, C. B. Thorn, and V. F. Weisskopf, "A new extended model of hadrons," Phys. Rev. D**9** (1974) 3471-3495. (Cited on page 28.)

[30] Y. Nambu and G. Jona-Lasinio, "Dynamical model of elementary particles based on an analogy with superconductivity I (and II)." Phys. Rev. **122** (1961) 345358. (Cited on page 28.)

[31] M. A. Stephanov, "QCD phase diagram and the critical point," Prog. Theor. Phys. Suppl. **153** (2004) 139 [Int. J. Mod. Phys. A **20** (2005) 4387] [hep-ph/0402115]. (Cited on page 28.)

[32] Z. Fodor, "Lattice QCD results at finite temperature and density," Nucl. Phys. A **715** (2003) 319-328 [arXiv:hep-lat/0209101v1]. (Cited on page 28.)

[33] H. Satz, "The Thermodynamics of Quarks and Gluons," Lect. Notes Phys. **785** (2010) 1 [arXiv:0803.1611 [hep-ph]]. (Cited on pages 29, 32, and 35.)

[34] S. Hands, "The phase diagram of QCD," Contemp. Phys. **42** (2001) 209225 [arXiv:0105022 [hep-ph]]. (Cited on pages 29 and 201.)

[35] F. D. Aaron, *et al.* [H1 and ZEUS Collaborations] JHEP 1001, 109 (2010). (Cited on page 30.)

[36] K. J. Eskola, "Global analysis of nuclear PDFs - latest developments," Nucl. Phys. A **910-911** (2013) 163 [arXiv:1209.1546 [hep-ph]] (Cited on page 30.)

[37] N. Armesto, "Nuclear shadowing," J. Phys. G **32**, R367R394 (2006). (Cited on page 30.)

[38] K.J. Eskola, V.J. Kolhinen, and P.V. Ruuskanen, "Scale evolution of nuclear parton distributions," Nucl. Phys., B **535** (1998) 351 [hep-ph/9802350]. (Cited on pages 30 and 31.)

[39] F. Gelis, "Color Glass Condensate and Glasma," Int. J. Mod. Phys. A **28** (2013) 1330001 [arXiv:1211.3327 [hep-ph]]. (Cited on pages 30 and 31.)

[40] H. Mueller and J. W. Qiu, "Gluon recombination and shadowing at small values of x," Nucl. Phys. B **268** (1986) 427. (Cited on page 31.)

[41] L. Mc Lerran, "A brief introduction to the Color Glass Condensate and the Glasma," (2008) [arxiv:0812.4989 [hep-ph]]. (Cited on page 31.)

[42] P. B. Arnold, G. D. Moore and L. G. Yaffe, "Transport coefficients in high temperature gauge theories. 2. Beyond leading log," JHEP **0305** (2003) 051 [hep-ph/0302165]. (Cited on page 32.)

[43] C. Ratti, "Lattice QCD: bulk and transport properties of QCD matter," talk at Quark Matter 2015. (Cited on page 32.)

[44] R.J. Glauber and G. Matthiae, "High-energy scattering of protons by nuclei," Nucl. Phys. B **21** (1970) 135-157. (Cited on pages 33, 37, 84, and 185.)

[45] P. Petro, "Charged particle multiplicity, centrality and the Glauber model in Pb-pb collisions at $\sqrt{s_{NN}} = 2.76$ TeV with Alice," Acta Physica Polonica B **5** Proceedings Supplement No 2 (2012). (Cited on page 33.)

[46] B. Alver *et al.*, "Elliptic Flow, Initial Eccentricity and Elliptic Flow fluctuations in Heavy Ion Collisions at RHIC." (2007) [arXiv:nucl-ex/0707.4424v1]. (Cited on page 34.)

[47] Aamodt *et al.* [ALICE Collaboration], "Elliptic flow of charged particles in Pb-Pb collisions at 2.76 TeV," Phys. Rev. Lett. **105** (2010) 252302 [arXiv:nucl-ex/1011.3914]. (Cited on page 34.)

[48] Th. Peitzmann and M.H. Thoma, "Direct photons from relativistic heavy-ion collisions," Phys. Rept., **364** (2002) 175 [arXiv:hep-ph/0111114v2]. (Cited on page 34.)

[49] R. Shahoyan *et al.* "NA60 results on charm and intermediate mass dimuons production in In-In 158 GeV/A collisions," J. Phys. G: Nucl. Part. Phys. **34** (2007) S1029. (Cited on page 34.)

[50] P. Koch, B. Muller, and J. Rafelski, "Strangeness in relativistic heavy ion collisions," Phys. Rept. **142** (1986) 167262. (Cited on page 34.)

[51] J. Takahashi *et al.* [STAR Collaboration], "Strangeness production in STAR," arXiv:0809.0823 [nucl-ex]. (Cited on page 34.)

[52] B. Abelev [ALICE Collaboration], "Strangeness with ALICE: from pp to Pb-Pb," arXiv:1209.3285 [nucl-ex]. (Cited on page 34.)

[53] Yen-Jie Lee, "nPDF sensitive observables in CMS," 3rd Heavy Ion Jet Workshop, Lisbon (2014). (Cited on page 34.)

[54] A. Florent "Production of W and Z bosons in heavy-ion collisions with CMS," Hard Probes 2013 proceeding, Nucl. Phys. A **932** (2014) 459465. (Cited on page 34.)

[55] A. Beraudo, "Heavy-ion collisions: theory review," presentation at "QCD at Cosmic Energies Paris, (2012). (Cited on page 34.)

[56] A. Andronic, P. Braun-Munzinger, K. Redlich and J. Stachel, "The statistical model in Pb-Pb collisions at the LHC," Nucl. Phys. A **904-905** (2013) 535c [arXiv:1210.7724 [nucl-th]]. (Cited on page 35.)

[57] J. Stachel, A. Andronic, P. Braun-Munzinger and K. Redlich, "Confronting LHC data with the statistical hadronization model," J. Phys. Conf. Ser. **509** (2014) 012019 [arXiv:1311.4662 [nucl-th]]. (Cited on page 35.)

[58] U. Heinz, P. F. Kolb and J. Sollfrank, "Anisotropic transverse flow and the quark-hadron phase transition," Phys. Rev. C **62** (2000) 054909. (Cited on page 36.)

[59] U. Heinz and R. Snellings, "Collective flow and viscosity in relativistic heavy-ion collisions," Ann. Rev. Nucl. Part. Sci. **63** (2013) 123 [arXiv:1301.2826 [nucl-th]]. (Cited on pages 36 and 37.)

[60] S. Voloshin and Y. Zhang, "Flow study in relativistic nuclear collisions by Fourier expansion of Azimuthal particle distributions," Z. Phys. C **70** (1996) 665 [hep-ph/9407282]. (Cited on page 36.)

[61] M. Gyulassy and L. McLerran, "New forms of QCD matter discovered at RHIC," Nucl. Phys. A **750** (2005) 30 [nucl-th/0405013]. (Cited on page 36.)

[62] P. F. Kolb and U. W. Heinz, "Hydrodynamic description of ultrarelativistic heavy ion collisions," In *Hwa, R.C. (ed.) et al.: Quark gluon plasma* 634-714 [nucl-th/0305084]. (Cited on pages 38, 83, 84, and 202.)

[63] S. A. Bass, M. Belkacem, M. Bleicher, M. Brandstetter, L. Bravina, C. Ernst, L. Gerland and M. Hofmann *et al.*, "Microscopic models for ultrarelativistic heavy ion collisions," Prog. Part. Nucl. Phys. **41** (1998) 255 [Prog. Part. Nucl. Phys. **41** (1998) 225] [nucl-th/9803035]. (Cited on pages 38, 55, and 202.)

[64] E. L. Bratkovskaya, W. Cassing, V. P. Konchakovski and O. Linnyk, "Parton-Hadron-String Dynamics at Relativistic Collider Energies," Nucl. Phys. A **856** (2011) 162 [arXiv:1101.5793 [nucl-th]]. (Cited on pages 38, 55, and 202.)

[65] M. van Leeuwen [ALICE Collaboration], "High-p_T results from ALICE," arXiv:1201.5205 [nucl-ex]. (Cited on pages 39 and 40.)

[66] B. G. Zakharov, "Parton energy loss in an expanding quark-gluon plasma: Radiative versus collisional," JETP Lett. **86** (2007) 444 [arXiv:0708.0816 [hep-ph]]. (Cited on page 39.)

[67] R. Baier, Y. L. Dokshitzer, A. H. Mueller, S. Peigné, and D. Schiff, Nucl. Phys. B **484** (1997) 265 [arXiv:hep-ph/9608322]. (Cited on page 39.)

[68] C. Adler *et al.* [STAR Collaboration], "Disappearance of back-to-back high p_T hadron correlations in central Au+Au collisions at $\sqrt{s_{NN}} = 200$-GeV," Phys. Rev. Lett. **90** (2003) 082302 [nucl-ex/0210033]. (Cited on page 39.)

[69] S. Chatrchyan *et al.* [CMS Collaboration], "Studies of jet quenching using isolated-photon+jet correlations in PbPb and pp collisions at $\sqrt{s_{NN}} = 2.76$ TeV," Phys. Lett. B **718** (2013) 773 [arXiv:1205.0206 [nucl-ex]]. (Cited on page 40.)

[70] S. Chatrchyan *et al.* [CMS Collaboration], "Study of high-pT charged particle suppression in PbPb compared to *pp* collisions at $\sqrt{s_{NN}} = 2.76$ TeV," Eur. Phys. J. C **72** (2012) 1945 [arXiv:1202.2554 [nucl-ex]]. (Cited on pages 38 and 39.)

[71] P. B. Gossiaux, "Tomographie du Plasma de Quarks et de Gluons Grâce aux Saveurs Lourdes: Eléments de Théorie, Phénoménologie et Applications," Dossier de Candidature au Diplôme d'Habilitation à Diriger des Recherches (2009). (Cited on page 45.)

[72] P. Braun-Munzinger and K. Redlich, "Charmonium production from the secondary collisions at LHC energy," Eur. Phys. J. C **16** (2000) 519525 [arXiv:hep-ph/0001008 [hep-ph]]. (Cited on page 45.)

[73] S. Jeon and J. Kapusta, "Linear Extrapolation of Ultrarelativistic Nucleon-Nucleon Scattering to Nucleus-Nucleus Collisions," Phys. Rev. C **56** (1997) 468-480 [arXiv :nucl-th/9703033]. (Cited on page 45.)

[74] B. I. Abelev *et al.* [STAR Collaboration], "Systematic Measurements of Identified Particle Spectra in pp, d^+ Au and Au+Au Collisions from STAR," Phys. Rev. C **79** (2009) 034909 [arXiv:0808.2041 [nucl-ex]]. (Cited on page 45.)

[75] R. Bailhache [ALICE Collaboration], "Heavy-flavour elliptic flow measured in PbPb collisions at $\sqrt{s_{NN}} = 2.76$ TeV with ALICE," Nucl. Phys. A **931** (2014) 530. (Cited on page 45.)

[76] A. Adare *et al.* [PHENIX Collaboration], "Heavy Quark Production in $p + p$ and Energy Loss and Flow of Heavy Quarks in Au+Au Collisions at $\sqrt{s_{NN}} =$ 200 GeV," Phys. Rev. C **84** (2011) 044905 [arXiv:1005.1627 [nucl-ex]]. (Cited on page 45.)

[77] B. Abelev *et al.* [ALICE Collaboration], "Suppression of high transverse momentum D mesons in central Pb-Pb collisions at $\sqrt{s_{NN}} = 2.76$ TeV," JHEP **1209** (2012) 112 [arXiv:1203.2160 [nucl-ex]]. (Cited on page 45.)

[78] A. Adare *et al.* [PHENIX Collaboration], "Energy Loss and Flow of Heavy Quarks in Au+Au Collisions at $\sqrt{s_{NN}} = 200$GeV," Phys. Rev. Lett. **98** (2007) 172301 [arXiv :nucl-ex/0611018]. (Cited on page 45.)

[79] Y. L. Dokshitzer and D. E. Kharzeev, "Heavy quark colorimetry of QCD matter," Phys. Lett. B **519** (2001) 199-206 [arXiv :hep-ph/0106202v1]. (Cited on page 46.)

[80] N. Armesto, C.A. Salgado and U.A. Wiedemann, "Medium-Induced Gluon Radiation off Massive Quarks Fills the Dead Cone," Phys. Rev. D **69** (2004) 114003 [arXiv :hep-ph/0312106]. (Cited on page 46.)

[81] M. Djordjevic and M. Gyulassy, "Heavy Quark Radiative Energy Loss in QCD Matter," Nucl. Phys. A **733** (2004) 265-298 [arXiv :nucl-th/0310076]. (Cited on page 46.)

[82] J.D. Bjorken, "Energy loss of energetic partons in quark gluon plasma: possible extinction of hight pT jets in hadron-hadron collisions," FERMILAB-Pub-82/59-THY (1982). (Cited on page 46.)

[83] E. Braaten and M. H. Thoma, "Energy loss of a heavy quark in the quark-gluon plasma," Phys. Rev. D **44** (1991) 2625-2630. (Cited on page 46.)

[84] S. Peigné and A. Peshier, "Collisional energy loss of a fast heavy quark in a quark-gluon plasma," Phys. Rev. D **77** (2008) 114017 [arXiv:hep-ph/0802.4364v1]. (Cited on page 46.)

[85] C. Peterson, D. Schlatter, I. Schmitt and P. M. Zerwas, Phys. Rev. D **27** (1983) 105. (Cited on page 46.)

[86] M. Cacciari, Nason and R. Vogt, Phys. Rev. Lett. **95** (2005) 122001 [arXiv :hep-ph/0502203]. (Cited on page 46.)

[87] F. Becattini, L. Maiani, F. Piccinini, A.D. Polosa, and V. Riquer, "Correlating strangeness enhancement and J/ψ suppression in heavy ion collisions at $\sqrt{s_{NN}} = 17.2$ GeV," Phys. Lett., B **632** (2006) 233237. (Cited on page 47.)

[88] K. Eskola, V. Kolhinen, and C. Salgado, "The Scale dependent nuclear effects in parton distributions for practical applications," Eur. Phys. J. C **9** (1999) 61 [arXiv:hep-ph/9807297 [hep-ph]]. (Cited on pages 47 and 49.)

[89] D. de Florian and R. Sassot, "Nuclear parton distributions at next-to-leading order," Phys. Rev. D **69** (2004) 074028 [arXiv:hep-ph/0311227 [hep-ph]]. (Cited on page 47.)

[90] F. Arleo and S. Peigné, "J/ψ suppression in p-A collisions from parton energy loss in cold QCD matter," Phys. Rev. Lett. **109** (2012) 122301 [arXiv:1204.4609 [hep-ph]]. (Cited on page 48.)

[91] M. Leoncino [ALICE Collaboration], "J/ψ and ψ(2S) production in p-Pb collisions with ALICE at the LHC," PoS Bormio **2014** (2014) 062 [arXiv:1410.1761 [hep-ex]]. (Cited on pages 48 and 63.)

[92] F. Arleo and S. Peigné, "Quarkonium suppression in heavy-ion collisions from coherent energy loss in cold nuclear matter," JHEP **1410** (2014) 73 [arXiv:1407.5054 [hep-ph]]. (Cited on page 48.)

[93] C. Lourenco, R. Vogt, and H. K. Wöhri, "Energy dependence of J/ψ absorption in proton-nucleus collisions," JHEP **0902** (2009) 014 [arXiv:0901.3054 [hep-ph]]. (Cited on page 49.)

[94] A. Capella, L. Bravina, E. G. Ferreiro, A. B. Kaidalov, K. Tywoniuk and E. Zabrodin, "Charmonium dissociation and recombination at RHIC and LHC," Eur. Phys. J. C **58** (2008) 437 [arXiv:0712.4331 [hep-ph]]. (Cited on page 50.)

[95] E. G. Ferreiro, "Charmonium dissociation and recombination at LHC: Revisiting comovers," Phys. Lett. B **731** (2014) 57 [arXiv:1210.3209 [hep-ph]]. (Cited on page 50.)

[96] D. Kharzeev and H. Satz, Phys. Lett. B **334** (1994) 155. (Cited on page 50.)

[97] H. Satz, "Colour deconfinement and quarkonium binding," J. Phys. G **32** (2006) R25 [hep-ph/0512217]. (Cited on pages 51, 52, and 53.)

[98] A. Adare *et al.* [PHENIX Collaboration], "Measurement of $\Upsilon(1S + 2S + 3S)$ production in $p + p$ and Au+Au collisions at $\sqrt{s_{NN}} = 200$ GeV," Phys. Rev. C **91** (2015) 2, 024913 [arXiv:1404.2246 [nucl-ex]]. (Cited on page 51.)

[99] W. M. Alberico, A. Beraudo, A. De Pace, and A. Molinari, "Heavy quark bound states above Tc," Phys. Rev. D **72**, 114011 (2005). (Cited on page 50.)

[100] A. Mocsy and P. Petreczky, "Can quarkonia survive deconfinement ?," Phys. Rev. D **77**, 014501 (2008). (Cited on page 50.)

[101] F. Riek and R. Rapp, "Quarkonia and Heavy-Quark Relaxation Times in the Quark-Gluon Plasma," Phys. Rev. C **82**, 035201 (2010). (Cited on page 50.)

[102] A. Jakovac, P. Petreczky, K. Petrov, and A. Velytsky, "Quarkonium correlators and spectral functions at zero and finite temperature," Phys. Rev. D **75**, 014506 (2007). (Cited on page 50.)

[103] G. Aarts, C. Allton, M. B. Oktay, M. Peardon, and J.-I. Skullerud, "Charmonium at high temperature in two-flavor QCD," Phys. Rev. D **76**, 094513 (2007). (Cited on page 50.)

[104] O. Kaczmarek and F. Zantow, "Quark antiquark energies and the screening mass in a quark-gluon plasma at low and high temperatures," Eur. Phys. J. C **43** (2005) 63 [hep-lat/0512031]. (Cited on pages 52, 79, and 202.)

[105] H. Satz, "The Quark-Gluon Plasma: A Short Introduction," Nucl. Phys. A **862-863** (2011) 4 [arXiv:1101.3937 [hep-ph]]. (Cited on page 52.)

[106] G. Bhanot and M. E. Peskin, "Short Distance Analysis for Heavy Quark Systems: 2. Applications," Nucl. Phys. B **156** (1979) 391. (Cited on pages 52, 53, 54, and 66.)

[107] S. H. Lee and Y. s. Oh, "Charmonium hadron interactions from QCD," J. Phys. G **28** (2002) 1903 [nucl-th/0201027]. (Cited on page 52.)

[108] D. Kharzeev, H. Satz, A. Syamtomov and G. Zinovev, "On the sum rule approach to quarkonium - hadron interactions," Phys. Lett. B **389** (1996) 595 [hep-ph/9605448]. (Cited on page 52.)

[109] Hamza Berrehrah, "Propagation et collectivité des quarkonia dans le plasma de quarks et de gluons: vers la suppression de la suppression du J/ψ à hautes températures", PhD thesis, Ecole des Mines de Nantes (2011). (Cited on pages 52, 54, 57, 77, 79, 80, 83, and 203.)

[110] L. Grandchamp and R. Rapp, "Thermal versus direct J/ψ production in ultrarelativistic heavy-ion collisions," Phys. Lett. B **523** (2001) 6066 [arXiv:hep-ph/0103124]. (Cited on page 53.)

[111] D. Kharzeev and H. Satz, "Quarkonium interactions in hadronic matter," Phys. Lett. B **334** (1994) 155 [hep-ph/9405414]. (Cited on page 54.)

[112] R. Rapp and H. van Hees, "Heavy Quarks in the Quark-Gluon Plasma," in Quark-Gluon Plasma 4 (R.C. Hwa, X.-N. Wang, eds.), World Scientific (2009) 111 [arXiv:0903.1096 [hep-ph]]. (Cited on pages 54, 55, 56, and 202.)

[113] R. L. Thews, "Quarkonium formation at high-energy," Nucl. Phys. A **702** (2002) 341345. (Cited on pages 54 and 201.)

[114] P. Braun-Munzinger and J. Stachel, "On charm production near the phase boundary," Nucl. Phys. A **690** (2001) 119126 [arXiv:nucl-th/0012064 [nucl-th]]. (Cited on pages 54 and 201.)

[115] P. Braun-Munzinger and J. Stachel, "Charmonium from Statistical Hadronization of Heavy Quarks: A Probe for Deconfinement in the Quark-Gluon Plasma," Landolt-Bornstein **23** (2010) 424 [arXiv:0901.2500 [nucl-th]]. (Cited on pages 54 and 201.)

[116] [ALICE Collaboration], "ALICE : Physics Performance Report, Volume II," J. of Phys. G **32** (2006) 1295. (Cited on page 54.)

[117] S. Adler, "Centrality dependence of charm production from a measurement of single electrons in Au+Au collisions at $\sqrt{s_{NN}} = 200$ GeV," Phys. Rev. Lett. **94** (2005) 082301. (Cited on page 54.)

[118] G. D. Moore and D. Teaney, "How much do heavy quarks thermalize in a heavy ion collision ?," Phys.Rev., C **71** (2005) 064904 [arXiv:hep-ph/0412346]. (Cited on pages 54, 124, and 125.)

[119] H. Satz, "Quarkonium analysis of nuclear collisions," Talk at the Sapore Gravis Workshop (2013). (Cited on page 55.)

[120] X. Zhao and R. Rapp, "Charmonium Production at High p(t) at RHIC," arXiv:0806.1239 [nucl-th]. (Cited on page 55.)

[121] M. Laine, O. Philipsen, P. Romatschke and M. Tassler, "Real-time static potential in hot QCD," JHEP **0703** (2007) 054 [hep-ph/0611300]. (Cited on pages 56, 66, and 113.)

[122] N. Brambilla, J. Ghiglieri, A. Vairo, and P. Petreczky, Phys. Rev. D **78** (2008) 014017. (Cited on pages 56 and 66.)

[123] A. Rothkopf, T. Hatsuda and S. Sasaki, "Complex Heavy-Quark Potential at Finite Temperature from Lattice QCD," Phys. Rev. Lett. **108** (2012) 162001 [arXiv:1108.1579 [hep-lat]]. (Cited on pages 56 and 66.)

[124] X. Zhao and R. Rapp, "Medium modifications and production of charmonia at LHC," Nucl. Phys. A **859** (2011) 114 [arXiv:1102.2194 [hep-ph]]. (Cited on pages 56 and 202.)

[125] A. Emerick, X. Zhao, and R. Rapp, "Bottomonia in the Quark-Gluon Plasma and their Production at RHIC and LHC," Eur. Phys. J. A **48** (2012) 72 [arXiv:1111.6537 [hep-ph]]. (Cited on pages 56 and 202.)

[126] L. Yan, P. Zhuang, and N. Xu, "J/ψ production in quark-gluon plasma," Phys. Rev. Lett. **97** (2006) 232301 [arXiv:nucl-th/0608010 [nucl-th]]. (Cited on pages 56 and 202.)

[127] Y.-P. Liu, Z. Qu, N. Xu, and P.-f. Zhuang, "J/ψ Transverse Momentum Distribution in High Energy Nuclear Collisions at RHIC," Phys. Lett. B **678** (2009) 72 [arXiv:0901.2757 [nucl-th]]. (Cited on pages 56 and 202.)

[128] N. Brambilla *et al.*, "Heavy quarkonium : progress, puzzles, and opportunities," The European Physical Journal C **71** (2011) 1178. (Cited on page 57.)

[129] G. Borges *et al.* [NA50 Collaboration], "Charmonia production at the CERN/SPS," J. Phys. G **32** (2006) S381 [hep-ex/0505065]. (Cited on page 57.)

[130] A. Adare *et al.* [PHENIX Collaboration], "J/ψ Production vs Centrality, Transverse Momentum, and Rapidity in Au+Au Collisions at $\sqrt{s_{NN}} = 200$ GeV," Phys. Rev. Lett. **98** (2007) 232301 [nucl-ex/0611020]. (Cited on page 58.)

[131] R. Granier de Cassagnac, "Heavy flavour and quarkonium experimental overview," Talk at Strangeness in Quark Matter (2013); E. Scomparin, "NA60 results on J/psi," Talk at Quark Matter (2006). (Cited on page 58.)

[132] A. Andronic, P. Braun-Munzinger, K. Redlich and J. Stachel, "Evidence for charmonium generation at the phase boundary in ultra-relativistic nuclear collisions," Phys. Lett. B **652** (2007) 259 [nucl-th/0701079 [nucl-th]]. (Cited on page 59.)

[133] A. Adare *et al.* [PHENIX Collaboration], Phys. Rev. C **84** (2011) 054912 [arXiv:1103.6269 [nucl-ex]]. (Cited on pages 59, 99, 127, and 179.)

[134] L. Adamczyk *et al.* [STAR Collaboration], Phys. Lett. B **722** (2013) 55 [arXiv:1208.2736 [nucl-ex]]. (Cited on pages 59, 99, 127, and 179.)

[135] R. Vertesi [STAR Collaboration], "Bottomonium production in heavy-ion collisions at STAR," (Cited on page 60.)

[136] L. Adamczyk *et al.* [STAR Collaboration], "Measurement of J/ψ Azimuthal Anisotropy in Au+Au Collisions at $\sqrt{s_{NN}} = 200$ GeV," Phys. Rev. Lett. **111** (2013) 5, 052301 [arXiv:1212.3304 [nucl-ex]]. (Cited on page 60.)

[137] A. Maire [ALICE Collaboration], "Measurements of inclusive J/ψ production in Pb-Pb collisions at $\sqrt{s_{NN}} = 2.76$ TeV with the ALICE experiment," PoS ConfinementX (2012) 211 [arXiv:1301.4058 [hep-ex]]. arXiv:1509.05359 [hep-ex]. (Cited on pages 61, 62, 99, 127, and 179.)

[138] S. Chatrchyan *et al.* [CMS Collaboration], "Suppression of non-prompt J/ψ, prompt J/ψ, and Υ(1S) in PbPb collisions at $\sqrt{s_{NN}} = 2.76$ TeV," JHEP **1205** (2012) 063 [arXiv:1201.5069 [nucl-ex]]. (Cited on pages 61, 62, 99, 127, and 179.)

[139] E. Abbas *et al.* [ALICE Collaboration], "J/Psi Elliptic Flow in Pb-Pb Collisions at $\sqrt{s_{\rm NN}} = 2.76$ TeV," Phys. Rev. Lett. **111** (2013) 162301 [arXiv:1303.5880 [nucl-ex]]. (Cited on pages 62 and 66.)

[140] [CMS Collaboration], "Measurement of the azimuthal anisotropy of prompt J/ψ in PbPb collisions at $\sqrt{s_{NN}} = 2.76$ TeV," CMS PAS HIN-12-001 (2013). (Cited on page 62.)

[141] B. Abelev *et al.* [ALICE Collaboration], "Anisotropic flow of charged hadrons, pions and (anti-)protons measured at high transverse momentum in Pb-Pb collisions at $\sqrt{s_{NN}}$=2.76 TeV," Phys. Lett. B **719** (2013) 18 [arXiv:1205.5761 [nucl-ex]]. (Cited on page 62.)

[142] A. Andronic, "Experimental results and phenomenology of quarkonium production in relativistic nuclear collisions," Nucl. Phys. A **931** (2014) 135 [arXiv:1409.5778 [nucl-ex]]. (Cited on page 63.)

[143] E. G. Ferreiro, "News from quarkonia," Talk at QGP France (2014). (Cited on page 63.)

[144] V. Khachatryan *et al.* [CMS Collaboration], "Measurement of Prompt $\psi(2S) \to J/\psi$ Yield Ratios in Pb-Pb and $p-p$ Collisions at $\sqrt{s_{NN}} = 2.76$TeV," Phys. Rev. Lett. **113** (2014) 26, 262301 [arXiv:1410.1804 [nucl-ex]]. (Cited on pages 63, 99, and 179.)

[145] [CMS Collaboration], "Suppression of $\Upsilon(1S)$, $\Upsilon(2S)$ and $\Upsilon(3S)$ in PbPb collisions at $\sqrt{s_{NN}} = 2.76$ TeV," CMS PAS HIN-15-001 (2015). (Cited on pages 63, 64, 184, and 188.)

[146] A. Andronic, "Quarkonium in the statistical hadronization model," talk at Heavy Flavor and Electromagnetic Probes in Heavy Ion Collisions (2014). (Cited on page 64.)

[147] S. Cao and S. A. Bass, "Thermalization of charm quarks in infinite and finite QGP matter," Phys. Rev. C **84** (2011) 064902 [arXiv:1108.5101 [nucl-th]]. (Cited on page 66.)

[148] J.-P. Blaizot and J.-Y. Ollitrault, "On the fate of a J/ψ produced in a nucleus-nucleus collision," Phys. Rev. D **39** (1989) 232. (Cited on page 67.)

[149] J. Cleymans and R. L. Thews, Z. Phys. C **45** (1990) 391. (Cited on page 67.)

[150] J. Cugnon and P. B. Gossiaux, "J/ψ, ψ', and χ_c suppression in nucleus-nuceus collisions at SPS energies," Phys. Lett. B **359** (1995) 375-381. (Cited on page 67.)

[151] N. Pottier, *Physique statistique hors d'équilibre*. EDP Sciences, CNRS Editions (2007) chap 10. (Cited on pages 68, 105, 106, 174, and 204.)

[152] C. Cohen-Tannoudji, B. Diu and F. Laloë, *Quantum Mechanics*, Wiley (1977) chap. 1 complement G. (Cited on page 68.)

[153] C. Cohen-Tannoudji, B. Diu and F. Laloë, *Quantum Mechanics*, Wiley (1977) chap. VII.B.1. (Cited on pages 75, 81, and 163.)

[154] E. Eichten et al. Phys. Rev D **17** (1978) 3090; **21** (1980) 313(E). (Cited on page 75.)

[155] O. Kaczmarek, S. Ejiri, F. Karsch, E. Laermann and F. Zantow, "Heavy quark free energies and the renormalized Polyakov loop in full QCD," Prog. Theor. Phys. Suppl. **153** (2004) 287 [arXiv:hep-lat/0312015]. (Cited on pages 75 and 78.)

[156] A. Mocsy and P. Petreczky, "Can quarkonia survive deconfinement?," Phys. Rev. D **77** (2008) 014501 [arXiv:0705.2559 [hep-ph]]. (Cited on pages 75, 78, and 202.)

[157] S. Necco and R. Sommer, Nucl. Phys. B **622** (2002) 328 [arXiv:hep-lat/0108008]. (Cited on page 75.)

[158] G. S. Bali, K. Schilling and A. Wachter, "Complete O (v**2) corrections to the static interquark potential from SU(3) gauge theory," Phys. Rev. D **56** (1997) 2566 [hep-lat/9703019]. (Cited on page 75.)

[159] H. Satz, "Colour deconfinement and quarkonium binding," J. Phys. G **32** (2006) R25 [hep-ph/0512217]. (Cited on page 75.)

[160] P. Debye and E. Hückel, "Zur Theorie der Elektrolyte. I. Gefrierpunktserniedrigung und verwandte Erscheinungen," [The theory of electrolytes. I. Lowering of freezing point and related phenomena], Physikalische Zeitschrift **24** (1923) 185-206. (Cited on page 76.)

[161] V. Marin, P. B. Gossiaux *Suppression of the J/ψ suppression*, Master thesis, 2008. (Cited on pages 78 and 81.)

[162] O. Kaczmarek, F. Karsch, F. Zantow and P. Petreczky, "Static quark anti-quark free energy and the running coupling at finite temperature," Phys. Rev. D **70** (2004) 074505 [Phys. Rev. D **72** (2005) 059903] [hep-lat/0406036]. (Cited on page 78.)

[163] PHENIX collaboration, results presented at Quark Matter 2009 conference, http://www.phy.ornl.gov/QM09/. (Cited on page 86.)

[164] T. Aaltonen *et al.* [CDF Collaboration], "Production of psi(2S) Mesons in p anti-p Collisions at 1.96-TeV," Phys. Rev. D **80** (2009) 031103 [arXiv:0905.1982 [hep-ex]]. (Cited on page 86.)

[165] J. Cleymans, H. Oeschler, K. Redlich and S. Wheaton, "Comparison of chemical freeze-out criteria in heavy-ion collisions," Phys. Rev. C **73** (2006) 034905 [hep-ph/0511094]. (Cited on page 88.)

[166] F. Becattini, M. Bleicher, T. Kollegger, T. Schuster, J. Steinheimer and R. Stock, "Hadron Formation in Relativistic Nuclear Collisions and the QCD Phase Diagram," Phys. Rev. Lett. **111** (2013) 082302 [arXiv:1212.2431 [nucl-th]]. (Cited on page 88.)

[167] L. Adamczyk *et al.* [STAR Collaboration], "Suppression of Υ production in d+Au and Au+Au collisions at $\sqrt{s_{NN}}$=200 GeV," Phys. Lett. B **735** (2014) 127 [Phys. Lett. B **743** (2015) 537] [arXiv:1312.3675 [nucl-ex]]. (Cited on pages 99 and 184.)

[168] S. Chatrchyan *et al.* [CMS Collaboration], "Observation of sequential Upsilon suppression in PbPb collisions," Phys. Rev. Lett. **109** (2012) 222301 [arXiv:1208.2826 [nucl-ex]]. (Cited on pages 99 and 184.)

[169] J. H. Weiner and R. E. Forman, "Rate theory for solids. V. Quantum Brownian-motion model.,' Phys. Rev. B **10** (1974) 325. (Cited on page 106.)

[170] S. Bhattacharya, S. Dutta and S. Roy, "Schrodinger-Langevin Equation and Ion Transport at Nano Scale.,' Journal of Modern Physics **2** (2011) 231-235. (Cited on page 106.)

[171] A. P. Jardine, E. Y. M. Lee, D. J. Ward, G. Alexandrowicz, H. Hedgeland, W. Allison, J. Ellis and E. Pollak, "Determination of the Quantum Contribution to the Activated Motion of Hydrogen on a Metal Surface: H/Pt(111)," Phys. Rev. Lett. **105** (2010) 136101. (Cited on page 106.)

[172] I. R. Senitzky, "Dissipation in Quantum Mechanics.,' Phys. Rev. **119** (1960) 670; **124** (1961) 642. (Cited on pages 106, 110, 112, 139, 143, 150, 159, 204, and 206.)

[173] J. J. Degman, D. B. Coyle and R. B. Kay, "Effects of thermalisation on Q-switched laser properties," IEEE J. Quantum Electron. **34** (1998) 887-899. (Cited on page 106.)

[174] J. M. Horowitz, "Quantum Trajectory Approach to the Stochastic Thermodynamics of a Forced Harmonic Oscillator," Phys. Rev. E 85 (2012) 031110. (Cited on pages 106 and 109.)

[175] D. H. E. Gross and H. Kalinowski, "Friction model of heavy ion collisions," Physics Reports **45** (1978) 176-210. (Cited on page 106.)

[176] Y. Hamdouni, "On quantum mechanical transport coefficients in nonequilibrium nuclear processes with application to heavy-ion collisions," J. Phys. G, **37** (2010) 125106. (Cited on page 106.)

[177] K. Yasue, "Quantum mechanics of Non-Conservative systems.,' Annals Phys. **114** (1978) 479-496. (Cited on pages 106, 111, and 135.)

[178] M. A. Nielsen and I. L. Chuang, Quantum Computation and Quantum Information, Cambridge University Press, Cambridge, 2000. (Cited on page 106.)

[179] J. P. Pekola, "Towards quantum thermodynamics in electronic circuits," Nat. Phys. 11 (2015) 118-123. (Cited on page 106.)

[180] L. Henriet, Z. Ristivojevic, P. P. Orth and K. Le Hur, "Quantum Dynamics of the Driven and Dissipative Rabi Model," Phys. Rev. A **90** (2014) 023820. (Cited on page 106.)

[181] G. Lindblad, "Brownian Motion of a Quantum Harmonic Oscillator.,' Rept. Math. Phys. **10** (1976) 393. (Cited on pages 106 and 139.)

[182] U. Weiss, Quantum dissipative systems, chap 2, World Scientific, 2012. (Cited on pages 106, 108, 109, 110, 144, 159, and 204.)

[183] K. Mølmer, Y. Castin and J. Dalibard, J. Opt. Soc. Am. **10** (1993) 524. (Cited on pages 106, 108, 109, 135, 138, and 204.)

[184] H.-P. Breuer and F. Petruccione, The theory of open quantum systems, chap 3 and 6, Oxford University Press, 2002. (Cited on pages 106, 107, 109, 110, 112, and 142.)

[185] G. W. Ford, M. Kac and P. Mazur, "Statistical Mechanics of Assemblies of Coupled Oscillators," J. Math. Phys. **6** (1965) 504. (Cited on pages 106, 110, 139, 143, 159, 204, and 206.)

[186] A. O. Caldeira and A. J. Leggett, "Path Integral Approach to Quantum Brownian Motion," Physica A **121** (1983) 587. (Cited on pages 106, 110, 139, and 204.)

[187] E. Nelson, Phys. Rev. **150** (1966) 1079. (Cited on pages 106 and 111.)

[188] M. Razavy, Z. Physik B **26** (1977) 201. (Cited on pages 106 and 135.)

[189] H. Dekker, "Quantization of the linearly damped harmonic oscillator," Phys. Rev. A **16** (1977) 2126-2134. (Cited on pages 106 and 111.)

[190] P. Caldirola, Nuevo Cimento **18** (1941) 393; E. Kanai, Prog. Theor. Phys. **3** (1948) 440. (Cited on pages 106, 111, and 137.)

[191] I. R. Svin'in, Teor. Mat. Fiz. **22** (1975) 107. (Cited on pages 106 and 111.)

[192] V. E. Tarasov, Theor. Math. Phys. **100** (1994) 1100. (Cited on pages 106 and 111.)

[193] A. O. Bolivar, "Quantization of non-Hamiltonian physical systems," Phys. Rev. A **58** (1998) 4330. (Cited on pages 106 and 135.)

[194] H. Dekker and Z. Physik B **21** (1975) 295; H. Dekker, Physica A **95** (1979) 311. (Cited on page 106.)

[195] K. K. Kan and J. J. Griffin, "Quantized friction and the correspondence principle: single particle with friction," Phys. Lett. B **50** (1974) 241-243. (Cited on pages 106, 111, 135, 138, 139, and 140.)

[196] S. Garashchuk, V. Dixit, B. Gu and J. Mazzuca, "The Schrödinger equation with friction from the quantum trajectory perspective," J. Chem. Phys. **138** (2013) 054107. (Cited on pages 106, 111, 135, 136, 137, 138, 139, and 140.)

[197] R. Biele, C. Timm and R. D'Agosta, "Application of a time-convolutionless stochastic Schrdinger equation to energy transport and thermal relaxation," J. Phys.: Condens. Matter **26** (2014) 395303. (Cited on pages 107, 109, 112, 144, and 146.)

[198] P. Cappellaro, Course: Quantum Theory of Radiation Interactions, Fall 2012, Massachusetts Institute of Technology OpenCourseWare. (Cited on page 107.)

[199] N. Gisin and I. Percival, Phys. Lett. A **167** (1992) 315; J. Phys. A **25** (1992) 5677. (Cited on pages 108, 109, 135, 138, and 204.)

[200] G. Lindblad, Commun. Math. Phys. **48** (1976) 119. (Cited on pages 109 and 204.)

[201] C. P. Slichter, *Principles of Magnetic Resonance* (Springer, Berlin, 1990). (Cited on page 109.)

[202] Y. R. Shen, *The Principles of Nonlinear Optics* (Wiley, New York, 1984). (Cited on page 109.)

[203] L. Diósi, N. Gisin and W. T. Strunz, "Non-Markovian Quantum State Diffusion," Phys. Rev. A **58** (1998) 1699. (Cited on pages 109 and 204.)

[204] P. Hänggii and G.-L. Ingold, "Fundamental Aspects of Quantum Brownian Motion," Chaos **15** (2005) 026105. (Cited on pages 111 and 159.)

[205] R. H. Koch, D. J. van Harlingen and J. Clarke, Phys. Rev. Lett. **45** (1980) 2132. (Cited on page 111.)

[206] K. L. Sebastian, Chem. Phys. Lett. **81** (1981) 14. (Cited on page 111.)

[207] A. Schmid, J. Low Temp. Phys. **49** (1982) 608. (Cited on page 111.)

[208] H. Metiu and G. Schön, Phys. Rev. Lett. **53** (1984) 13. (Cited on page 111.)

[209] U. Eckern, W. Lehr, A. Menzel-Dorwarth, F. Pelzer and A. Schmid, "The quasiclassical Langevin equation and its application to the decay of a metastable state and to quantum fluctuations," J. Stat. Phys. **59** (1990) 885. (Cited on pages 111 and 159.)

[210] D. Banerjee, B. Chandra Bag, S. Kumar Banik and D. Shankar Ray, "A numerical method for generation of quantum noise and solution of generalized c-number quantum Langevin equation," (Unpublished results) [arXiv: cond-mat/0303059]. (Cited on page 111.)

[211] D. Banerjee, B. Chandra Bag, S. Kumar Banik and D. Shankar Ray, "Solution of quantum Langevin equation: Approximations, theoretical and numerical aspects," J. Chem. Phys. **120** (2004) 8960. (Cited on page 111.)

[212] R. Benguria and M. Kac, Phys. Rev. Lett. **46**, 1 (1981). (Cited on pages 111, 112, and 143.)

[213] C. Gardiner and P. Zoller, *Quantum Noise, A Handbook of Markovian and Non-Markovian Quantum Stochastic Methods with Applications to Quantum Optics*, (Springer, Berlin, 2000), chap. 3.6 and chap. 1.2. (Cited on pages 111, 112, 143, and 144.)

[214] N. Brambilla, J. Ghiglieri, A. Vairo and P. Petreczky, "Static quark-antiquark pairs at finite temperature," Phys. Rev. D **78** (2008) 014017 [arXiv:0804.0993 [hep-ph]]. (Cited on page 113.)

[215] N. Brambilla, M. A. Escobedo, J. Ghiglieri, J. Soto and A. Vairo, "Heavy Quarkonium in a weakly-coupled quark-gluon plasma below the melting temperature," JHEP **1009** (2010) 038 [arXiv:1007.4156 [hep-ph]]. (Cited on page 113.)

[216] Y. Burnier, O. Kaczmarek and A. Rothkopf, "Static quark-antiquark potential in the quark-gluon plasma from lattice QCD," Phys. Rev. Lett. **114** (2015) 8, 082001 [arXiv:1410.2546 [hep-lat]]. (Cited on page 113.)

[217] M. Strickland, "Thermal υ_{1S} and χ_{b1} suppression in $\sqrt{s_{NN}} = 2.76$ TeV Pb-Pb collisions at the LHC," Phys. Rev. Lett. **107** (2011) 132301 [arXiv:1106.2571 [hep-ph]]. (Cited on page 113.)

[218] M. Strickland, "Thermal Bottomonium Suppression," AIP Conf. Proc. **1520** (2013) 179 [arXiv:1207.5327 [hep-ph]]. (Cited on page 113.)

[219] N. Dutta and N. Borghini, "Sequential suppression of quarkonia and high-energy nucleus-nucleus collisions," arXiv:1206.2149 [nucl-th]. (Cited on page 113.)

[220] J. P. Blaizot, D. De Boni, P. Faccioli and G. Garberoglio, "Heavy quark bound states in a quark-gluon plasma: dissociation and recombination," arXiv:1503.03857 [nucl-th]. (Cited on page 114.)

[221] C. Young and K. Dusling, "Quarkonium above deconfinement as an open quantum system," Phys. Rev. C **87** (2013) 6, 065206 [arXiv:1001.0935 [nucl-th]]. (Cited on pages 114 and 115.)

[222] Y. Akamatsu, "Real-time quantum dynamics of heavy quark systems at high temperature," Phys. Rev. D **87** (2013) 4, 045016 [arXiv:1209.5068 [hep-ph]]. (Cited on pages 114, 115, and 205.)

[223] N. Borghini and C. Gombeaud, "Heavy quarkonia in a medium as a quantum dissipative system: Master equation approach," Eur. Phys. J. C **72** (2012) 2000 [arXiv:1109.4271 [nucl-th]]. (Cited on pages 114, 115, and 205.)

[224] Y. Akamatsu and A. Rothkopf, "Stochastic potential and quantum decoherence of heavy quarkonium in the quark-gluon plasma," Phys. Rev. D **85** (2012) 105011 [arXiv:1110.1203 [hep-ph]]. (Cited on pages 114, 116, and 205.)

[225] Y. Akamatsu, "Master equation of quarkonia in the Lindblad form," Poster at QM (2014). (Cited on page 115.)

[226] R. Katz and P. B. Gossiaux, "Semi-classical approach to J/ψ suppression in high energy heavy-ion collisions," J. Phys. Conf. Ser. **509** (2014) 012095 [arXiv:1312.0881 [hep-ph]]. (Cited on pages 120, 127, and 206.)

[227] Liboff R L 1990 *Kinetic Theory: Classical, Quantum, and Relativistic Descriptions* (Wiley-interscience) (Cited on page 121.)

[228] V. Marin, "Suppression de la suppression du J/ψ," DEA report (2008). (Cited on page 122.)

[229] C. Cohen-Tannoudji, B. Diu and F. Lalo, *Quantum Mechanics*, Wiley (1977). (Cited on page 123.)

[230] H. Risken, *The Fokker-Planck equation*, Springer Series in Synergistics (1996). (Cited on page 124.)

[231] P. B. Gossiaux and J. Aichelin, "Towards an understanding of the RHIC single electron data," Phys. Rev. C **78** (2008) 014904 [arXiv:0802.2525 [hep-ph]]. (Cited on pages 124, 125, and 180.)

[232] H. Ding, A. Francis, O. Kaczmarek, F. Karsch, H. Satz, *et al.*, "Charmonium properties in hot quenched lattice QCD," Phys. Rev. D **86** (2012) 014509 [arXiv:1204.4945 [hep-lat]]. (Cited on page 124.)

[233] D. Banerjee, S. Datta, R. Gavai, and P. Majumdar, "Heavy Quark Momentum Diffusion Coefficient from Lattice QCD, Phys. Rev. D **85** (2012) 014510 [arXiv:1109.5738 [hep-lat]]. (Cited on page 124.)

[234] H. Berrehrah, P. B. Gossiaux, J. Aichelin, W. Cassing, J. M. Torres-Rincon and E. Bratkovskaya, "Transport coefficients of heavy quarks around T_c at finite quark chemical potential," Phys. Rev. C **90** (2014) 051901 [arXiv:1406.5322 [hep-ph]]. (Cited on page 124.)

[235] P. B. Gossiaux, "Some notes on suppression of suppression," Internal note (2013). (Cited on page 128.)

[236] C. Sparber, J. A. Carrillo, and J. Dolbeault and P. A. Markowich, *On the Long-Time Behavior of the Quantum Fokker-Planck Equation*, Monatshefte fr Mathematik, March 2004, Volume 141, Issue 3, pp 237-257 (Cited on pages 129 and 130.)

[237] D. J. Tannor, *Introduction to Quantum Mechanics: A Time-Dependent Perspective,* University Science Books (2006) Chap 5.4. (Cited on page 130.)

[238] R. Katz and P. B. Gossiaux, "The Schrödinger-Langevin equation with and without thermal fluctuations," DOI: 10.1016/j.aop.2016.02.005 (2015) [arXiv: quant-ph/1504.08087]. (Cited on pages 134 and 207.)

[239] H. D. Doebner, G. A. Goldin and P. Nattermann, "Gauge transformations in quantum mechanics and the unification of nonlinear Schrodinger equations',' J. Math. Phys. **40** (1999) 49 [arXiv: quant-ph/9709036]. (Cited on page 135.)

[240] R. J. Wysocki, Phys.l Rev. A, **61** (2000) 022104. (Cited on page 135.)

[241] T. Fulop and S. D. Katz, (1998) [arXiv: quant-ph/9806067]. (Cited on page 135.)

[242] P. Ruggiero and M. Zannetti, La Rivista Del Nuovo Cimento Series 3, **8** (5) (1985) 1-47. (Cited on page 135.)

[243] R. Tsekov, "Nonlinear theory of quantum Brownian motion," Ann. Univ. Sofia, Fac. Phys. **105** (2012) 14-21 [arXiv 1003.0304]. (Cited on page 137.)

[244] A.L. Sanin and A.A. Smirnovsky, "Computer simulation of quantum systems with friction and feedback," Materials Physics and Mechanics, **20** (2014) 98-105 . (Cited on pages 137, 139, and 144.)

[245] H. Dekker, Physics Reports, **80** (1) (1981) 1110. (Cited on pages 137, 138, and 144.)

[246] R. Tsekov, "Nonlinear theory of quantum Brownian motion," Int. J. Theor. Phys. 48 (2009) 85-94 [arXiv: 0711.1442]. (Cited on page 138.)

[247] A.J. Leggett, Suppl. Prog. Theor. Phys. **69** (1980) 80. (Cited on page 138.)

[248] P. Bargueño and S. Miret-Artés, "The generalized SchrdingerLangevin equation," Ann. Phys. **346** (2014) 5965. (Cited on page 138.)

[249] A. F. Vargas, N. Morales-Durán and P. Bargueño, "A Bohmian approach to the non-Markovian non-linear SchrdingerLangevin equation," Ann. Phys. **356** (2015) 59-65. (Cited on page 138.)

[250] J. D. Immele, K. K. Kan and J. J. Griffin, Nucl. Phys. A **241** (1975) 47. (Cited on page 138.)

[251] R. W. Hasse, J. Math. Phys. **16** (1975) 2005. (Cited on page 138.)

[252] B. S. Skargerstam, Phys. Lett. B **58** (1975) 21. (Cited on pages 138, 139, and 140.)

[253] L. Brüll and H. Lange, "The Schrödinger-Langevin equation: Special solutions and nonexistence of solitary waves," J. Math. Phys. **25** (1984) 786790. (Cited on page 138.)

[254] D. de Falcoa and D. Tamascelli, Phys. Rev. A **79** (2009) 012315. (Cited on page 138.)

[255] T. Wells, J. D. Immele, K. K. Kan and J. J. Griffin, Bull. Am. Phys. Soc. **19** (1974) 527. (Cited on page 138.)

[256] M. Razavy, Can. J. Phys. **56** (1978) 311. (Cited on page 138.)

[257] A. Sandulescu, M. Petrovici, A. Pop, M.S. Popa, J. Hahn, K.H. Ziegenhain and W. Greiner, "On the dynamics of charge equilibration in deep inelastic reactions," J. Phys. G: Nucl. Phys. **7** L55 (1981). (Cited on pages 139 and 140.)

[258] E.S. Hernandez, W.D. Myers, J. Randrup and B. Remaud, "Quantal dynamics of charge equilibration in damped nuclear collisions," Nucl. Phys. A **361** (1981) 483-501. (Cited on pages 139 and 140.)

[259] J. Messer, Acta Phys. Austriaca **50** (1979) 75-91. (Cited on pages 139, 143, and 159.)

[260] J. H. Weiner and R. E. Forman, "Rate theory for solids. V. Quantum Brownian-motion model," Phys. Rev. B **10** (1974) 325. (Cited on page 139.)

[261] A.L. Sanin and A.A. Smirnovsky, "Oscillatory motion in conned potential systems with dissipation in the context of the SchrödingerLangevinKostin equation," Phys. Lett. A **372** (2007) 21-27. (Cited on pages 139 and 151.)

[262] P. Van and T. Fulop, "Stability of stationary solutions of the Schrödinger-Langevin equation," Phys. Lett. A **323** (5-6) (2004) 374-381. (Cited on page 140.)

[263] V. E. Tarasov, "Stationary States of Dissipative Quantum Systems," Phys. Lett. A **299** (2002) 173-178. (Cited on page 142.)

[264] X.L. Li, G.W. Ford and R.F. O'Connell, Phys. Rev. E **51** (5) (1995) 5169-5171. (Cited on page 143.)

[265] R. H. Koch, D. J. van Harlingen and J. Clarke, Phys. Rev. Lett. **47** (17) (1981) 1216. (Cited on page 144.)

[266] R. S. Whitney, J. Phys. A: Math. Theor. **41** (2008) 175304. (Cited on page 144.)

[267] W. H. Zurek, "Decoherence, einselection, and the quantum origins of the classica," Rev. Mod. Phys. **75** (2003) 715. (Cited on page 152.)

[268] B. B. Abelev *et al.* [ALICE Collaboration], "Suppression of $\Upsilon(1S)$ at forward rapidity in PbPb collisions at $\sqrt{s_{NN}} = 2.76$TeV," Phys. Lett. B **738** (2012) 361. (Cited on page 184.)

[269] K. Werner, I. Karpenko, T. Pierog, M. Bleicher and K. Mikhailov, Phys. Rev. C **82** (2010) 044904. (Cited on page 185.)

[270] K. Werner, I. Karpenko, M. Bleicher, T. Pierog and S. Porteboeuf-Houssais, Phys. Rev. C **85** (2012) 064907. (Cited on page 185.)

[271] S. Borsanyi *et al.* [Wuppertal-Budapest Collaboration], "Transition temperature and the equation of state from lattice QCD, Wuppertal-Budapest results," Acta Phys. Polon. Supp. **4** (2011) 593 [arXiv:1109.5032 [hep-lat]]. (Cited on page 185.)

[272] B. Abelev *et al.* [ALICE Collaboration], "Centrality dependence of π, K, p production in Pb-Pb collisions at $\sqrt{s_{NN}} = 2.76$ TeV," Phys. Rev. C **88** (2013) 044910 [arXiv:1303.0737 [hep-ex]]. (Cited on page 185.)

[273] P. B. Gossiaux and R. Katz, "Upsilon suppression in the Schrödinger-Langevin approach," [arXiv:1601.01443 [hep-ph]]. (Cited on pages 189 and 207.)

Thèse de Doctorat

Roland KATZ

Une approche quantique de la suppression dynamique des quarkonia dans les collisions d'ions lourds à haute énergie

A quantum approach to dynamical quarkonia suppression in high energy heavy ion collisions

Résumé

La chromodynamique quantique (QCD) prédit l'existence d'un nouvel état de la matière: le plasma de quarks et de gluons (PQG). Celui-ci aurait existé dans les premiers instants suivant le Big Bang et peut en principe être produit sous les conditions extrêmes de température et de densité atteintes lors de collisions d'ions lourds à haute énergie (au LHC par exemple). Un des marqueurs de sa présence est la suppression des quarkonia (états liés de quark/antiquark lourds), caractérisée par une production inférieure de ces états dans les collisions d'ions lourds relativement aux collisions proton-proton où le PQG ne pourrait être créé. Cette suppression a bien été observée expérimentalement, mais l'évolution de ses tendances aux énergies du RHIC et du LHC est un véritable défi qui requiert une meilleure compréhension théorique. La présente thèse a pour but d'étudier l'évolution en temps réel de paires corrélées de quark/antiquark lourds considérées comme des systèmes quantiques ouverts en interaction permanente avec un PQG en refroidissement. Explicitement, l'interaction continue entre le milieu et les degrés de liberté internes de la paire est obtenue par 1) un écrantage de couleur dit « de Debye » dû à la présence de charges de couleur dans leur voisinage et 2) des mécanismes de fluctuation/dissipation qui reflètent les collisions permanentes. Cela mène à une image dynamique et continue de la dissociation des quarkonia, de leur recombinaison et des transitions entre états liés. L'étude est transversale à différents cadres théoriques: semi-classique, quantique et quantique des champs. Les prédictions du modèle sont comparées aux résultats expérimentaux et aux résultats d'autres modèles théoriques.

Mots clés

Plasma de quarks et gluons, suppression des quarkonia, approche dynamique, système quantique ouvert, équation de Schrödinger-Langevin

Abstract

The theory of quantum chromodynamics (QCD) predicts the existence of a new state of matter: the Quark-Gluon Plasma (QGP). The latter may have existed at the first moments of the Universe following the Big Bang and can be, in theory, re-produced under the extreme conditions of temperature and density reached in high energy heavy ion collisions (at the LHC for instance). One of the QGP observables is the suppression of the quarkonia (heavy quark/antiquark bound states), characterised by a smaller production of these states in heavy ion collisions in comparison to proton-proton collisions, in which no QGP production would be possible. This suppression has indeed been observed experimentally, but the puzzling evolution of its trend from RHIC to LHC energies requires a better theoretical understanding. The present thesis aims at studying the real-time evolution of correlated heavy quark/antiquark pairs described as open quantum systems which permanently interact with a cooling QGP. More explicitly, the continuous interaction between the medium and the pair internal degrees of freedom is obtained through 1) a temperature dependent color screening ("Debye" like) due to color charges in their vicinity and 2) some fluctuation/dissipation mechanisms reflecting the continuous collisions. It leads to a dynamical and continuous picture of the dissociation, recombination and possible transitions to other bound states. This investigation is at the crossroads of different theoretical frameworks: semi-classic, quantum and quantum fields. The deduced predictions are compared to experimental data and to the results of other theoretical models.

Key Words

Quark-Gluon Plasma, quarkonia suppression, dynamical approach, open quantum system, Schrödinger-Langevin equation

L'Université Nantes Angers Le Mans